PB88-140819

Study of the Mechanical Behavior of a 2-D Carbon-Carbon Composite

Virginia Tech Center for Composite Materials and Structures, Blacksburg

Prepared for

National Aeronautics and Space Administration
Hampton, VA

Aug 87

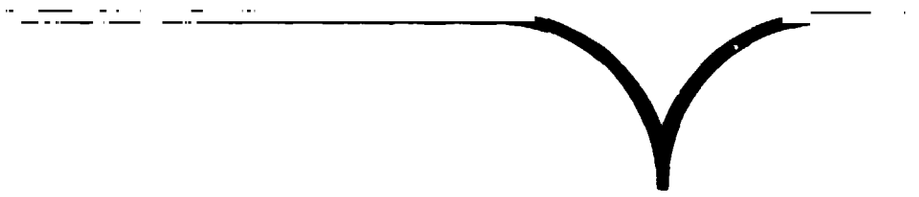

PB88-140819

CCMS-87-13
VPI-E-87-15

VIRGINIA TECH

CENTER FOR COMPOSITE MATERIALS AND STRUCTURES

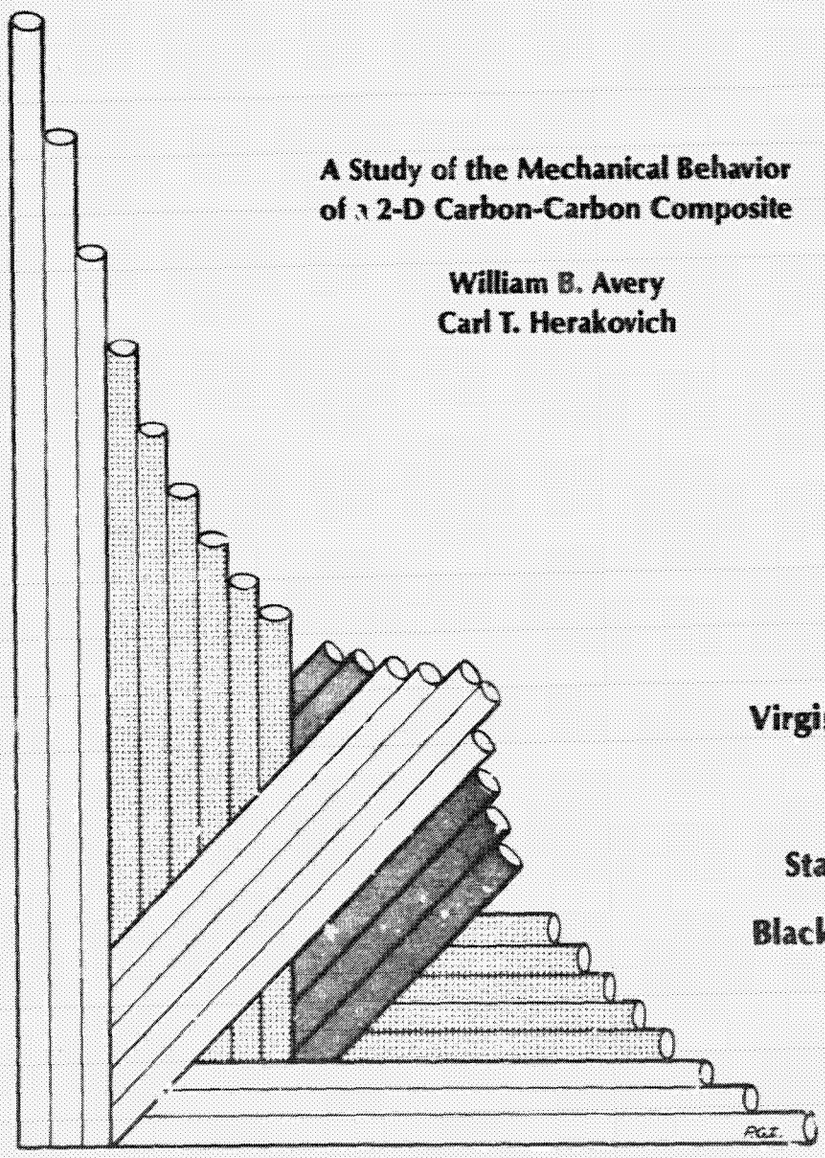

A Study of the Mechanical Behavior of a 2-D Carbon-Carbon Composite

William B. Avery
Carl T. Herakovich

Virginia Polytechnic Institute
and
State University

Blacksburg, Virginia
24061

BIBLIOGRAPHIC DATA SHEET	1. Report No. CCMS-87-13, VPI-E-87-15	2.	3. Recipient's Accession No. PB88 140819/AS
4. Title and Subtitle A STUDY OF THE MECHANICAL BEHAVIOR OF A 2-D CARBON-CARBON COMPOSITE			5. Report Date Aug 1987 6.
7. Author(s) W. B. Avery and C. T. Herakovich			8. Performing Organization Rept. No. VPI-E-87-15
9. Performing Organization Name and Address Virginia Polytechnic Institute & State University Dept of Engineering Science & Mechanics 106 Norris Hall Blacksburg, Virginia 24061			10. Project/Task/Work Unit No. 11. Contract/Grant No. NAG-1-343
12. Sponsoring Organization Name and Address Applied Materials Branch National Aeronautics and Space Administration Langley Research Center Hampton, Virginia 23665			13. Type of Report & Period Covered 14.

15. Supplementary Notes

16. Abstracts

The objective of this study was to observe and characterize the out-of-plane fracture of a 2-D carbon-carbon composite and to gain an understanding of the factors influencing the stress distribution in such a laminate.

Finite element analyses of a two-ply carbon-carbon composite under in-plane, out-of-plane, and thermal loading were performed. The results indicated that under out-of-plane loading σ_z and τ_{xz} were strongly dependent on stacking sequence, undulation aspect ratio, and undulation offset ratio, but σ_x and σ_y were relatively independent of geometry. Under in-plane loading all components of stress were strong functions of geometry. Additionally, large thermal stresses were predicted. Out-of-plane tensile tests revealed that failure was interlaminar, and that cracks propagated along the fiber-matrix interface.

An elasticity solution was utilized to analyze an orthotropic fiber in an isotropic matrix under uniform thermal load. The analysis reveals that the stress distributions in a transversely orthotropic fiber are radically different than those predicted assuming the fiber to be transversely isotropic.

17. Key Words and Document Analysis. 17a. Descriptors

carbon-carbon composites, woven fabric composites, finite element analysis, anisotropic elasticity, thermal stresses, mechanical stresses, interlaminar stresses

17b. Identifiers/Open-Ended Terms

17c. COSATI Field/Group

18. Availability Statement	19. Security Class (This Report)	21. No. of Pages
unlimited	UNCLASSIFIED	
	20. Security Class (This Page) UNCLASSIFIED	22. Price

College of Engineering
Virginia Polytechnic Institute and State University
Blacksburg, Virginia 24061

August 1987

CCMS-87-13
VPI-E-87-15

A Study of the Mechanical Behavior of a 2-D Carbon-Carbon Composite

William B. Avery[1]
Carl T. Herakovich[2]

Department of Engineering Science & Mechanics

Interim Report 66
The NASA-Virginia Tech Composites Program
NASA Grant NAG-1-343

Prepared for

Applied Materials Branch
National Aeronautics and Space Administration
Langley Research Center
Hampton, Virginia 23665

---

[1] Graduate Student, Department of Engineering Science & Mechanics

[2] Professor, Department of Engineering Science & Mechanics

A Study of the Mechanical Behavior of a 2-D Carbon-Carbon Composite

(ABSTRACT)

The objective of this study was to observe and characterize the out-of-plane fracture of a 2-D carbon-carbon composite and to gain an understanding of the factors influencing the stress distribution in such a laminate. The experimental portion of this study consisted of performing an out-of-plane tensile test in a scanning electron microscope and determining the modes of failure. Failure was found to be interlaminar, with cracks propagating along the fiber-matrix interface.

Finite element analyses of a two-ply carbon-carbon composite under in-plane, out-of-plane, and thermal loading were performed. Stress distributions were studied as a function of stacking sequence, undulation aspect ratio, and undulation offset ratio. The results indicated that under out-of-plane loading σ_x and τ_{xz} were strongly dependent on the geometric parameters studied, but σ_z and σ_y were relatively independent of geometry. Under in-plane loading all components of stress were strong functions of the geometry, and large interlaminar stresses were predicted in regions of undulation. The thermal analysis predicted the presence of large in-plane normal stresses throughout the laminate and large interlaminar stresses in regions of undulation.

An elasticity solution was utilized to analyze an orthotropic fiber in an isotropic matrix under uniform thermal load. The analysis reveals that the stress distributions in the fiber are singular when the radial stiffness C_{rr} is greater than the hoop stiffness $C_{\theta\theta}$. Conversely, if $C_{rr} < C_{\theta\theta}$ the maximum stress in the composite is finite and occurs at the fiber-matrix interface. In both cases the stress distributions are radically different than those predicted assuming the fiber to be transversely isotropic ($C_{rr} = C_{\theta\theta}$).

Acknowledgements

The authors would like to thank Dr. Howard Maahs of the NASA Langley Research Center for his assistance in monitoring this research, Phillip Ransone and Elsie Illg, also of NASA Langley, for their assistance with the experimental portion of this study, and Dr. Daniel Leiser of the NASA Ames Research Center for use of their scanning electron microscope facilities.

This study was supported by the NASA-Virginia Tech Composites Program under the NASA Contract Grant NAG 1-3[illegible]

Table of Contents

List of Illustrations

List of Tables

1.0 Introduction and Literature Review

1.1 Introduction

Carbon-carbon composites are one of the more unusual composites in that they consist of a carbon matrix reinforced with carbon fibers. Since carbon-carbon composites are composed of elemental carbon, they can withstand very high temperatures (up to 2200 °C) and heating rates without appreciable degradation in their properties. In fact, they can actually be made stronger at high temperatures. Additional advantages of carbon-carbon composites include high thermal shock resistance, high temperature shape stability, chemical inertness (except in highly oxidizing environments), and high strength efficiency. Figure 1 compares the strength efficiency of carbon-carbon composites with ceramics and superalloys.[1] As is shown, the major advantage of carbon-carbon composites for high-temperature applications is that they do not lose strength as the temperature is increased in vacuum. This is in marked contrast to other high temperature materials such as ceramics and superalloys. The figure shows two levels of carbon-carbon strength efficiency. The first, labeled Shuttle material, is the strength level of the Reinforced Carbon-Carbon (RCC) used on the nose cap and leading edges of the Space Shuttle. Although this material is made with low-strength carbon fibers,

its strength efficiency is still greater than superalloys and ceramics at temperatures greater than 1000 °C. More recent research has led to the development of an advanced carbon-carbon (ACC), which uses a woven carbon cloth and has twice the strength of RCC and is therefore much more strength efficient.

One of the driving forces behind the development of ACC has been the desire for an alternative thermal protection system (TPS) for the lower surface of the Shuttle Orbiter. Currently the lower surface TPS of the Shuttle consists of High-temperature Reusable Surface Insulation (HRSI) tiles. The tiles are a low density silica-based ceramic. Although the HRSI tiles adequately withstand the thermal environment (1260 °C) seen by the Orbiter during re-entry, the tiles exhibit low strength and lack desirable impact, handling, and other damage tolerance characteristics. A thin panel of carbon-carbon, on the order of 0.10 inches thick, would be more damage tolerant than HRSI and would most likely result in a significant weight saving. Such properties not only make carbon-carbon a desirable material for the TPS of the Shuttle Orbiter, but also for more advanced aerospace vehicles.

Carbon-carbon composites are not without their disadvantages, however. The manufacture of carbon-carbon composites is a multi-step process, which results in long fabrication and processing times and high fabrication costs. The strain-to-failure is also low, ranging from 0.3 to about 1.1%. The high thermal conductivity of carbon-carbon typically requires the use of additional insulation material between the carbon-carbon and the aircraft structure. Additionally, carbon-carbon composites exhibit low oxidation resistance; therefore, they must be treated with oxidation resistant coatings. The general advantages and limitations of carbon-carbon composites are have been discussed by Schmidt [2] and are summarized in Table 1.

It has long been recognized that carbon-carbon composites exhibit low strength in the unreinforced directions; therefore, three-dimensionally reinforced carbon-carbon has been the norm.[2 3 4] A representative 3-D carbon-carbon is AVCO Mod-3, which has a woven layer of orthogonal fibers in the x-y plane and is pierced with fibers in the z direction [5] It has been used for re-entry nose tips and for re-entry cassettes, which are containment vessels for radioactive

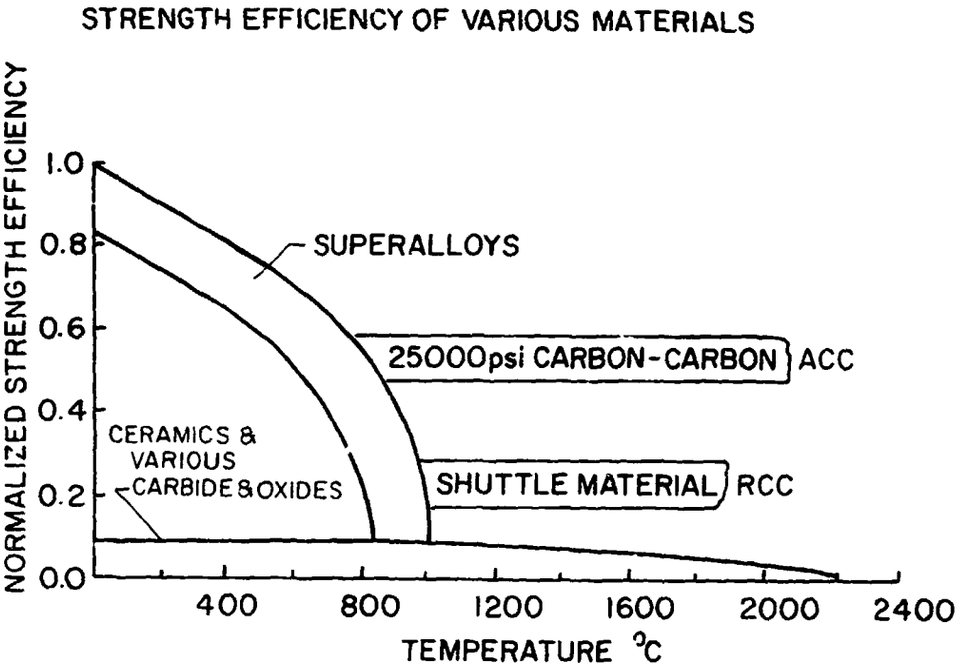

Figure 1. Strength efficiency of various materials.

isotopes. For rocket nozzle applications cylindrically woven 3-D carbon-carbon composites have been developed and utilized.

The disadvantages of 3-D carbon-carbon for thin-gauge thermal protection systems are four-fold: three-dimensional fabrics are expensive to weave and thus would increase the cost of the material; they tend to lack conformability to sharp or multiple contours; parts of different thickness or parts with graded thickness cannot be fabricated; reinforcement in the out-of-plane direction reduces the volume fraction of reinforcement in the in-plane directions with a resulting decrease in in-plane properties.

The logical alternative to 3-D carbon-carbon is 2-D carbon-carbon, which is reinforced in the in-plane directions only and thus has none of the disadvantages of the 3-D material listed above. However, the absence of thru-thickness reinforcement in 2-D carbon-carbon manifests itself in its low tensile strength in the out-of-plane direction. Current out-of-plane tensile strengths are on the order of 500 psi whereas a tensile strength of at least 1000 psi is needed for the foreseeable applications.

The purpose of this study is to observe and characterize the out-of-plane fracture of 2-D carbon-carbon and to gain an understanding of the parameters influencing the out-of-plane strength of the material. It is hoped that such an understanding will help guide researchers towards a material system that will result in improved out-of-plane tensile properties.

Chapter 2 presents the results of an experimental program in which a carbon-carbon laminate was tested under out-of-plane loading conditions. A discussion of the modes of laminate failure is given.

The application of the stress analysis to the region in the carbon-carbon laminate where failure occurred is presented in Chapters 3. Chapter 3 focuses on the influence of the woven nature of the composite and the ply stacking sequence on the stress distribution in the laminate.

Chapter 4 addresses the issue of fiber microstructure, its influence on the transverse elastic constants, and the resulting thermal stress distributions. Results are presented for a the case of graphite fiber and surrounding matrix under uniform thermal load.

Table 1. General advantages and limitations of carbon-carbon.

ADVANTAGES	LIMITATIONS
High Temperature Shape Stability	MATERIALS
High Sublimation Temperature	Low Off-Axis Mechanical Properties
Low Ablation Recession	Low Strain-To-Failure
High Strength and Stiffness Parallel to Reinforcement Direction	High Costs
	High Void Content
Retention of Strength and Stiffness at Elevated Temperatures	Low Fiber/Matrix Bond Strength
Thermal Stress Resistant	High Thermal Conductivity
Thermal Shock Resistant	Low Oxidation Resistance
Pseudo-Plastic Mechanical Behavior	Low Particle Erosion Resistance
Crack Propagation Resistant	Nonuniform Pore Distribution
Nonbrittle Fracture	PROCESSING
Impulse Attenuating	Long Fabrication and Processing Times
Chemical Inertness	Reproducibility
Machinability	
Lightweight	DESIGN
Radiation Resistant	Limited Design and Engineering Properties
Tailorable Properties	Failure Criteria Lacking
Nonstrategic Materials	Attachments and Joints
Fabricability	Complex Design Methodology
	Complex Response to Environment
	Anisotropic Behavior
	Nondestructive Inspection Not Well Developed
	Limited Applications Experience

1.2 Literature Review

Woven fabric composites have been in commercial use for some time. Elevators on the Boeing 727 are a honeycomb structure with woven fabric face sheets. Boeing also uses a graphite/epoxy woven fabric composite in the horizontal stabilizer of the 737. McDonnell Douglas manufactured DC-10 rudders utilizing woven fabric composites in the early 1970's. The wing of the McDonnell Douglas AV-8B Harrier is mostly woven fabric composites. Kevlar 49 and graphite fabrics are used in the farings and ailerons, respectively, of the Lockheed L-1011. [6] However, research on the mechanical behavior of woven fabric composites has generally been neglected by the research community. The exception has been Ishikawa and Chou, who have published several papers on the in-plane elastic behavior of woven fabric composites. [7-13] In their analyses, Ishikawa and Chou developed several 2-D models for simulating the in-plane behavior of woven fabric composites. In the "mosaic model" [7,8] a plain weave composite is modeled as an assemblage of pieces of cross-ply laminates from which the upper and lower bounds of elastic constants are estimated. The "fiber undulation model"[9] is a refinement of the "mosaic model" that accounts for fiber continuity and the effect of fiber undulations on the stiffness of the composite. The mosaic and fiber undulation models, however, are insufficient for modeling satin fabrics, where each undulation is surrounded by straight fibers. Therefore, a "bridging model" has been developed, which attempts to simulate the load transfer between the regions of undulation and the regions of straight fibers. [10,11] These models have also been extended to the thermal loading case and for nonlinear material behavior.[12,13]

Kriz used the finite element method to study the response of plain weave glass-epoxy laminates to cryogenic temperatures. Stiffness and stress distributions were calculated for an undamaged composite under thermal-mechanical loading.[14] This was later extended to the case of a damaged composite.[15] Free edge effects were also investigated.[16] Kimpara et al.

used finite element analysis and acoustic emission to analyze the first knee behavior of a fiberglass cloth reinforced plastic.[17]

Jortner presented a mechanistic model for the delamination of 2-D carbon-carbon composites.[18] In this analysis a two-layer model of a plain weave composite was constructed in which the weave was approximated by a sine wave. The interface is thus a sine wave, the angle of rotation between each point on the interface and the far-field stress was found, and the local stresses along the interface were found using standard stress transformation techniques. Delamination was then predicted using a fracture criteria proposed by Wu and Reuter [19] that was modified for friction along the interface.

Stanton and Kipp used the finite element method to model the nonlinear behavior of plain weave 2-D carbon-carbon composites.[20] The model was confined to the low modulus material used in involute cylinders for rocket nozzle applications.

Walrath and Adams have done an excellent literature review of the finite element and analytical micromechanics and minimechanics models of carbon-carbon composites.[21] They review the early efforts to model unidirectional carbon-carbon composites, including attempts to examine the influence of the crystallographic orientation of the matrix on the elastic modulus of the composite. Also discussed are the analytical predictions of the stress-strain behavior of unidirectional carbon-carbon. The review also reveals that the majority of the minimechanics analyses were applied to 3-D carbon-carbon. These analyses ranged from relatively simple linear elastic models to those that addressed void content and matrix cracking.

2.0 Experimental Investigation

2.1 *Introduction*

The experimental phase of this study constituted what could be considered a first step in the investigation of the out-of-plane tensile strength of a 2-D carbon-carbon laminate, namely, the identification of the failure mode(s). Failure analysis of engineering materials, be they metallic or non-metallic, usually consists of visual and/or microscopic examination of the failed components. Investigators don't normally have the luxury of observing failure. If the investigators happen to be present, such as in a laboratory environment, they may observe failure in the macroscopic sense. However, the facilities to observe microscopic events during failure are not usually available. Thus, the investigator must rely on post-failure analysis and engineering judgement in order to determine the cause and mode of failure. The object of this experiment was to observe and characterize the out-of-plane tensile failure of a 2-D carbon-carbon composite on a microscopic level. This was done by placing a carbon-carbon specimen into a scanning electron microscope (SEM) equipped with a tensile stage and video taping an out-of-plane tensile test. This was followed by post-failure microscopy of the frac-

ture surfaces of the specimen. The testing was performed at the facilities of the Entry Technology Branch, NASA-Ames Research Center, Moffett Field, California.

2.2 Material Description

The carbon-carbon panel prepared for this study utilized an eight-harness satin fabric of T-300 graphite tows, with each tow consisting of approximately 3000 filaments. The fabric consists of what is known as warp tows and fill tows. When the fabric is woven the warp tows remain straight and the fill tows are arranged such that they go under every eighth tow (Figure 2).

After the fabric is removed from the loom, however, the fabric relaxes and curvature exists in both the warp and fill tows. It should be noted that fabrics do not necessarily have an equal number of warp and fill tows. Thus, the mechanical properties in the warp and fill directions are not necessarily the same. For example, a T300/5208 graphite cloth/epoxy laminate was found to have have an axial modulus of 10 MSI in the warp direction versus 9.4 MSI in the fill direction. The tensile strength decreased from 83 ksi in the warp direction to 70 ksi in the fill direction.[52] Additionally, fill tows tend to have more twist due to the weaving process, which also affects mechanical properties. The fabric used in this study had 24 tows per inch in the warp direction and 23 tows per inch in the fill direction. The fabric was Fiberite Corporation's Style W-133. Its specifications are given in Table 2.

The panel was supplied by NASA-Langley Research Center. It was prepared by stacking nine layers of fabric together in a cross-ply type configuration, with the warp direction of each layer oriented 90° with respect to its neighbor. Since there are an odd number of layers, the laminate has a warp-predominate direction, a fill-predominate direction, and is therefore unsymmetric. The layers of fabric were impregnated with a phenolic resin, cured similarly to that of a graphite/epoxy composite, then pyrolized at high temperature in order to convert the

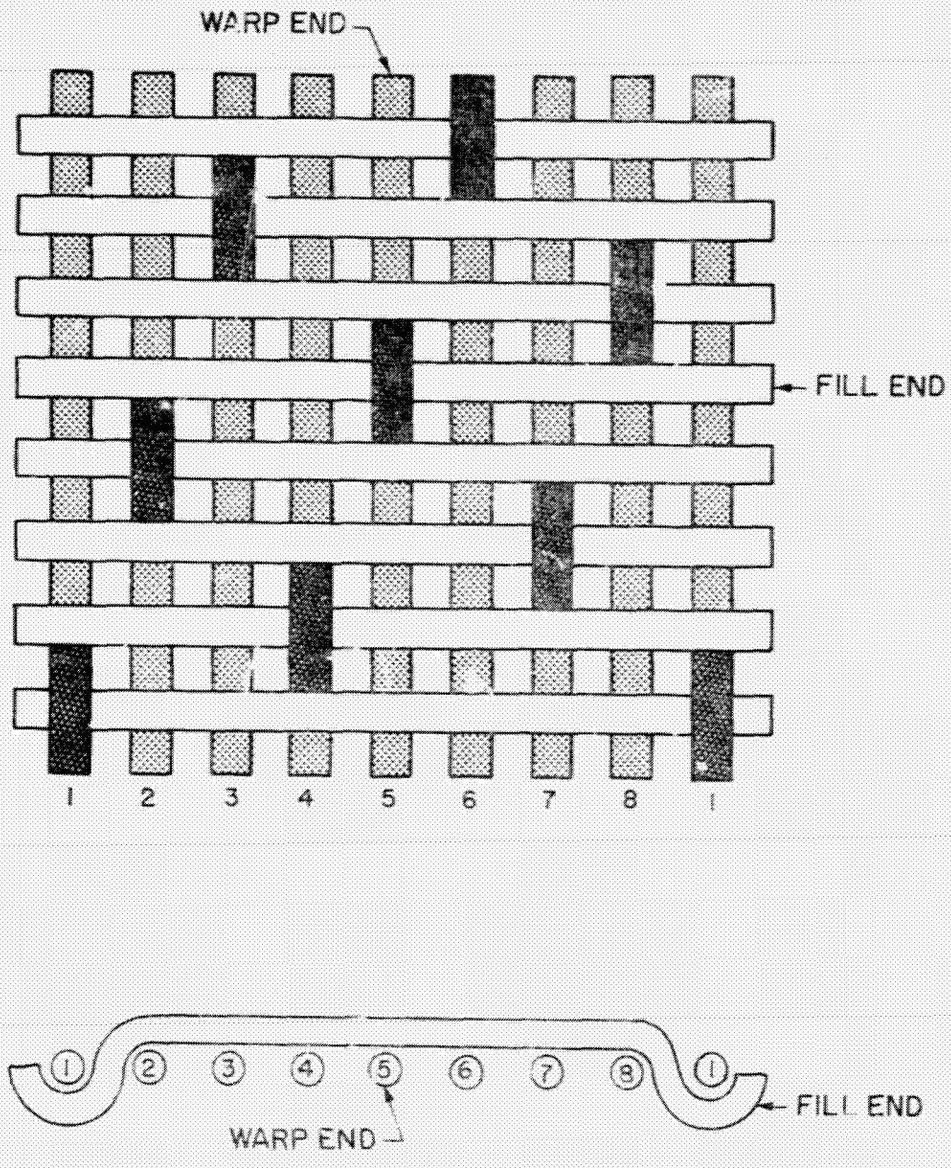

Figure 2. 8 Harness satin weave.

Table 2. Graphite Fabric Specifications.

Fabric Styie	W-133
Warp Yarn	T-300 (3K)
Fill Yarn	T-300 (3K)
Thickness (mils) (ASTM-D-1777)	17.0
Weight (oz/yd^2) (ASTM-D-1910)	10.80
Weave	8 HARNESS SATIN
Thread Count: Warp x Filling	24 x 23
Tracer Yarns:	
Warp	2 INCH CENTERS
Fill	6 INCH CENTERS

phenolic resin to carbon. It should be noted that the phenolic resin is only about 60 percent solids, with the remaining 40 percent volatilizing off. Therefore, it was necessary to expose the laminate to several cycles of resin impregnation and pyrolysis in order to obtain a structurally sound material. The final thickness of the panel was 0.10 inches (2.54 mm).

Optical photomicrographs of the cross-section of the panel before its initial pyrolysis step and after final processing are shown in Figures 3 and 4, respectively.

Both specimens were prepared for photomicrography by infiltrating them with room-temperature hardening resin prior to surface polishing. This step reduces the amount of damage done to the specimen during the polishing procedure. Figure 3 shows a partial cross-sectional view of the laminate in the as-cured state. This micrograph illustrates the woven nature of the composite. Additionally, it shows that there are regions of large voids. These voids show up as the dark grey areas as they have been filled in by the resin infiltrated into the specimen prior to polishing. They tend to occur at the undulation areas where fill tows cross over warp tows. These voids, called macrovoids, occur during the mold step because the pressure applied to the laminate is insufficient to fully deform the tows such that all the available volume is filled.

Figure 4 shows a cross-sectional view of the laminate in the fully processed state. The fully processed laminate is significantly different from the as-cured laminate in that, in addition to the fact that the phenolic matrix is now carbonized, the processed laminate contains a large number of transverse cracks. Crack density was determined from the micrographs and found to be approximately 100 cracks/inch. These transverse cracks are most certainly caused by the high thermal stresses generated during the high-temperature pyrolysis steps. Additionally, there is a significant amount of microporosity, which shows up in the micrograph as small black dots. This is closed porosity, which cannot be removed by the repeated infiltration and pyrolysis steps described above.

A low magnification scanning electron micrograph of the composite is shown in Figure 5. This micrograph shows a larger area than Figure 4 and further illustrates the

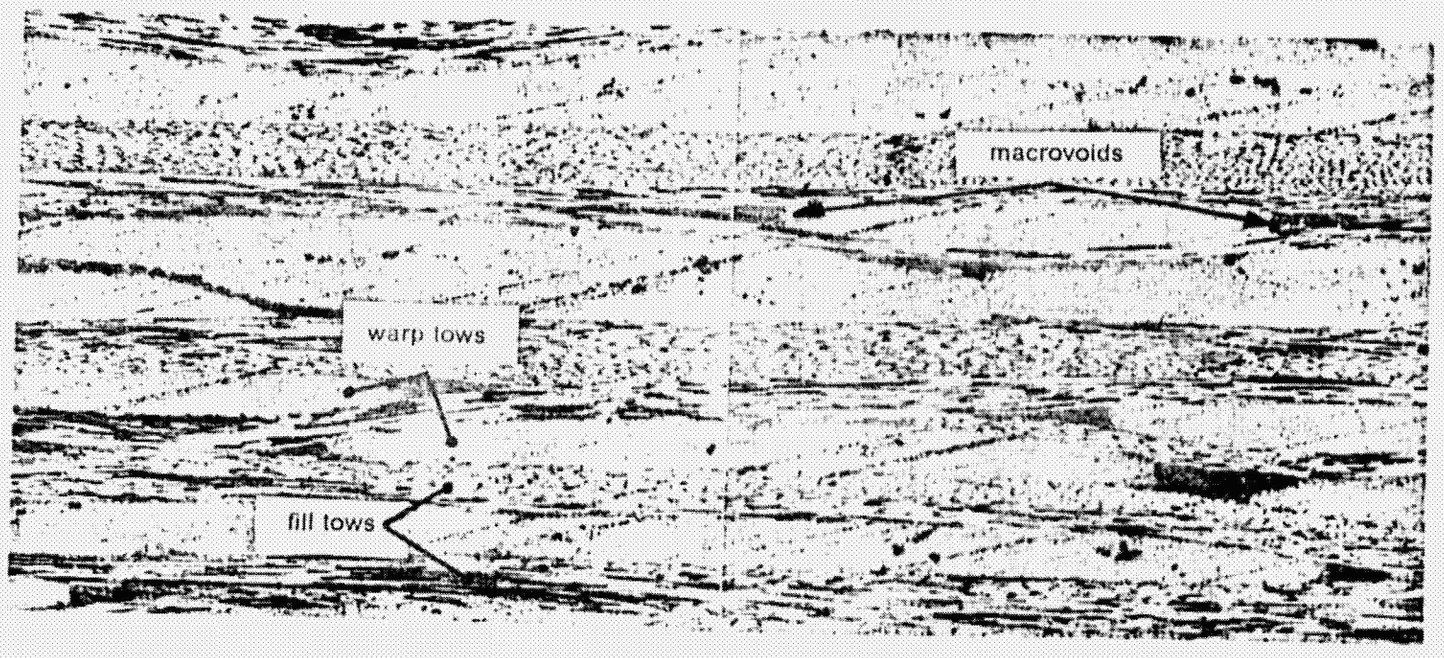

Figure 3. Optical micrograph of as-cured laminate prior to pyrolysis.

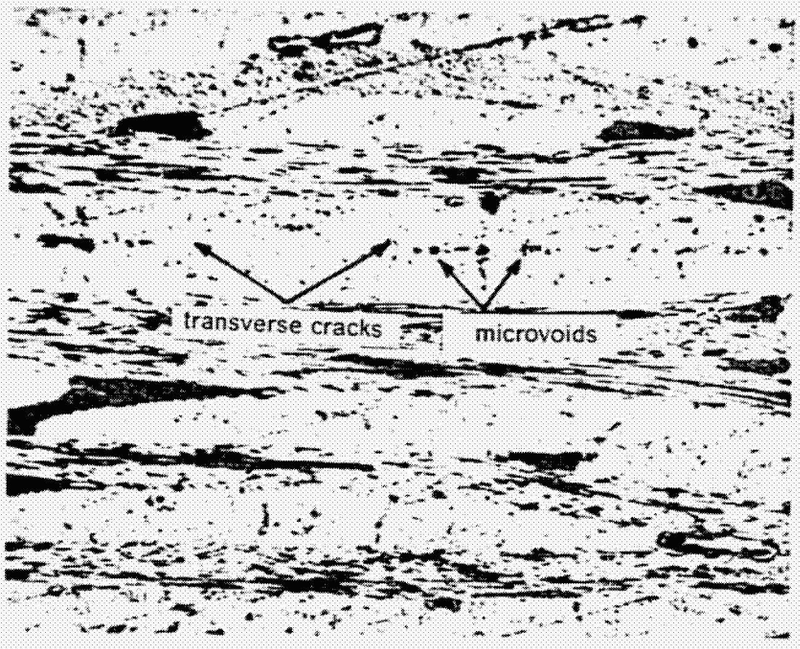

Figure 4. Optical micrograph of pyrolized laminate.

macroporosity associated with the regions of undulations. Some microporosity is visible, but transverse cracks are not.

2.3 *Experimental Procedure*

Several specimens measuring approximately 0.25 x 0.25 in. (6.35 x 6.35 mm) were cut from the panel with a diamond saw. The specimens were limited to the above geometry by the size and load capacity of the tensile stage. The specimens were then ultrasonically cleaned in water in order to remove any foreign matter present due to the cutting process and allowed to dry. Each specimen was bonded to two aluminum grips such that its transverse cross-section would be the surface of view (Figure 6). The specimens were then sputtered with a gold-palladium (Au-Pd) alloy in order to reduce charging effects when in the scanning electron microscope (SEM). The specimen to be tested was placed in a Hitachi Model HH-TS2 tensile stage (Figure 7 and Figure 8a) where the specimen grips were screwed to opposite sides of the load frame. The tensile stage was then inserted into a Hitachi Model S-415A scanning electron microscope (Figure 8b) equipped with a videotape recording system.

The videotape recording system was activated and a tensile displacement was applied until a crack became visible. The path of the crack was traced until its tip was found. Then the load was increased and the propagation of the crack tip along the surface of the specimen was recorded. Most often, crack propagation extended beyond the field of view of the microscope. Thus, it was necessary to go through several steps of applying a displacement, finding the new crack tip, increasing the displacement, and video recording crack propagation. Occasionally, photomicrographs of regions of interest were taken between displacement increments. This procedure was carried out until failure of the specimen into two pieces occurred. Following failure, one of the two pieces of the failed specimen was remounted in the microscope such that the fracture surface could be examined and photographed.

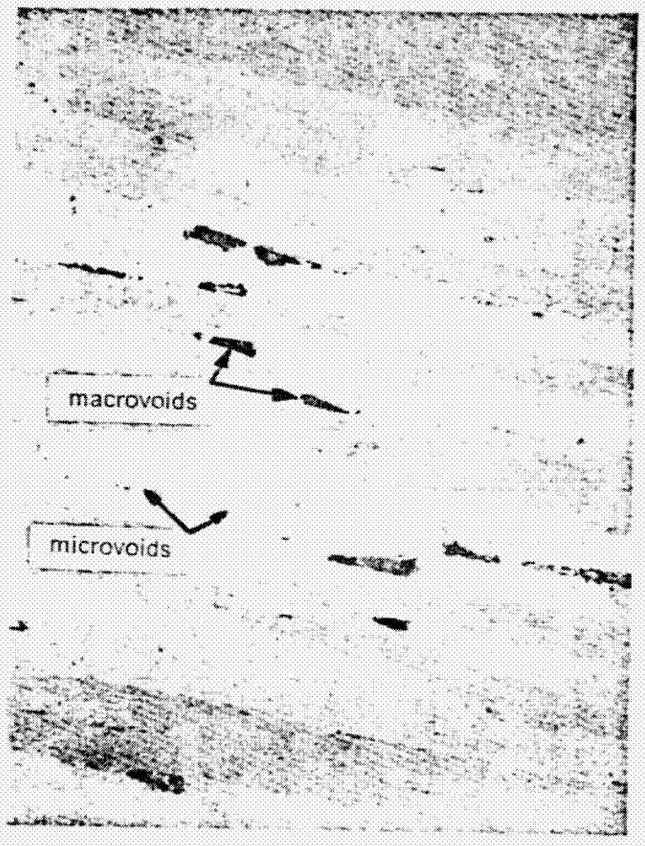

Figure 5. Scanning electron micrograph of carbon-carbon laminate.

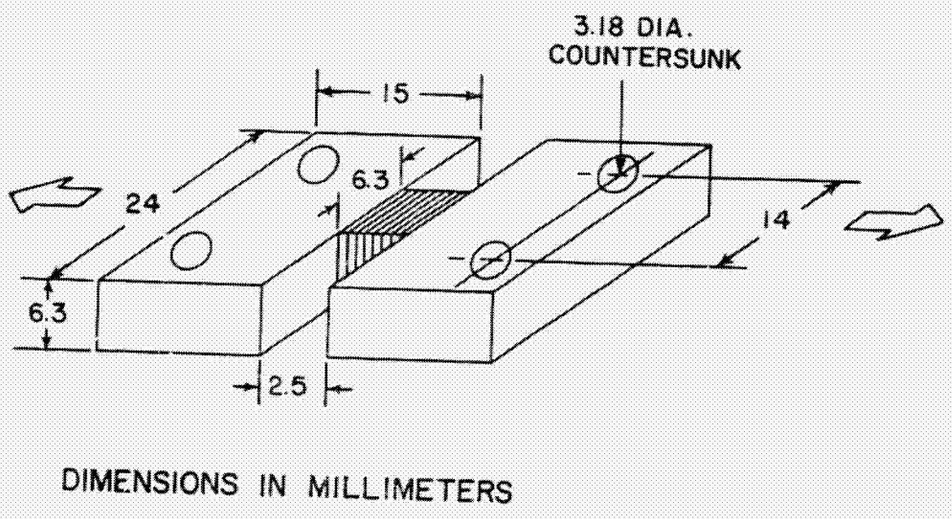

Figure 6. Schematic of carbon-carbon specimen adhesively bonded to aluminum grips.

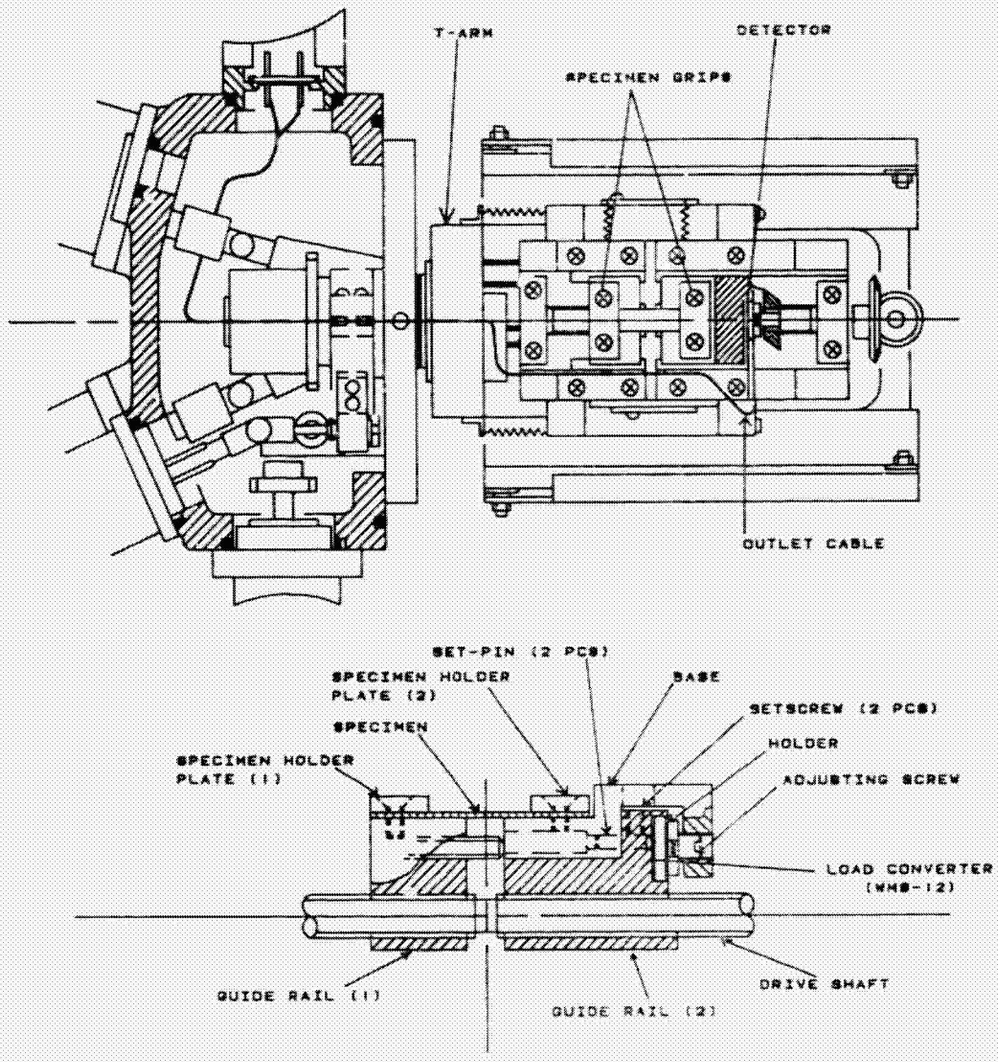

Figure 7. Section view of specimen holder assembly.

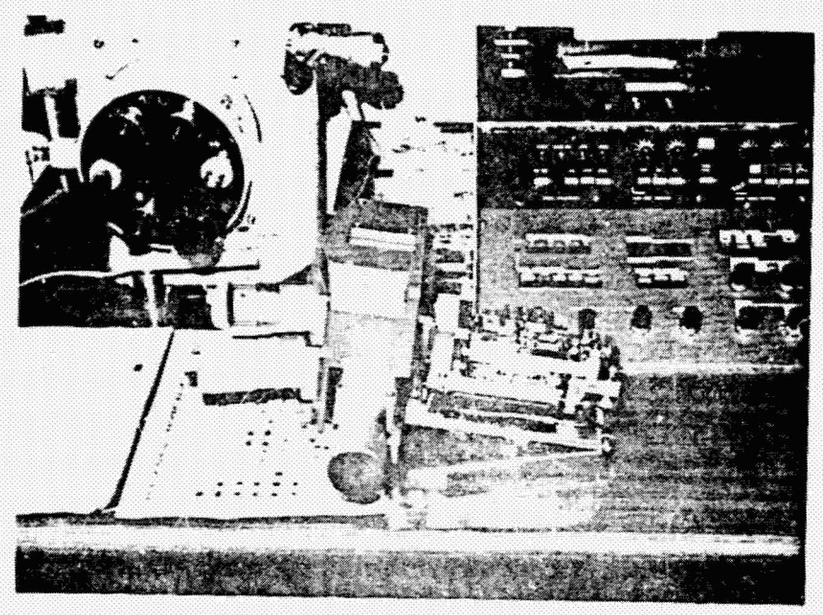

b) Hitachi Model HH-TS2 Tensile Stage.

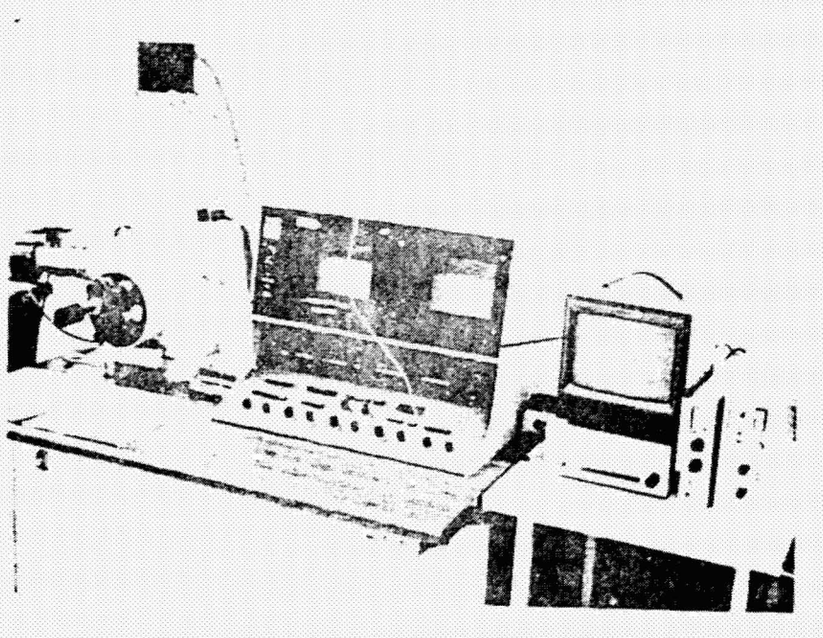

a) Hitachi Model S-415A Scanning Electron Microscope.

Figure 8. Scanning electron microscope and tensile stage.

2.4 Results

Figure 9 shows a sequence of crack propagation photos from an out-of-plane tensile test. These photographs were obtained by freeze-framing selected frames of the SEM videotape on a high resolution monitor and then photographing the screen with a 35 mm camera. Figure 9a shows two areas of crack propagation. An inter-tow crack at location **A**, is propagating between tows of opposite orientation. An intra-tow crack, at location **B**, is propagating within a tow. In Figure 9b the inter-tow crack (**A**) has continued to propagate and has resulted in the splitting of a graphite filament (**C**). The intra-tow crack (**B**) has not extended any further. Figure 9c shows no apparent extension of the inter-tow crack, but it does show that the intra-tow crack has branched into two additional cracks (**D** and **E**). Figure 9d shows additional branching of the intra-tow crack; however, the inter-tow crack has undergone little apparent propagation beyond that exhibited in Figure 9b. It should be noted that the inter-tow crack is not necessarily an interlaminar crack. Each ply is a woven fabric; therefore, interfaces between fibers of opposite orientation may belong to the same ply. An interesting feature of the intra-tow crack is that the crack shows multiple scallops (**F-G**), which is indicative of failure at the filament-matrix interface. This feature is illustrated more clearly at higher magnification in Figure 10. The large crack at the center of Figure 10 shows several individual kidney-shaped T-300 graphite filaments and the associated scallop-shaped regions of matrix (**A**) where the filaments have been pulled away. Filament-matrix interface failure is also indicated by the smaller crack at (**B**).

High and low magnification scanning electron micrographs of the fracture surface are shown in Figure 11 and Figure 12, respectively. The upper portion of Figure 11 (region **A**) reveals that the fibers have no residual matrix bonded to them. The lower portion (region **B**), upon close inspection, shows not fibers but residual matrix material left after the fibers have been pulled away. The cylindrical geometry corresponds to the shape of the carbon fi-

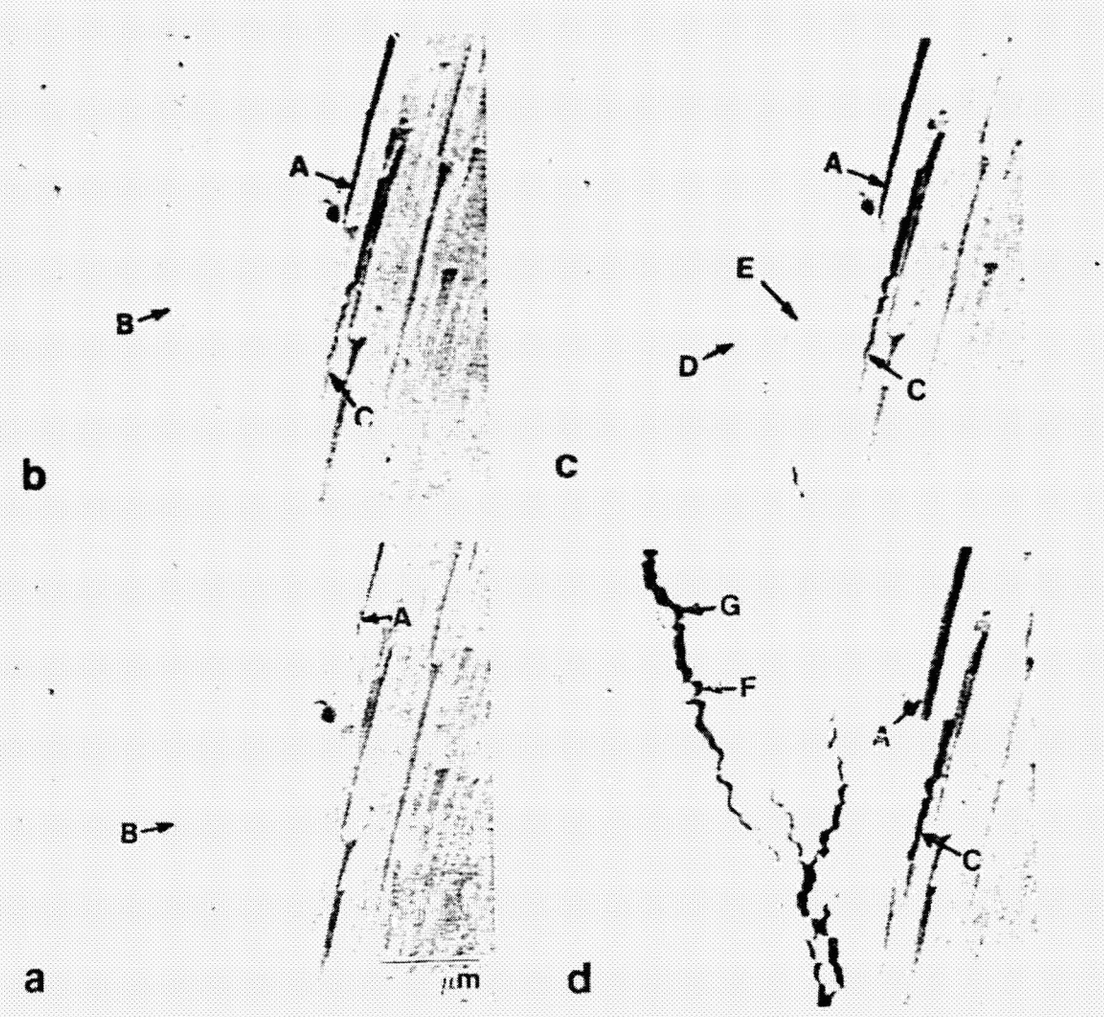

Figure 9. Scanning electron micrographs of crack propagation sequence.

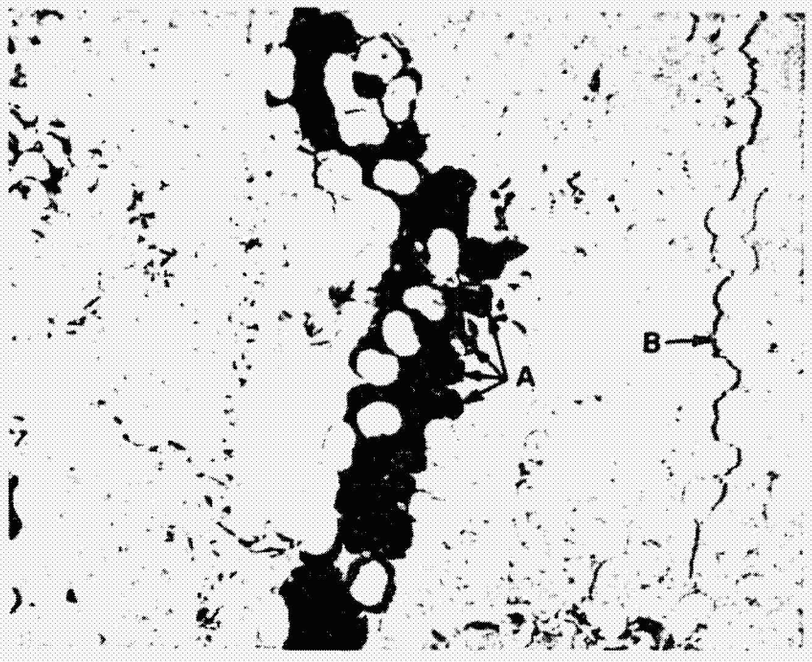

Figure 10. Scanning electron micrograph of carbon-carbon specimen during out-of-plane tensile test.

bers and demonstrates an apparent absence of any fiber-matrix bond. This feature is consistent with the scalloped crack pattern exhibited in Figure 9d.

Figure 12, the low magnification micrograph of the fracture surface, shows some regions of tow undulations. In the lower-right portion of the micrograph there appears to be a region of short fibers (**A**) aligned 90 ° to the direction of the fibers in the bulk of the fracture surface. This is not a region of fibers, but a region of matrix similar to that shown at location **B** in Figure 11. This is a result of an undulation from the other half of the failed specimen being in contact with it. A similar though less conspicuous region is shown at **B** in Figure 12. However, in this case the undulations are part of the ply shown.

Intuitively, it would be expected that transverse failure would be interlaminar in nature. Intralaminar failure would not be expected because each ply is reinforced in the transverse direction due to the woven nature of the fabric. Figure 11and Figure 12 show that the failure is indeed interlaminar. The nature of the failure can best be illustrated by considering Figure 13. Figure 13 shows a schematic of a two-ply woven fabric laminate. In the particular geometric configuration shown, the interface consists of filaments of similar orientation except for the small regions of undulation. A crack propagating along the interface would explain the tendency for cracks to propagate between fibers of similar orientation, as exhibited by Figure 9a-d, and the morphology of the fracture surfaces exhibited by Figure 11a-b.

The ultimate out-of-plane tensile strength of the composite was approximately 250 psi. This differs significantly from the 500 psi tensile strength measured by Maahs.[22] It is surmised that the difference in strengths is a result of the relative contributions of free edge stresses. In the present experiment the specimen was rectangular and much smaller (0.25 in. x 0.25 in.) than the round, one-inch diameter specimen used by Maahs. Therefore, the contribution of the free edge to the magnitude of the stresses in the interior of Maahs' specimen would be expected to to be less than if the smaller specimen were used. Thus, greater strength would be exhibited from the larger specimen.

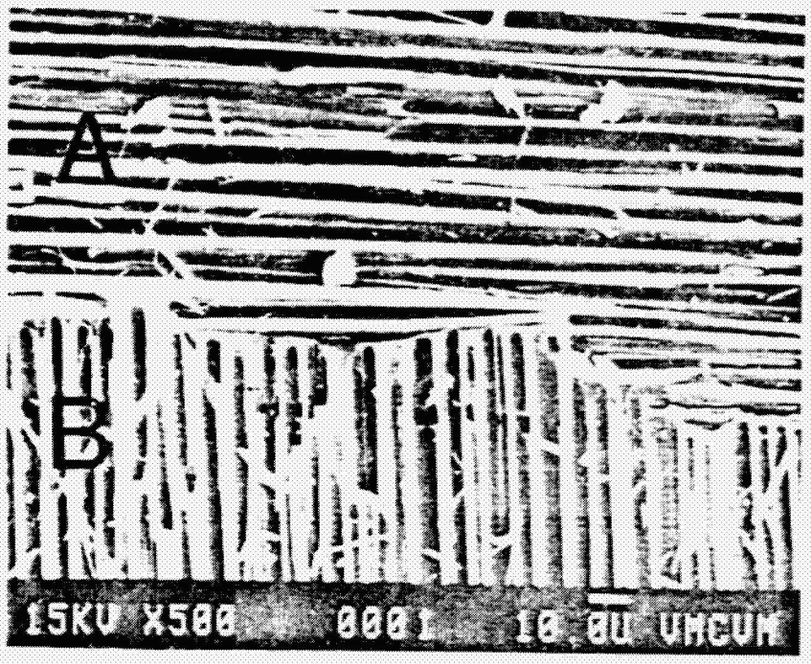

500x

Figure 11. Scanning electron micrograph of fracture surface at high magnification.

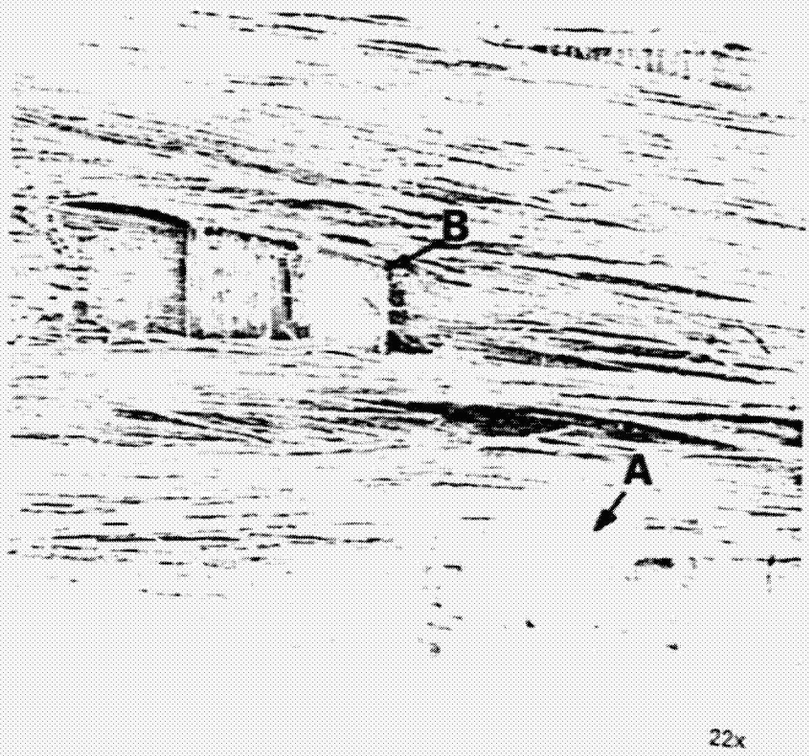

Figure 12. Scanning electron micrograph of fracture surface at low magnification.

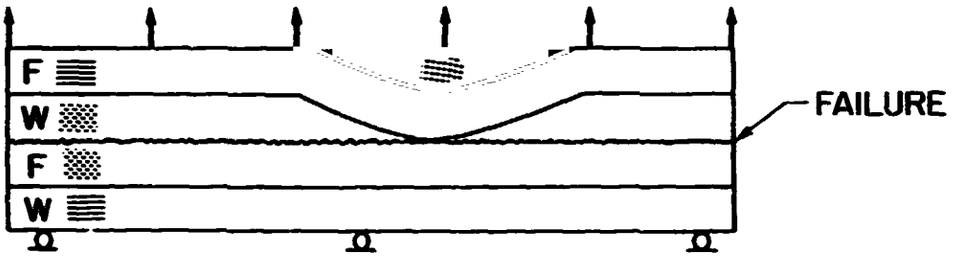

Figure 13. Schematic of location of failure in 2-ply woven fabric composite.

2.5 *Summary*

It has been shown that the failure of 2-D carbon-carbon composites due to out-of-plane loading is interlaminar. Most significant, however, is the lack of fiber-matrix bond strength, as exhibited by the tendency of cracks to propagate along the fiber-matrix interface (Figure 10) and the cleanliness of the fiber surface after failure (Figure 11a). Therefore, the apparent key to improving the out-of-plane strength of 2-D carbon-carbon is to improve the fiber-matrix bond strength, or reduce the stresses in such regions.

3.0 Finite Element Stress Analysis

3.1 Introduction

This chapter presents the results of finite element analyses of a two-layer woven fabric carbon-carbon laminate under out-of-plane, in-plane, and thermal loading conditions. The influence of stacking sequence and fabric geometry on stress states and elastic properties is investigated. Of particular interest is the stress distribution at the interface between plies, as this is where failure was observed to initiate in experiments on laminates subjected to out-of-plane loading (Chapter 5).

3.1.1 Laminate Geometry

Consider the geometry of the eight-harness satin fabric exhibited in Fig. 2. Two possible stacking arrangements of a two-layer laminate are illustrated in Figure 14 and Figure 15. In Figure 14 the laminate is stacked such that the warp tows are adjacent. The cross-sections **A-A** and **B-B** illustrate the curvatures associated with the warp and fill tows in the laminate.

In section **A-A** the fill tows exhibit curvature and the warp tows do not. In section **B-B**, however, it is the warp tows that exhibit curvature. Borrowing from the nomenclature used to describe the stacking sequence of laminates made from unidirectional plies, this stacking sequence can be designated as $(F/W_2/F)$. For notational purposes the cross-sections of the stacking sequences associated with sections **A-A** and **B-B** in Figure 14 are designated $(F/W_2/F)_f$ and $(F/W_2/F)_w$, respectively, where the subscripts f and w identify the tows in the cross-section which exhibit curvature. Cross-sections **A-A** and **B-B** are identical to those that would be exhibited should the laminate be stacked such that the fill tows are adjacent (i.e $(W/F_2/W)$ laminate). A different stacking sequence is illustrated in Figure 15. In this laminate the stacking is such that the warp and fill tows alternate. Thus, the stacking sequence may be described as $(F/W)_2$. Comparison of sections **A-A** and **B-B** show that one of the sections is just the inverted form of the other.

It should be noted that the undulations are not likely to nest together as shown in Figure 14 and Figure 15. A generic offset of the undulations in a $(F/W_2/F)_w$ laminate is illustrated in Figure 16. The offset ratio, **R** is defined as

$$R = \frac{\delta}{\lambda} \tag{3.1}$$

where δ and λ are defined as shown in Figure 16. Offset ratios of 0, 1, 2, 3, 4, and 5 for a $(F/W_2/F)_w$ laminate are shown schematically in Figure 17. Close examination of the geometries with $R=3$ and $R=5$ show that one is just the inverted form of the other; therefore, of the six offset ratios exhibited, only five are unique. Although not pictured, **R** values of 6, 7, and 8 would have the same geometries as the inverted forms of $R=2$, 1, and 0, respectively. The offset ratio **R** can have values ranging from 0 to 4 in an eight-harness satin. It is important to note that R can take on any value between 0 and 4; therefore, there are an infinite number of possible offset ratios. It should also be noted that **R** would be very difficult to control in the manufacture of woven fabric laminates. Woven fabrics cannot be handled precisely enough to allow laminates with specified values of **R** to be fabricated using existing fabrication techniques.

Also of interest is the aspect ratio Ω of the undulation. Ω is defined as the height H of the undulation divided by its wavelength λ (Figure 16). The aspect ratio is influenced by both the tow size and the processing. A larger tow size, due to either increased filament diameter or an increase in the number of filaments in the tow bundle, will result in an increase in Ω. Increased autoclave pressure during processing tends to flatten the laminate and decreases Ω.

3.1.2 Material Properties

3.1.2.1 Matrix Properties

The matrix material in this study is carbonized Karbon 640, a phenolic resin marketed by the Fiberite Corporation. Pyrolysis of the matrix results in a glassy structure, thus the matrix can be assumed to be isotropic. The elastic constants of pyrolized Karbon 640 have not been published; however, the elastic modulus of pyrolized SC1008, a Monsanto phenolic resin with a chemical composition very similar to that of Karbon 640 [22], has been determined by Bradshaw et al[23] [24] to be 4-5 MSI. For this research, an intermediate value of 4.5 MSI was assumed for pyrolized Karbon 640. The Poisson's ratio of unreinforced glassy carbon was found by Zhao [25] to lie in the range 0.12-0.17 with the average value being 0.15. Thus, a Poisson's ratio of 0.15 is assumed for this study. For an isotropic solid there are only two independent elastic constants. The shear modulus G, determined from the above E and v, is 1.95 MSI. The thermal expansion coefficient of glassy carbon was found by Zhao to range from 7.9×10^{-6}/°F to 9.7×10^{-6}/°F. For this study the intermediate value 8.8×10^{-6}/°F was used.

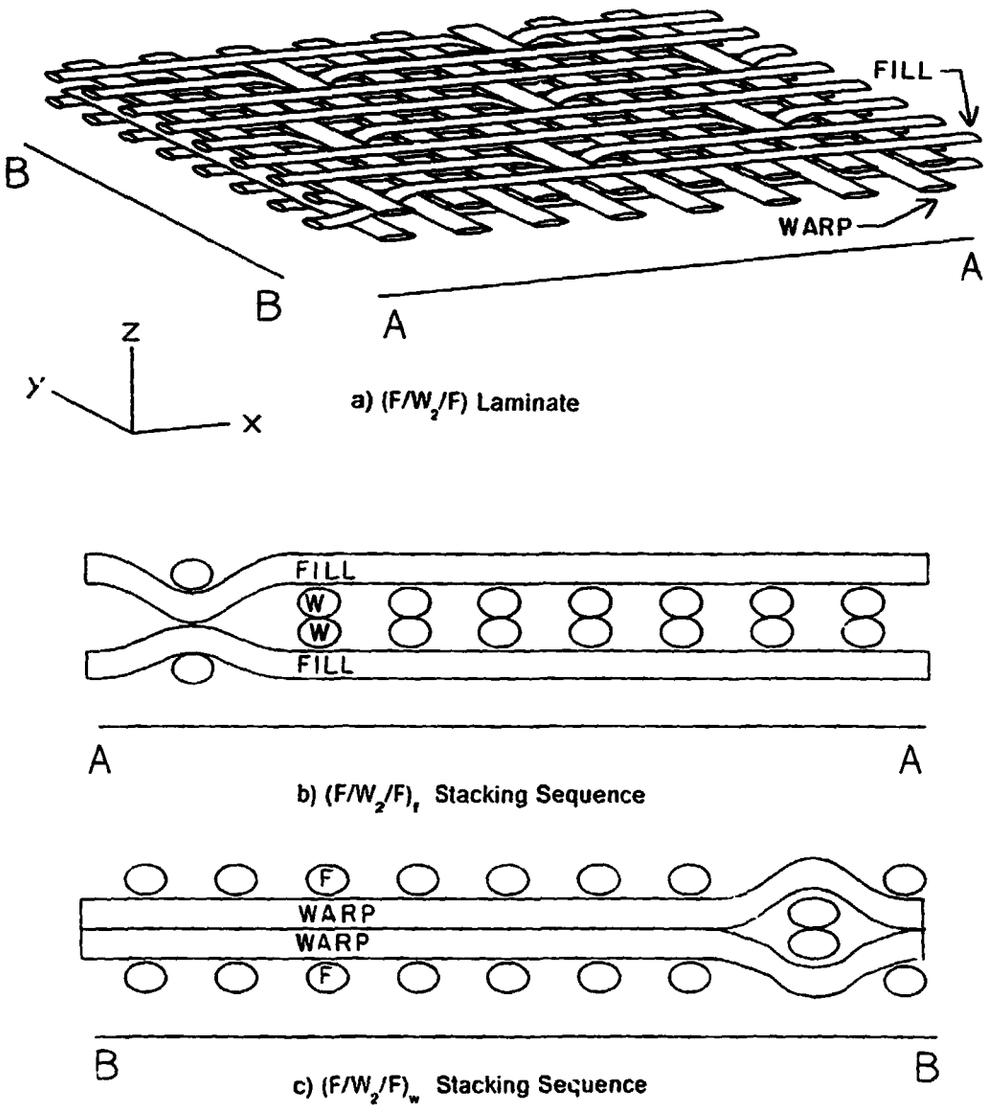

Figure 14. **(F/W_2/F) stacking sequence in a woven fabric laminate.**

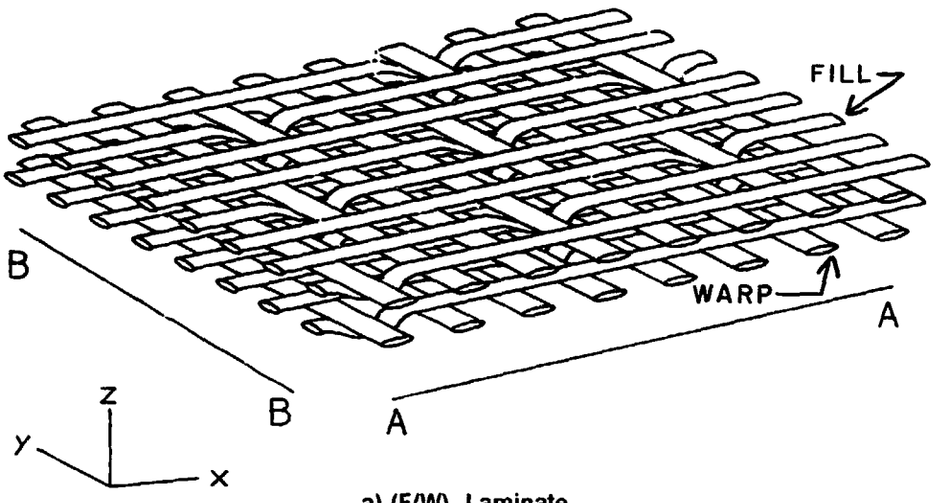

a) $(F/W)_2$ Laminate

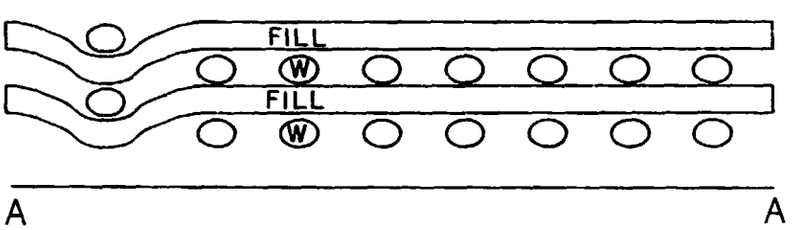

b) $(F/W)_2$ Laminate Stacking Sequence **A-A**

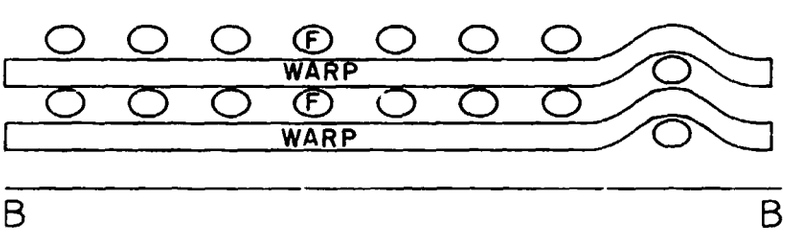

c) $(F/W)_2$ Laminate Stacking Sequence **B-B**

Figure 15. $(F/W)_2$ **stacking sequence in a woven fabric laminate.**

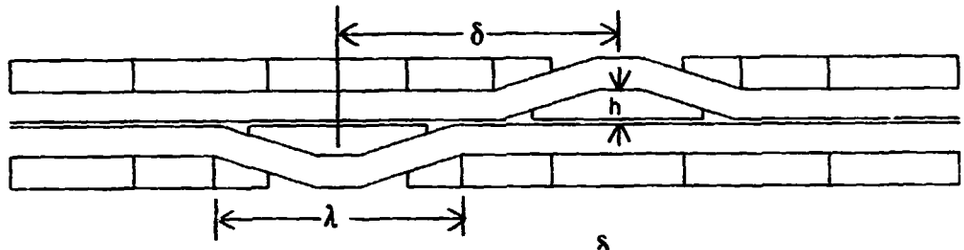

$$R = \frac{\delta}{\lambda}$$

$$\Omega = \frac{h}{\lambda}$$

Figure 16. Definition of Offset Ratio.

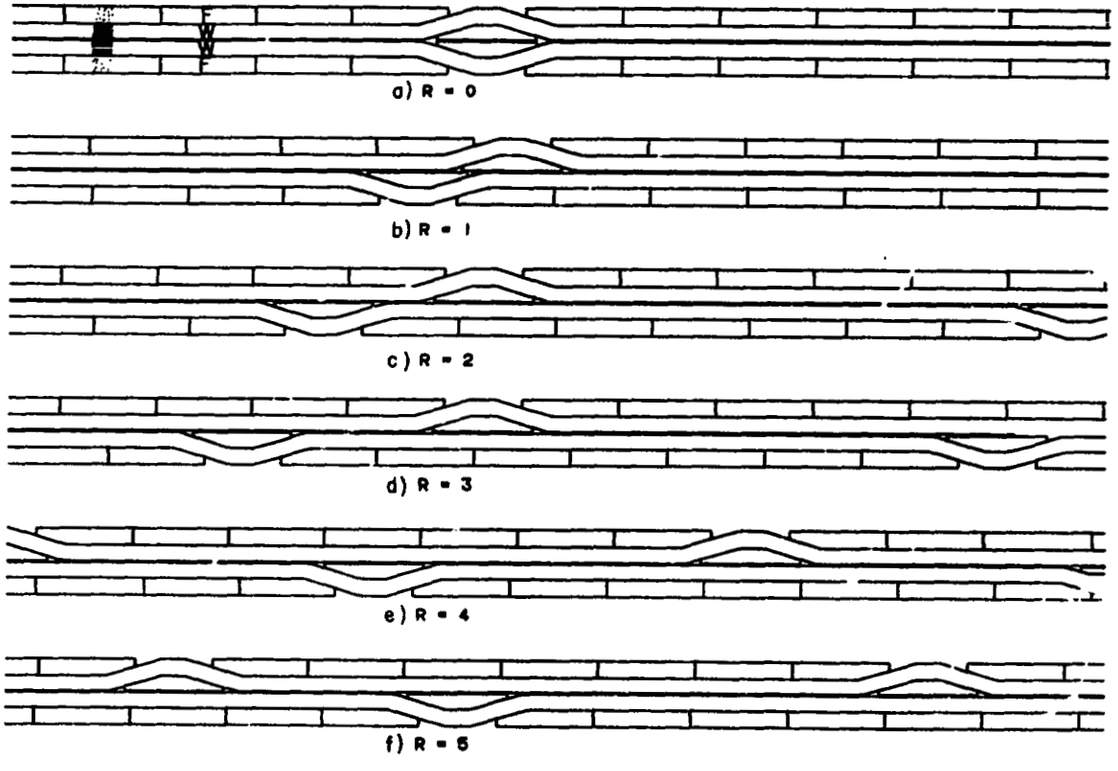

Figure 17. Offset ratios in $(F/W_2/F)_w$ laminates.

3.1.2.2 *Fiber Properties*

The fiber modeled in this study is Thornel T-300. The complete set of elastic properties for such a fiber are not available. The difficulty in knowing the fiber properties is complicated further by the fact that Eitman [26] estimated that the modulus of a different graphite fiber (T-50) increased by as much as 50% when exposed to a 2800 °C carbon-carbon processing cycle. Additional work by Maahs [22] on the properties of carbon-carbon suggested that the properties of T-300 in a carbon-carbon composite are the same as a virgin T-50 fiber. The axial modulus of a T-50 fiber is 57 MSI. [27] Unfortunately, no published data could be found for the other elastic properties of the T-50 fiber. Thus, for the purposes of modeling, the remaining elastic properties of the T-300 fiber were assumed to be the same as those of Hercules HM fiber because: (1) the HM and virgin T-50 fibers exhibit axial moduli which are approximately the same (12% difference), and (2) E_2, ν_{12}, G_{12}, and ν_{23} values for the HM fiber have been published by Walrath and Adams [21].

The thermal expansion coefficients were assumed to the same as those of the HM fiber and were obtained from Walrath and Adams. They are listed in Table 3.

3.1.2.3 *Tow Properties*

Standard engineering procedure normally entails that the tow properties (in this study a 'tow' consists of fiber and matrix) be obtained experimentally from a unidirectional carbon-carbon laminate. However, the unidirectional material necessary to obtain the elastic constants is extremely difficult to manufacture. Thus it was necessary to use a micromechanics approach and inferences from properties of other material systems available in the literature to obtain the tow properties.

The fiber volume fraction of the tow was determined via optical microscopy to be 0.69. Using rule-of-mixtures and the fiber and matrix properties identified in the previous sections,

E_1 of the composite tow was determined to be 40.7 MSI. The remaining elastic constants were more difficult to determine due to the unusual nature of carbon-carbon composites. The results of the previous chapter indicated a lack of bonding between the fiber and the matrix. Therefore, standard micromechanics formulae for the determination of the elastic constants of the tow, which assume an ideal bond between the fiber and the matrix, could not be applied. Consider, for example, the transverse elastic modulus. The lack of an interfacial bond between the fiber and the matrix results in the matrix behaving like a material containing cylindrical voids. The fibers prevent distortion of the holes so the transverse modulus of the tow is greater than that of a matrix with unfilled holes. Adams[3] examined the transverse tensile and longitudinal shear properties of several unidirectional carbon-carbon systems and found that the transverse moduli ranged from 0.16-2.11 MSI. One system that he studied was the T-50/SC1008 system. As previousiy mentioned the SC1008 resin is virtually the same as the Karbon 640 resin used in this study. Adams obtained a transverse modulus of 0.75 MSI for a material that had gone through three carbonization/densification cycles, which is similar to the processing that the material in this study went through. Therefore, a value of 0.75 MSI was assumed for the transverse modulus E_2 for this study.

Adams did not report values of Poisson's ratios or shear moduli, nor has any other experimental data for these constants been located in the literature. However, Goetzel [28] reported values of Poisson's ratio for a 2-D carbon-carbon material fabricated using a thermosetting resin as matrix precursor and a PAN fiber as a fiber precursor. For this composite ν_{xz} was reported to be in the range 0.10 to 0.17. Since ν_{xz} in the 2-D composite is somewhat analogous to ν_{12} in the unidirectional composite, it may be reasonably expected that ν_{12} will lie in the same range. For this study the intermediate value of 0.15 was assumed. Additionally, no data have been located in the literature for ν_{23}. Recall, however, that the lack of a bond between the fiber and the matrix enables the matrix to be modeled as a material containing an array of cylindrical voids. Therefore, it can be assumed that the contribution to ν_{23} from the fibers is to prevent distortion of the shape of the voids. Thus, it is expected that

ν_{23} of the tow would vary little from ν of the matrix itself. Therefore, a value of 0.15 was assumed for ν_{23}.

If the tow is assumed to be transversely isotropic in the 2-3 plane then the following equations hold:

$$E_3 = E_2 \tag{3.2}$$

$$\nu_{13} = \nu_{12} \tag{3.3}$$

$$G_{23} = \frac{E_2}{2(1 + \&\nu 23)} \qquad G_{13} = G_{12} \tag{3.4}$$

In order to check if the Poisson ratios used in this study were reasonable, a finite element model of a two-layer woven fabric laminate was made in which each layer was approximated by a (0/90) laminate. The resulting $(0/90)_s$ laminate was analyzed and the through-thickness Poisson ratio ν_{xz} was found to be 0.16, which is within the range reported by Goetzel. Thus, the values of ν used in this study appear to be reasonable.

Experimentally determined values for the longitudinal shear modulus G_{12} of unidirectional carbon-carbon composites are not available. However, since the value of G_{12} of the fiber is 2.1 MSI, and the value of G for the matrix is 1.9 MSI, then it can be expected that for an ideally bonded composite G_{12} would be approximately 2.0 MSI. For this analysis, a value of 2.0 MSI for G_{12} of the tow was assumed.

The tow thermal expansion coefficients were determined from the fiber and matrix properties using the method of Hashin.[29]

The elastic constants of the fiber, matrix, and tow used in this study are summarized in Table 3.

Table 3. Material Properties.

Property	T-300 Fiber	Glassy Carbon Matrix	Composite
E_1 (MSI)	57.0	4.5	40.7
E_2 (MSI)	1.5	4.5	0.75
E_3 (MSI)	1.5	4.5	0.75
ν_{23}	0.36	0.15	0.15
ν_{13}	0.26	0.15	0.15
ν_{12}	0.26	0.15	0.15
G_{23} (MSI)	0.55	1.95	0.326
G_{13} (MSI)	2.1	1.95	2.0
G_{12} (MSI)	2.1	1.95	2.0
$\alpha_1(10^{-6}/°F)$	-0.4	8.8	-0.074
$\alpha_2(10^{-6}/°F)$	15.0	8.8	12.9
$\alpha_3(10^{-6}/°F)$	15.0	8.8	12.9

3.2 *Finite Element Model and Implementation*

3.2.1 The Finite Element Model

As indicated in Figure 14 and Figure 15, a woven fabric laminate is a three dimensional structure. In this analysis, however, the laminate is modeled according to the 2-D cross-sectional geometries illustrated in Figure 14b and c and Figure 15b and c. This is consistent with the work of previous researchers who used two-dimensional analyses to model woven fabric lamina in order to avoid the extreme complexity and computational expense associated with 3-D modeling [7,8,9]. It is felt that a 2-D approach adequately addresses the influence of the laminate geometry on the resulting stress state. As such, the warp and fill tows are modeled as homogeneous orthotropic sheets, and the laminate is assumed to be homogeneous and orthotropic with no variation in geometry in the y direction. The latter assumption allows a generalized plane strain analysis using a two dimensional mesh. Additionally, the τ_{xy} and τ_{yz} components of stress are identically zero.

This model represents the stress state in a generic section **A-A** or **B-B** in Figure 14 and Figure 15. As mentioned previously, the geometries associated with sections **A-A** and **B-B** in Figure 14 are designated the $(F/W_z/F)_f$ and $(F/W_z/F)_w$ laminates, respectively, and the geometry associated with the cross-sections in Figure 15 is designated the $(F/W)_z$ laminate. Additionally, for purposes of analysis and presentation of results, the modeled regions occupy the x-z plane.

One characteristic of a two-layer woven fabric composite is that the geometry is periodic in x. Thus it can be divided into repeating units (i.e. 'unit cells'). A typical unit cell of a $(F/W)_z$ laminate is illustrated in Figure 20a.

The finite element model is based on the assumptions of linear elastic material behavior and linear strain-displacement relationships. Eight-node rectangular and six-node triangular

plane elasticity, isoparametric elements are incorporated in the model. In addition to these six and eight-node elements, a special element has been developed in which the material properties are allowed to vary within the element. This eight-node quadrilateral element, designated the S8Q, is used to model the curved portions of the tow in the region of undulation. The finite element model, the concept of generalized plane strain, and the S8Q element are fully discussed in Appendix C.

3.2.2 Finite Element Test Matrix

The geometric parameters of interest are the stacking sequence, the undulation offset ratio R, and the undulation aspect ratio Ω. A test matrix was developed which enabled each of the above parameters to be investigated. For both in-plane and out-of-plane mechanical loading, each of the three stacking sequences, $(F/W_z/F)_s$, $(F/W_z/F)_s$, and $(F/W)_z$, were investigated for the offset ratios R = 0, 0.5, 1, and 4. In each case the aspect ratio Ω = 12 was used. This value was obtained by measuring optical micrographs of the material used in the experimental portion of this study (Chapter 2).

In order to investigate the influence of Ω, additional finite element studies were conducted for both in-plane and out-of-plane loading on the $(F/W_z/F)_s$ laminate for Ω values ranging from 6 to 24. The offset ratio R was held constant at 0.5 for these studies.

One way woven fabric composites differ from composites made of unidirectional plies is that the geometry of woven fabric composites varies with axial coordinate. This is illustrated in Figure 18 for two $(F/W_z/F)_s$ laminates. Each laminate can be divided into two regions of primary interest. One of these regions contains the undulation. The other region is designated the 'far-field' region, and has the geometry of a cross-ply laminate. Thus, it is expected that the elastic constants and hence the stress distribution in the laminate will vary with axial coordinate. In order to investigate the influence of laminate geometry on laminate stiffness, average axial stiffness values were calculated for each of the laminates analyzed under in-

plane loading. Also, in order to investigate local variations in stiffness within a laminate (intralaminate stiffness variations) additional finite element studies were conducted on the far-field region and the regions of undulation associated with the $(F/W_z/F)_w$, R=0, 1, and 4 laminates and the $(F/W_z/F)_f$, R=0 laminate. These regions are illustrated in Figure 19. Analyses were performed such that the moduli E_x, E_y, and E_z could be determined. For all cases the undulation aspect ratio Ω was held constant at 12.

As carbon-carbon composites are exposed to elevated temperatures, thermal stress distributions in such laminates are very important. Thermal stresses were investigated for a $(F/W_z/F)_f$ laminate with R=0.5 and Ω=12.

The finite element test matrix used in this study is compiled in Table 4.

3.2.3 Boundary Conditions and Loading

3.2.3.1 Out-of-Plane Loading

The boundary and loading conditions for the out-of-plane analysis are illustrated in Figure 20b. The lower surface of the laminate (z=0) was specified to have zero w displacement (z direction). A displacement corresponding to an applied out-of-plane strain ε_z = 0.1% was specified at each node on the top surface of the laminate (z=H). The left-hand side of the mesh (x=0) was specified to have zero displacement in the x direction. Although this boundary condition implies that the mesh has symmetry about the y-z plane, which is true only when the offset ratio R equals zero, the results show that this boundary condition does not significantly effect the stress distribution in the laminate. The right-hand side of the laminate (x=L) was free to translate in the x direction, but constrained to remain straight and vertical. Absence of this latter boundary condition would have introduced a free edge to the model, which does not exist in a unit cell. However, the boundary conditions on the model

Table 4. Finite Element Test Matrix.

	Loading					
	In-Plane		Out-of-Plane		Thermal	
Laminate	R	Ω	R	Ω	R	Ω
$(F/W_z/F)_w$	0.0	12	0.0	12	N/A	N/A
	0.5	12	0.5	12		
	1.0	12	1.0	12		
	4.0	12	4.0	12		
$(F/W_z/F)_t$	0.0	12	0.0	12	0.5	12
	0.5	12	0.5	12	-	-
	1.0	12	1.0	12	-	-
	4.0	12	4.0	12	-	-
	0.5	6	0.5	6	-	-
	0.5	9	0.5	24	-	-
	0.5	15	-	-	-	-
	0.5	18	-	-	-	-
	0.5	24	-	-	-	-
$(F/W)_z$	0.0	12	0.0	12	N/A	N/A
	0.5	12	0.5	12		
	1.0	12	1.0	12		
	4.0	12	4.0	12		

at x=0 and on the right-hand side (x=L) do require that the interlaminar shear stress τ_{xz} equals zero at those points. This is discussed in depth later in the text. The final boundary condition was that the net force in the y direction, F_y, equal zero.

3.2.3.2 *In-Plane Loading*

The boundary and loading conditions for the in-plane analysis are illustrated in Figure 20c. The left-hand side of the mesh (x=0) was specified to have zero displacement in the x direction. In addition, one corner node was specified to have zero displacement in the z direction in order to eliminate rigid body displacements. The right hand side was given a specified displacement corresponding to an applied axial strain ε_x = 0.1%. The final boundary condition was that the net force in the y direction, F_y, equal zero.

3.2.3.3 *Thermal Loading*

The boundary and loading conditions for the thermal analysis are illustrated in Figure 20d. As in the case of in-plane loading, the left side of the mesh (x=0) was specified to have zero displacement in the x direction. Also, as in the out-of-plane loading case, the right side (x=L) was constrained to remain straight and vertical in order to represent a repeating unit cell.

3.2.3.4 *Analysis of Far-Field Region and Regions of Undulation*

The boundary and loading conditions for the analysis of the far-field region and the regions of undulation are illustrated in Figure 21. The boundary conditions used in order to evaluate E_z corresponded to those of a uniaxial tensile test (Figure 21a). The left side of the

mesh (x=0) was specified to have zero displacement in the x direction. The right side ($x = \lambda$) was given a specified displacement corresponding to an applied axial strain $\varepsilon_x = 0.1\%$. Additionally, the midplane w displacement at either edge of the mesh (x=0, λ) was specified to remain zero. The final boundary condition was that the net force in the y direction, F_y , equal zero. It should be noted that these boundary conditions do not result in a state of pure uniaxial tensile stress. Pagano and Halpin [30] showed that significant shear stresses are introduced into off-axis tensile specimens due to end grip constraints. The geometry of the undulations modeled in this study result in the introduction of τ_{xz} at the edges of the laminate (x=0, λ).

To evaluate the in-plane stiffness E_y the left side of the mesh (x=0) was constrained to have zero displacement in the x direction and the right side of the mesh (x= λ) was constrained to remain straight and vertical (Figure 21b). An in-plane force F_y, corresponding to the average in-plane stress σ_y = 1000 psi was then applied to the model.

The boundary conditions for determining the out-of-plane modulus E_z (Figure 21c) were the same as those used for analysis of the full unit cells under out-of-plane loading (Figure 20a).

3.3 Results: Variations in Laminate Stiffness

3.3.1 Local Variations In Stiffness

The in-plane elastic modulus E_x and the out-of-plane elastic modulus E_z of the geometries illustrated in Figure 19 were determined by calculating the average stress and dividing by the strain. This is expressed mathematically as

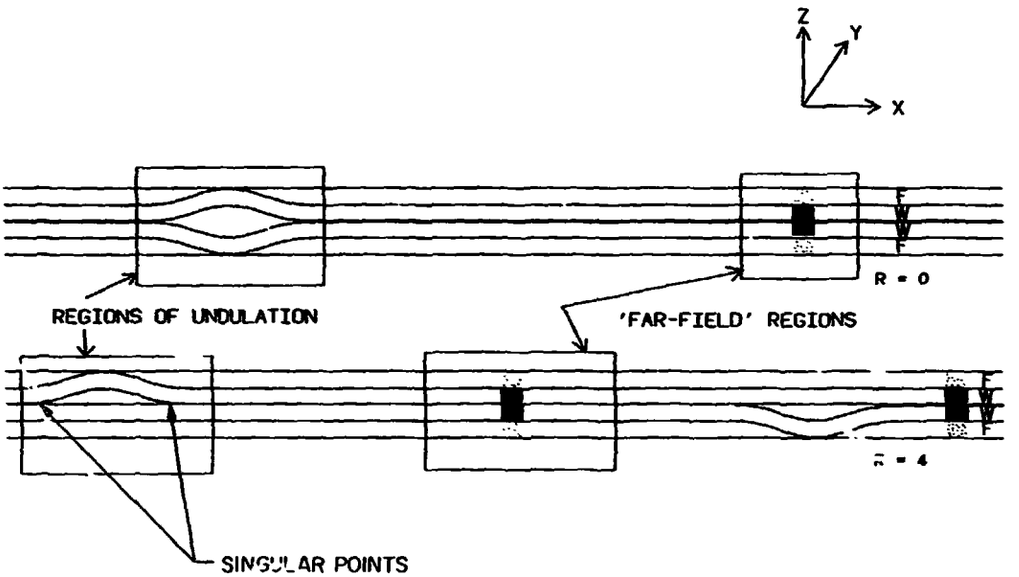

Figure 18. Regions of interest in $(F/W_2/F)_w$ laminates.

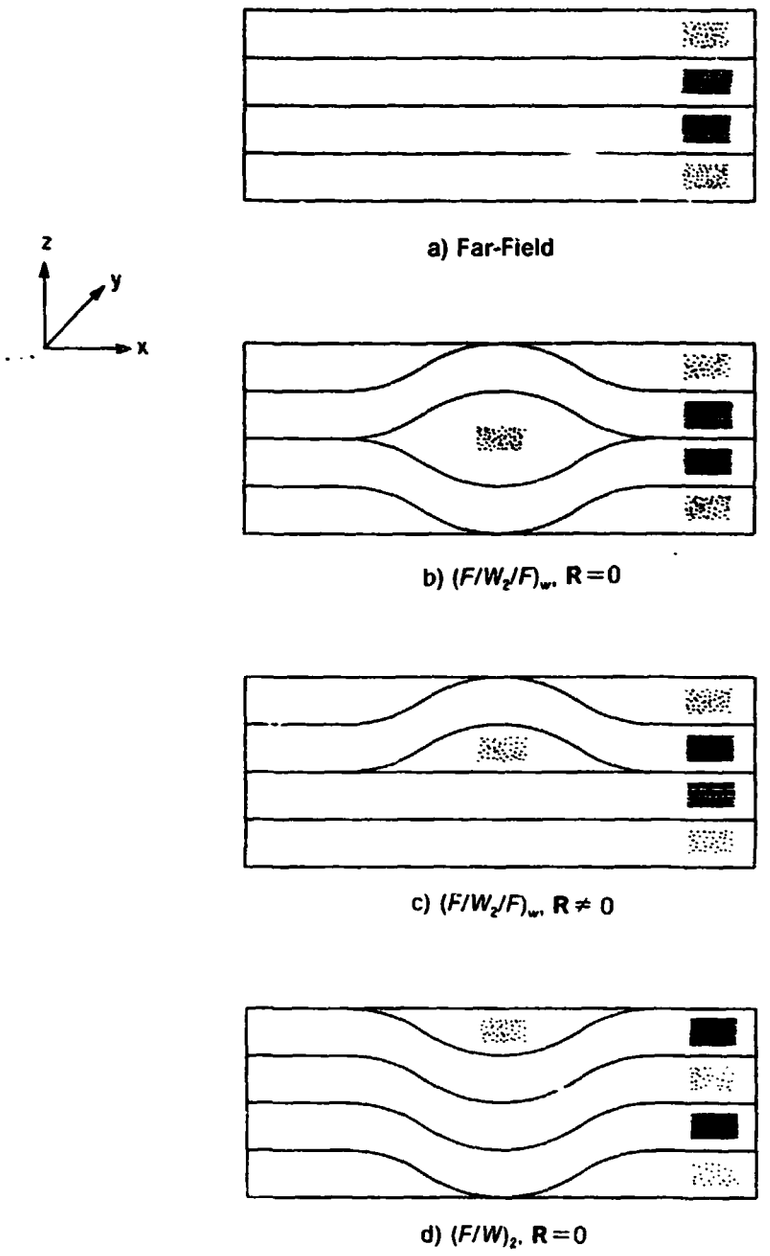

Figure 19. Regions of different laminate stiffness in $(F/W_2/F)_w$ laminates.

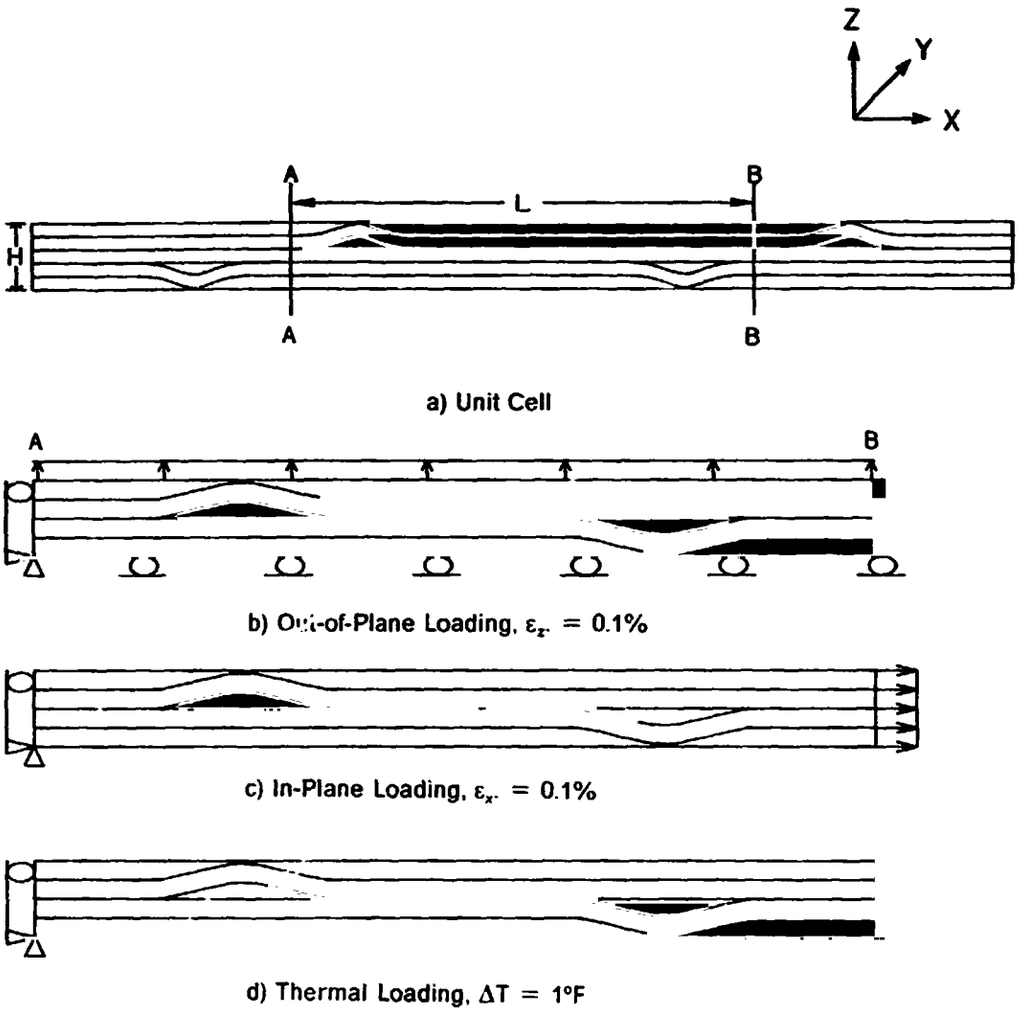

Figure 20. Boundary conditions and applied loads for analysis of unit cells in a $(F/W_2/F)_t$ laminate.

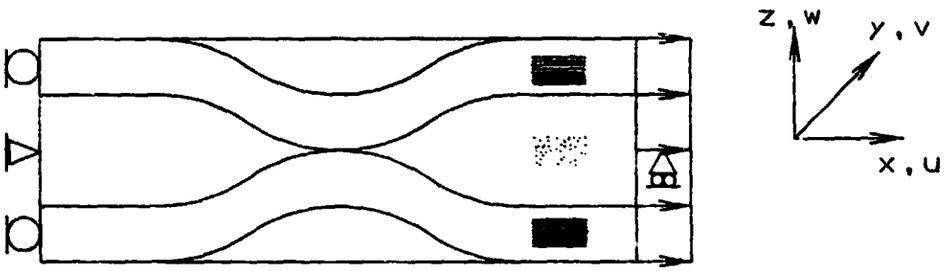

a) Analysis To Determine E_x. ε_x = 0.1%.

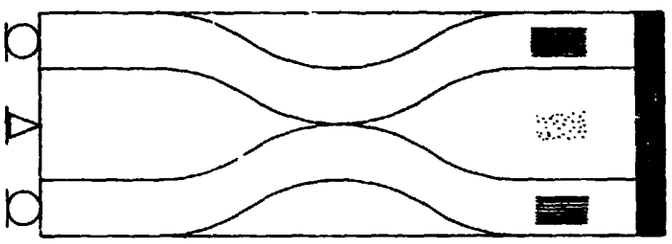

b) Analysis To Determine E_y. σ_y = 1000 psi.

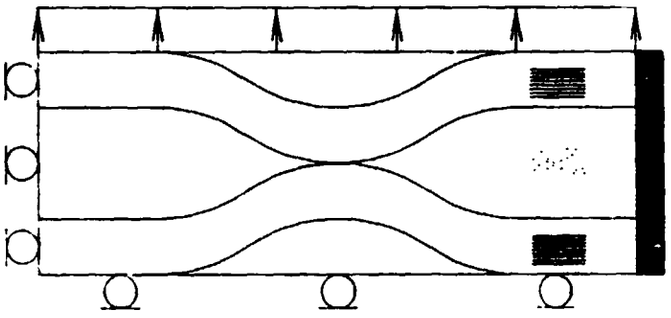

c) Analysis To Determine E_z. ε_z = 0.1%.

Figure 21. Boundary conditions and applied loads for analysis of far-field region and regions of undulation

$$E_i = \frac{1}{\varepsilon_i A}\int \sigma_i \, dA \qquad i = x,y,z \tag{3.5}$$

The results of this analysis are presented in Table 5. They show that the greatest variation in stiffness is in E_x. It varies from a maximum of 20.7 MSI in the far-field region (Figure 19a) to a minimum of 8.9 MSI in the $(F/W)_2$ undulation (Figure 19d). This low value of E_x in the regions of undulation is a direct result of the curvature of the tows. The fill tows, which are straight in the far-field region, dominate the axial stiffness. In the undulation, the curvature of the fill tows decreases the reinforcement in the x direction and reduces axial stiffness (E_x). The large difference in E_x between the $(F/W)_2$, **R**=0 and $(F/W_2/F)_w$, **R**=0 undulations is attributed to the influence of the model geometries on the deformation of the fill tows. In the $(F/W_2/F)_w$, **R**=0 laminate the fill tows tend to deform towards the midplane of the laminate, but deformation is restricted by the warp tows between the peaks of the undulations. The fill tows in the $(F/W)_2$ laminate, however, are nested such that there is relatively little constraint on out-of-plane displacement. Thus, the fill tows in the $(F/W)_2$, **R**=0 laminate are more easily able to straighten under tensile load and hence the axial modulus E_x is reduced.

The curvature of the fill tows also tends to increase the out-of-plane stiffness E_z. However, the maximum increase in E_z is less than 4 percent. The changes in E_x and E_z follow the transformation equations associated with classical laminated plate theory (CLPT), which state that a small variation in fiber orientation from the x axis greatly reduces E_x but has negligible effect on E_z.

The modulus E_y changed very little because E_y is dominated by the warp tows, which exhibit maximum stiffness in the y direction, and whose geometry does not vary with x for the generalized plane strain analysis.

Table 5. Moduli in Specific Regions of 8-Harness Woven Fabric Laminate

Region	E_x (MSI)	E_y (MSI)	E_z (MSI)
Far-Field	20.7	20.7	0.77
$(F/W_2/F)_w$, R=0	15.2	20.4	0.80
$(F/W_2/F)_w$, R=1,4	16.3	20.6	0.79
$(F/W)_2$, R=0	8.9	20.4	0.79

3.3.2 Laminate In-Plane Stiffness

The axial modulus E_x was evaluated for the complete repeating unit cell for each of the three stacking sequences ($(F/W_2/F)_f$, $(F/W_2/F)_w$, and $(F/W)_2$) for all four offset ratios (**R** = 0, 0.5, 1, and 4). For each of the above cases the undulation aspect ratio Ω was held constant at 12. Additionally, the influence of Ω on E_x was investigated for the $(F/W_2/F)_f$, **R** = 0 laminate. For this analysis Ω values of 6, 9, 12, 18, and 24 were used.

3.3.2.1 Effect of Stacking Sequence and Offset Ratio

The predicted values of E_x as a function of stacking sequence and offset ratio **R** are presented in Table 6. The predicted values of E_x range between 16.9 MSI and 19.8 MSI. The same maximum E_x (19.8 MSI) is predicted for the $(F/W_2/F)_f$ and $(F/W_2/F)_w$ laminates with **R** = 0. This is attributed to the symmetry of the laminates. These laminates are symmetric about the x-y plane. As discussed in the previous section, symmetry of the laminates reduces the out-of-plane deformation that results in lower modulus. Minimum E_x is found in the $(F/W)_2$, **R** = 0 laminate. This result is reasonable because this laminate contains the undulation illustrated in Figure 19d, which exhibits the lowest E_x of the undulations evaluated (Table 5).

Comparison of the axial moduli in all three stacking sequences indicate that E_x is essentially independent of offset ratio for **R** ≠ 0. However, E_x appears to be a function of stacking sequence. The average values of E_x for **R** ≠ 0 (Table 6) indicate that maximum and minimum E_x is associated with the $(F/W_2/F)_w$ and $(F/W_2/F)_f$ stacking sequences, respectively. Recalling that the $(F/W_2/F)_f$ and $(F/W_2/F)_w$ stacking sequences are associated with cross-sections **A-A** and **B-B**, respectively, in the $(F/W_2/F)$ laminate (Figure 14), these results indicate that E_x and E_y are not equal in the $(F/W_2/F)$ laminate, but differ by approximately 10 percent. The average value of E_x in the $(F/W)_2$ laminate is 18.4 MSI, which is between those of the $(F/W_2/F)_f$ and $(F/W_2/F)_w$ stacking sequences.

3.3.2.2 *Effect of Undulation Aspect Ratio* Ω

The influence of the undulation aspect ratio Ω on the axial modulus E_x of the $(F/W_2/F)_R$, R=0.5 laminate is illustrated in Figure 22. The increase in E_x from $\Omega=6$ to $\Omega=24$ is approximately 6 MSI (44 percent). Most of the increase occurs in the range $\Omega=6$-12, where E_x increases from 13.5 MSI to 18.2 MSI. In the range $\Omega=12$-24, E_x increases less than 3%, from 18.9 MSI to 19.4 MSI. The increase in E_x is attributed to the change in curvature of the fill tows. The fill tows exhibit less curvature with increasing Ω. Thus the axial modulus E_x increases.

3.4 *Results: Out-of-Plane Loading*

3.4.1 Stress Distributions In Regions of Undulation

As discussed in the previous section, each woven fabric laminate contains a far-field region and one or more regions of undulation. The far-field region behaves essentially like a cross-ply laminate, but the response of the undulation region is more complex. To illustrate the complex state of stress in the undulations, stress distributions in the $(F/W_2/F)_R$ laminates are presented in this section.

The stress distributions in the undulations are presented as contour plots. The σ_x and σ_y components of stress are discontinuous at the interfaces between the warp and fill tows. Additionally, there tends to be large variations in the magnitudes of σ_x and τ_{xz} between the warp and fill regions (σ_y and τ_{yz} are continous at the warp-fill interface). Therefore, the distributions in the warp and fill regions are presented in different figures. The contour plots presented were generated using the computer program CAEDS. CAEDS uses the nodal values of the stresses and applies a proprietary algorithm to generate the plot data. It should

Table 6. In-Plane Modulus E_x of Woven Fabric Laminates.

Laminate	R	Ω	E_x (MSI)
$(F/W_2/F)_f$	0.0	12	19.8
	0.5	12	17.5
	1.0	12	17.5
	4.0	12	17.5
			Avg (R ≠ 0) 17.5
$(F/W_2/F)_w$	0.0	12	19.3
	0.5	12	18.2
	1.0	12	19.3
	4.0	12	19.3
			Avg (R ≠ 0) 18.9
$(F/W)_2$	0.0	12	16.9
	0.5	12	18.5
	1.0	12	18.3
	4.0	12	18.3
			Avg (R ≠ 0) 18.4

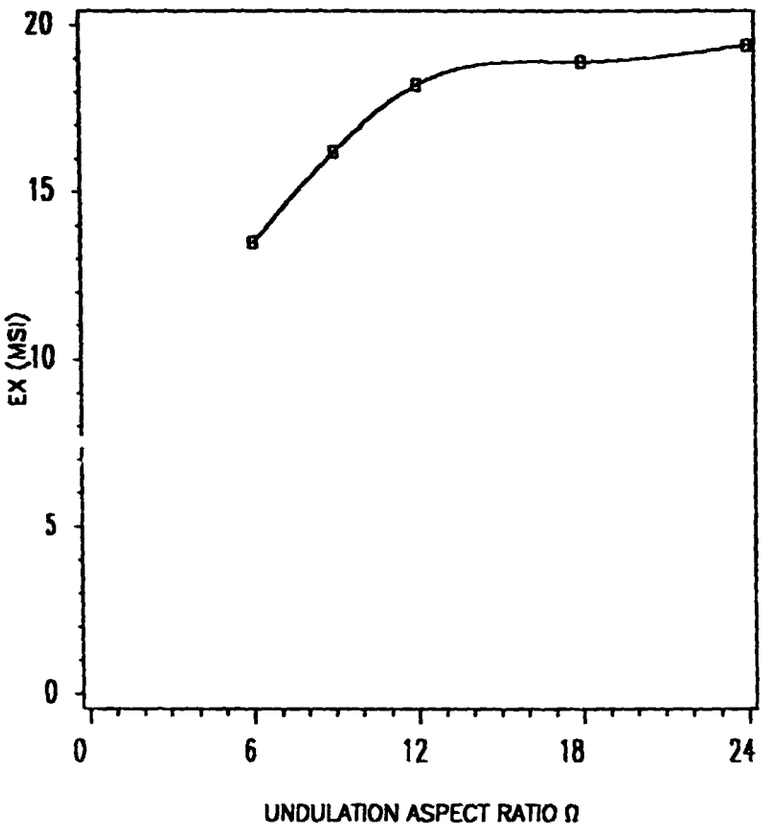

Figure 22. Influence of Undulation Aspect Ratio Ω on E_x

be noted that the algorithm tends to smooth the data, which can result in the loss of areas of high stress gradients from the plot. However, within this limitation, the figures adequately represent the stress distributions in the undulations.

Contour plots of the normal stresses σ_x, σ_y, σ_z, and the shear stress τ_{xz} for the $(F/W_z/F)$, stacking sequence, R values of 0 and 0.5, are presented in Figure 23 and Figure 25 through Figure 31. The contour plots for the cases R=1 and 4 are presented in Appendix A.

3.4.1.1 Stress Concentrations

Prior to presenting the stress distributions in the undulations it is appropriate to address the presence of stress concentrations in the laminates. Stress concentrations in structures are normally associated with abrupt changes in cross-section. They occur in such frequently encountered configurations as holes, notches, and fillets. In heterogenous materials stress concentrations also occur in areas where there are point-wise discontinuities in material properties. At these point-wise discontinuites the stresses are predicted by linear elasticity to be infinite. These points are called "singularities" or "singular points", and the stresses are said to be "singular". Several of the laminates modeled in this study contain singular points at the midplane. The number of singular points in each laminate depends on its stacking sequence and offset ratio R. The locations of the singularities in several of the laminates are labelled in Figure 18. In the finite element method used in this study, the magnitude of a stress at a singular point is a function of the density of the mesh at that point. In this analysis no attempt was made to refine the mesh near the stress concentration. The density of the mesh was constant for all cases. Therefore, relative comparisons of the stress distributions between different cases can be made. The number and axial coordinate of singular points in each of the laminates modeled in this study are listed in Table 7. Their locations are also identified as appropriate in the discussions on stress distributions.

Table 7. Stress Concentrations in Woven Fabric Laminates

Laminate	R	No. of Singular Points	Coordinate ($\frac{x}{\lambda}$)
$(F/W_2/F)_f$	0.0	1	3.0
	0.5	0	-
	1.0	0	-
	4.0	0	-
$(F/W_2/F)_w$	0.0	2	2.2, 3.8
	0.5	2	2.2, 4.8
	1.0	4	2.2, 3.8, 4.2, 5.8
	4.0	4	2.2, 3.8, 10.2 11.8
$(F/W)_2$	0.0	0	-
	0.5	1	3.0
	1.0	1	3.0
	4.0	1	3.0

3.4.1.2 *R=0 Laminate*

The contour plot of the in-plane normal stress σ_x for the $(F/W_z/F)_f$, R=0 laminate subjected to out-of-plane loading is shown in Figure 23. Only the upper half of laminate is shown since the laminate is symmetric about the x-y plane. The fill tow (Figure 23a) exhibits a fairly uniform far-field compressive stress of approximately -100 psi at points A and E. Within the undulation, however, there is a significant variation in the stress. At locations where the curvature of the fill tow is convex (B, D, and G) the magnitude of σ_x approaches a tensile stress of 3000 psi. Where the curvature of the fill tow is concave (C, F, and H) the magnitude of σ_x approaches -3000 psi. In the warp tow (Figure 23b), the far-field tensile value of σ_x is 100 psi (A and E). It decreases to approximately 70 psi at points F and H and increases to 180 psi at point G. The warp tow above the fill tow (B-C-D) exhibits σ_x values approaching 180 psi at points B and D, but the stress is relatively constant in the remaining area with a value of about 60 psi. The nonzero far-field σ_x is a the result of the mismatch in Poisson's ratio between the warp and fill tows and the requirement of displacement continuity at the warp-fill interface. The warp tow has a higher ν_{xz} than the fill tow, and thus the fill tows are in compression and the warp tows are in tension. The far-field σ_y in the warp and fill tows are also of equal magnitude and opposite sign and thus indicates that equilibrium in both the x and y directions is satisfied.

The stress distributions near the undulation can best be explained by considering the deformation of the laminate. Figure 24 shows the deformation of the fill tows in the $(F/W_z/F)_f$ laminates with R values of 0 and 0.5. (The deformations of the other laminates are similar.) The fill tows not only undergo displacement in the z direction, but they also contract in the x direction and undergo a change in curvature, which is illustrated by the change in angle θ between the undeformed and deformed fill tows. Thus, the deformation of the fill tow is analogous to the bending of a beam. This causes compression along the concave portions of the tow (points C, F, and H in Figure 23a) and tension at locations of convex curvature (B, D, and G). The axial contraction δ in the fill tow (Figure 23a) is indicative of additional

compressive σ_x in the undulation. This contraction is responsible for the decrease in σ_x at points F and H in the warp tow (Figure 23b). The increase in σ_x at point G in the warp tow is a result of the bending at that location. It should be noted that this laminate does exhibit a stress concentation in the form of a singularity at G due to the vanishing warp tows at that point.

The σ_y stress contour is illustrated in Figure 25. The form of the σ_y distribution is similar to that of σ_x, but the magnitude of σ_y is lower. The fill tow is in tension throughout, with maximum values of σ_y approaching 140 psi at points B, D, and G and minimum values of 94 psi at points C, F, and H. The far-field value of σ_y is approximately 100 psi. The warp tow is in compression throughout, and has a far-field magnitude of approximately -100 psi at points A and E. The far-field values of σ_y in the warp and fill tows indicate that equilibrium in the y direction is satisfied. The normal stress σ_y increases to a compressive value of -85 psi at G. As with the σ_x component of stress, σ_y is a result of the mismatch in Poisson's ratios between the warp and fill tows. The small, but definite, variations in σ_y at the undulation are also a result of the deformation of the fill tow.

The σ_z stress contour is illustrated in Figure 26. The far-field value of σ_z is approximately 750 psi in both the warp and fill tows. The maximum values of σ_z are found in the regions F-G and G-H, where the fill tow is inclined and E_z is maximum. In these regions σ_z averages 800-850 psi with a maximum value of about 1000 psi at points B and D. This distribution is the result of a change in the stiffness in the z direction due to the orientation of the fill tow. As discussed earlier, the variation in the orientation of the fill tow at the undulation results in localized variation in laminate stiffness. In this case the orientation of the fill tow increases the stiffness in the z direction. Thus, under a uniform applied ε_z a higher stress is expected.

The τ_{xz} stress contour is shown in Figure 27. The τ_{xz} component does not approach the far-field value as quickly as the other components of stress. The far-field value of τ_{xz} should be zero, which corresponds to the value expected from a cross-ply laminate. τ_{xz} does reach zero, but not within the domain shown in Figure 27. At points A and E, τ_{xz} is about 20 psi. The largest values of τ_{xz} are in the curved regions of the fill tow, between C and D where τ_{xz} re-

aches a maximum of 300 psi, and between **B** and **C**, where τ_{xz} reaches a maximum of -300 psi. In these locations the orientation of the fill tow with respect to the load axis is analogous to that of an off-axis unidirectional laminate under tensile load, and results in a large shear stress.

3.4.1.3 R=0.5 Laminates

The stress contours in the **R**=0.5 laminate are shown in Figure 28 through Figure 31. The σ_x, σ_y and σ_z distributions in this laminate are very similar to those of the **R**=0 laminate. The shear stresses in the fill tows are also similar. In both laminates the maximum τ_{xz} in the fill tows are ± 300 psi. The major difference between the laminates is in the τ_{xz} distribution in the warp tows. The shear stress in the warp tow region between fill tows (**B-C**) in the **R**=0.5 laminate is approximately 40 psi. On either side (**A-B**, **C-D**), τ_{xz} is approximately -40 psi. The difference in τ_{xz} between the **R**=0 and 0.5 laminates is attributed to the offset of the undulations in the **R**=0.5 laminate, which results in greater shear deformation of the layers.

3.4.1.4 R=1 and 4 Laminates

For completeness, the stress contours in the undulations of the **R**=1 and **R**=4 laminates are presented in Figure 99 through Figure 106 in Appendix A. (For the **R**=4 laminate the stress contour is presented for only one of the regions of undulation. In the **R**=4 laminates it has been found that the distance between the undulations is large enough that they do not influence each other. This is discussed in more detail in the following section on interfacial stress distributions.) Comparison of the figures shows that they all exhibit similar trends in their stress distributions. Therefore, the stress distributions are not discussed in detail. However, the maximum value of each component of stress for all offset ratios is presented in Table 8.

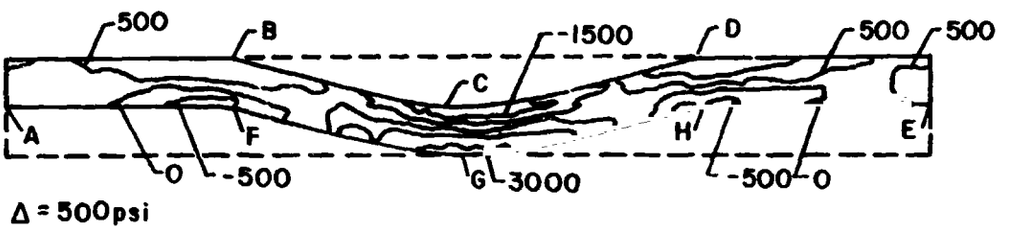

a) Fill Tow

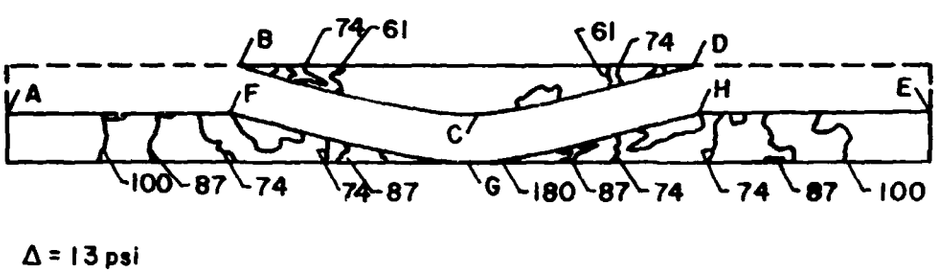

b) Warp Tows

Figure 23. Contour plot of σ_x in $(F/W_2/F)_1$ laminate. $R = 0$, $\varepsilon_z = 0.1\%$.

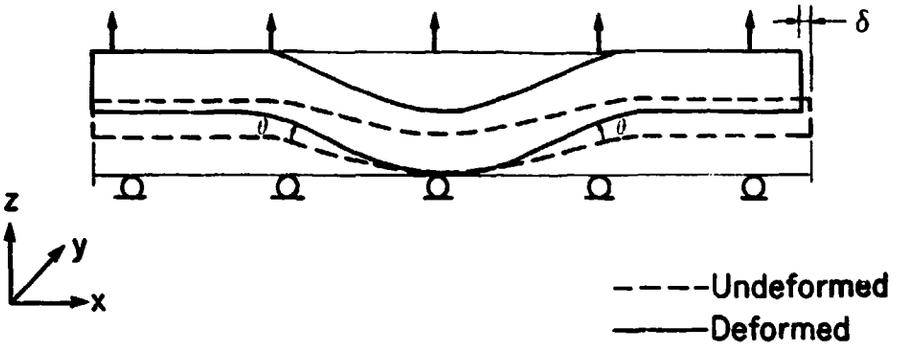

a) Undulation Offset Ratio **R** = 0

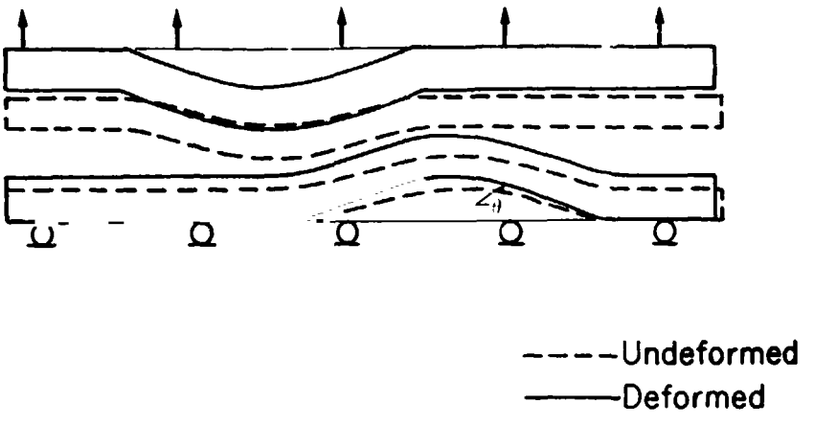

b) Undulation Offset Ratio **R** = 0.5

Figure 24. Fill tow deformations in $(F/W_2/F)_1$ laminate. R = 0, 0.5. $\varepsilon_z = 0.1\%$.

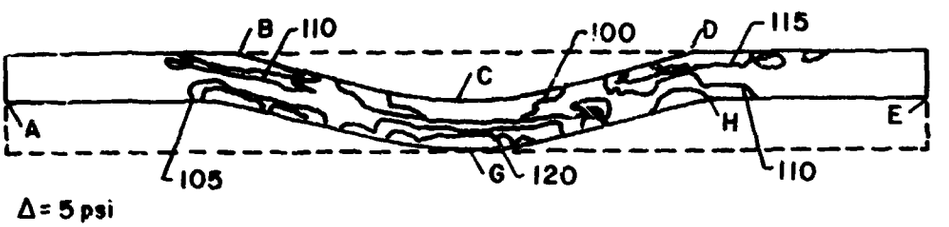

a) Fill Tow

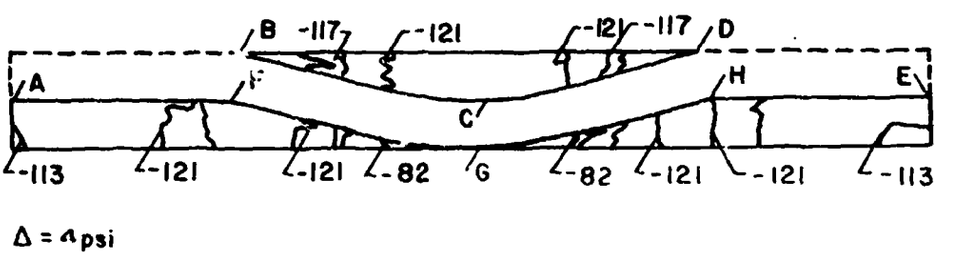

b) Warp Tows

Figure 25. Contour plot of σ_y in $(F/W_2/F)_1$ laminate. $R=0$, $\varepsilon_z=0.1\%$.

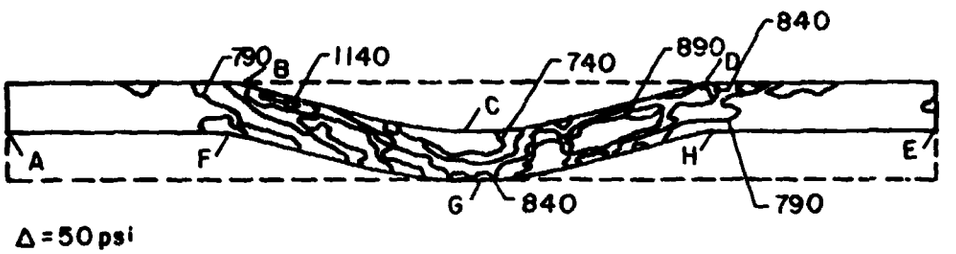

a) Fill Tow

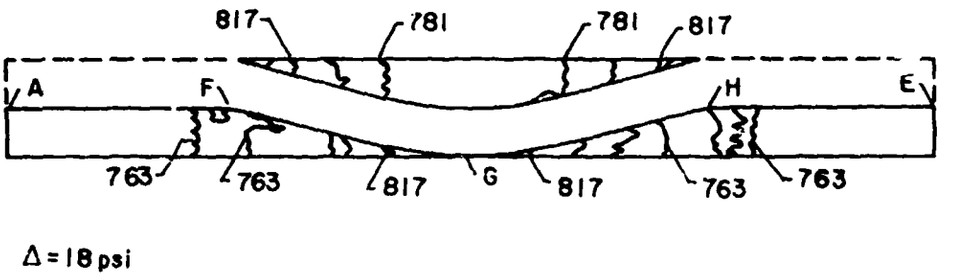

b) Warp Tows

Figure 26. Contour plot of σ_z in $(F/W_2/F)_1$ laminate. $R=0, \varepsilon_z=0.1\%$.

The results presented in Table 8 indicates the degree of interaction between the undulations for all components of stress. The in-plane normal stress σ_x is greatest for the **R**=0.5 case (3300 psi) and decreases with increase of the separation distance between the undulations (σ_x = 2690 psi at **R**=4). The variations in the normal stresses σ_y and σ_z are similar to σ_x in that the maximum values occur in the **R**=0.5 laminate. The maximum interlaminar shear stress τ_{xz} in the undulation is relatively independent of offset ratio, differing by less than seven percent in the range **R**=0-4. These results indicate that maximum interaction between the undulations occurs for the case **R**=0.5. This is attributed to the complex stress state that exists because the undulations are close together yet oriented such that the laminate is unsymmetric about the x-y plane.

3.4.2 Interfacial Stress Distributions: $(F/W_2/F)_t$ Laminates

Interfacial stress distributions for the $(F/W_2/F)_t$ laminates for **R** values of 0 and 0.5 are presented in Figure 32 through Figure 35. (Here and throughout the remainder of the text, the interface is defined as the plane between adjacent woven fabric plies. For the two-layer laminate modeled in this study, the interface corresponds to the midplane of the laminate.) Stresses were evaluated at the Gauss points nearest the interface for each side of the interface. In the far-field region the interface is bounded by warp tows on either side. The undulation aspect ratio Ω was constant at 1? for all cases. As stated previously, the applied load corresponds to out-of-plane strain ε_z = 0.1% .

3.4.2.1 R=0 Laminate

In-plane Normal Stresses σ_x and σ_y: The interfacial σ_x and σ_y distributions in the **R**=0 laminate are shown in Figure 32 The stress distributions show that the effect of the tow undulations

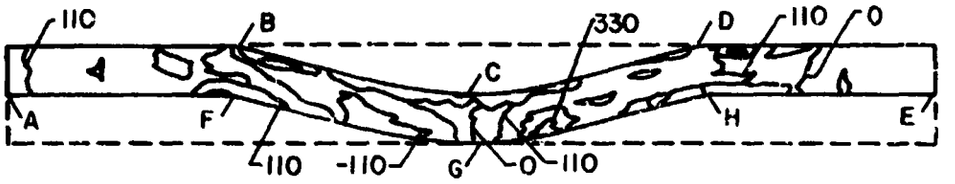

Δ = 110 psi

a) Fill Tow

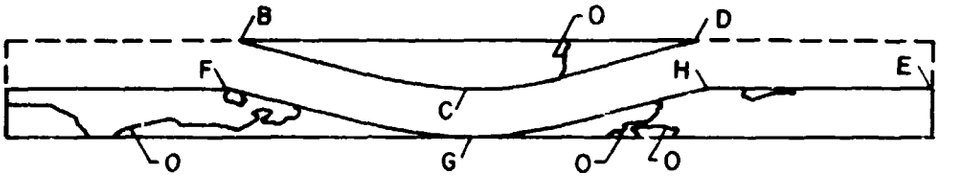

Δ = 1^ i

b) Warp Tows

Figure 27. Contour plot of τ_{xz} in $(F/W_2/F)_t$ laminate. $R=0$, $\varepsilon_z = 0.1\%$.

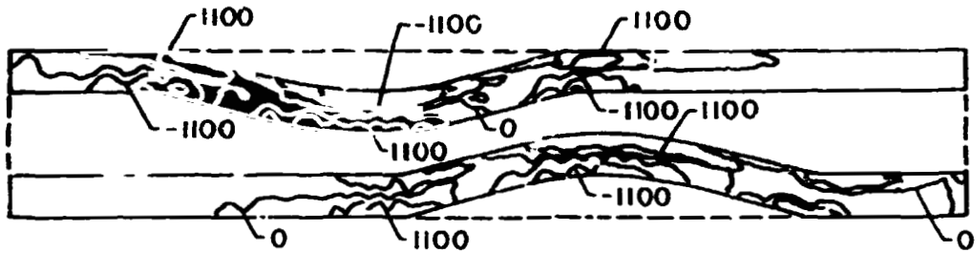

Δ=550 psi

a) Fill Tows

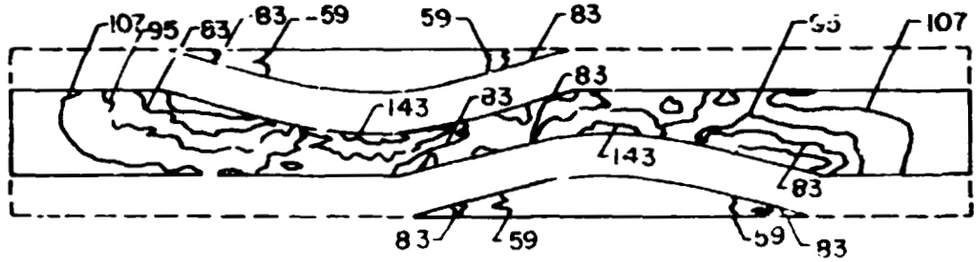

Δ = 12 psi

b) Warp Tows

Figure 28. Contour plot of σ_x in $(F/W_j/F)_i$ laminate. R=0.5, ϵ_x =0.1%.

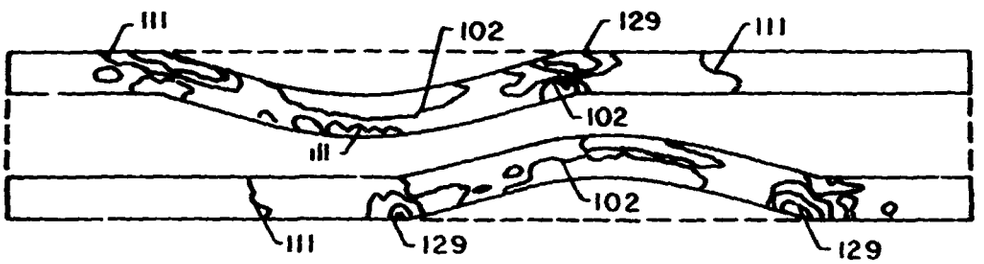

Δ = 9 psi

a) Fill Tows

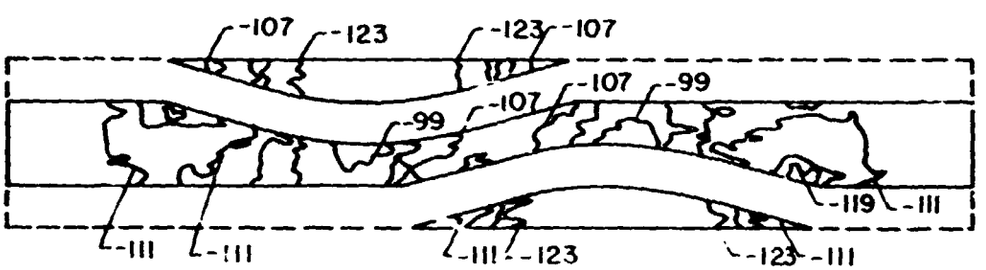

Δ = 4 psi

b) Warp Tows

Figure 29. Contour plot of σ_y in $(F/W_2/F)_t$ laminate. $R=0.5$, $\varepsilon_z =$

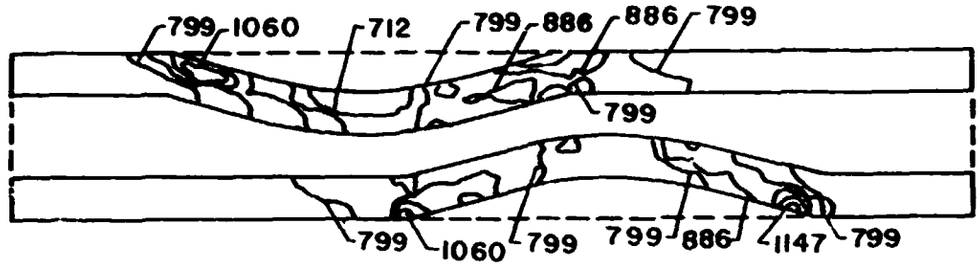

a) Fill Tows

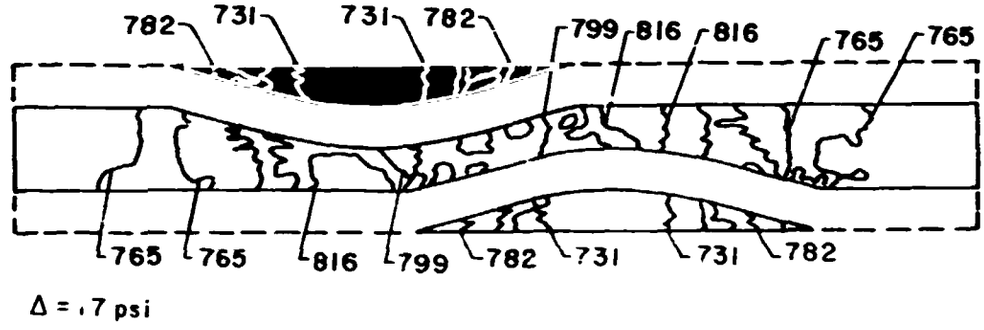

b) Warp Tows

Figure 30. Contour plot of σ_z in $(F/W_2/F)_t$ laminate. $R = 0.5$, $\varepsilon_z = 0.1\%$.

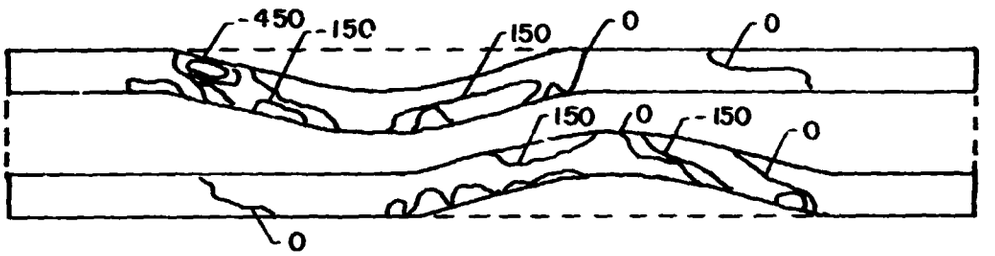

Δ = 150 psi

a) Fill Tows

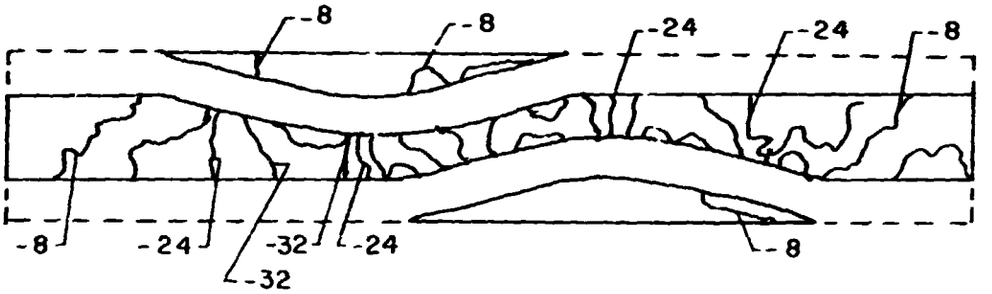

Δ = 8 psi

b) Warp Tows

Figure 31. Contour plot of τ_{xz} in $(F/W_2/F)_1$ laminate. $R = 0.5$, $\varepsilon_z = 0.1\%$.

Table 8. Maximum stress values in undulation of $(F/W_2/F)_t$ laminate under out-of-plane loading. $\varepsilon_z = 0.1\%$.

Maximum Stress (psi)				
R	σ_x^{max}	σ_y^{max}	σ_z^{max}	τ_{xz}^{max}
0.0	3000	140	1180	630
0.5	3300	184	1500	620
1.0	2860	173	1500	600
4.0	2590	143	1200	650

is local. Both components of stress approach far-field values away from the undulation. The distribution of in-plane normal stress, σ_x, at the interface is relatively constant in the far-field regions at about 100 psi with small decreases at points B and D, which are within the region of undulation. A discontinuous jump in σ_x exists at point C. As discussed in the previous section, the presence of a normal stress σ_x in the far-field regions is due primarily to the mismatch in Poisson's ratios between the warp and fill tows. The behavior at points B, C, and D can be explained by recalling the discussion on the deformation of the laminate. The reduction in σ_x at points B and D is due to a compressive component of stress resulting from contraction of the fill tow (Figure 24). The jump in σ_x at point C is a result of the change in material properties at that point. The stress at C is evaluated in a fill tow, which is much stiffer in the x direction than the warp tow. Additionally, the magnitude of σ_x at C can also be related to the deformation of the laminate and the presence of a stress concentration. As discussed previously, the geometry at the undulation results in bending of the fill tow. This results in an increase in σ_x at C. For the plots presented here the stresses are evaluated at the Gauss points, which are near but not at the location of the stress concentration (C); therefore, the contribution of the stress concentration to the magnitude of σ_x at C is believed to be small compared to the contributions from the change in material properties and the bending of the tow.

The interfacial σ_y distribution (Figure 32b) is very similar to that of σ_x with the exception of much lower maximum values at C. As was the case for σ_x, the σ_y stresses are a result of the mismatch in Poisson's ratios between the warp and fill tows. The far-field value of σ_y in the warp tows is approximately -110 psi. At point C, σ_y is evaluated in a fill tow, at which the magnitude of σ_y is approximately 130 psi. The decrease in σ_y at points B and D is a result of the axial contraction of the undulation (Figure 24) that caused localized decreases at B and D in the σ_x component of stress (Figure 32a).

Interlaminar Stresses σ_z and τ_{xz}: The distribution of the interlaminar normal stress σ_z along the interface is illustrated in Figure 33a. As was the case for the in-plane normal stresses

σ_x and σ_y, the effect of the undulations is local. Both σ_z and τ_{xz} approach far-field values away from the undulation. The far-field value of σ_z is approximately 760 psi (**A** and **E**). At points **B** and **D**, σ_z decreases to about 740 psi then increases to a maximum of 880 psi at the points on either side of **C**. The decrease in σ_z at points **B** and **D** are attributed to a small compressive σ_z resulting from the change in curvature of the fill tows at the shoulders of the undulation (point *S*). The increase in σ_z between **B** and **D** is due to the increased out-of-plane stiffness (E_z) in the region. As discussed previously, the change in orientation of the fill tows increases the out-of-plane laminate stiffness at the undulation; therefore, under uniform applied strain ε_z , the σ_z component of stress can be expected to be larger than in the far-field regions. The location of the maximum values of σ_z, on either side of **C**, appears to be associated with the location of largest out-of-plane stiffness along the interface. The local decrease in σ_z at point **C** can be explained as follows. At point **C** the curvature of the fill tows is zero; therefore, the stacking sequence of the laminate at **C** is $(F/W_z/F)_s$. At this location, the laminate is similar to a regular cross-ply laminate. Thus σ_z has a tendency to approach the far-field value.

The interlaminar shear stress τ_{xz} (Figure 33b.) is essentially zero throughout. This is predicted for a cross-ply symmetric laminate. The exception is at **C** where τ_{xz} exhibits values of +20 and -20 psi. This is the point of stress concentration, again a result of the idealized geometry of the model.

3.4.2.2 R=0.5 Laminate

In-plane Normal Stresses σ_x and σ_y: The interfacial stress distributions in the **R**=0.5 laminate are shown in Figure 34. The distributions of the in-plane normal stresses, σ_x and σ_y are very similar to those of the **R**=0 laminate. The far-field value of σ_x (Figure 34a) is approximately 100 psi and reaches 2100 psi at points **C** and **D**, where changes in material properties occur. This stress is less than the maximum σ_x of 2800 psi exhibited by the **R**=0 laminate. This difference is due to two factors. First, the stiffness of the undulation region changes with offset

ratio. Secondly, in the R=0.5 laminate the undulations are offset such that no region of stress concentration exists. There is virtually no difference in the σ_y stress distribution (Figure 34b) between the R=0 and R=0.5 laminates.

Interlaminar Stresses σ_z and τ_{xz}: The interlaminar normal stress σ_z (Figure 35a) exhibits a far-field magnitude of 760 psi, which is equal to that of the R=0 laminate. Between points B and F, σ_z undergoes changes in magnitude which are caused by changes in stiffness due to curvature of the fill tows. The maximum value of σ_z is approximately 840 psi, which is a decrease of about five percent from the R=0 laminate. As with σ_x, this is attributed to the reduction in stiffness associated with the offset of the undulations and the absence of a point of stress concentration. The difference of about five percent between the maximum values of σ_z in the R=0 laminate which has a singular point, and the R=0.5 laminate, which lacks a singular point, suggests that for this analysis the influence of the singularity on the stress distribution in these laminates is minimal. As discussed previously, this may be a result of the density of the finite element mesh at the singular points. Had the mesh been finer at the singular points their effect might be more noticeable.

The distribution of τ_{xz} in the R=0.5 laminate (Figure 35b) differs significantly from that of the R=0 laminate. Whereas the R=0 laminate exhibited essentially zero shear stresses, τ_{xz} in the R=0.5 laminate ranges from -50 psi at points B and F to 40 psi at point D. This is a result of the offset of the undulations in the laminate. As discussed earlier, the fill tows undergo a decrease in radius of curvature during deformation. This results in greater contraction of the fill tows in the x direction than is attributed to standard Poisson ratio effects. In this laminate, the offset of the undulations causes a mismatch in the contraction between the two plies of the laminate. Therefore, a significant shear stress is generated at the interface.

3.4.2.3 *R=1 and 4 Laminates*

The interfacial stress distributions in the **R=1** and **R=4** laminates are shown in Figure 115 through Figure 118 in Appendix A. The distributions of the normal stresses σ_x, σ_y, σ_z in the laminates differ very little from the **R=0** and **R=0.5** laminates, and their further discussion is not warranted. (The differences and similarities between the laminates are summarized in a later section.) However, significant differences do exist for the interlaminar shear stress τ_{xz}. The τ_{xz} distribution in the **R=1** laminate is shown in Figure 116b. In this laminate, τ_{xz} ranges from approximately 12 psi to -48 psi. In the **R=4** laminate (Figure 118b) τ_{xz} ranges from 30 to -30 psi. Thus, the magnitude of τ_{xz} decreases with separation distance (**R**) between the undulations. This indicates that there is significant interaction between the undulations, with respect to the τ_{xz} component of stress, for small non-zero offset ratios.

Of special interest is the shear stress distribution in the regions $\frac{x}{\lambda}$ = 0-2 and $\frac{x}{\lambda}$ = 12-14 in the **R=4** laminate (Figure 118b). In the large far-field region between points **B** and **C**, τ_{xz} is non-zero, ranging from -7 to -15 psi. This implies that τ_{xz} should also be non-zero at **A** and **D** This contradicts the boundary condition of the finite element model which requires τ_{xz} = 0 at the boundaries of the unit cell. Clearly then, modeling a single unit cell does not accurately predict the the τ_{xz} distribution in the **R=4** laminates. To address the question of the accuracy of the one unit cell model, a two unit cell model was generated and the results from the two unit cells were compared. This was done for all components of stress for the $(F/W_2/F)_f$, **R=4** laminate for both in-plane and out of-plane loading. The results, which are presented in detail in Appendix B, indicate that the only deviation in the results between the one and two unit cell models is in the τ_{xz} for the out-of-plane loading condition. Still, there was no difference between the two models in the maximum predicted value of τ_{xz}. Thus, the one unit cell model is considered sufficient for modeling the τ_{xz} distribution for all offset ratios.

3.4.3 Interfacial Stress Distributions: $(F/W_2/F)_w$ Laminates

The interfacial stress distributions for the $(F/W_2/F)_w$ laminates are shown in Figure 36 through Figure 43. These laminates are different from the $(F/W_2/F)_f$ laminates in that the warp tows exhibit curvature (Figure 14c). Additionally, the geometry of the $(F/W_2/F)_w$ laminate is such that it contains more sources of stress concentration than the $(F/W_2/F)_f$ laminates (Table 7).

3.4.3.1 R=0 Laminate

In-plane Normal Stresses σ_x and σ_y: The σ_x and σ_y stress distributions in the **R**=0 laminate are shown in Figure 36. The far-field σ_x and σ_y values are -110 psi and 110 psi, respectively. Both components of stress are maximum at points **B** and **D**. In this case, the high values of stress at these points are due to bending of the warp tows. The decrease in σ_x and σ_y at **C** is a result of the change in material properties at the interface between **B** and **D**. In this region both components of stress are are evaluated along a fill tow, which is in tension in the x direction and compression in the y direction due to Poisson effects.

Interlaminar Stresses σ_z and τ_{xz}: The distributions of σ_z and τ_{xz} are shown in Figure 37. The magnitude of σ_z is 760 psi in the far-field regions while the maximum values of approximately 950 psi occur at points **B'** and **D'**. These points correspond to the locations along the interface of the laminate where the maximum values of E_z exist. At **C** the geometry of the laminate is similar to that of a cross-ply laminate. Thus σ_z tends toward the far-field value. In the far-field region τ_{xz} is zero, which is consistant with the response of a cross-ply laminate. This laminate is symmetric, so τ_{xz} would be expected to vanish along the interface. The magnitude of τ_{xz} at points **B'** and **D'** and the presence of oscillations in the stresses near these points, are due to numerical instabilities associated with the presence of stress concentrations in the model.

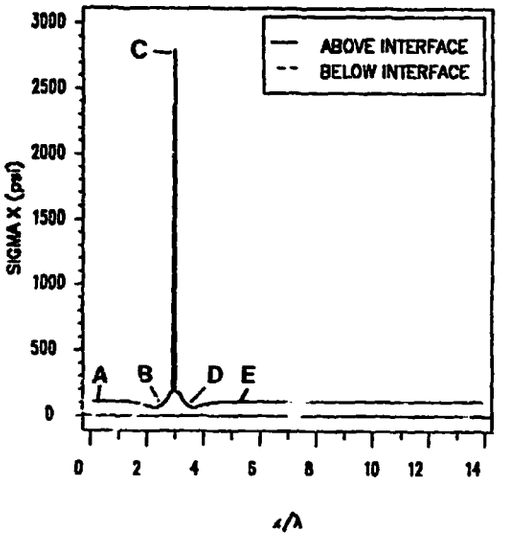

a) Interfacial σ_x.

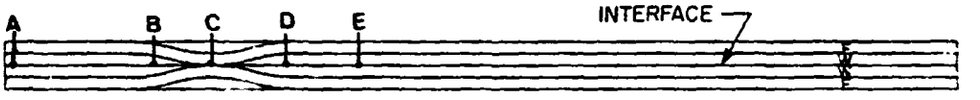

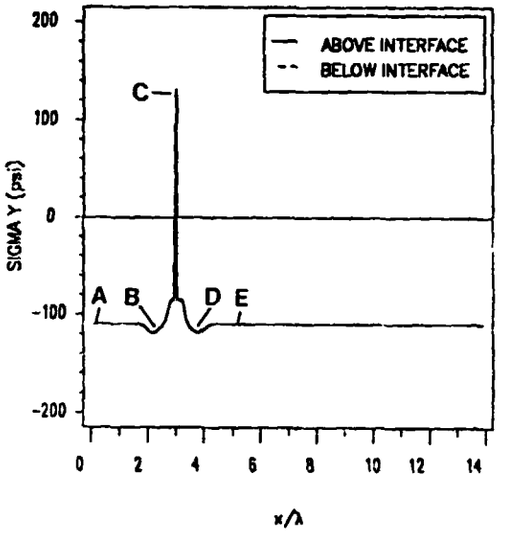

b) Interfacial σ_y

Figure 32. Interfacial σ_x and σ_y in $(F/W_2/F)_1$ laminate. R=0, ε_x =0.1%.

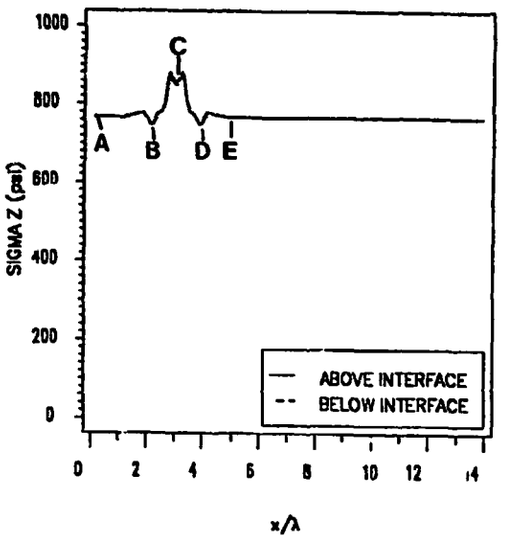

a) Interfacial σ_z.

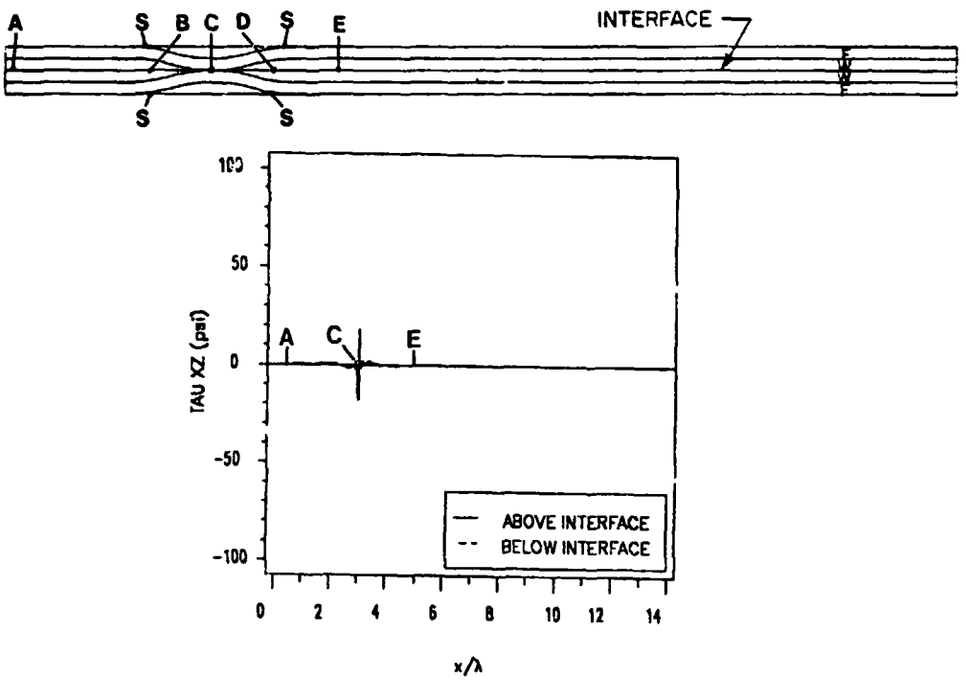

b) Interfacial τ_{xz}.

Figure 33. Interfacial σ_z and τ_{xz} in $(F/W_2/F)_t$ laminate. R=0, ϵ =0.1%.

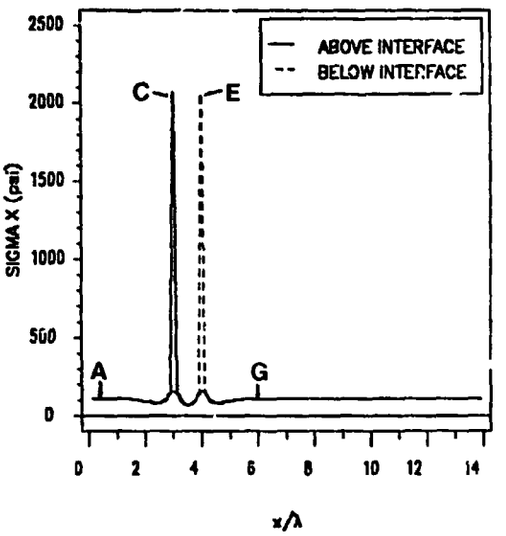

a) Interfacial σ_x.

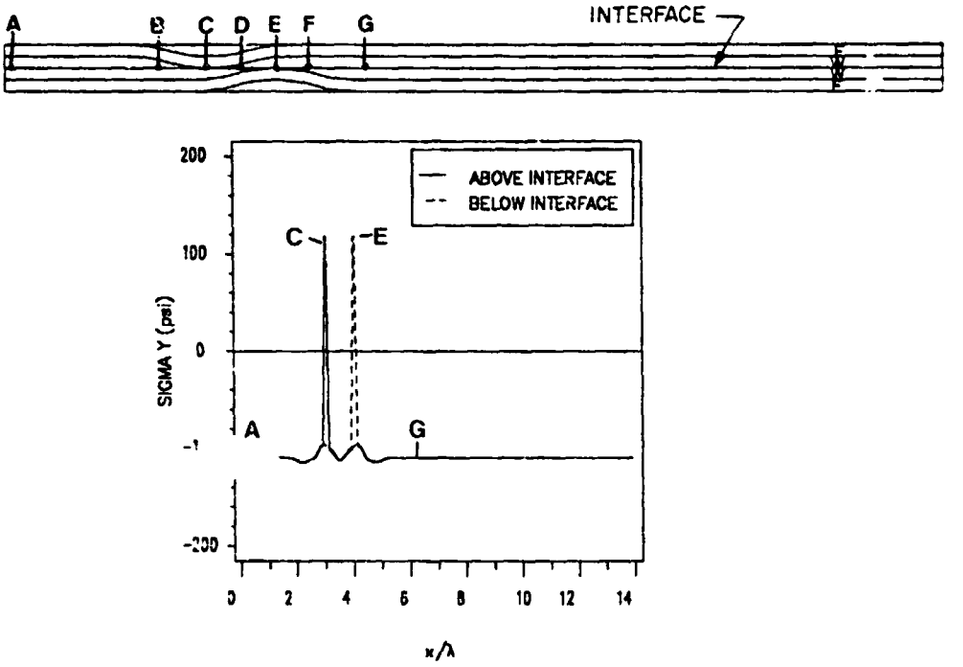

b) Interfacial σ_y.

Figure 34. Interfacial σ_x and σ_y in $(F/W_2/F)_t$ laminate. R=0.5, ε_x =0.1%.

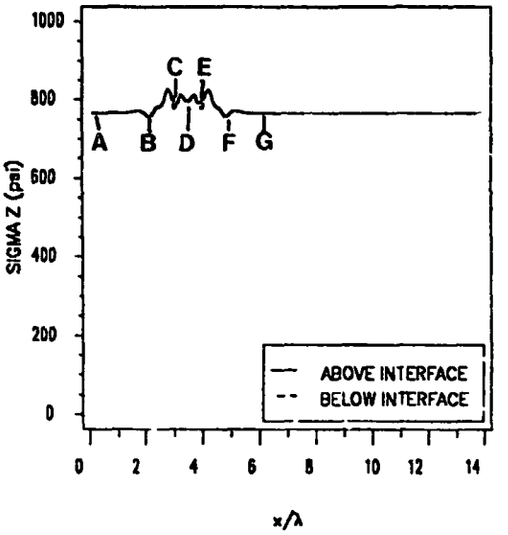

a) Interfacial σ_z.

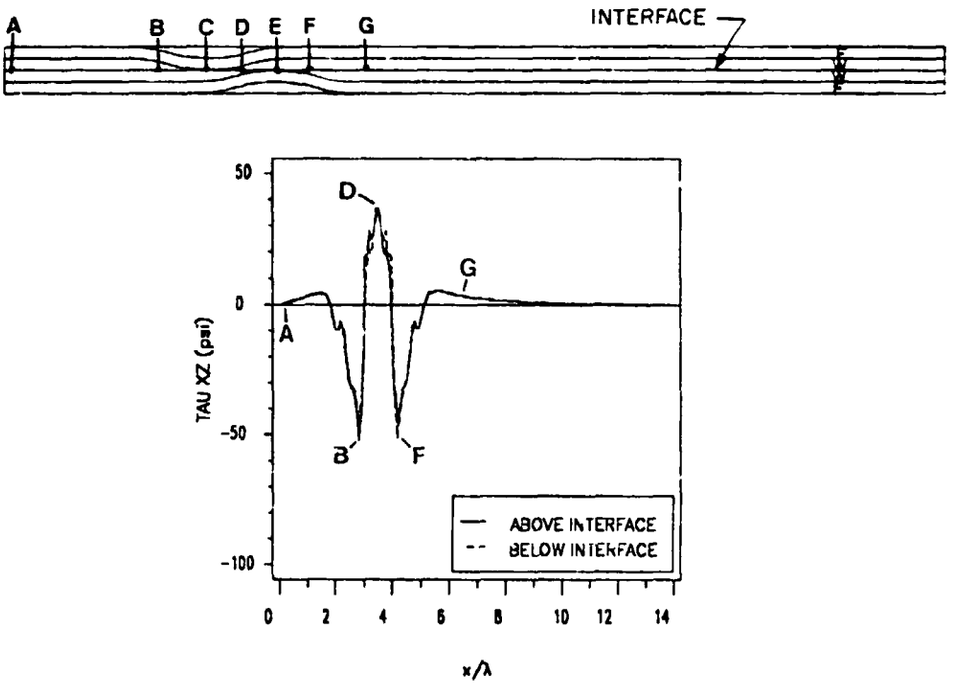

b) Interfacial τ_{xz}.

Figure 35. Interfacial σ_z and τ_{xz} in $(F/W_2/F)_t$ laminate. R = 0.5, ε_z = 0.1%.

3.4.3.2 R=0.5 Laminate

In-plane Normal Stresses σ_x and σ_y: The σ_x and σ_y stress distributions in the R=0.5 laminate are shown in Figure 38. The high values of σ_x at points B, D, E, and G, relative to the far-field σ_{x_∞}, are due to bending of the warp tows. The presence of negative components of σ_x at points C and F requires some discussion. Consider the negative σ_x stress at point C, which occurs in the warp tow below the midplane of the laminate. The presence of this compressive stress is caused by the deformation of the curved portion of the warp tow in the top layer. Deformation of the warp tow causes its shoulders (points C and E) to be pulled in toward each other. The result is compression in the warp tow below the interface at point C. The response at point F is similar; however, in this case the deformation of the bottom layer fill tow causes compression in the top layer fill tow at F. The σ_y distribution is very similar to that of the R=0 laminate. The peaks in σ_y at points B, D, E, and G are due to bending of the fill twos at the undulations. The negative components of σ_y are due to changes in material properties along the interface.

Interlaminar Stresses σ_z and τ_{xz}: The interfacial stresses σ_z and τ_{xz} for the R=0.5 laminate are shown in Figure 39. The σ_z is very similar to that of the R=0 laminate. The interlaminar shear stress τ_{xz} is non-zero due to the asymmetry of this laminate. Points B and G are sources of stress concentration.

3.4.3.3 R=1 and 4 Laminates

The interfacial stress distributions for the R=1 and R=4 laminates are shown in Figure 40 through Figure 43. These laminates contain four sources of stress concentration, compared to only two each for the R=0, 0.5 laminates. This is especially noticeable in the σ_z and τ_{xz} distributions (Figure 41b, and Figure 43b), where continuity of these components

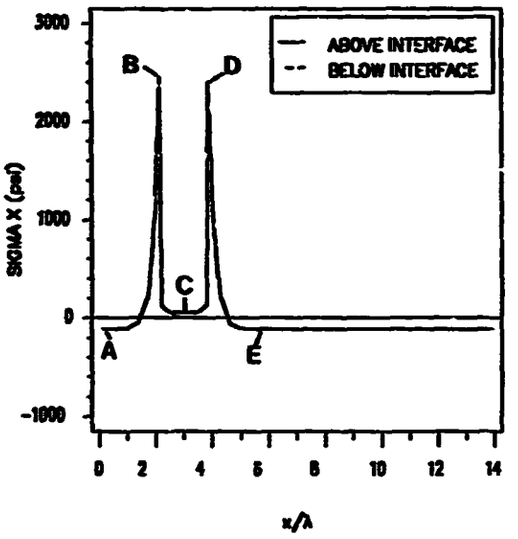

a) Interfacial σ_x.

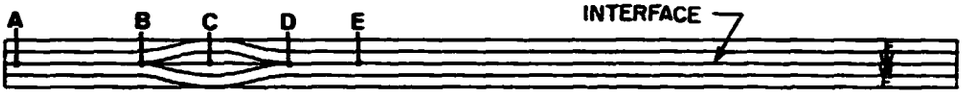

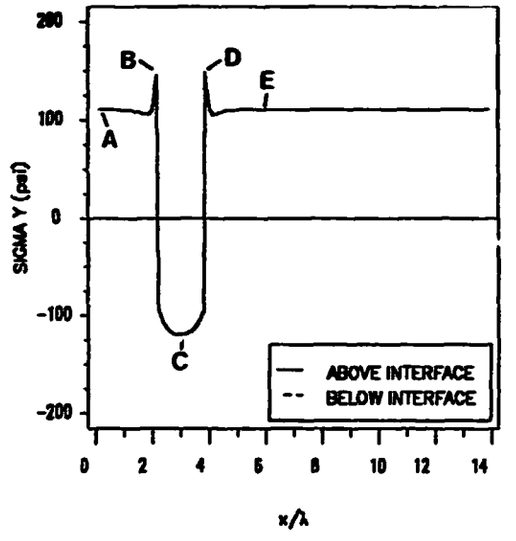

b) Interfacial σ_y.

Figure 36. Interfacial σ_x and σ_y in $(F/W_2/F)_w$ laminate. R=0, ε_z =0.1%.

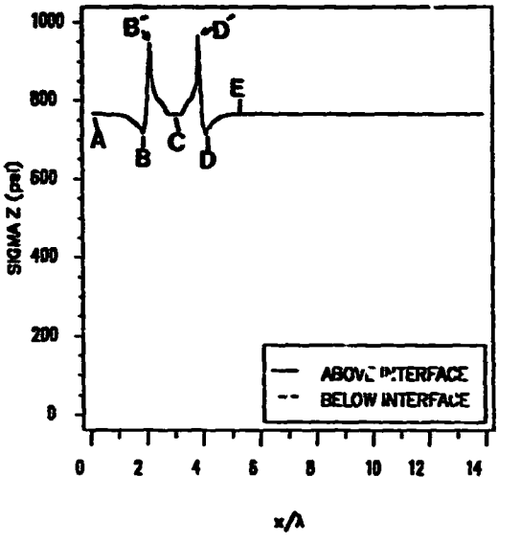

a) Interfacial σ_z

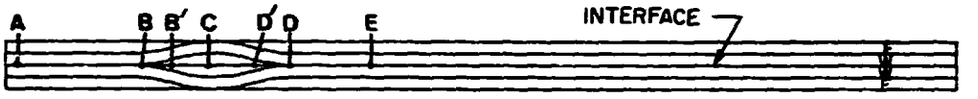

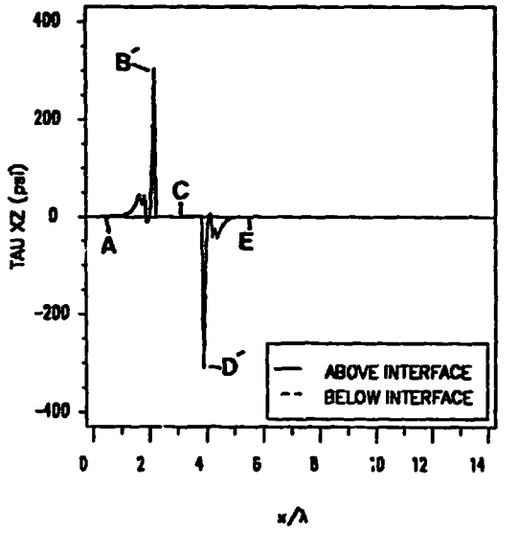

b) Interfacial τ_{xz}

Figure 37. Interfacial σ_z and τ_{xz} in $(F/W_2/F)_w$ laminate. $R=0$, $\varepsilon_z=0.1\%$.

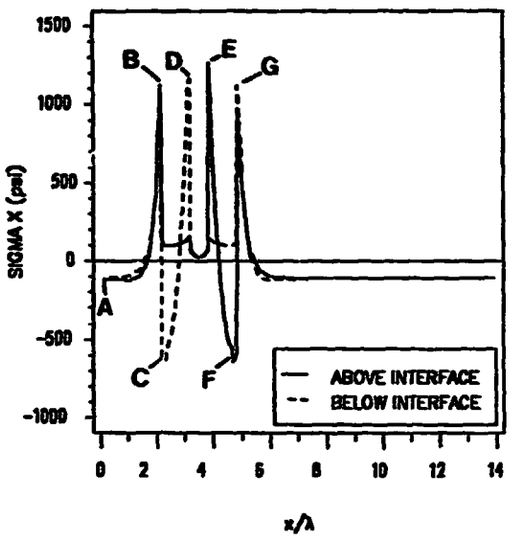

a) Interfacial σ_x.

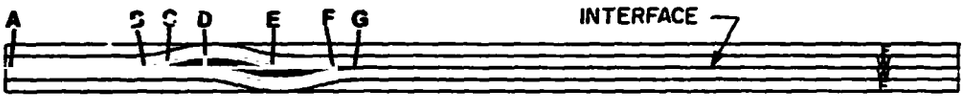

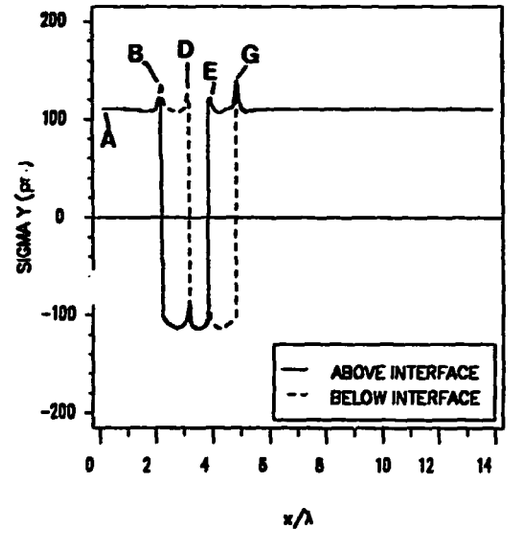

b) Interfacial σ_y.

Figure 38. Interfacial σ_x and σ_y in $(F/W_2/F)_w$ laminate. R=0.5, ε_z =0.1%.

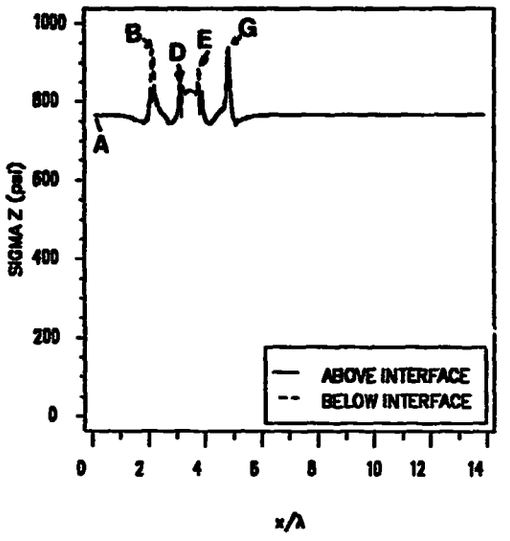

a) Interfacial σ_z.

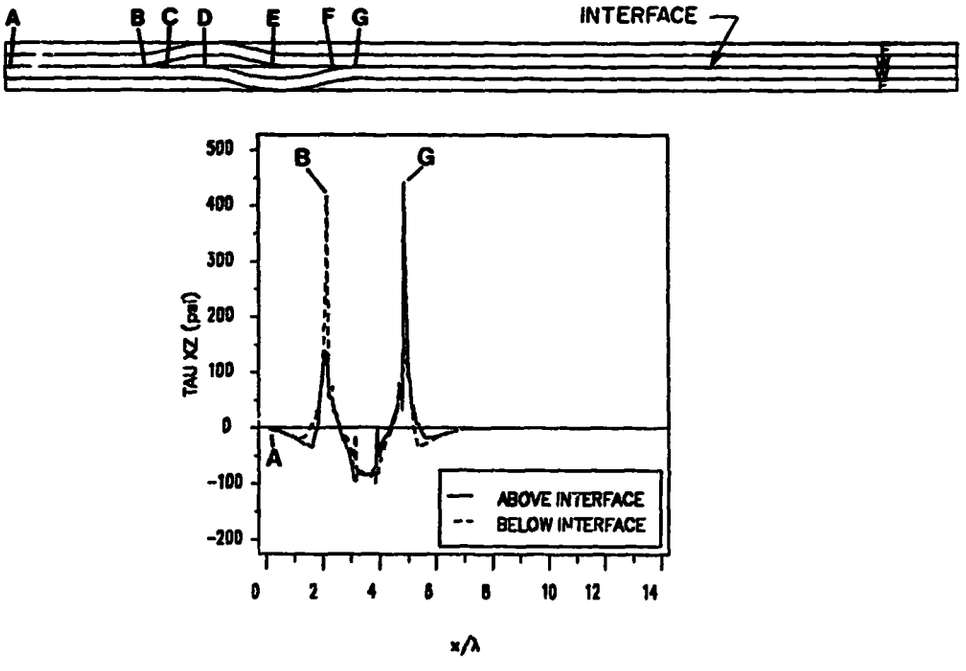

b) Interfacial τ_{xz}.

Figure 39. Interfacial σ_z and τ_{xz} in $(F/W_2/F)_w$ laminate. R=0.5, ε_z =0.1%.

of stress does not exist at the sources of stress concentra · · Generally, the stress distributions in the R = 1, 4 laminates are very similar to those of t = 0, 0.5 laminates. The similarities and differences between them are summarized in section 3.7.

3.4.4 Interfacial Stress Distributions: $(F/W)_2$ Laminates

The stacking sequence of this laminate differs from the other laminates considered in that it is not symmetric in the far-field region. This results in the midplane being bounded by tows of opposite orientations. The tow above the interface is a warp tow and the tow below the interface is a fill tow.

3.4.4.1 R=0 Laminate

In-plane Normal Stresses σ_x and σ_y: The interfacial σ_x and σ_y distributions for the R=0 laminate are shown in Figure 44. The distributions in this laminate are very similar to the distributions in the laminates previously discussed. This laminate exhibits far-field σ_x and σ_y values of 110 psi and -110 psi, respectively, in the warp tow (above the interface), with a discontinuity at C due to a change in material properties. The fill tow (below the interface) has far-field σ_x and σ_y values of -110 psi and -110 psi, respectively, with large changes in magnitude at points B and D. The change in σ_x at B and D is due to bending of the fill tows at those points. The change in σ_y at B and D is due to a change in material properties. Between B and D, σ_y is evaluated in a warp tow.

Interlaminar Stresses σ_z and τ_{xz}: The σ_z and τ_{xz} distributions (Figure 45) are very similar to those of the other laminates. Maximum values of σ_z occur at B and D where the out-of-plane stiffening effect of the undulations is greatest. The interlaminar shear stress τ_{xz} shows maxi-

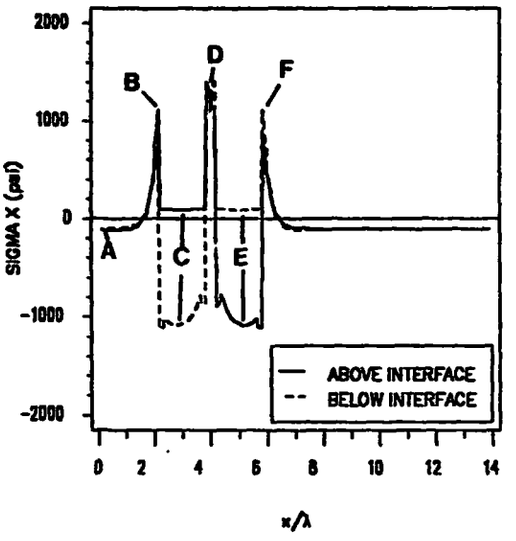

a) Interfacial σ_x.

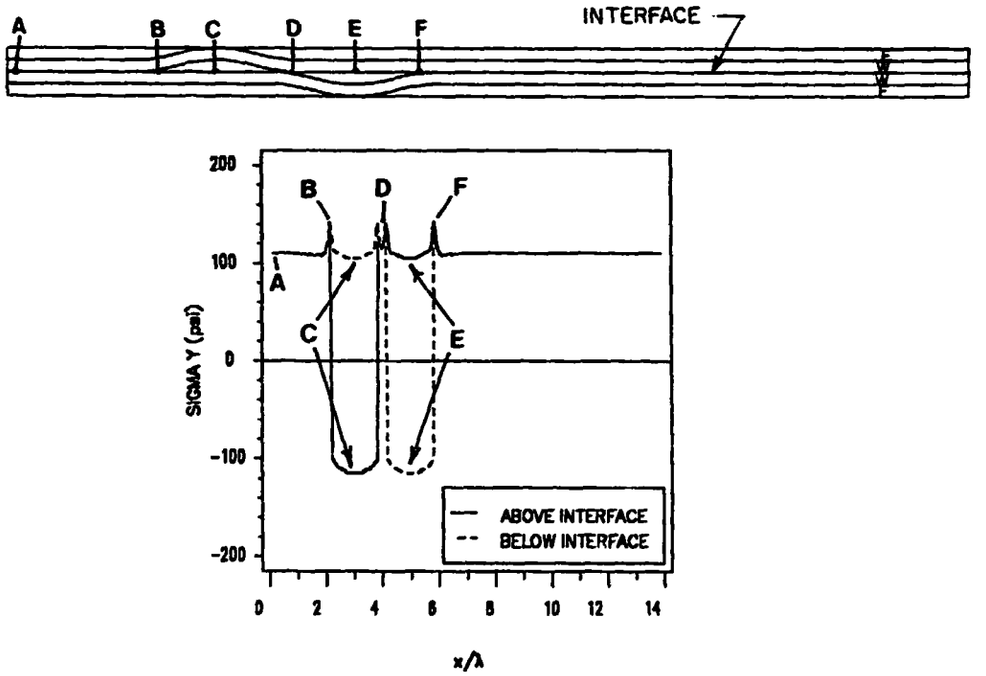

b) Interfacial σ_y.

Figure 40. Interfacial σ_x and σ_y in $(F/W_2/F)_w$ laminate. R = 1, ε_z = 0.1%.

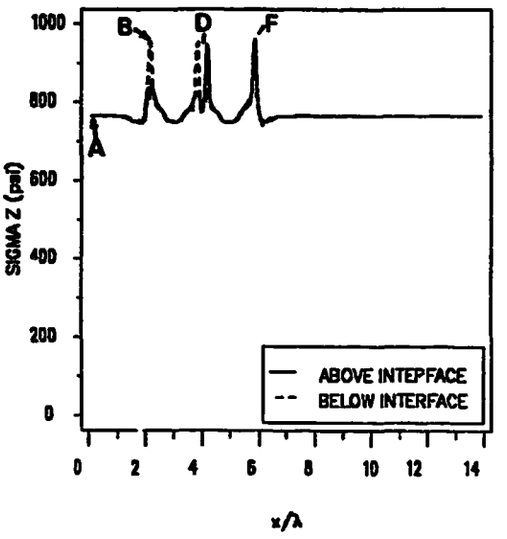

a) Interfacial σ_z.

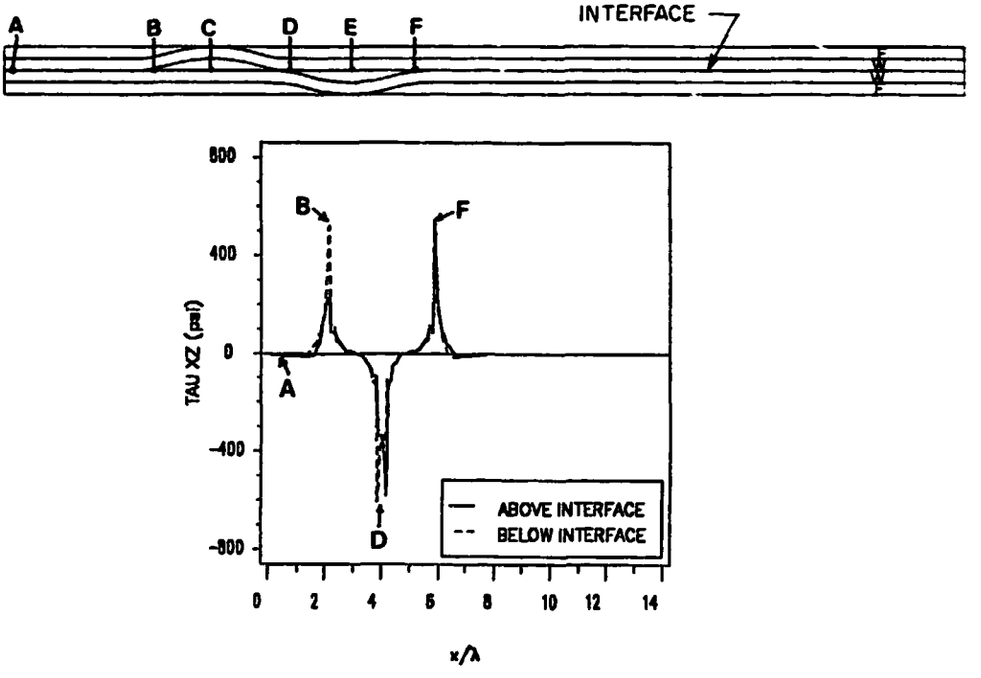

b) Interfacial τ_{xz}.

Figure 41. Interfacial σ_z and τ_{xz} in $(F/W_2/F)_w$ laminate. $R=1$, $\varepsilon_z=0.1\%$.

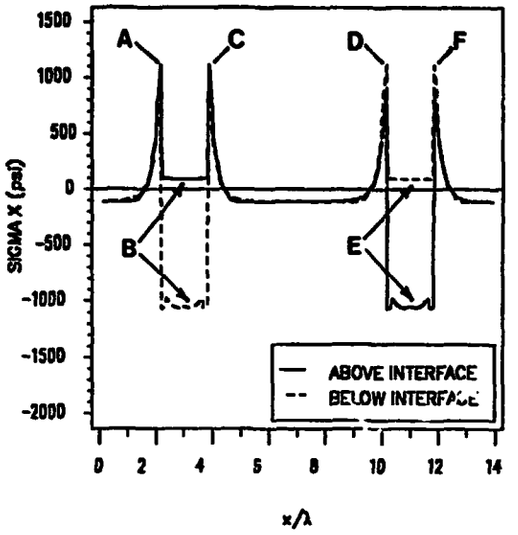

a) Interfacial σ_x.

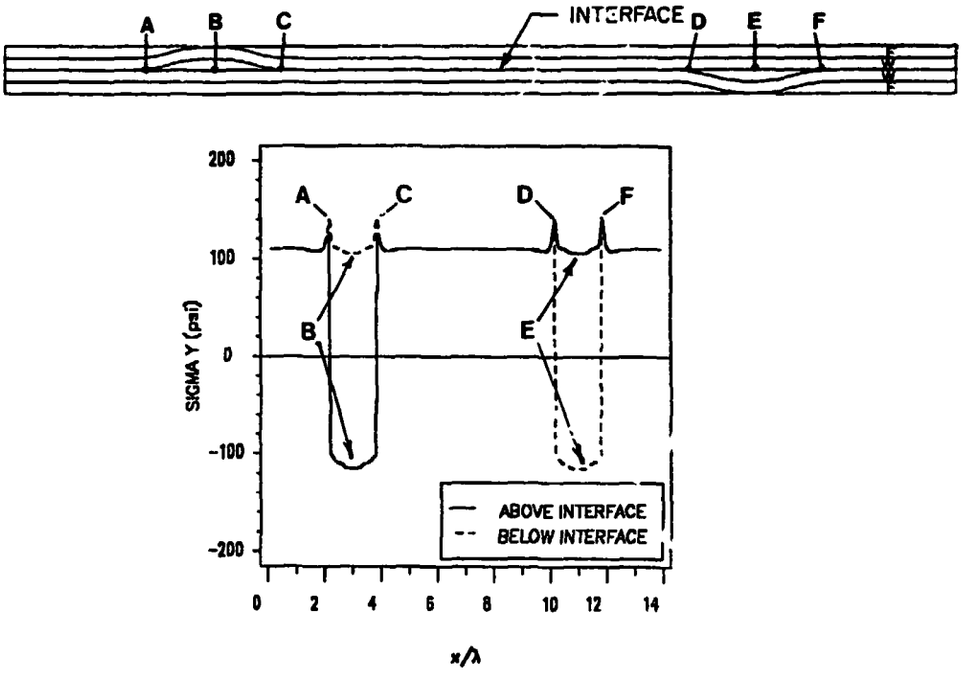

b) Interfacial σ_y.

Figure 42. Interfacial σ_x and σ_y in $(F/W_2/F)_w$ laminate. R=4, ε_z =0.1%.

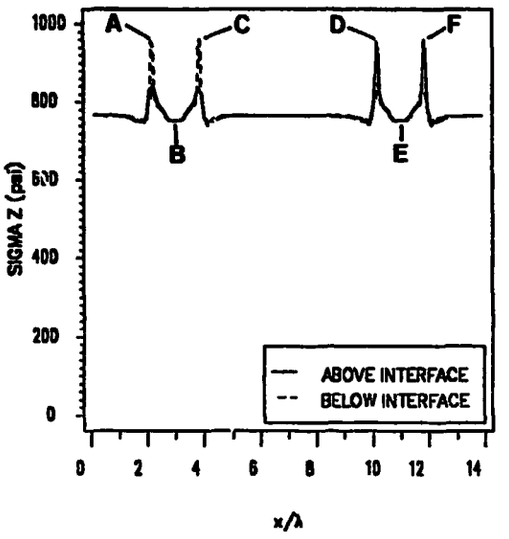

a) Interfacial σ_z.

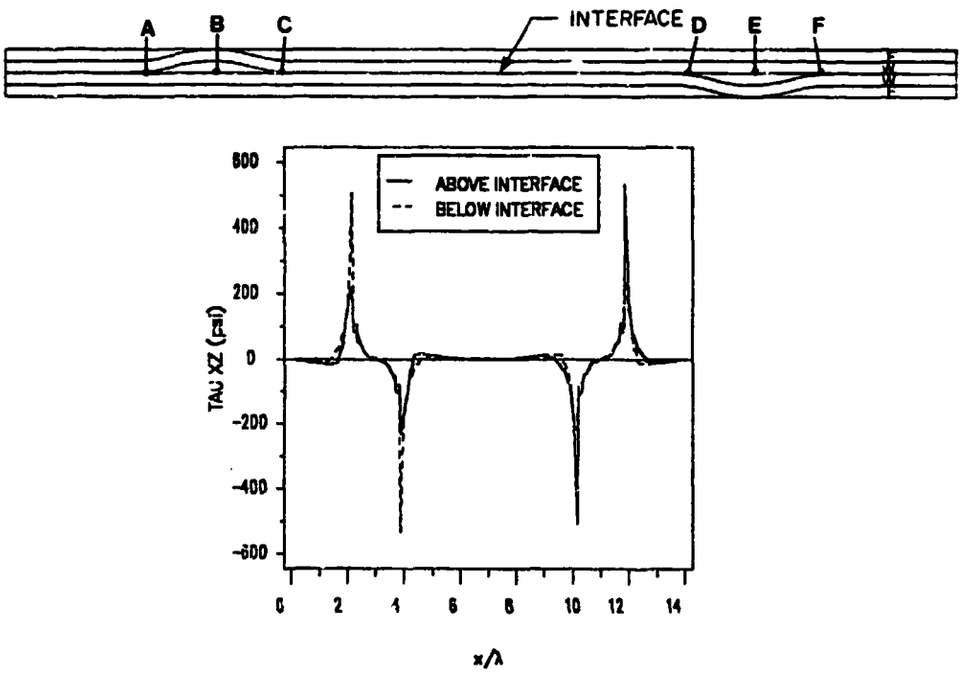

b) Interfacial τ_{xz}.

Figure 43. Interfacial σ_z and τ_{xz} in $(F/W_2/F)_w$ laminate. R=4, ε_z =0.1%.

mum values at points **B** and **D** (Figure 45b). It is at these points where maximum interfacial shear exists. Of particular interest is the difference between the two τ_{xz} distributions presented in Figure 45b. Satisfaction of the stress continuity requirements at the interface requires that τ_{xz} be the same in both layers. In this case, continuity of τ_{xz} is not satisfied between points **A** and **B** and between **D** and **E**. This is due to the presence of a coarse finite element mesh in these regions. The mesh density between **B** and **D** was four times greater than between **A** and **B** and **D** and **E**. The existing mesh was fine enough to satisfy continuity at the points of maximum shear stress (**B** and **D**).

3.4.4.2 R=0.5, 1 and 4 Laminates

The remaining laminates in this stacking sequence (those with **R**=0.5, 1 and 4) exhibit stress distributions similar to the previously discussed; therefore, the specifics of the distribution of each component of stress for each of the remaining laminates will not be presented. For completeness, however, the interfacial stress distributions are presented in Appendix A. A summary of the results for out-of-plane loading is presented in section 3.4.

3.4.5 Influence of Undulation Aspect Ratio Ω

The influence of the undulation aspect ratio (Ω) on the maximum interfacial stress was evaluated for a $(F/W_2/F)_f$ laminate with an offset ratio **R**=0.5. The maximum values of σ_x, σ_y, σ_z, and τ_{xz} along the interface, as a function of Ω are shown in Figure 46 through Figure 49. The in-plane normal stress σ_y exhibits the greatest dependence on Ω (Figure 46). At $\Omega=6$, σ_x is approximately 3200 psi. It decreases to 2100 psi at $\Omega=12$ and to approximately 700 psi at $\Omega=24$. The decrease in maximum σ_x is due to the reduction in curvature of the fill tow with increasing Ω. As discussed previously, the deformation of the fill tow is analogous to a beam

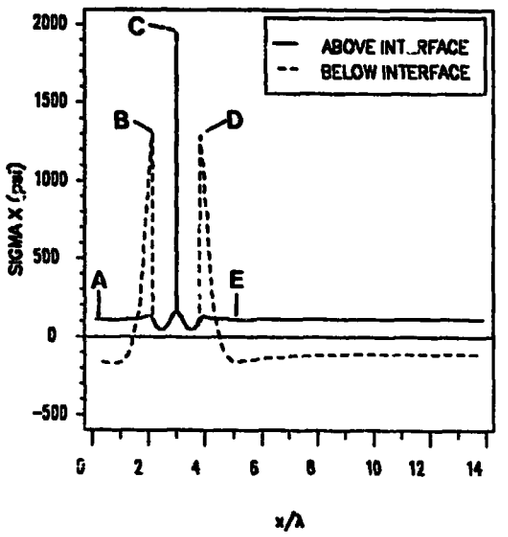

a) Interfacial σ_x.

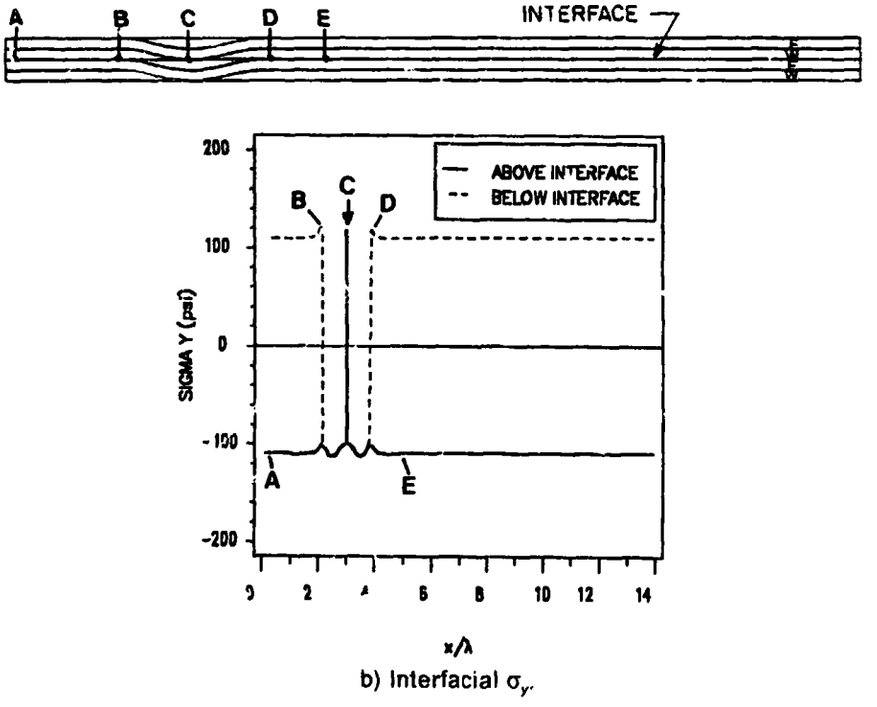

b) Interfacial σ_y.

Figure 44. Interfacial σ_x and σ_y in $(F/W)_2$ laminate. $R=0$, $\varepsilon_z=0.1\%$.

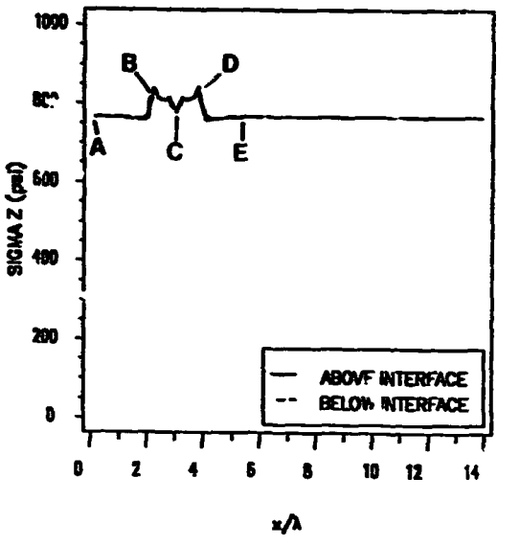

a) Interfacial σ_z.

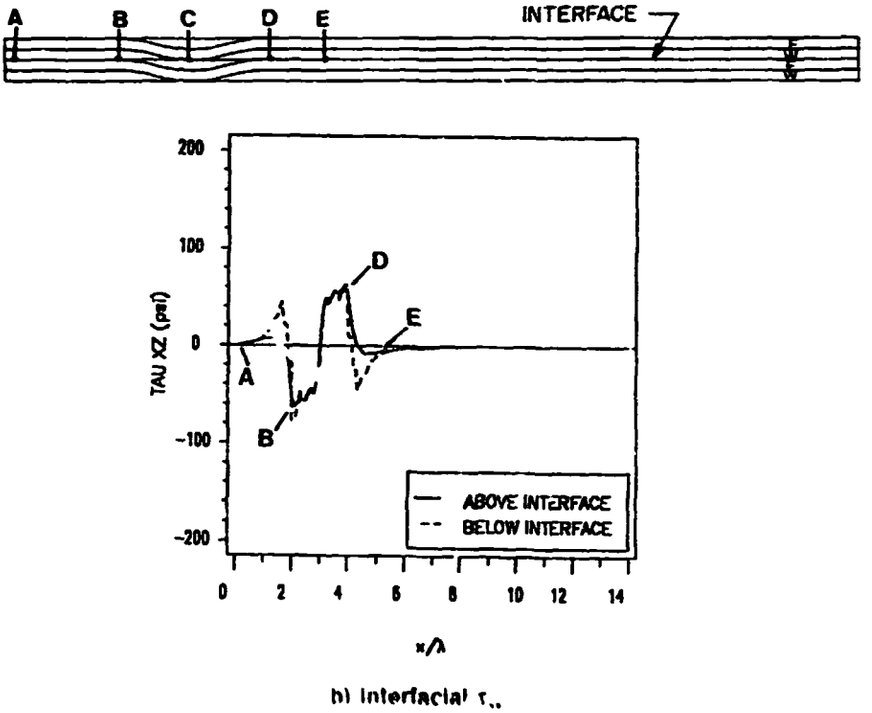

b) Interfacial τ_{xz}.

Figure 45 Interfacial σ_z and τ_{xz} in $(F/W)_2$ laminate. $R=0$, $\varepsilon_z=0.1\%$.

bending problem. The increase in Ω effectively 'straightens' the fill tow and thus reduces the σ_x component of stress attributed to bending.

The other components of stress, σ_y , σ_z, and τ_{xz} are effected less by Ω. The decrease in σ_y (Figure 47) is less than 10% between $\Omega=6$ and $\Omega=12$, and does not decrease for $\Omega > 12$. The interlaminar normal stress σ_z (Figure 48) decreases from approximately 1000 psi at $\Omega=6$ to 820 psi at $\Omega=12$, and is approximately 780 psi at $\Omega=24$. The interlaminar shear stress τ_{xz} (Figure 49) decreases from 78 psi at $\Omega=6$ to 52 psi at $\Omega=12$ and equals psi 40 at $\Omega=24$.

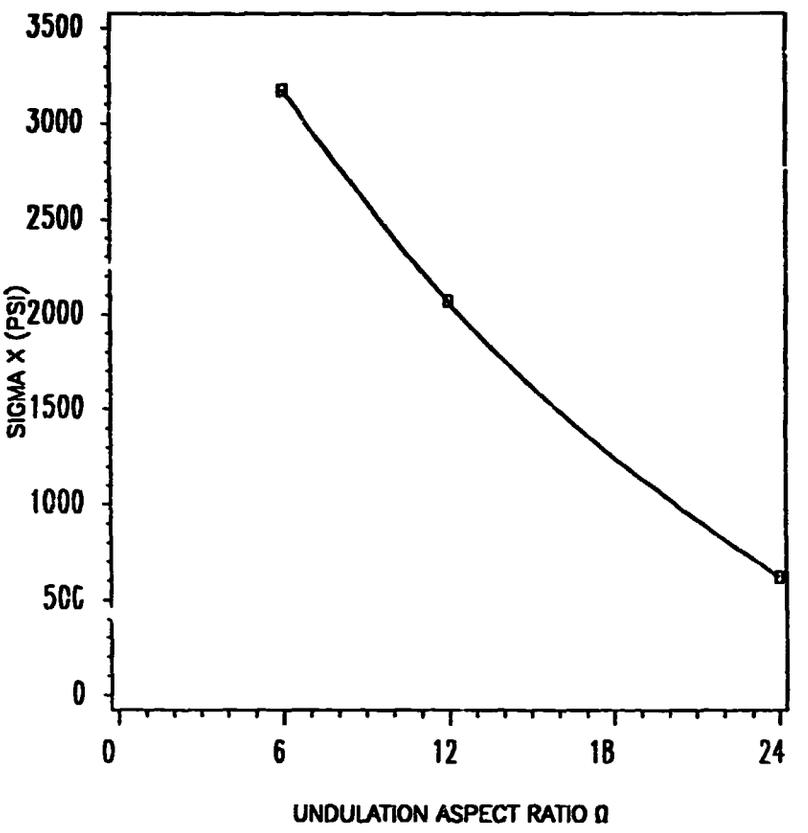

Figure 46. Maximum interfacial σ_x as a function of Ω. $\varepsilon_z = 0.1\%$.

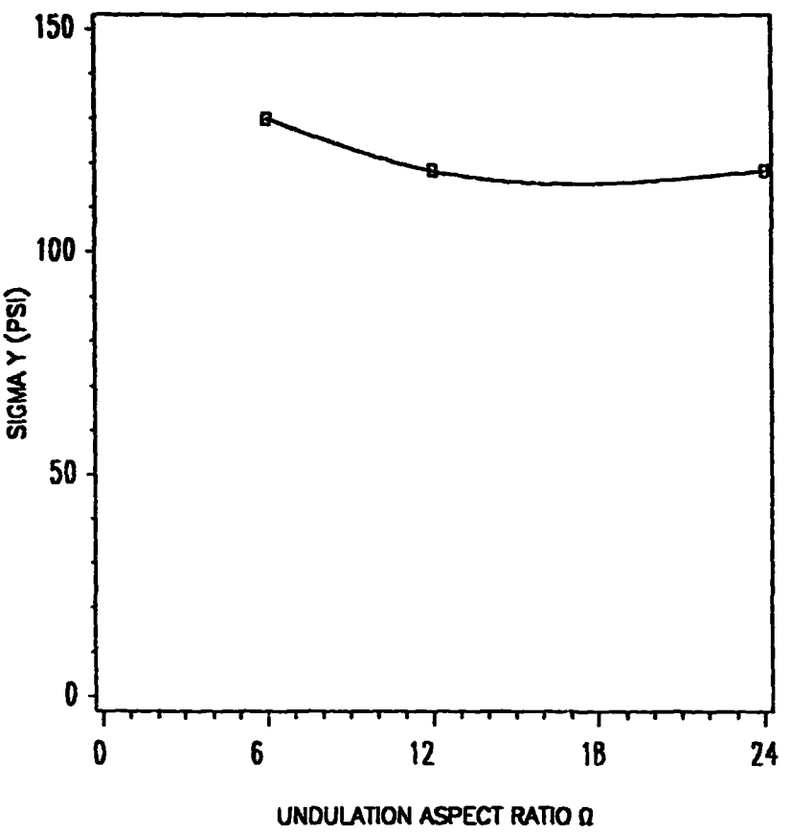

Figure 47. Maximum interfacial σ_y as a function of Ω. $\varepsilon_z = 0.1\%$.

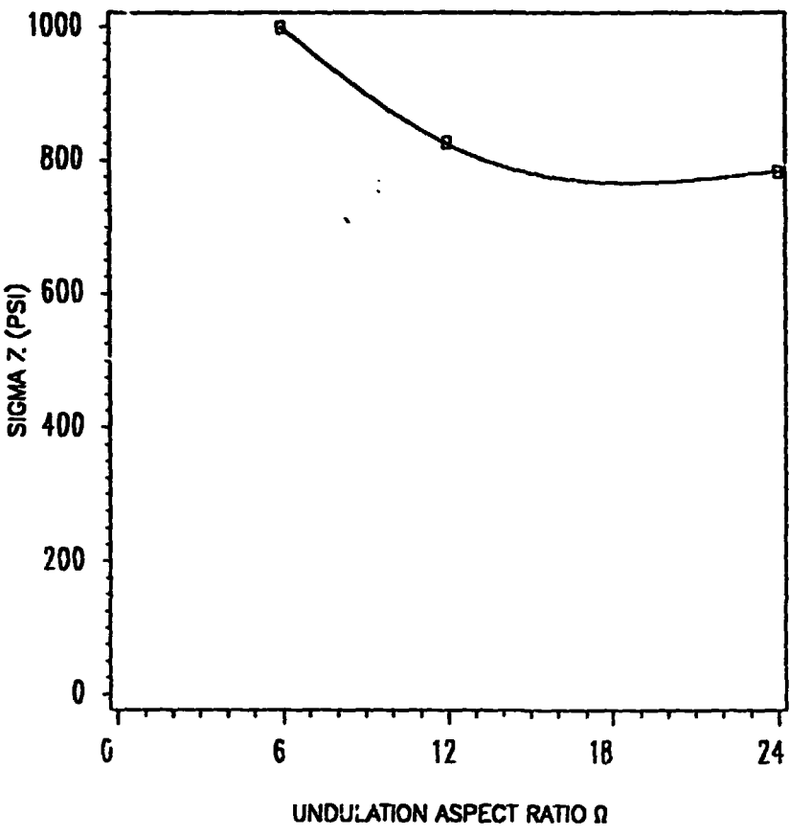

Figure 48. Maximum interfacial σ_z as a function of Ω. $\varepsilon_z = 0.1\%$.

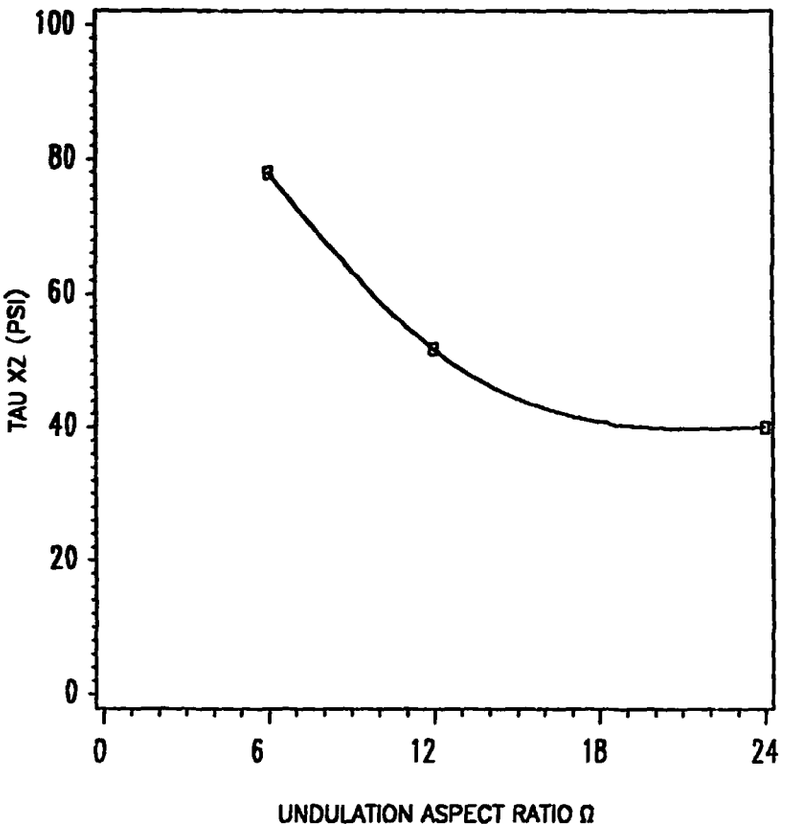

Figure 49. Maximum interfacial τ_{xz} as a function of Ω. $\varepsilon_z = 0.1\%$.

3.5 *Results: In-Plane Loading*

3.5.1 Laminate Deformations

As was the case for out-of-plane loading, the response of the woven fabric laminates to in-plane loading (ε_x = 0.1%) is best understood by first considering the deformations of the laminates. The deformations of the $(F/W_2/F)_f$ laminates for **R** values of 0 and 0.5 are illustrated in Figure 50. The **R**=0 laminate (Figure 50a-b) illustrates the tendency of the curved tow to straighten under axial loading. As was the case for out-of-plane loading, the deformation of the fill tows is analogous to the bending of a curved beam. Figure 50c-d illustrates the effect of a lack of symmetry on the deformation of the **R**=0.5 laminate. The laminate is straight in the far-field regions (which is expected because the laminate is symmetric in those regions) and curved in the region of undulation. The deformation is similar to that of a single lap joint.

The deformations of the fill tows themselves are illustrated in more detail in Figure 51. The fill tow in the **R**=0 laminate (Figure 51a) shows not only translation and axial extension, but also a reduction in curvature. This is in contrast to the out-of-plane loading condition, where the tendency is for the curvature of the fill tows to increase. The fill tows of the **R**=0.5 laminate (Figure 51b) exhibits the same characteristics of the **R**=0 laminate. Additionally, there is cantilever-type bending of the tows. As discussed previously, this is due to the lack of symmetry of the laminate.

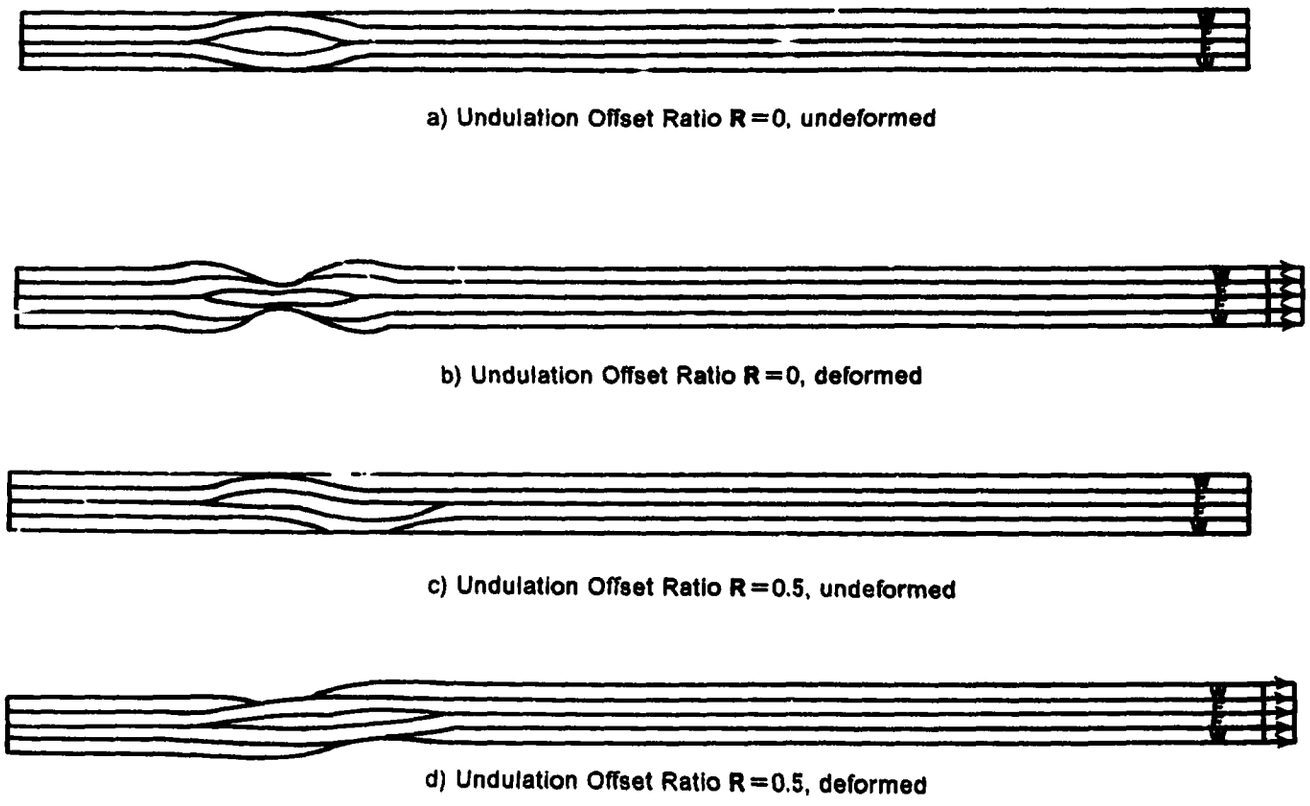

a) Undulation Offset Ratio R = 0, undeformed

b) Undulation Offset Ratio R = 0, deformed

c) Undulation Offset Ratio R = 0.5, undeformed

d) Undulation Offset Ratio R = 0.5, deformed

Figure 50. Deformations of $(F/W_2/F)_f$ laminates. $\varepsilon_x = 0.1\%$. R = 0, 0.5.

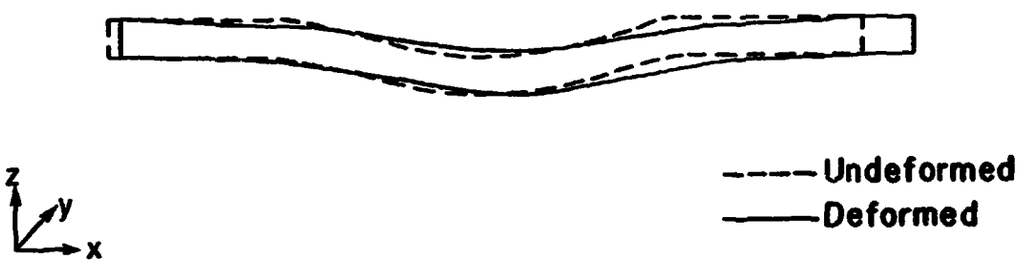

a) Undulation Offset Ratio R = 0

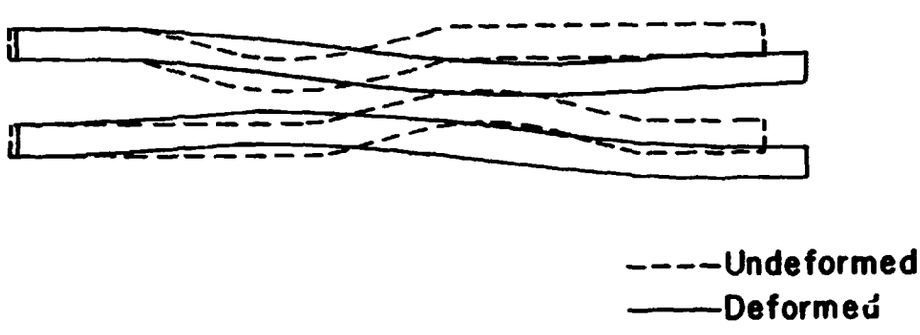

b) Undulation Offset Ratio R = 0.5

Figure 51. Fill tow deformations in $(F/W_2/F)_1$ laminate. $\varepsilon_x = 0.1\%$. R = 0, 0.5.

3.5.2 Stress Distributions in Regions of Undulation

In this section the stress distributions in the undulations are discussed for the in-plane loading condition. Results are presented for the $(F/W_z/F)_t$ laminates for R values of 0, 0.5, 1, and 4.

3.5.2.1 R=0 Laminate

The in-plane normal stress σ_x for the R=0 laminate subjected to in-plane loading is shown in Figure 52. This laminate is symmetric about the x-y plane, thus only the results for the upper half of the laminate are presented. The laminate is in axial tension throughout, with far-field σ_x values (locations A and E) of approximately 40 ksi in the fill tow and and less than 1 ksi in the warp tows. The fill tow exhibits regions of local maximums at locations C, F and G, where σ_x is approximately 54 ksi. The minimum values of σ_x in the fill tow are at locations B and D, where σ_x it is approximately 20 ksi. A local minimum of 34 ksi exists at location G. The overall stress distribution is a result of contributions from the bending of the tow as well as the axial extension of the tow. In this case, the contribution of the bending of the tow is to reduce σ_x in the fill tow at locations B, D, and G, and to increase σ_x at locations C, F, and H. In the warp tow, maximum deformation occurs at point I, and is caused by the deformation of the fill tow below it (Figure 50a). The deformation of the fill tow causes the warp tow above it to bend as it is translates in the z direction, thus increasing σ_x to approximately 1.5 ksi at I. A local maximum in σ_x also exists at location G. The reason for this is two-fold. First, the reduction in axial stiffness in the region of undulation, which is due to the curvature of the fill tow, results in a larger component of the load being absorbed by the warp tows. Secondly, location G is a point of stress concentration in this laminate (Table 7).

The σ_y stress contour is illustrated in Figure 53. As was the case for out-of-plane loading, the presence of a σ_y component of stress is due to the mismatch in Poisson's ratios between

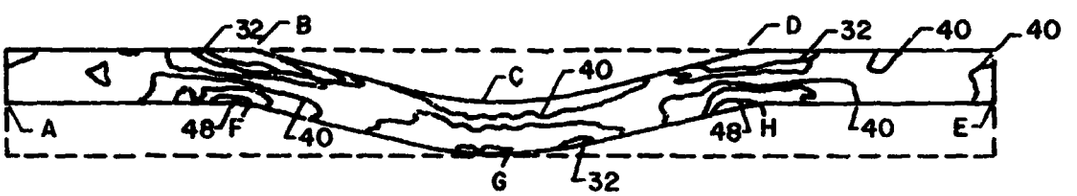

Δ = 4 ksi

a) Fill Tow

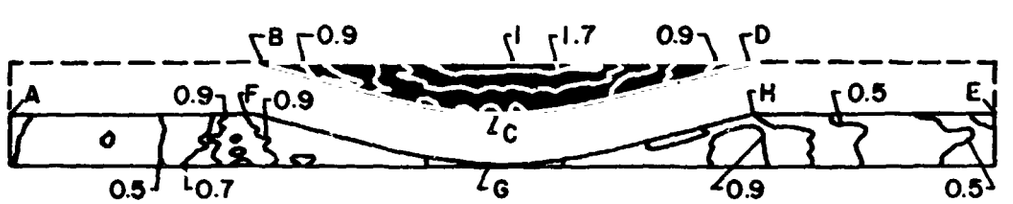

Δ = 0.2 ksi

b) Warp Tows

Figure 52. Contour plot of σ_x in $(F/W_2/F)_f$ laminate. $R=0$, $\varepsilon_x = 0.1\%$.

the warp and fill tows. In the fill tow σ_y is maximum at location **G**, reaching a value of approximately 850 psi. Local maxima of approximately 200 psi are found at locations **F** and **H**. The far-field value of σ_y (locations **A** and **E**) is about 100 psi. In the warp region the maximum value of σ_y is 740 psi at location **G**. A local maximum of 50 psi is found at location **I**. The remainder of the warp region is in compression, and is about -100 psi. The far-field values of σ_y in the warp and fill tows indicate that equilibrium in the y directions is satisfied.

The σ_z stress contour is shown in Figure 54. The interlaminar stress σ_z is zero in the far-field regions, which is consistent with CLPT. In the undulation σ_z is nonzero and reaches a maximum value of approximately 5 ksi at location **G**. The magnitude of σ_z resulting from in-plane loading is significantly greater than that due to out-of-plane loading. The maximum value of σ_z under out-of-plane loading for this laminate was less than 1 ksi (Figure 26).

The τ_{xz} stress contour is shown in Figure 55. The interlaminar shear stress τ_{xz} is zero in the far-field regions (locations **A** and **E**), but varies from -11 ksi to 11 ksi in the curved portion of the laminate between locations **F** and **H**. As was the case for out-of-plane loading, the orientation of the fill tow results in a response that is analogous to that of an off-axis unidirectional coupon under tensile load. The orientation of the fill tow results in negative shear stress between locations **F** and **G**, and positive shear between **G** and **H**. The maximum value of τ_{xz} is over twice that of σ_z in the fill tow. In the warp tows τ_{xz} ranges from -0.5 ksi to 0.5 ksi. In most of the warp tows τ_{xz} is very small, which is expected due to the relatively small shear modulus (G_{xz}) of the warp tows.

3.5.2.2 R=0.5 Laminate

Contour plots of the stress distributions in the undulations of the **R**=0.5 laminate are shown in Figure 56 through Figure 59. The σ_x stress contour is shown in Figure 56. In contrast to the **R**=0 laminate (Figure 52), the fill tows in the **R**=0.5 laminate exhibit both tension and compression. The magnitude of σ_x ranges from a maximum of approximately 95 ksi at

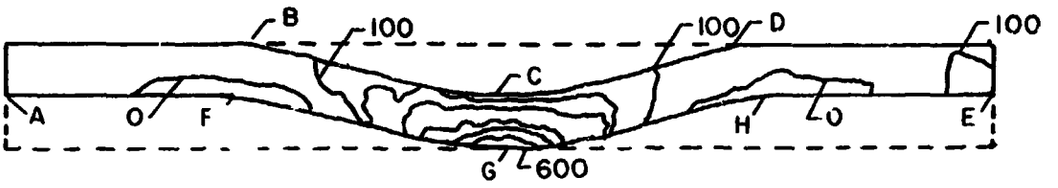

Δ = 100 psi

a) Fill Tow

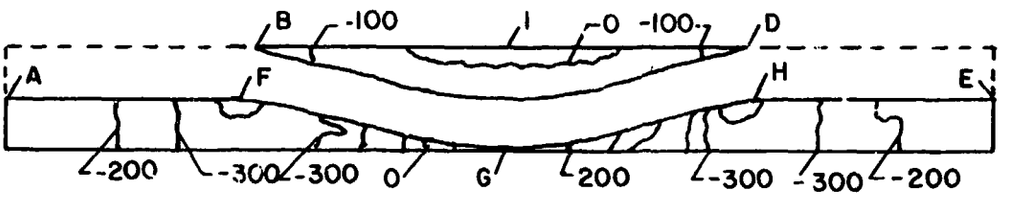

Δ = 100 psi

b) Warp Tows

Figure 53. Contour plot of σ_y in $(F/W_2/F)_f$ laminate. R=0, ε_x = 0.1%.

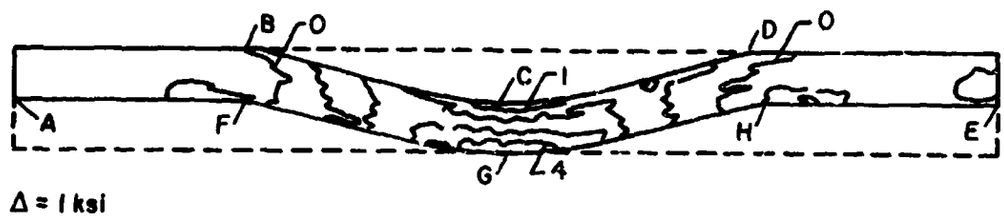

a) Fill Tow

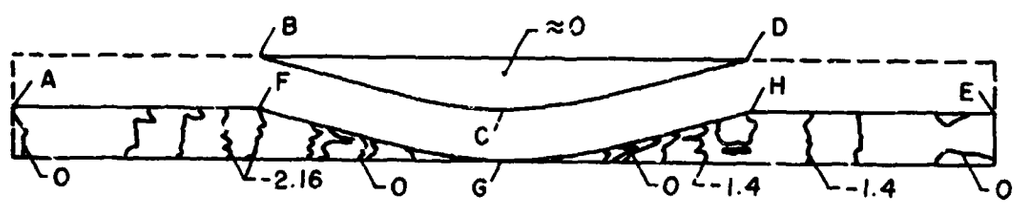

b) Warp Tows

Figure 54. Contour plot of σ_z in $(F/W_2/F)_f$ laminate. R=0, ε_x = 0.1%.

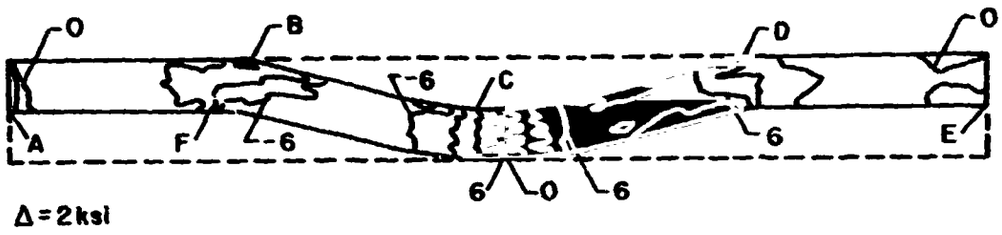

a) Fill Tow

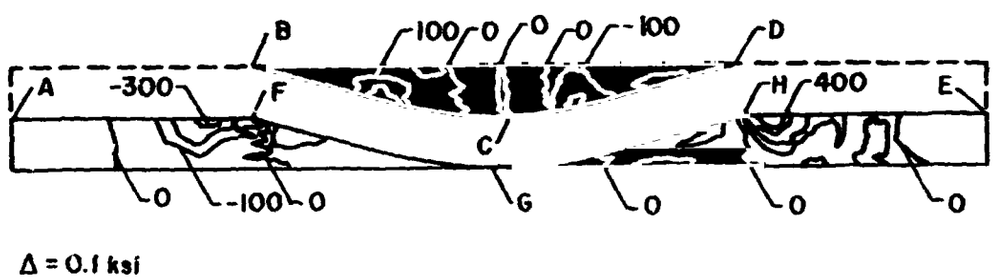

b) Warp Tows

Figure 55. Contour plot of τ_{xz} in $(F/W_2/F)_t$ laminate. $R=0$, $\varepsilon_x = 0.1\%$.

locations A, E, and I, to a minimum of -10 ksi at locations B, D, H, and G. The form of the σ_x distribution in the fill tows is attributed to three factors: first, the axial load of ε_x = 0.1% contributes a tensile component of σ_x to the entire laminate; second, the tendency of the fill tows to straighten contributes additional tensile stresses to the fill tows at locations with concave curvature (e.g. A and I) and contributes compressive components of σ_x to locations of convex curvature (e.g. D and G); third, the overall bending of the laminate, as illustrated in Figure 50 and Figure 51, contributes additional compressive σ_x to the fill tows. The net result is that the fill tows exhibit areas of tension and compression even though the overall loading state is tensile. It is also of interest to note that the maximum value of σ_x in the R=0.5 laminate is approximately 95 ksi, which is much larger than the 60 ksi maximum observed in the R=0 laminate. Again, this is attributed to the increased bending of the laminate. In the warp tows (Figure 56b) σ_x is less than 1 ksi except in locations A, B, and C. At these locations σ_x approaches 4 ksi, and is attributed to bending effects.

The σ_y stress contour is shown in Figure 57. The maximum value of σ_y in the curved regions of the fill tows is approximately 400 psi. As was the case for the R=0 laminate, local maximums and minimums in the σ_y distributions correspond to their counterpart locations in the σ_x distribution. The maximum value of σ_y in the R=0.5 laminate (400 psi) is only about half that of the R=0 laminate (850 psi). This is attributed to the boundary condition on both laminates that F_y = 0. In the R=0 laminate the regions of high σ_x, which generates high σ_y due to Poisson effects, are concentrated a smaller area than in the R=0.5 laminate. Therefore, regions of σ_y are very localized and must be of greater magnitude in order to satisfy the boundary condition on F_y.

The σ_z stress contour is shown in Figure 58. The magnitude of σ_z is approximately 3 ksi in the fill tows between locations B and C and between locations J and K. Between locations G and H and between I and J, however, σ_z is near zero. In these regions the upper and lower fill tows are bending in the same direction. Thus, the relative z displacement between them is small and results in no contribution to the σ_z component of stress.

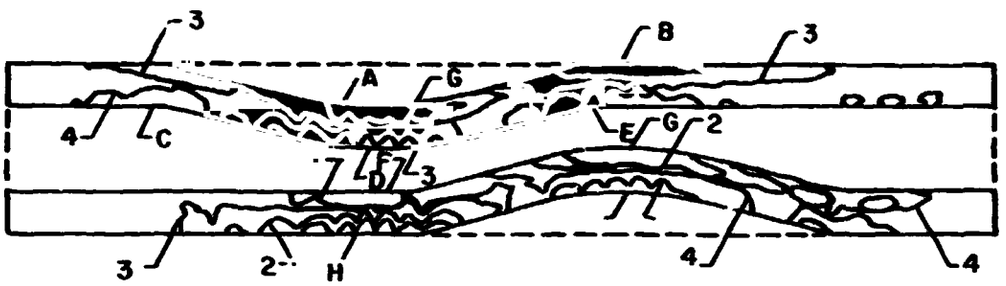

Δ = 1 ksi

a) Fill Tows

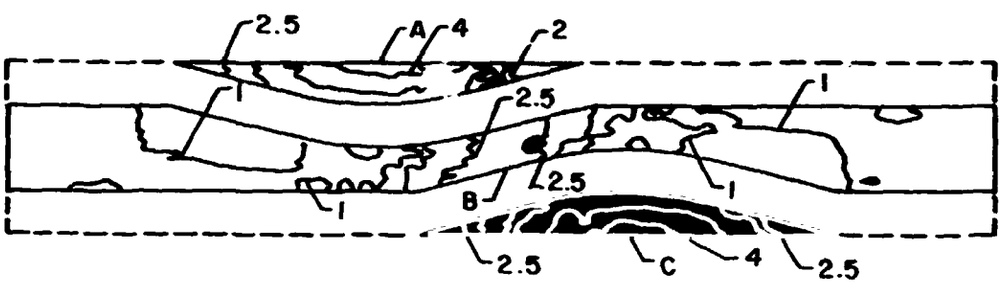

Δ = 0.5 ksi

b) Warp Tows

Figure 56. Contour plot of σ_x in $(F/W_2/F)_t$ laminate. R=0.5, ε_x = 0.1%.

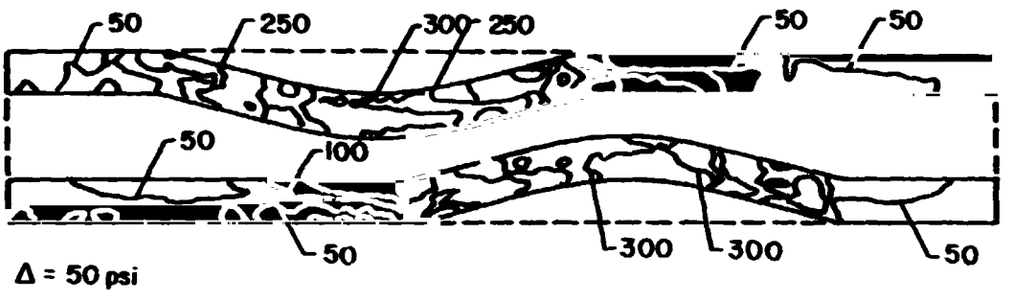

a) Fill Tows

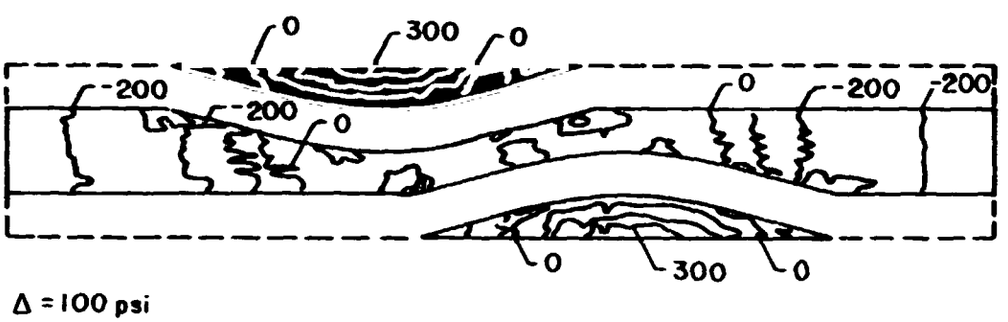

b) Warp Tows

Figure 57. Contour plot of σ_y in $(F/W_2/F)_f$ laminate. $R=0.5$, $\varepsilon_x=0.1\%$.

The τ_{xz} stress contour is shown in Figure 59. It is continuous within the laminate and ranges from -15 ksi to about 11 ksi in the fill tows and from -4 ksi to about 2 ksi in the warp tows. The τ_{xz} distribution in the fill tows is very similar to that of the R=0 laminate. The τ_{xz} distribution in the warp tows does differ between the R=0 and R=0.5 laminates. In the R=0 laminate, τ_{xz} in the warp tows is negligible. In the R=0.5 laminate, however, τ_{xz} is nonzero due to lack of laminate symmetry. The maximum τ_{xz} is found in the region between points B and C, and results from shear deformation between the fill tows as the laminate deforms. In region B-C, τ_{xz} is approximately -4 ksi. On either side, between A and B and between C and D, τ_{xz} is positive and approaches 2 ksi.

The stress distributions in the R=1 and R=4 laminates are illustrated in Figure 107 through Figure 114. The stress distributions in these laminates are very similar to those previously discussed; therefore, they are not discussed in detail. However, the maximum stress values found in the undulation are compared for all offset ratios in Table 9. As was the case for out-of-plane loading, these results indicate the degree of interaction between the undulations. The in-plane normal stress σ_x appears to be a function of the degree of bending of the laminate. The lowest value of σ_x (69.8 ksi) is found in the case R=0, which exhibits the least amount of fill tow bending because the laminate is symmetric about the the x-y plane. The maximum value of σ_x (94.7 ksi) is found in the R=0.5 case, which exhibits the greatest amount of fill tow bending of the cases studied. The in-plane normal stress σ_y and the interlaminar normal stress σ_z are maximum in the R=0 case. The maximum value of σ_z is located in the fill tow at the midplane of the laminate (location G in Figure 54). Location G is the point where both of the fill tows in the R=0 laminate will tend towards maximum deformation in the out-of-plane direction under in-plane loading. Since the fill tow above the midplane will tends toward displacement in the +z direction, and the fill tow below the midplane tends toward displacement in the -z direction, a condition of maximum σ_z develops. The distribution of σ_y is a result of Poisson effects due to σ_x and σ_z. The interlaminar shear stress τ_{yz} does not appear to be a simple function of R. The maximum value (14.3 ksi) occurs

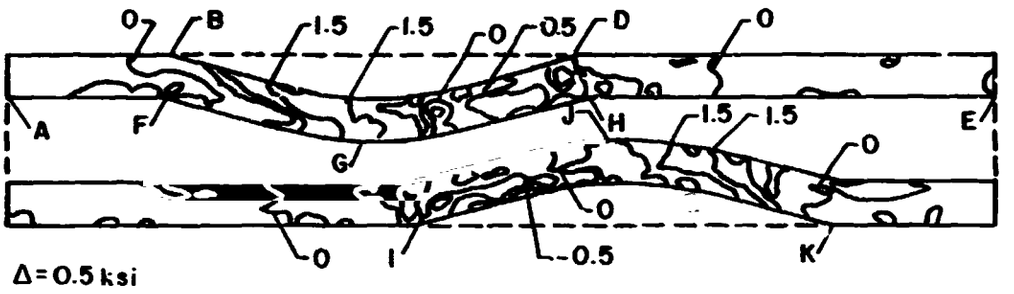

a) Fill Tows

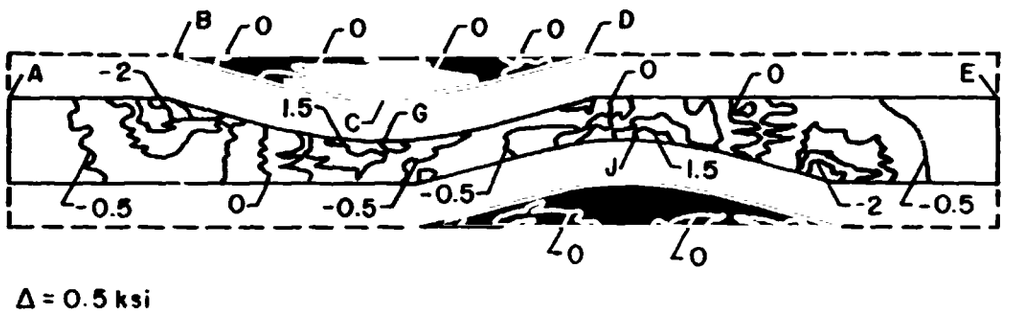

b) Warp Tows

Figure 58. Contour plot of σ_z in $(F/W_2/F)_f$ laminate. R=0.5, ε_x = 0.1%.

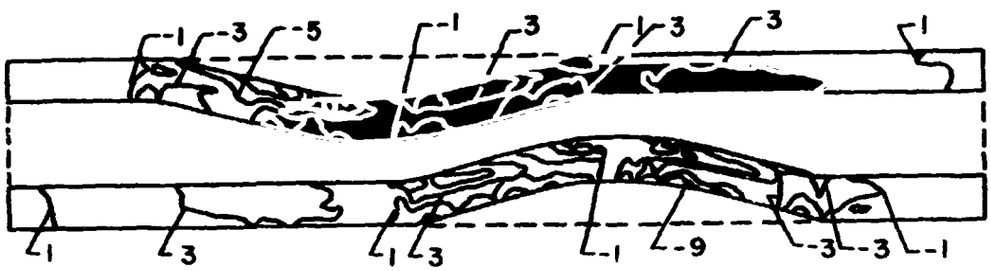

Δ = 2 ksi

a) Fill Tows

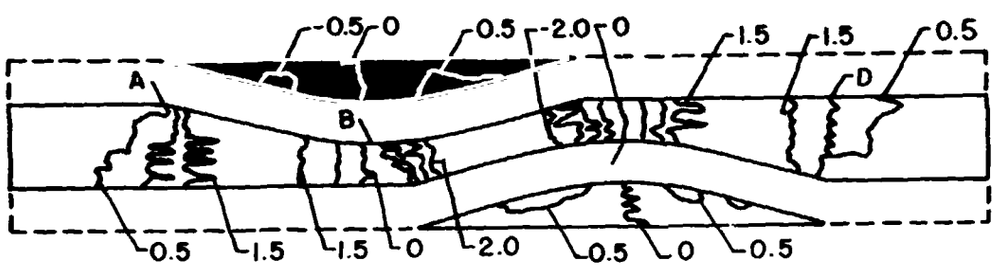

Δ = 0.5 ksi

b) Warp Tows

Figure 59. Contour plot of τ_{xz} in $(F/W_2/F)_t$ laminate. R=0.5, ε_x = 0.1%.

in the R=1 case and the minimum value (10.2 ksi) occurs in the R=4 case. The magnitudes of τ_{xz} for the R=0 and 0.5 cases fall between those listed above.

3.5.3 Interfacial Stress Distributions: $(F/W_2/F)_t$ Laminates

In this section and the following sections on stress distributions in the $(F/W_2/F)_w$ and $(F/W)_2$ laminates, the stress distributions along the interface of the laminates are discussed in detail. As was discussed previously, each ply of the laminate is reinforced in the thru-thickness direction due to the woven nature of the fabric; however, no thru-thickness reinforcement exists between adjacent plies. Therefore, the stress state, particularly the interlaminar stress state, at the interface between adjacent plies is of interest.

3.5.3.1 R=0 Laminate

In-plane Normal Stresses σ_x and σ_y: The interfacial σ_x distribution in the R=0 laminate is shown in Figure 60a. In the far-field region σ_x is relatively constant at about 0.75 ksi. Small increases in σ_x occur at points B and D, which are within the region of undulation. The discontinuous jump in σ_x at C can be explained by considering the mismatch in axial modulus, E_x between the warp and fill tows. Examination of Table 3 shows that E_1 of the tow used in this study is 40.7 MSI and E_2 is 0.75 MSI. In the far-field region the warp tow is oriented such that its axial stiffness corresponds to E_2 of the tow (0.75 MSI). At point C, however, σ_x is evaluated in a fill tow, which is oriented such that its axial stiffness corresponds to E_1 of the tow (40.7 MSI). Thus, under the in-plane strain loading ε_x = 0.1% the far-field value of σ_x in the warp tows should be 0.75 ksi and σ_x at point C should be 40.7 ksi. As indicated previously, the far-field value of σ_x in the warp tows is 0.75 ksi. At point C, however, σ_x is approximately 38 ksi, which is lower than the 40.7 ksi value predicted by CLPT. This difference is attributed to the

Table 9. Maximum stress values in undulation of $(F/W_2/F)_t$ laminate under in-plane loading. $\varepsilon_x = 0.1\%$.

Maximum Stress (ksi)				
R	σ_x^{max}	σ_y^{max}	σ_z^{max}	$\lvert\tau_{xz}^{max}\rvert$
0.0	69.8	.85	5.0	11.7
0.5	94.7	.44	3.7	11.5
1.0	93.3	.51	3.5	14.3
4.0	76.3	.51	2.8	10.2

bending of the fill tows under axial load, which induces compressive σ_x at **C**. A contributing factor may be the location of the Gauss point at which the stress is evaluated, which is slightly offset from **C** and is at a location where there is slight curvature of the fill tow. As mentioned in the discussion of laminate stiffness (section 5.3.2), small changes in fiber orientation result in significant reductions in axial modulus. The slight increases in σ_x at points **B** and **D** are attributed to two factors. First, the reduction in axial stiffness at the undulation due to the curvature of the fill tows. At points **B** and **D** the contribution of the fill tows to the axial stiffness of the laminate is at a minimum due to their orientation with respect to the load axis; therefore, the warp tows must absorb a greater share of the load. Second, the deformation of the fill tows (Figure 51b) towards the midplane induces compressive σ_z in the warp tows near the undulation. The compressive σ_z causes a local increase in ε_x due to Poisson effects and hence increases σ_x.

The interfacial σ_y distribution is shown in Figure 60b. As was the case for out-of-plane loading, σ_y stresses are a result of the mismatch in Poisson's ratio between the warp and fill tows. In the far-field region σ_y is evaluated in a warp tow and is compressive at approximately -100 psi. In the region of undulation σ_y exhibits a maximum compressive stress of -400 psi at points **B** and **D**, but becomes tensile at point **C** where σ_y is evaluated in a fill tow. The magnitude of σ_y at **C** is approximately 800 psi. The behavior of σ_y at points **B**, **C**, and **D** is attributed to Poisson effects from σ_x and σ_z.

Interlaminar Stresses σ_z and τ_{xz}: The distribution of the interlaminar normal stress σ_z along the interface is illustrated in Figure 61a. The far-field value of σ_z is zero, which is consistent with classical laminated plate theory (CLPT). At points **B** and **D**, σ_z is compressive (approximately -2.5 ksi). At point **C**, σ_z is tensile (approximately 5 ksi). The σ_z distribution at the undulation is explained by considering the deformation of the fill tow (Figure 51). As discussed previously, the tendency of the fill tow is to straighten under axial load. This induces tensile stresses at **C** and compressive stresses at points **B** and **D**..

The interlaminar shear stress τ_{xz} (Figure 61b) is essentially zero throughout, which is consistent with CLPT. The exception occurs on either side of **C**, where τ_{xz} exhibits values of 0.3 and -0.3 ksi. This is a point of stress concentration and is a result of the idealized geometry of the model. The oscillation of τ_{xz} about $\tau_{xz} = 0$ in the region of undulation is attributed to numerical instabilities associated with the finite element method. These instabilities are often associated with regions of stress singularities, where linear elasticity predicts infinite stresses.

3.5.3.2 R=0.5 Laminate

In-plane Normal Stresses σ_x and σ_y: The distribution of the in-plane normal stresses σ_x and σ_y along the interface for the **R**=0.5 laminate are illustrated in Figure 62. The far-field value of σ_x is approximately 0.75 ksi, which is consistent with CLPT. The distribution of σ_x in the region of undulation is relatively complex. At points **C** and **E**, σ_x is evaluated in fill tows and is approximately 3.5 ksi. The increase in σ_x at points **B** and **F** is attributed to the deformation of the fill tows (Figure 51). As was the case for the **R**=0 laminate, the tendency of the fill tows to straighten under axial load results in compressive σ_z at locations **B** and **F**. This induces Poisson expansion of the warp tows in the x direction and thus increases σ_x at these points. The distribution of σ_x at location **D** is attributed to bending of the laminate. This laminate is unsymmetric about the x-y plane, with maximum asymmetry existing at location **D**. Therefore, bending of the laminate is greatest at **D** and σ_x due to bending is maximum.

The σ_y distribution in the **R**=0.5 laminate is similar to that of the **R**=0 laminate. The far-field region is in compression and is approximately -125 psi. At locations **B** and **F**, σ_y is approximately -300 psi. As was the case for the **R**=0 laminate, this behavior is due to deformation of the fill tows, which increases σ_y at **B** and **F** At locations **C** and **E**, σ_y is evaluated in fill tows and is approximately 300 psi.

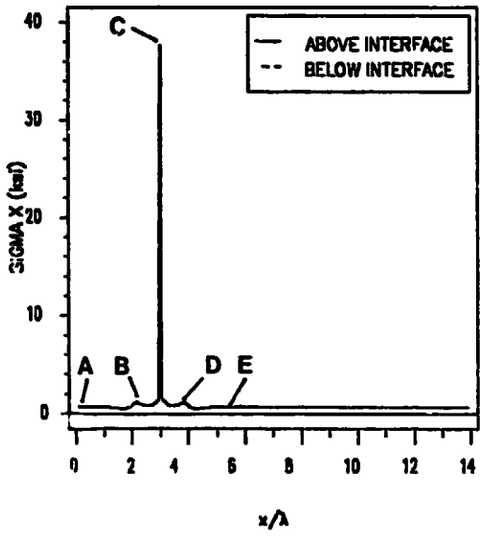

a) Interfacial σ_x.

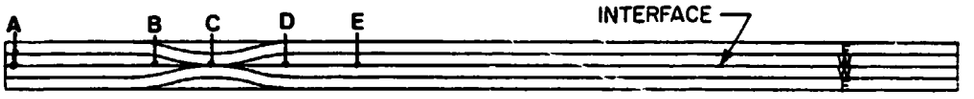

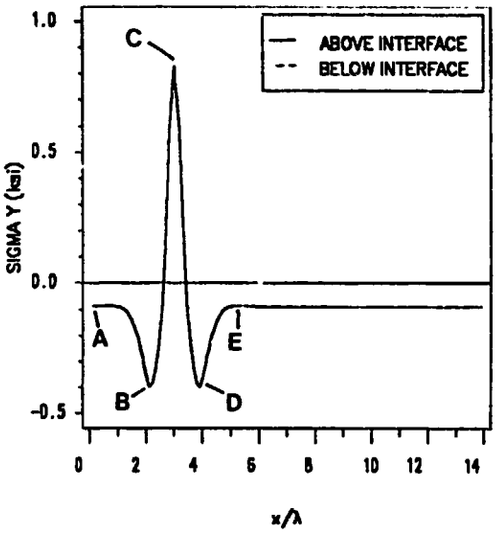

b) Interfacial σ_y.

Figure 60. Interfacial σ_x and σ_y in $(F/W_2/F)_t$ laminate. R=0, ε_x = 0.1%.

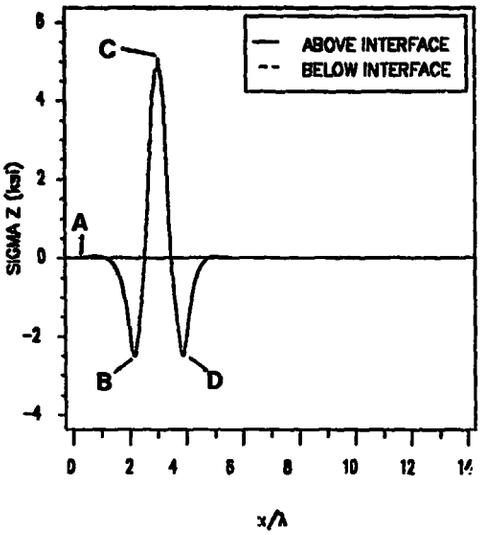

a) Interfacial σ_z.

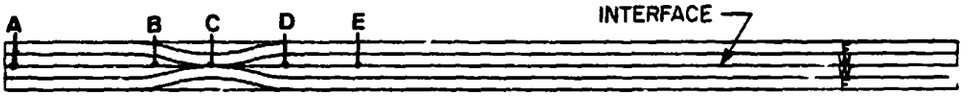

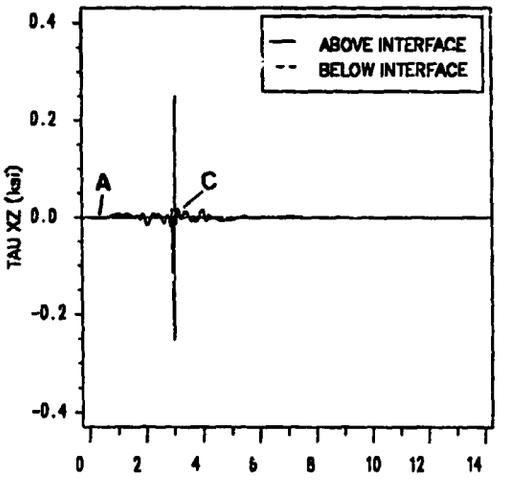

b) Interfacial τ_{xz}.

Figure 61. Interfacial σ_z and τ_{xz} in $(F/W_2/F)_t$ laminate. $P = 0$, $\varepsilon_x = 0.1\%$.

Interlaminar Stresses σ_z and τ_{xz}: The distributions of the interlaminar stresses σ_z and τ_{xz} are illustrated in Figure 63. In the region of undulation σ_z is tensile at locations **C** and **E** and compressive at points **B, D,** and **F**. As was the case for the **R**=0 laminate, this behavior is attributed to the tendency of the fill tows to straighten during deformation, which induces tensile stresses at the peaks of the undulation (**C** and **E**) and compressive stresses away from the peaks (**B, D,** and **F**).

The interlaminar shear stress τ_{xz} is nonzero throughout the undulation region. Unlike the **R**=0 laminate, the **R**=0.5 laminate is unsymmetric about the x-y plane. Therefore, bending of the laminate occurs under axial strain and shear stresses result. The maximum τ_{xz} is -4 ksi and occurs at location **D**, which is midway between the undulations. Point **D** is the location of maximum asymmetry; therefore, it is the location of maximum shear stress. Positive values of τ_{xz} ($\cong$ 2 ksi) occur midway between points **B** and **C**, and between points **E** and **F**.. This behavior is also due to bending and shear deformation of the laminate.

3.5.3.3 R=1 and 4 Laminates

The interfacial stress distributions for the **R**=1 and **R**=4 laminates are presented in Appendix A (Figure 125 through Figure 128). The form of the stress distributions in these laminates are similar to those of the **R**=0 and **R**=0.5 laminates. Similarities and differences between the laminates are summarized in section 3.7.

3.5.4 Interfacial Stress Distributions: $(W/W_2/F)_w$ Laminates

The interfacial stress distributions for the $(F/W_2/F)_w$ for **R**=0 and 0.5 laminates, under in-plane loading are shown in Figure 64 through Figure 66. As previously mentioned in the discussion on out-of-plane loading, these laminates differ from the $(F/W_2/F)_t$ laminates in that

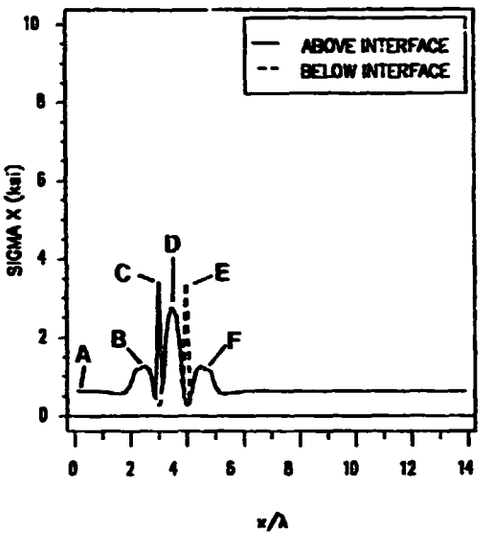

a) Interfacial σ_x.

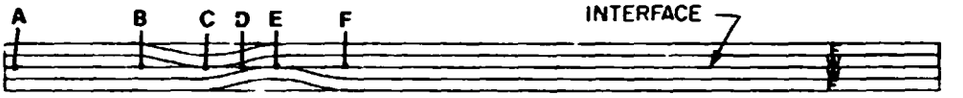

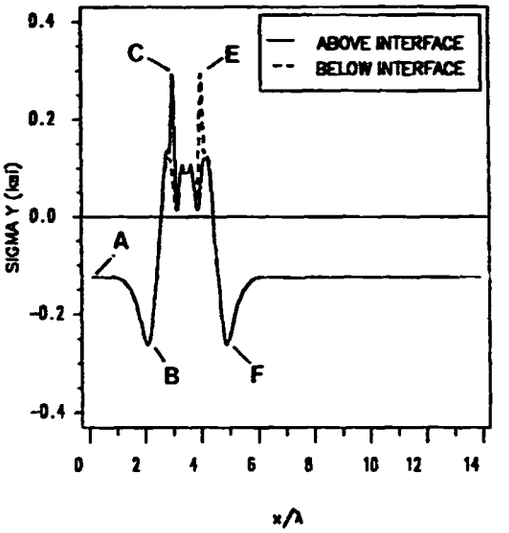

b) Interfacial σ_y.

Figure 62. Interfacial σ_x and σ_y in $(F/W_2/F)_1$ laminate. $R=0.5$, $\varepsilon_x = 0.1\%$.

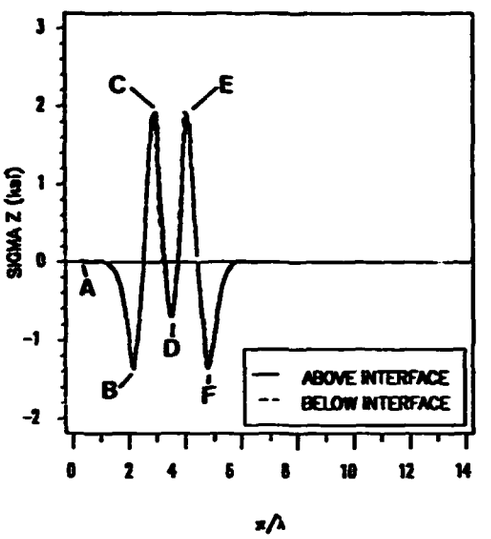

a) Interfacial σ_z.

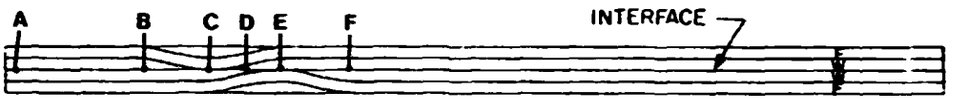

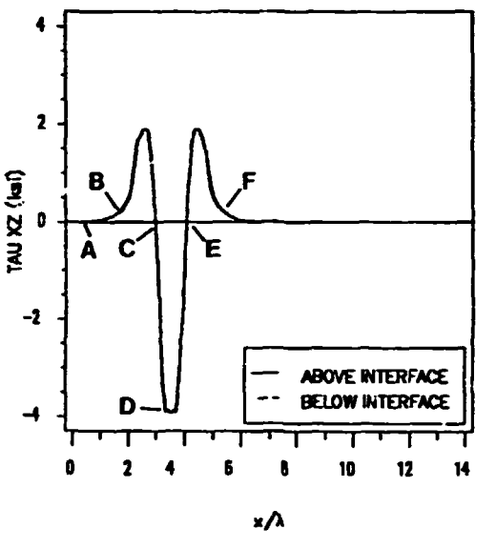

b) Interfacial τ_{xz}.

Figure 63. Interfacial σ_z and τ_{xz} in $(F/W_2/F)_t$ laminate. R=0.5, ε_x = 0.1%.

the warp tows in the $(F/W_2/F)_n$ laminates exhibit curvature and bound the midplane, whereas in the $(F/W_2/F)_n$ laminates the fill tows exhibit curvature and bound the midplane (Figure 18).

3.5.4.1 R=0 Laminate

In-plane Normal Stresses σ_x and σ_y: The σ_x and σ_y stress distributions in the R=0 laminate are shown in Figure 64. In the far-field region σ_x is evaluated in a warp tow, which exhibits an axial modulus E_x of 40.7 MSI. The magnitude of σ_x is approximately 39 ksi, which is less than the 40.7 ksi predicted for an in-plane strain $\varepsilon_x = 0.1\%$ using CLPT. This difference is due to the presence of the undulation, which is a region of low axial stiffness in the laminate. Therefore, there is nonuniform ε_x distribution along the laminate, with the region of undulation under an axial strain $\varepsilon_x > 0.1\%$ and the far-field region under a strain $\varepsilon_x < 0.1\%$. In the region of undulation, σ_x is evaluated in a fill tow, which has a low axial modulus (0.75 MSI). The magnitude of σ_x in the undulation is approximately 0.75 ksi.

The σ_y component of stress is tensile and approximately 100 psi in the far-field region. At location **C**, σ_y is compressive and approximately -600 psi. At locations **B** and **D**, σ_y is approximately 700 psi. The σ_y at **B** and **D** is attributed to large σ_z -induced Poisson extension of the warp tows in the y direction.

Interlaminar Stresses σ_z and τ_{xz}: The distribution of the interlaminar normal stress σ_z is shown in Figure 65a. At point **C**, σ_z is -4 ksi. The laminate is in compression at **C** because the tendency of the warp tows to straighten under load causes the peaks of the undulation to move towards the midplane, putting the central warp region under compression. At locations **B** and **D** the tendency is for the warp tows to separate, resulting in tensile σ_z.

The interlaminar shear stress τ_{xz} (Figure 65b)is zero in far-field region, but is nonzero in the region of undulation. This laminate is symmetric about the x-y plane and thus should exhibit zero τ_{xz} everywhere along the midplane. As mentioned in the discussion on the

$(F/W_z/F)_f$, R=0 laminate, this discrepancy is attributed to the presence of stress singularities (points B and D in the $(F/W_z/F)_m$, R=0 laminate) and the numerical instabilities associated with them.

3.5.4.2 R=0.5 Laminate

In-plane Normal Stresses σ_x and σ_y: The interfacial σ_x distribution in the R=0.5 laminate is shown in Figure 66a. In the region of undulation the σ_x distribution is complex, and is best understood by considering the deformation of the laminate (Figure 67). Figure 67 indicates that the laminate exhibits severe bending, which results in a radically different σ_x above and below the interface. Below the interface, σ_x is high at B and above the interface σ_x is high at F (Figure 66a). The low value of σ_x at location D is due to the change in material properties. At point D, σ_x is evaluated in a fill tow, which has a low axial modulus.

The interfacial σ_y distribution (Figure 66b) follows that of the σ_x and σ_x distributions due to Poisson effects. As was the case for σ_x the σ_y distribution is different above and below the interface. In the far-field region σ_y is tensile and approximately 100 psi. At locations C and E, which are above and below the interface, respectively, σ_y is compressive and is approximately -250 psi. At locations B and F, σ_y is tensile and approximately 350 psi.

Interlaminar Stresses σ_z and τ_{xz}: The interlaminar normal stress σ_z is shown in Figure 68a. As in the laminates discussed previously, the σ_z distribution can be related to the tendency for the warp tows to straighten under axial strain. In this laminate the deformation of the warp tows results in compressive σ_z at location D and tensile σ_z at locations B, C, E, and F. The maximum tensile σ_z is approximately 1.8 ksi, at points B and F. The maximum compressive σ_z is approximately -1.2 ksi, at point D.. Continuity of σ_z does not appear to be satisfied at locations B, C, E, and F. Locations B and F are singular points, which are not accurately modeled by the finite element method. Locations C and E are regions of high stress gradients,

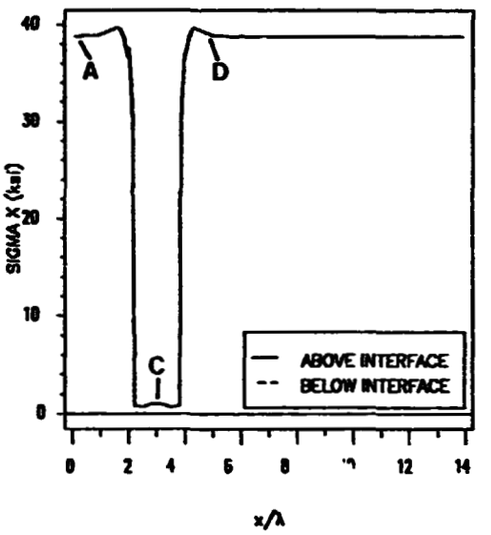

a) Interfacial σ_x.

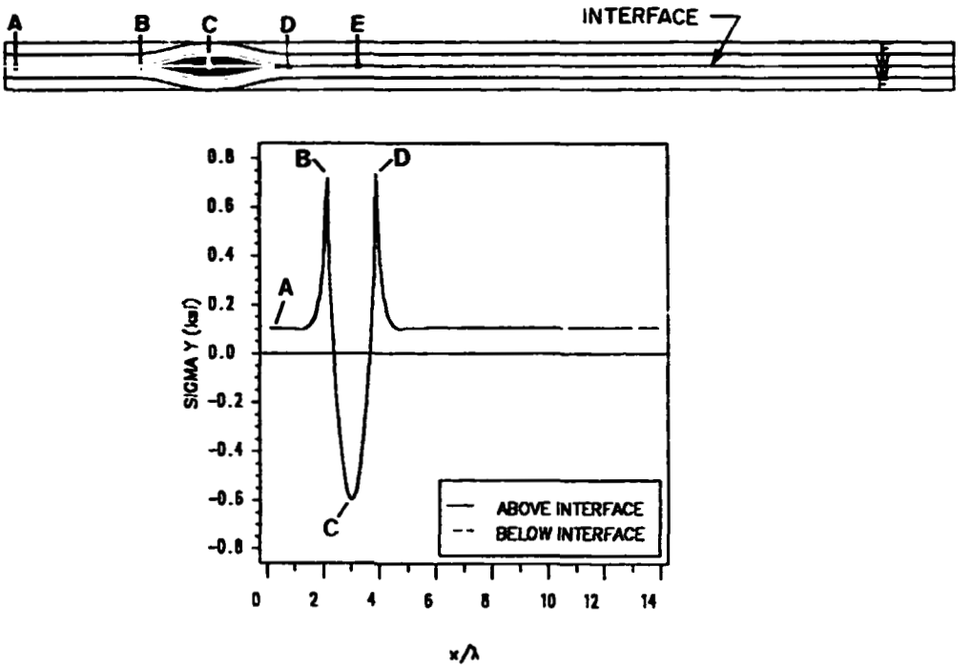

b) Interfacial σ_y.

Figure 64. Interfacial σ_x and σ_y in $(F/W_2/F)_w$ laminate. R = 0, ε_x = 0.1%.

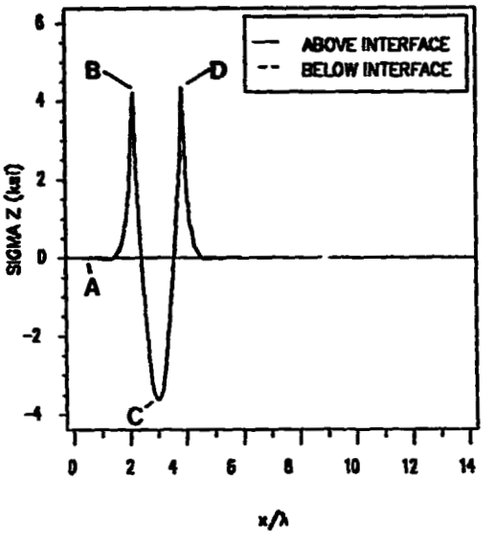

a) Interfacial σ_z.

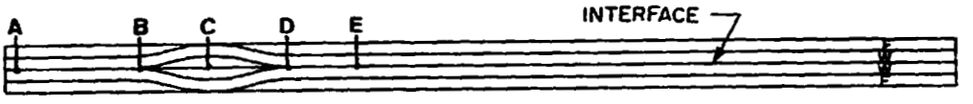

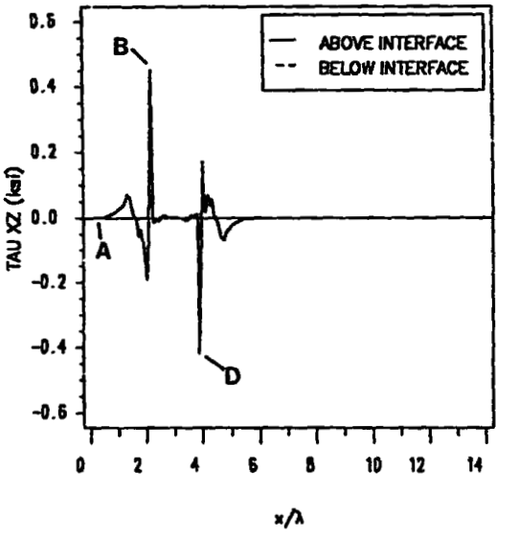

b) Interfacial τ_{xz}.

Figure 65. Interfacial σ_z and τ_{xz} in $(F/W_2/F)_w$ laminate. R=0, ε_x = 0.1%.

which require a denser mesh than that used in this study in order to be accurately predicted. The interlaminar shear stress τ_{xz} (Figure 68b) is induced by the bending of the laminate under axial load, and ranges from +4 ksi at location **D** to -5.5 ksi at locations **D** and **F**. The τ_{xz} distribution indicates that continuity is satisfied at the interface.

3.5.4.3 R=1 and 4 Laminates

The interfacial stress distributions for the **R=1** and 4 laminates exhibit many of the same characteristics those already discussed, and the physical arguments used to explain their behavior are similar. As such, further discussion is left to a later section where the similarities and differences between the laminates are summarized. The distributions, however, are presented in Appendix A.

3.5.5 Interfacial Stress Distributions: $(F/W)_2$ Laminates

As may be recalled from the discussion of the out-of-plane loading results, the stacking sequence of the $(F/W)_2$ laminate differs from that of the $(F/W_2/F)$ laminate in that the $(F/W)_2$ laminate is not symmetric in the far-field region. This results in the midplane being bounded by tows of opposite orientation. The tow above the midplane is a warp and the tow below the midplane is a fill.

3.5.5.1 R=0 Laminate

In-plane Normal Stresses σ_x and σ_y: The interfacial σ_x distribution in the **R=0** laminate is shown in Figure 69a. The far-field value of σ_x in the warp tow (above the interface) is approximately 0.75 ksi, and agrees with CLPT. In the fill tow (below the interface) σ_x is approxi-

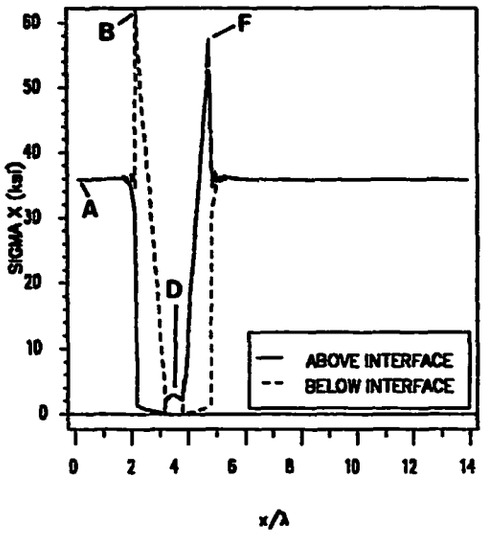

a) Interfacial σ_x.

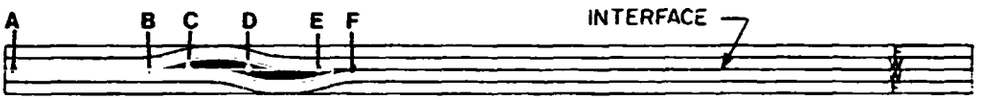

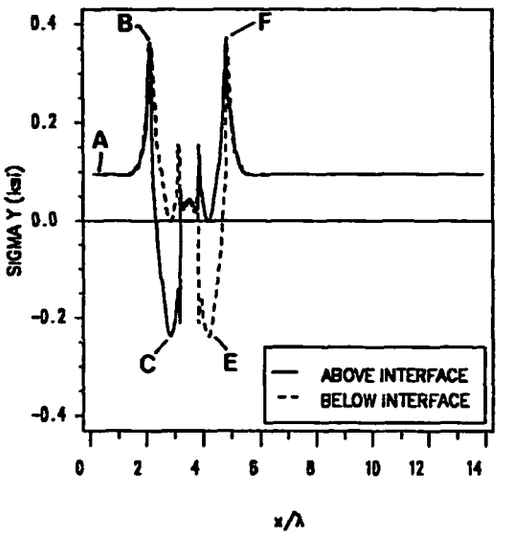

b) Interfacial σ_y.

Figure 66. Interfacial σ_x and σ_y in $(F/W_2/F)_w$ laminate. R=0.5, ε_x = 0.1%.

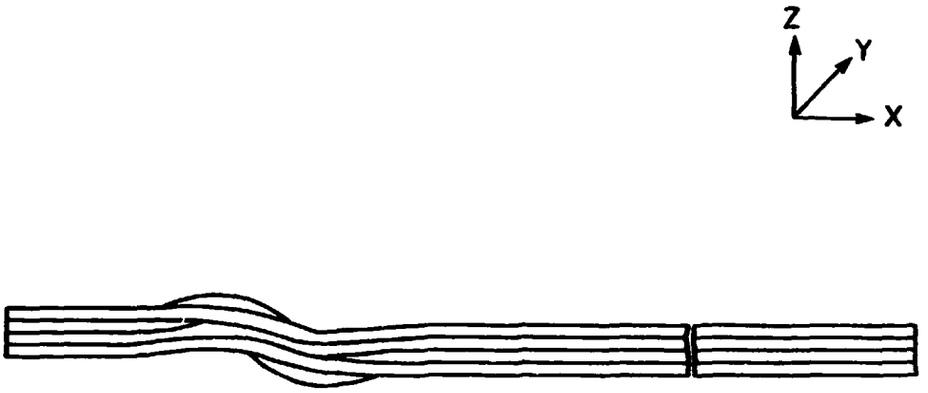

Figure 67. Deformation of $(F/W_2/F)_w$, R=0.5 laminate. $\varepsilon_x = 0.1\%$

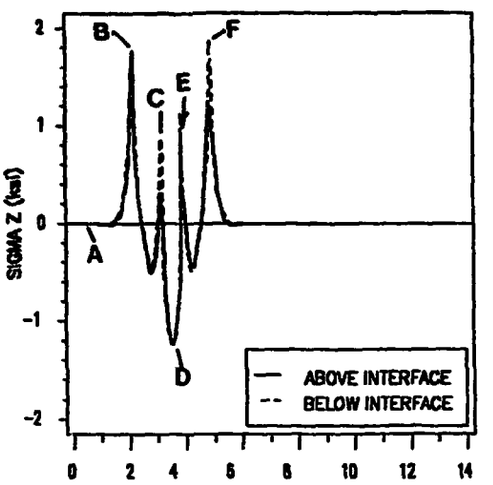

a) Interfacial σ_z.

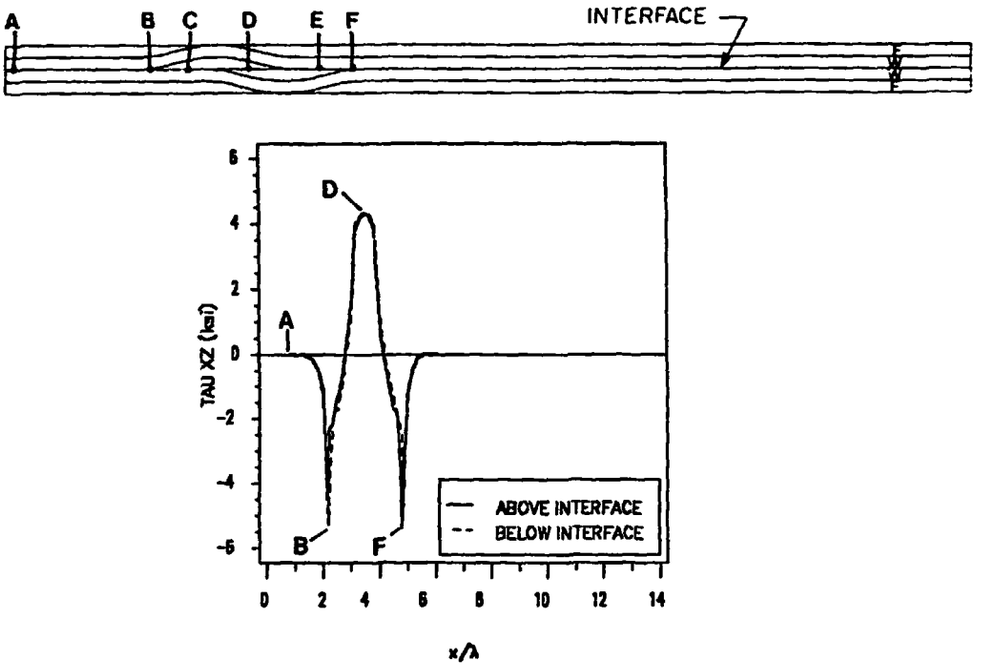

b) Interfacial τ_{xz}.

Figure 68. Interfacial σ_z and τ_{xz} in $(F/W_2/F)_w$ laminate. R=0.5, ε_x = 0.1%.

mately 34 ksi, which is far less than the 40.7 ksi predicted by CLPT. As was the case for the $(F/W_2/F)_w$ laminate, this result is due to the presence of the undulation, which is a region of low axial stiffness and hence causes a nonuniform ε_x distribution to exist in the laminate. Consequently, $\varepsilon_x < 0.1\%$ and σ_x in the fill tow is reduced. The effect is negligible in the warp tow due to its low axial modulus. The σ_x distribution in the region of undulation is more complex. At point **C**, σ_x is compressive at about -4 ksi. This is due to bending of the laminate, which leaves the fill tow in compression at **C**. The slight increase in σ_x at locations **B** and **D** is also attributed to bending of the laminate, which increases σ_x in the warp tows near the undulation.

The σ_y distribution (Figure 69b) indicates that in the far-field regions the warp tow (above the interface) is in tension and the fill tow in compression. The magnitudes of σ_y in the far-field regions of the warp and fill tows are 100 psi and -125 psi, respectively. This indicates an apparent lack of force equilibrium in the far-field region. However, in an unsymmetric laminate neither stresses nor strains are constant within each tow; therefore, midplane stresses are not an accurate indicator of force equilibrium in the laminate. The σ_y distribution in the region of undulation can be related by Poisson effects to the σ_x and σ_z distributions.

Interlaminar Stresses σ_z and τ_{xz}: The interlaminar normal stress σ_z (Figure 70a) is maximum and tensile ($\cong$ 2 ksi) at location **C**. At locations **B** and **D**, σ_z is compressive at approximately -1.2 ksi. As was the case for the $(F/W_2/F)_w$ and $(F/W_2/F)_f$ laminates, the σ_z distribution is due to the tendency of the fill tows to straighten under the applied strain. This induces tension at the peak of the undulation (**C**) and compression on either side (**B** and **D**). The far-field value of τ_{xz} is zero, which is consistent with CLPT.

The interlaminar shear stress τ_{xz} (Figure 70b) is 4 ksi and -4 ksi at locations **B** and **D**, respectively. The shear stress is a result of shear deformation which in turn results from the asymmetry of the laminate in the region of undulation. The far-field value of τ_{xz} is zero, which is consistent with CLPT.

3.5.5.2 *R=0.5, 1, and 4*

The stress distributions in the **R**=0.5, 1, and 4 laminates can be described using the same physical arguments used to describe the laminates discussed previously; therefore, the specifics of the distribution of each component of stress for each of the remaining offset ratios will not be presented. However, the interfacial stress distributions for these laminates are presented in Appendix A. A summary of the results for in-plane loading is presented in Section 3.7.

3.5.6 Influence of Undulation Aspect Ratio Ω

The influence of the undulation aspect ratio Ω on the maximum interfacial stress was evaluated for a $(F/W_z/F)_f$ laminate with an offset ratio **R**=0.5. The maximum values of σ_x, σ_y, σ_z, and τ_{xz} along the interface, as a function of Ω, are presented in Figure through Figure 74. The variation of σ_x (Figure 71) can be divided into two distinct regions. For undulation aspect ratios Ω ≥ 12, the maximum σ_x occurs at location **C** and increases approximately linearly with increasing Ω. This can be explained by recalling from the discussion of the out-of-plane loading results that as Ω increases the geometry of the laminate approaches that of a symmetric cross-ply laminate, which does not bend under axial load. Therefore, σ_x will increase since no compressive σ_x due to bending exists at **C**. At Ω values less than 12, the curvature of the fill tow is large enough that significant bending occurs under applied axial strain and location **C** is in compression; the location of the maximum tensile σ_x changes from location **C** to location **D**. The σ_y distribution (Figure 72) shows that σ_y decreases with increasing Ω. At Ω=6, σ_y is approximately 0.46 ksi and decreases to 0.22 ksi at Ω=24. The form of the σ_y distribution follows that of the σ_z distribution, which is shown in Figure 73.

The interlaminar normal stress σ_z (Figure 73) is maximum (≅3.1 ksi) at Ω=6 and decreases to approximately 1 ksi at Ω=24. This is also due to the reduction in curvature of the

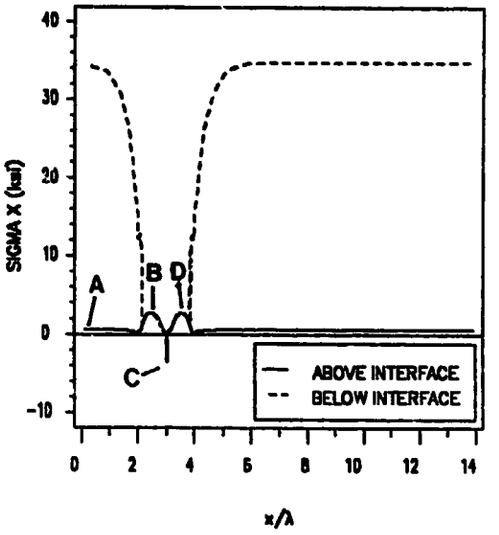

a) Interfacial σ_x.

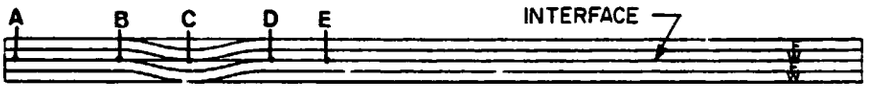

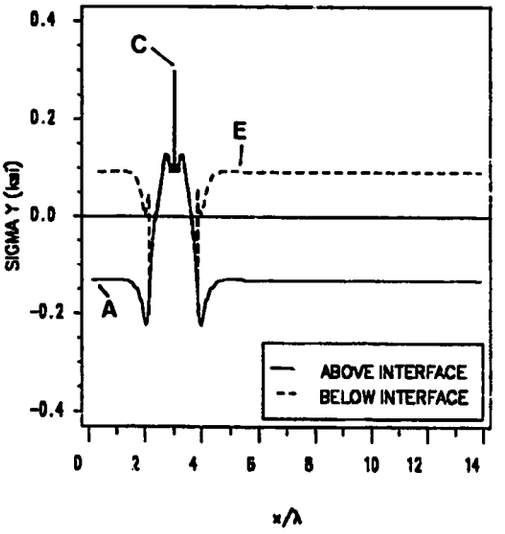

b) Interfacial σ_y.

Figure 69. Interfacial σ_x and σ_y in $(F/W)_2$ laminate. R=0, ε_a=0.1%.

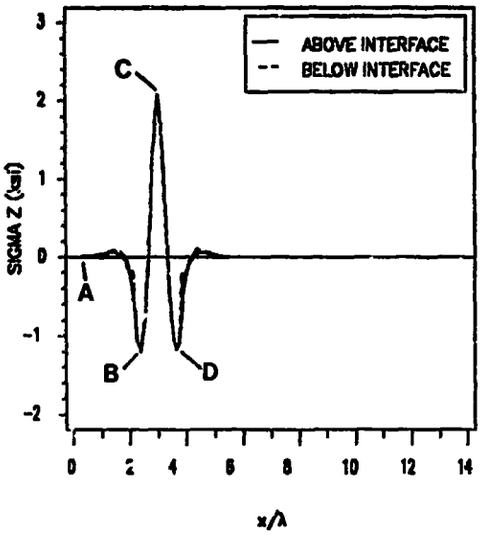

a) Interfacial σ_z.

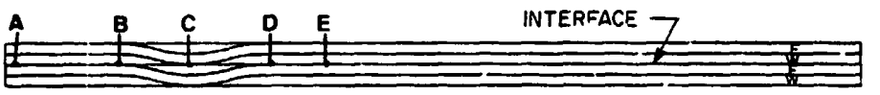

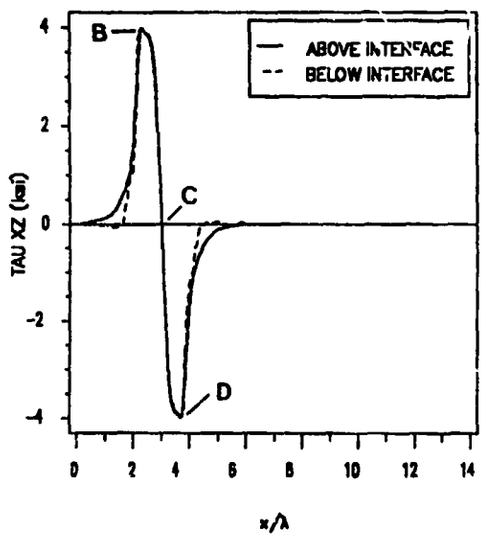

b) Interfacial τ_{xz}.

Figure 70. Interfacial σ_z and τ_{xz} in $(F/W)_2$ laminate. R = 0, $\varepsilon_x = 0.1\%$.

fill tows with increasing Ω. As Ω increases the response of the laminate approaches CLPT, for which σ_z is zero. The interlaminar shear stress τ_{xz} (Figure 74) does not vary significantly with Ω. The magnitudes of τ_{xz} ranges from 3.9 ksi at Ω=9 to 3.4 ksi at Ω=24, which is a difference of approximately 15 percent. The form of the τ_{xz} distribution is attributed to the orientation of the curved portion of the fill tows with respect to the load axis. At Ω=9 the fill tows at the undulation are oriented approximately 45° with respect to the load axis, which is the condition for maximum shear. Thus, at Ω≠ 9 the magnitude of τ_{xz} is expected to decrease.

3.6 *Results: Thermal Loading*

3.6.1 Stress Distributions In Region Of Undulation

The thermal stress distributions (per °F temperature change) in the undulations of a $(F/W_2/F)_r$, R=0.5 laminate are presented as contour plots in Figure 75 through Figure 79. The in-plane normal stress σ_x is tensile and approximately 10 psi in the far-field regions (D and E) of the fill tow (Figure 75a). The far-field σ_x in the warp region (Figure 75b) is approximately -10 psi, indicating satisfaction of force equilibrium in the x direction. These stresses are due to the mismatch in the coefficients of thermal expansion between the fill tows and the warp tows. The CTE of the fill tows is much less than that of the warp tows (Table 3); therefore, under a positive ΔT the fill tows are in tension and the warp tows in compression. The σ_x stress contour in the region of undulation is more complex and is attributed to the deformation of the fill tows under thermal load, which is analogous to the straightening of a curved beam (Figure 76). This response induces tension in the fill tows at locations A and H (25 psi) and axial compression in the regions between B and C and between F and G, where σ_x ranges from -5 to -15 psi. The warp region is in axial compression throughout.

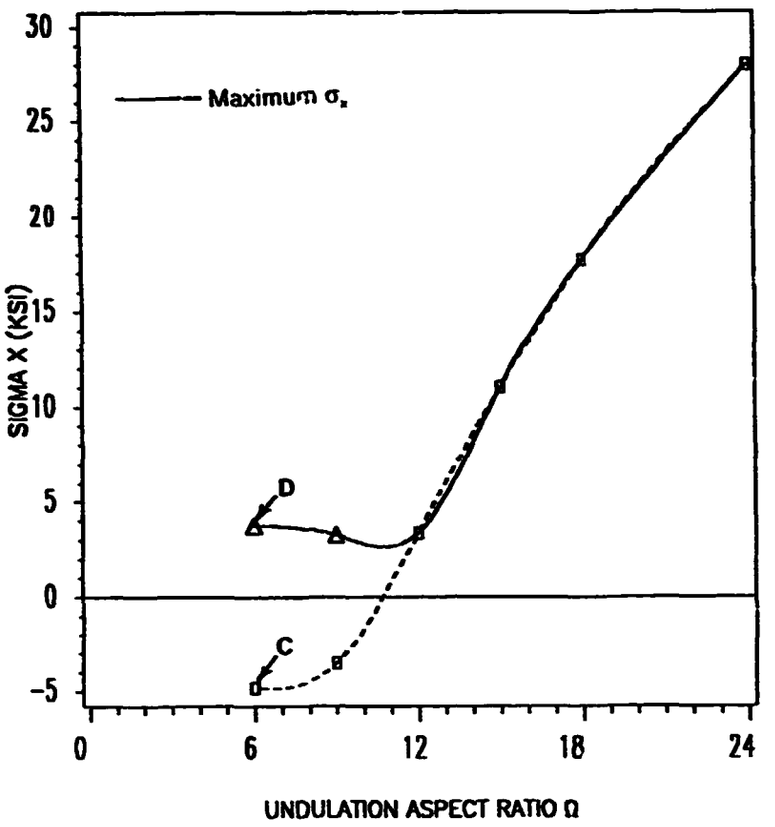

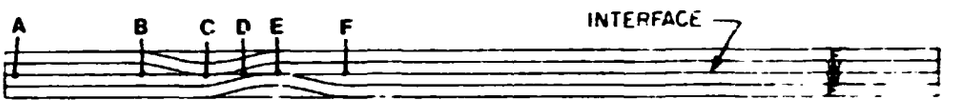

Figure 71. Maximum interfacial σ_x as a function of Ω. ε_x =0.1%.

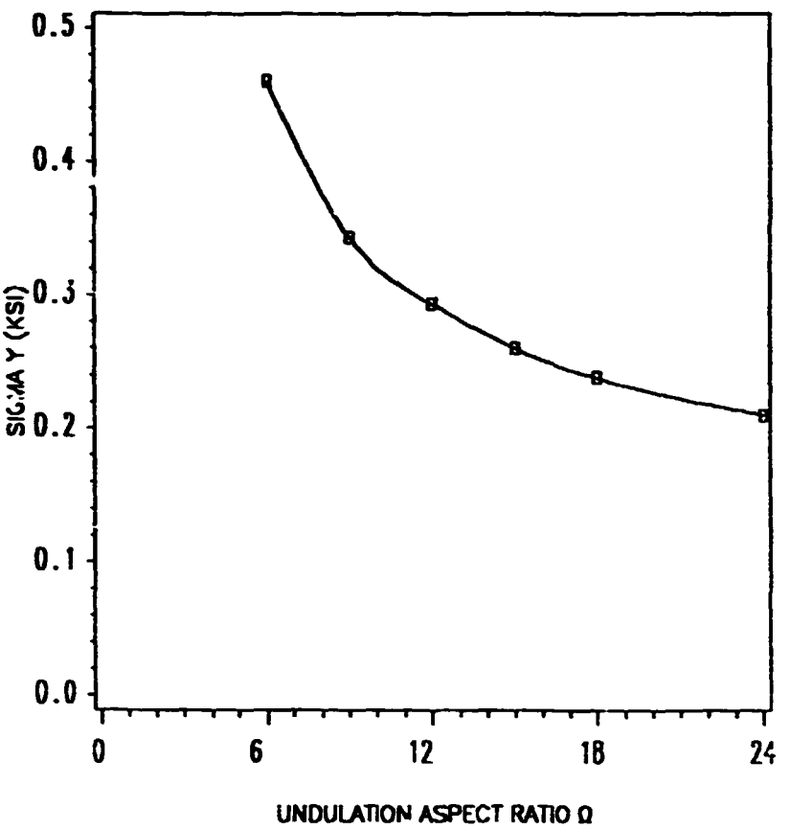

Figure 72. Maximum interfacial σ_y as a function of Ω. $\varepsilon_a = 0.1\%$.

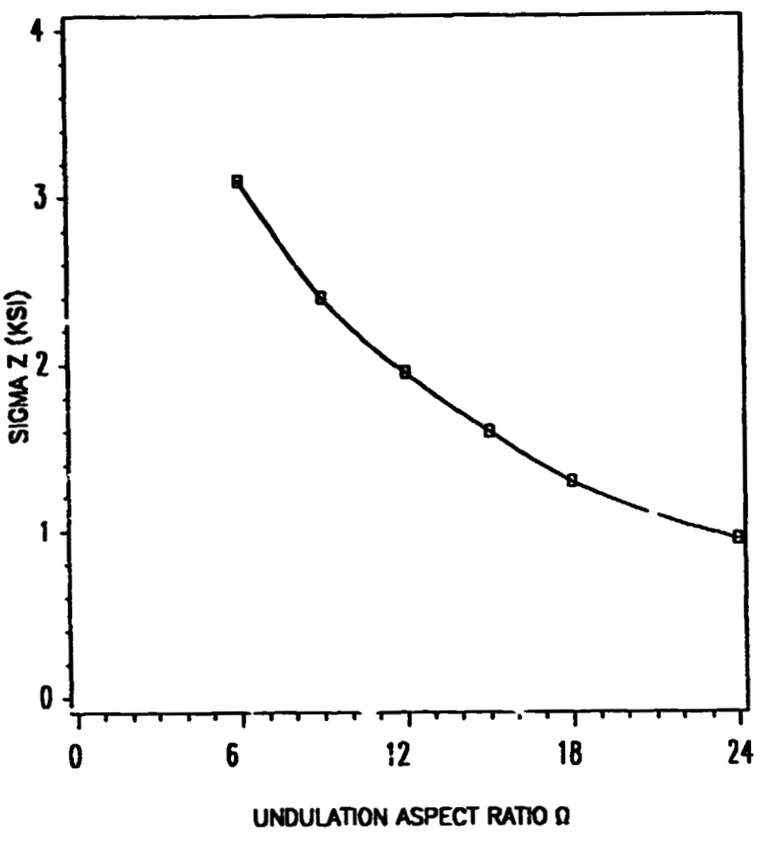

Figure 73. Maximum interfacial σ_z as a function of Ω. $\varepsilon_a = 0.1\%$.

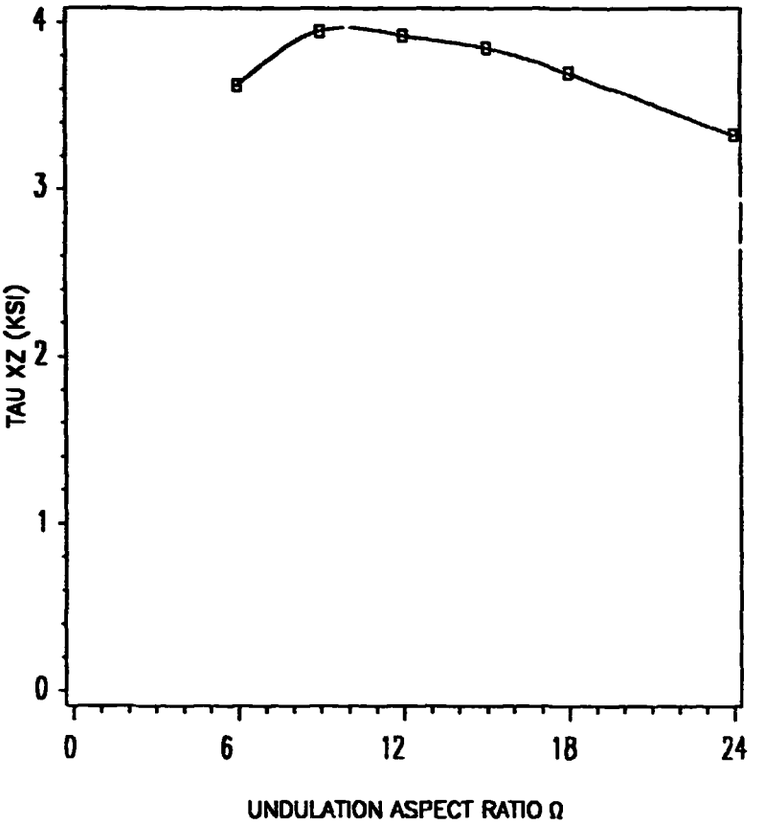

Figure 74. Maximum interfacial τ_{xz} as a function of Ω. $\varepsilon_x = 0.1\%$.

The σ_y contour (Figure 77) shows that σ_y varies little within the undulation. In the fill tows σ_y is compressive and ranges from -9 to -10 psi. In the warp region σ_y is tensile and ranges from 9 to 10 psi, satisfying equilibrium. This result is also due to the mismatch in CTE's between the warp and fill tows. In the y direction the CTE of the fill tows is greater than that of the warp tows. Therefore, under uniform positive ΔT the fill tows are under compression in the y direction and the warp tows are in tension.

The contour of the interlaminar normal stress σ_z is shown in Figure 78. In the far-field regions σ_z is zero for both the warp and fill regions, which is consistent with CLPT. A large gradient in σ_z exists in the regions **B-D** and **E-G**. Maximum tensile σ_z is found in the regions between **C** and **D** and between **E** and **F**, where σ_z is approximately 1.5 psi. These regions correspond to the regions in the deformed laminate where the fill tows are most oriented towards the z direction (**C-D** and **E-F** in Figure 76). Therefore, the stiffness in the z direction is greatest and hence σ_z is maximum. At locations **B** and **G**, σ_z is compressive (approximately -3 psi). This result is attributed to bending of the fill tows under thermal load, which forces the fill to towards the midplane of the laminate at these points, and results in compressive σ_z. Inspection of the σ_z distribution indicates that continuity is satisfied.

The contour of the interlaminar shear stress τ_{xz} is shown in Figure 79. In the far-field regions (**A** and **F**) τ_{xz} is zero as expected. Within the undulation, however, τ_{xz} is nonzero due to the asymmetry of the laminate. As was the case for in-plane loading, lack of symmetry in the laminate induces shear deformation in the undulation and hence shear stresses. In the fill tows (Figure 79a) τ_{xz} is negative (-3 to -5 psi) in the regions **B-C** and **H-I** and is positive (1 to 3 psi) in the regions **C-E** and **G-H**. The shear stress in the warp tows (Figure 79b) is positive in regions **B-C** and **D-E** at about 1 psi. Between the undulations (region **C-D**) τ_{xz} is negative and ranges from about -2 psi to -3 psi.

3.6.2 Interfacial Stress Distributions

3.6.2.1 In-Plane Normal Stresses σ_x and σ_y

The interfacial thermal stress distributions are presented in Figure 80 and Figure 81. Again, these stresses result from the mismatch in thermal expansion coefficients between the warp and fill tows. The in-plane normal stress σ_x is compressive ($\cong -9.5$ psi) in the far-field region. At locations **C** and **E**, σ_x is evaluated in fill tows and is tensile at approximately 12 psi. The σ_y distribution (Figure 80b) shows that the warp tows (far-field region) are in tension (9.5 psi) and the fill tows are in compression (-9.5 psi at **C** and **E**). This indicates satisfaction of force equilibrium in the y direction.

3.6.2.2 Interlaminar Stresses σ_z and τ_y

The interlaminar normal stress σ_z distribution (Figure 81a) indicates that σ_z is tensile at the undulation peaks (**C** and **E**) and compressive on either side of the undulations (**B**, **D**,and **F**). This distribution is attributed to the deformation of the laminate under thermal load. The deformation of the fill tows is such that they tend to separate from the midplane at locations **C** and **E** compress the midplane at locations **B**, **D** and **F**. The interlaminar shear stress, τ_{xz}, distribution is presented in Figure 81b. Positive shear stresses of approximately 1.6 psi exist at locations **B** and **F**. At location **D**, which is the location of maximum asymmetry, τ_{xz} is approximately -3.1 psi. In the far-field region τ_{xz} is zero, which is consistent with CLPT. Both the σ_z and τ_{xz} distributions indicate that stress continuity is satisfied at the interface.

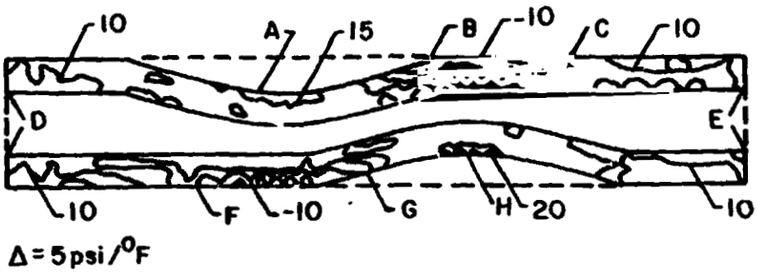

a) Fill Tows

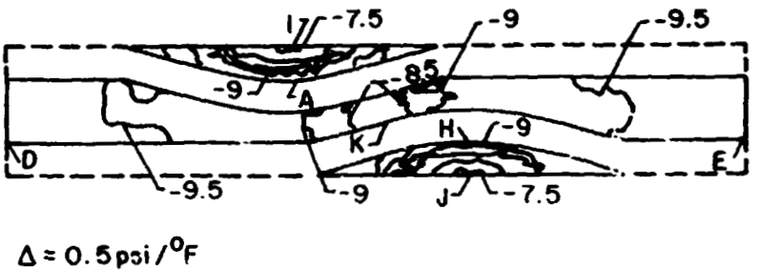

b) Warp Tows

Figure 75. Contour plot of σ_x in $(F/W_2/F)_1$ laminate under thermal load. R = 0.5, $\Delta T = +1°F$.

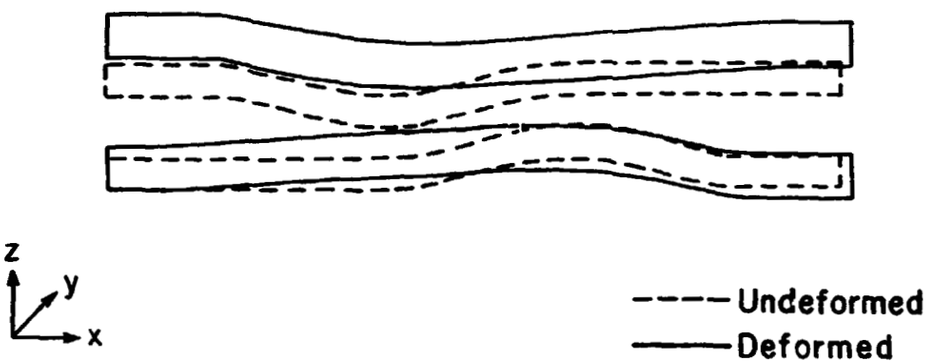

Figure 76. Deformation of fill towe in $(F/W_2/F)_1$ laminate under thermal load. R=0.5, $\Delta T = +1°F$.

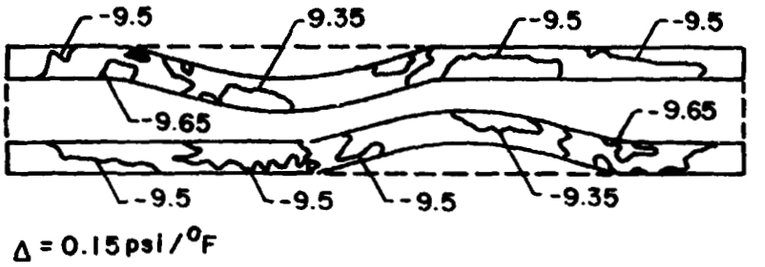

a) Fill Tows

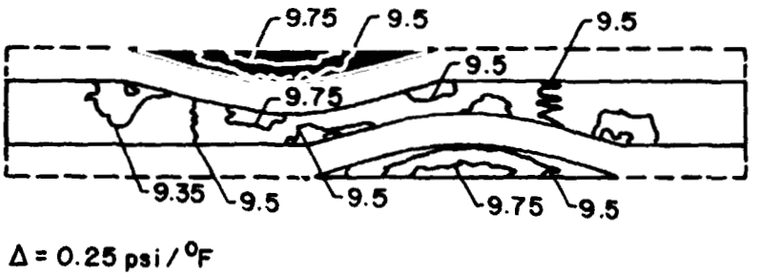

b) Warp Tows

Figure 77. Contour plot of σ_y in $(F/W_2/F)_f$ laminate under thermal load. R = 0.5, $\Delta T = +1°F$.

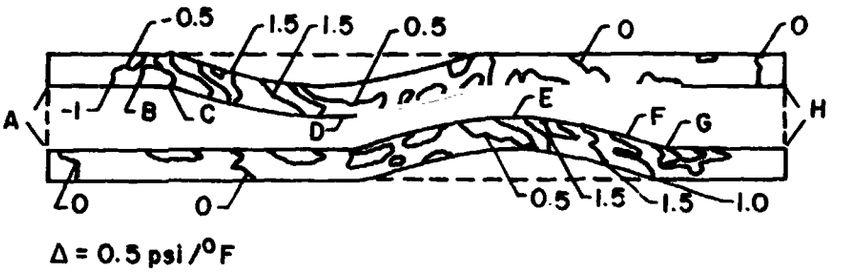

a) Fill Tows

b) Warp Tows

Figure 78. Contour plot of σ_z in $(F/W_2/F)_t$ laminate under thermal load. R = 0.5, $\Delta T = +1°F$.

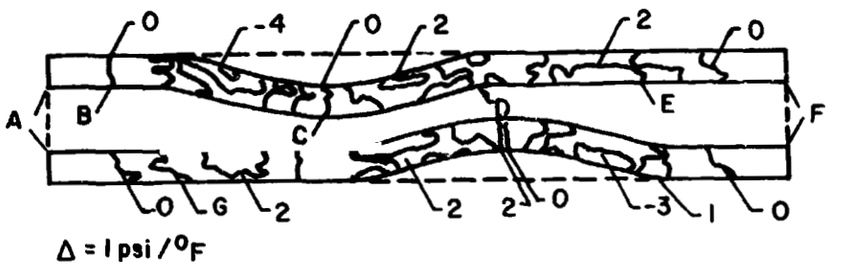

a) Fill Tows

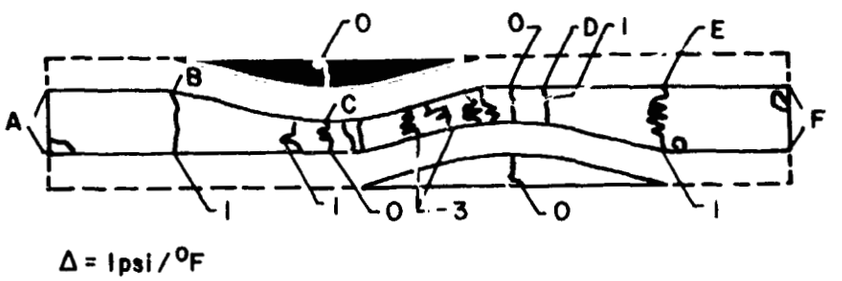

b) Warp Tows

Figure 79. Contour plot of τ_{xz} in $(F/W_2/F)_t$ laminate under thermal load. R = 0.5, $\Delta T = +1°F$.

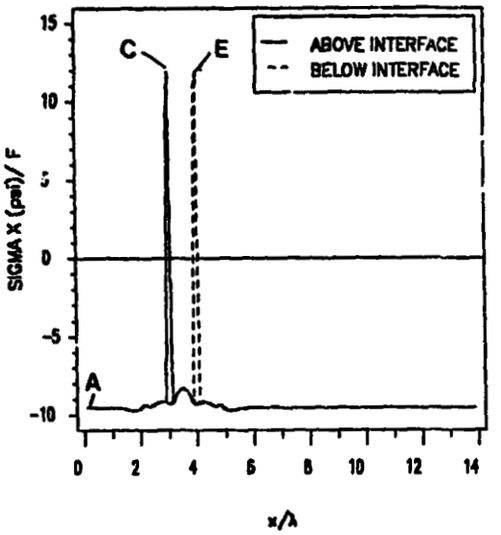

a) Interfacial σ_x.

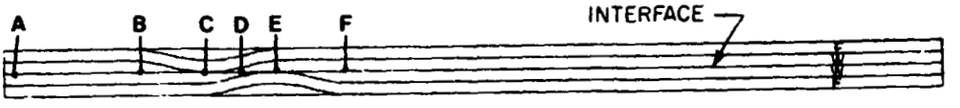

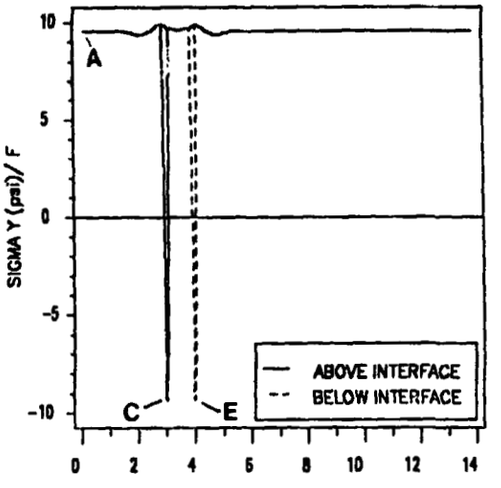

b) Interfacial σ_y.

Figure 80. Interfacial σ_x and σ_y in $(F/W_2/F)_1$ laminate under thermal load. R = 0.5, $\Delta T = +1°F$.

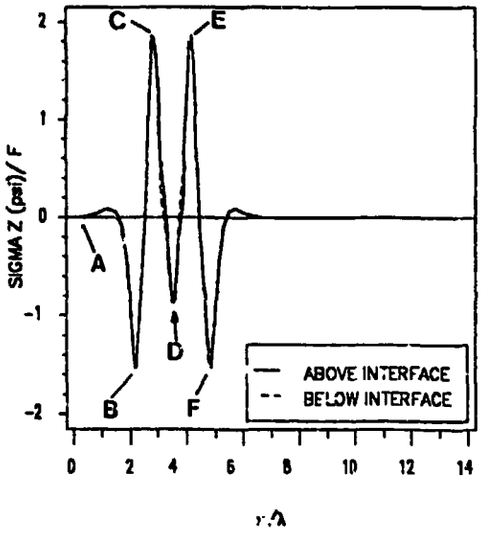

a) Interfacial σ_z.

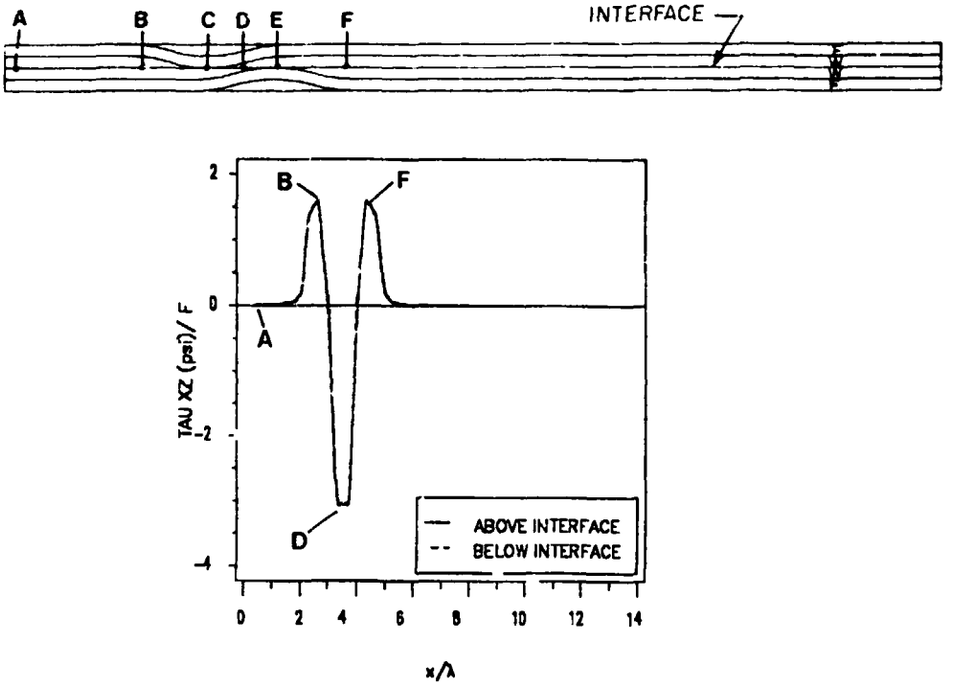

b) Interfacial τ_{xz}.

Figure 81. Interfacial σ_z and τ_{xz} in $(F/W_2/F)_t$ laminate under thermal load. R = 0.5, $\Delta T = +1°F$

3.7 Summary and Discussion

3.7.1 Stiffness

Woven fabric composites are unique in that laminate stiffness varies along the axial coordinate. The far-field region, which has the geometry of a cross-ply laminate, exhibits elastic moduli which can be predicted from classical laminated plate theory (CLPT). In the regions of undulation the moduli are a function of stacking sequence and offset ratio **R** (Table 5). The in-plane modulus E_x is most influenced by the above geometric parameters, with reductions of greater than 50% of the far-field modulus predicted for the cases considered. The moduli E_y and E_z are relatively independent of stacking sequence and offset ratio.

The effect of the undulation on E_x of the unit cell is presented in Table 6. The results indicate that undulations reduce the axial modulus, E_x, up to 18% from that of the far-field value. The average reduction in E_x is about 12%, and is relatively independent of **R**.

3.7.2 Out-of-Plane Loading

3.7.2.1 Region of Undulation

The results of the out-of-plane loading analysis show that the stress distribution in the laminates is relatively complex, and can be related to the two distinct regions of interest that exist in each stacking sequence ($(F/W_z/F)_f$ $(F/W_z/F)_w$, and $(F/W)_z$) for all offset ratios **R**. In the far-field region the geometry of the laminate is analogous to a cross-ply laminate. As such, the normal components of stress σ_x, σ_y, and σ_z are constant throughout each tow and the interlaminar shear stress τ_{xz} is zero. In the region of undulation, all components of stress are

nonzero and are a function of stacking sequence, offset ratio R, and undulation aspect ratio Ω. The stress distributions in the region of undulation can be explained in terms of local deformation of the tows, which is analogous to bending and shear of a beam (Fig 24). Under out-of-plane loading the bending of the tows generates large σ_x as well as increases the magnitudes of σ_y, σ_z, and τ_{xz} over the far-field values.

3.7.2.2 *Interfacial Stresses*

The stress distribution along the interface between the two woven fabric lamina is of special interest because interlaminar failure was observed experimentally (Chapter 2). The maximum interfacial stresses, as a function of stacking sequence and offset ratio R, are summarized in Figure 82 through Figure 85.

In-plane Normal Stresses σ_x and σ_y: The in-plane normal stress σ_x (Figure 82) is largest in the $(F/W_2/F)$, laminate and smallest in the $(F/W_2/F)_w$ laminate. This can be explained by considering the geometry of the laminates as illustrated in Figure 14. In the $(F/W_2/F)$, laminate the convex side of the fill tow, which exhibits maximum σ_x, lies along the interface. In the $(F/W_2/F)_w$ laminate, however, the convex side of the tow lie along the top and bottom surfaces of the laminate. Thus, in the $(F/W_2/F)_w$ laminate the region of maximum σ_x is not part of the interfacial stress distribution. The σ_x in the $(F/W)_2$ laminate differs from the other laminates in that the maximum value of σ_x is found in the R = 0.5 case. This is attributed to the geometry of that particular laminate. Apparently, the orientation of the fill tows is such that maximum interaction, in the form of bending between the two undulations, occurs, and results in high σ_x. It should also be noted that σ_x varies little with offset ratio for $R \geq 1$.

The maximum σ_y (Figure 83) is found in the $(F/W_2/F)_w$ laminate, and is approximately 10% higher than the largest σ_y predicted for both the $(F/W_2/F)$, and $(F/W)_2$ laminates. Additionally, σ_y is essentially independent of R.

Interlaminar Stresses σ_z and τ_{xz}: The variation of the interlaminar normal stress σ_z (Figure 84) exhibits the same characteristics as the σ_y variation. The maximum σ_z is found in the $(F/W_2/F)_\infty$ laminate and is nearly independent of R. It should also be noted that σ_z is relatively independent of axial coordinate. The maximum σ_z predicted for the region of undulation was less than 15% greater than that predicted for the far-field region.

The variation in the interlaminar shear stress τ_{xz} (Figure 85) differs from the other components of stress in that τ_{xz} is strongly dependent on laminate stacking sequence. The largest τ_{xz} is found in the $(F/W_2/F)_\infty$ laminate and the smallest τ_{xz} is found in the $(F/W_2/F)_t$ laminate. For all three cases studied τ_{xz} is essentially independent of R for $R \geq 1$. The variation in τ_{xz} for $R < 1$ is attributed to relative changes in shear deformation of the laminate associated with the proximity of the undulations to each other.

Recognizing that the $(F/W_2/F)_t$ and $(F/W_2/F)_\infty$ stacking sequences represent the two cross-sections of the $(F/W_2/F)$ laminate (Figure 14), it appears that the $(F/W)_2$ laminate would be least susceptible to interlaminar failure due to the low τ_{xz} predicted. However, short-beam shear and transverse tensile strength tests of several unidirectional carbon-carbon materials conducted by Perry and Adams [4] indicate shear strengths approximately five times greater than the transverse tensile strength. Consequently, it is predicted that σ_z, which is not a strong function of laminate geometry, dominates failure; hence, all the stacking sequences evaluated are equally susceptible to interlaminar failure.

3.7.3 In-Plane Loading

3.7.3.1 Region of Undulation

Similar to the out-of-plane loading case, the stresses due to in-plane loading can be described in terms of the geometry of the laminate, namely the region of undulation and the

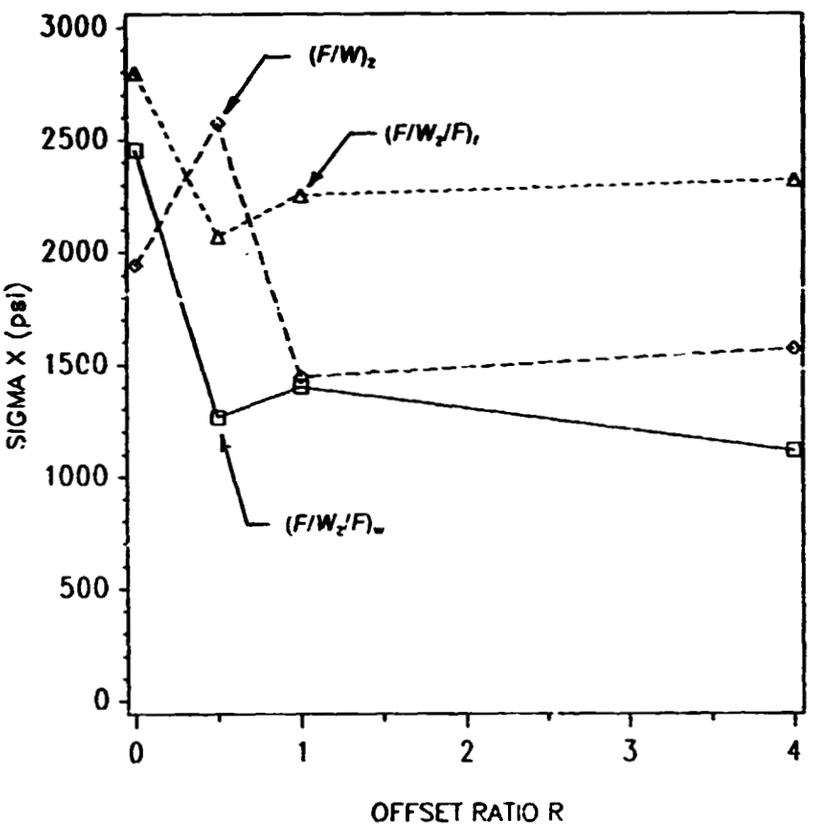

Figure 82. Maximum interfacial σ_x as a function of offset ratio and stacking sequence. $\varepsilon_z = 0.1\%$.

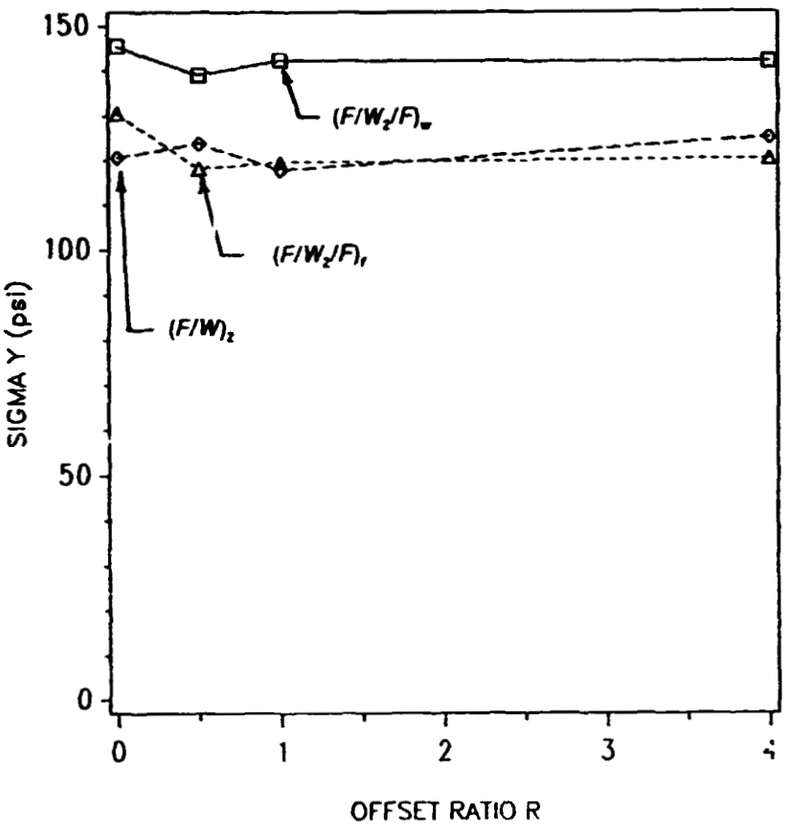

Figure 83. Maximum interfacial σ_y as a function of offset ratio and stacking sequence. $\varepsilon_z = 0.1\%$.

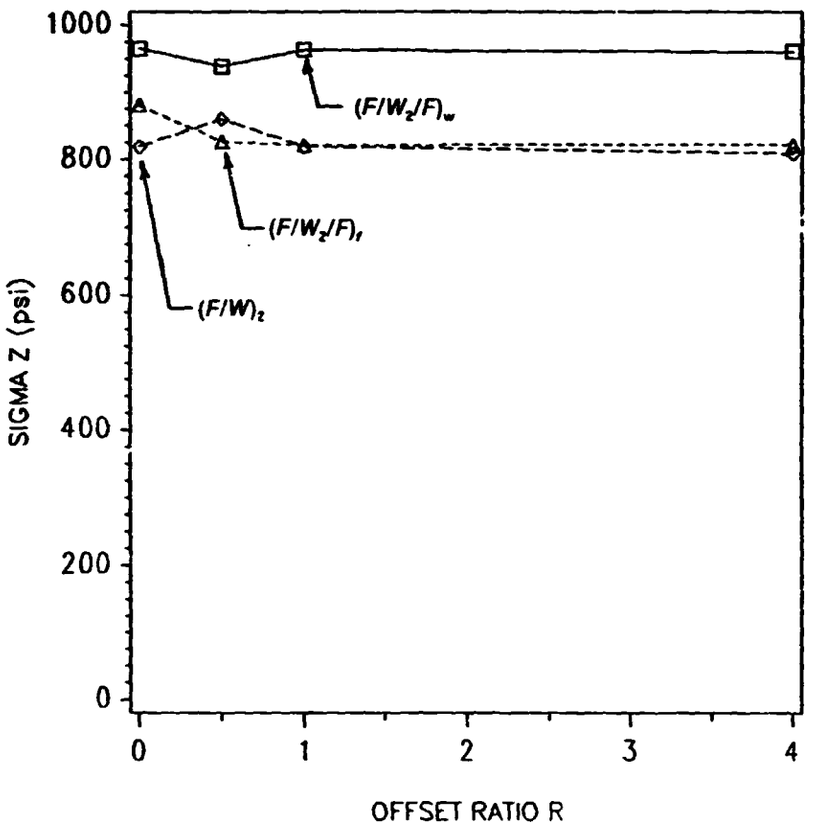

Figure 84. Maximum interfacial σ_z as a function of offset ratio and stacking sequence. $\varepsilon_z = 0.1\%$.

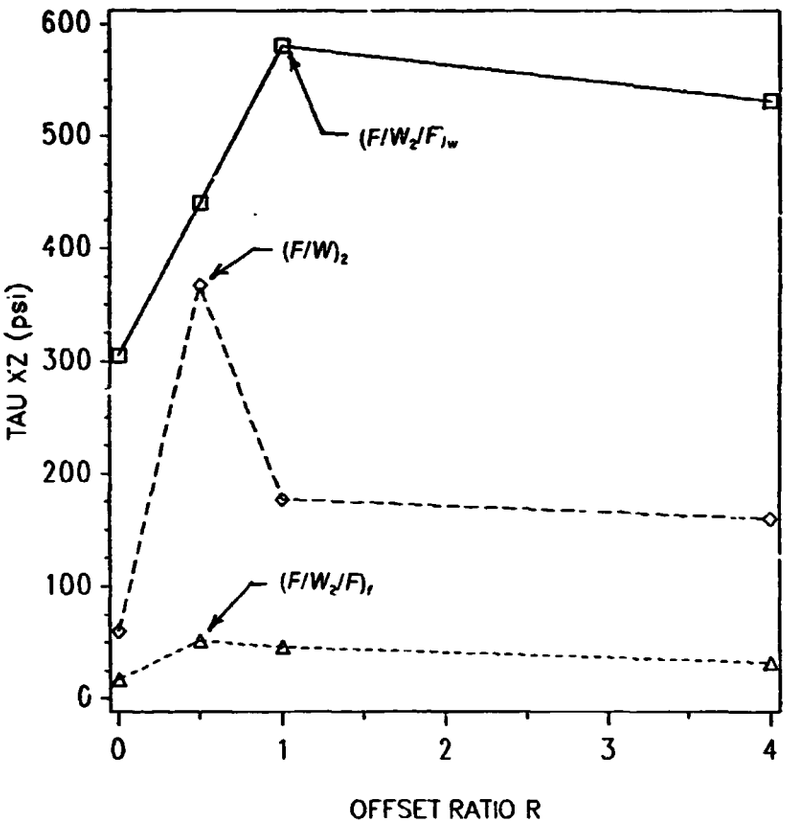

Figure 85. Maximum interfacial τ_{xz} as a function of offset ratio and stacking sequence. $\varepsilon_z = 0.1\%$.

far-field region. In the far-field region the interlaminar stresses σ_z and τ_{xz} are zero and the in-plane normal stresses σ_x and σ_y are essentially those predicted from CLPT. In the region of undulation, however, all components of stress are nonzero and, like the out-of-plane loading case, can be related to the bending of the tows. Under in-plane loading the tendency is for the tows to straighten (Fig. 68). Thus, on the convex side of the tows $\sigma_x < 0$ and on the concave side $\sigma_x > 0$. Additionally, significant σ_z and τ_{xz} are generated due to the orientation of the curved tows in the undulation, which is analogous to an off-axis unidirectional laminate under tensile load.

3.7.3.2 *Interfacial Stresses*

The maximum interfacial stresses as functions of laminate and offset ratio **R** are summarized in Figure 86 through Figure 89.

In-plane Normal Stresses σ_x and σ_y: The in-plane normal stress σ_x (Figure 86) is largest in the $(F/W_2/F)_w$ laminate and smallest in the $(F/W_2/F)_f$ laminate. Also, σ_x is relatively independent of **R** for $\mathbf{R} \geq 0.5$ for all three laminates. The radical difference in σ_x for $\mathbf{R}=0$ is attributed to the degree of symmetry of the laminates. The $(F/W_2/F)_w$ and $(F/W_2/F)_f$ laminates are symmetric about the x y plane. Thus, no bending of the laminate occurs during in-plane loading. For the $(F/W_2/F)_w$ laminate the bending contribution to σ_x , which is tensile, is eliminated. In the $(F/W_2/F)_f$ laminate the curved tows are oriented such that under in-plane load compressive σ_x is exhibited at the interface between the plies. Therefore, for the case $\mathbf{R}=0$, compressive σ_x is eliminated due to symmetry. In the $(F/W)_2$ laminate the tows nest such that the laminate exhibits the lowest axial modulus E_x of those analyzed; consequently, for an applied axial strain ε_x, σ_x is significantly reduced.

The σ_y distribution (Figure 87) shows that for all three laminates, σ_y is relatively independent of $R \geq 1$. For $R < 1$, σ_y follows the trend of σ_x for the $(F/W_2/F)_f$ and $(F/W)_2$ laminates. For the $(F/W_2/F)_w$ laminate, σ_y follows the trend of the σ_z distribution.

Interlaminar Stresses σ_z and τ_{xz}: The variation of the interlaminar stress σ_z, as a function of stacking sequence and offset ratio, is presented in Figure 88. In the $(F/W_2/F)_f$ and $(F/W_2/F)_w$ laminates the maximum σ_z is found at $R=0$. In the $(F/W)_2$ laminate σ_z is minimum at $R=0$. For $R \geq 1$, σ_z is relatively independent of R. It should also be noted that the maximum interfacial σ_z generated by the applied in-plane strain $\varepsilon_x = 0.1\%$ is much greater than σ_z generated by the applied out-of-plane strain $\varepsilon_z = 0.1\%$. Under in-plane loading the maximum σ_z is approximately 5.1 ksi; under out-of-plane loading the maximum σ_z is approximately 0.9 ksi (Figure 84).

The maximum interlaminar shear stress τ_{xz} (Figure 89) is found in the $(F/W_2/F)_f$ laminate. It ranges from approximately 0.4 ksi at $R=0$ to about 6.8 ksi at $R=1$. In the $(F/W_2/F)_w$ laminate τ_{xz} ranges from about 0.2 ksi at $R=0$ to approximately 4 ksi at $R=0.5$. In the $(F/W)_2$ laminate, τ_{xz} ranges from 4 to approximately 5 ksi. As was the case for the other components of stress, τ_{xz} is essentially independent of R for $R \geq 1$.

The magnitudes of the interlaminar shear stresses indicate that the regions of undulations are possible sites for delamination. The interlaminar normal stress, σ_z, which ranges from 2 ksi to 5 ksi for the cases studied, is much larger than the 1 ksi out-of-plane tensile strength reported by Maahs [22]. Additionally, the predicted τ_{xz} is large, ranging from 2 ksi to almost 7 ksi. This is consistent with the results of Wagnecz, who observed delamination at the undulation in an incrementally loaded Celion 3000/PMR-15 graphite/polyimide woven fabric composite [31]

3.7.4 Thermal Loading

The analysis of the $(F/W_2/F)_f$, R = 0.5 laminate under thermal load conditions indicates that significant thermal stresses can be generated during processing and application. The magnitude of the predicted σ_x is on the order of 25 psi/°F. The magnitude of the predicted σ_y is on the order of 10 psi/°F. The interlaminar thermal stresses σ_z and τ_{xz} generated are on the order of 3 psi/°F and 6 psi/°F, respectively.

The possible failure modes associated with thermal loading may differ depending on whether the laminate is undergoing positive ΔT (e.g. an increase from room temperature to application temperature) or negative ΔT (e.g. a decrease from fabrication temperature to room temperature). A positive ΔT will result in the stress distributions exhibited in Figure 80 and Figure 81 such that both the warp and fill tows will be in axial tension ($\sigma_1 > 0$) and transverse compression ($\sigma_2 < 0$). Consequently, the direction of maximum tensile stress will correspond to the direction of maximum strength and the direction of minimum strength will be in compression. Failure, should it occur, would be expected to be due to axial breakage of the tows. The distribution of the interlaminar normal stress σ_z (Figure 81) indicates that under positive ΔT delamination may occur at peaks of the undulations (locations **C** and **E**). The nonzero interlaminar shear stress τ_{xz} can also be expected to contribute to delamination. If the laminate is subjected to negative ΔT the interfacial stress distributions will be of opposite sign to those shown in Figure 80 and Figure 81. Thus, the sign of the in-plane normal stresses will be such that the tows will be in axial compression and transverse tension. This indicates that transverse cracking of the tows can be expected, which is consistant with the observed microstructure of the material used in the out-of-plane tensile tests (Figure 5). In those micrographs the crack density was observed to be approximately 100 cracks/inch. The distribution of the interlaminar normal stress σ_z indicates that σ_z will be tensile at locations **B**, **D**, and **F**. Thus, under negative ΔT delamination could be expected to initiate at those sites.

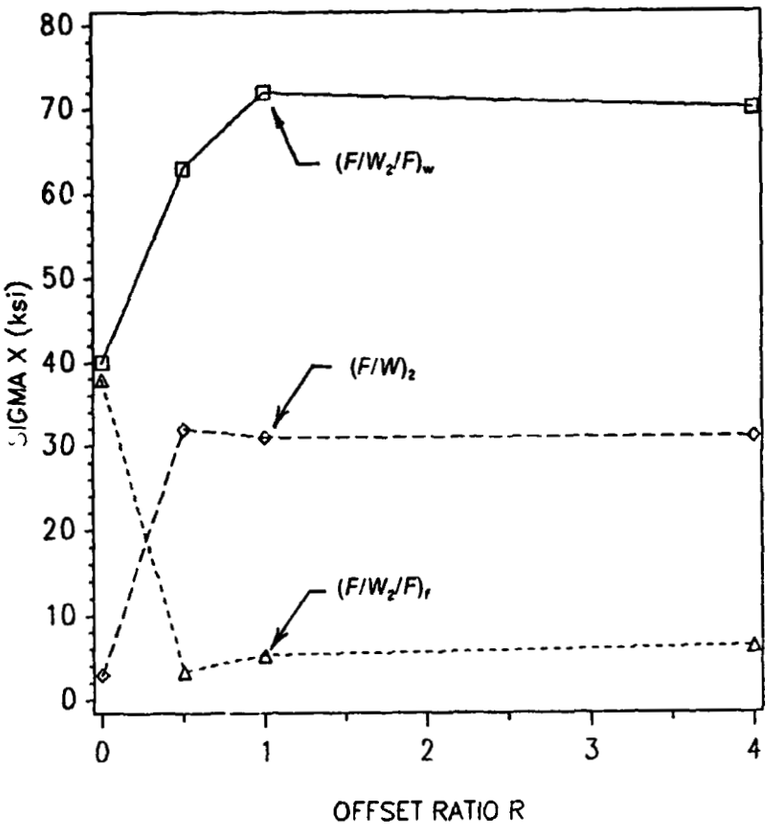

Figure 86. Maximum interfacial σ_x as a function of offset ratio and stacking sequence. $\varepsilon_x = 0.1\%$.

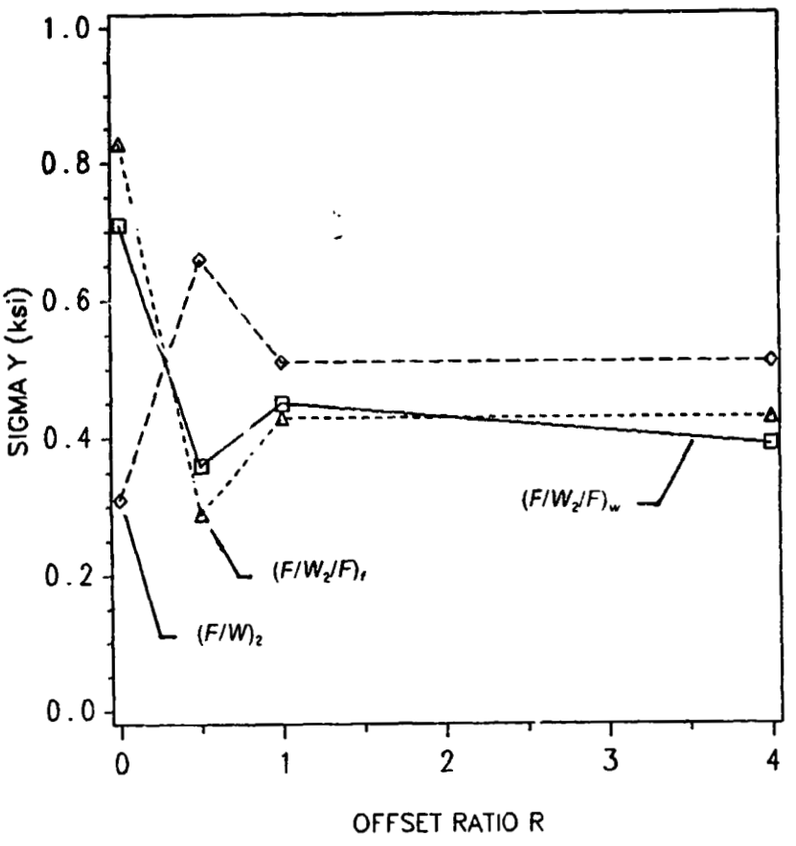

Figure 87. Maximum interfacial σ_y as a function of offset ratio and stacking sequence. $\varepsilon_x = 0.1\%$.

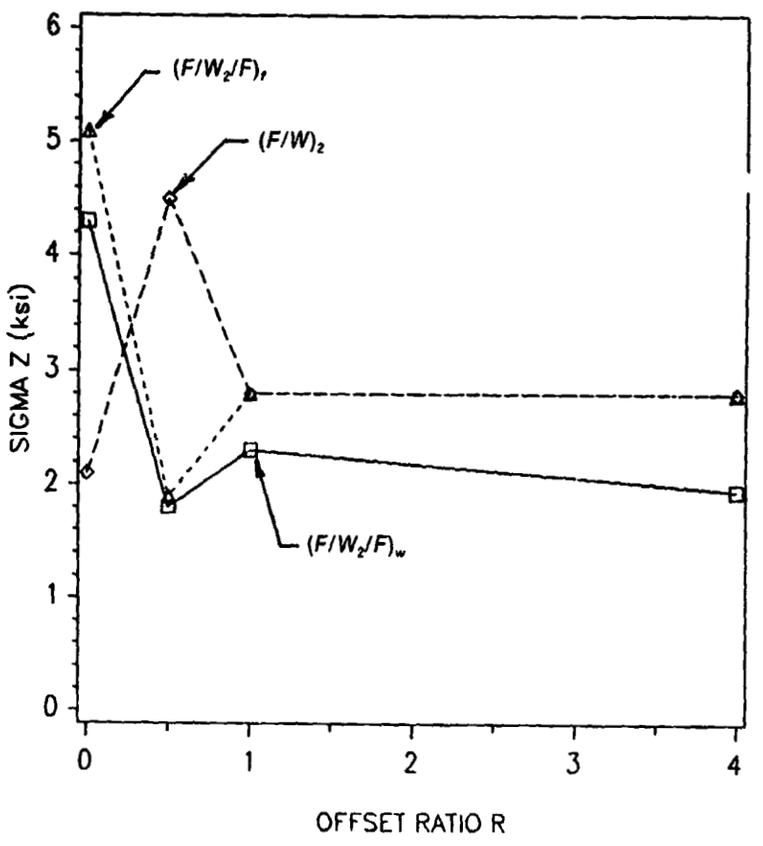

Figure 88. Maximum interfacial σ_z as a function of offset ratio and stacking sequence. $\varepsilon_x = 0.1\%$.

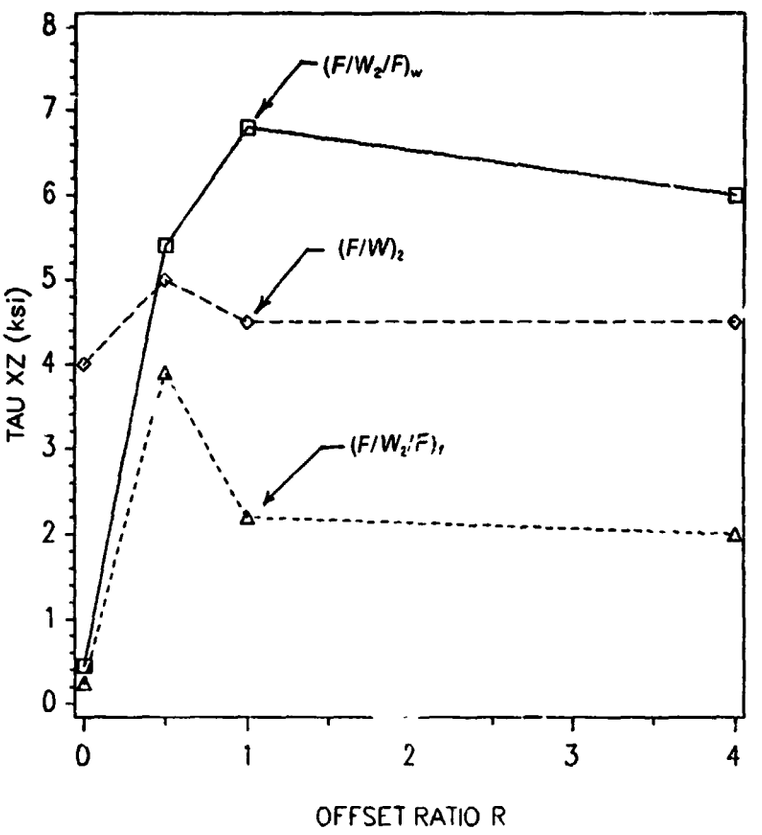

Figure 89. Maximum interfacial τ_{xz} as a function of offset ratio and stacking sequence. $\varepsilon_x = 0.1\%$.

4.0 Effect of Fiber Anisotropy on Thermal Stresses in Fibrous Composites

4.1 Introduction

The extreme thermal environment seen by carbon-carbon composites during fabrication and application requires more careful consideration of the choice of fiber than would be required for graphite-epoxy composites used in room-temperature applications. In most graphite-epoxy composite applications the choice of fiber is based on fiber strength and stiffness in the axial direction. In applications where thermal loads exist the axial coefficient of thermal expansion also becomes important. In carbon-carbon composites, however, high thermal loads and the presence of a brittle matrix suggests that, in addition to axial properties, the transverse fiber properties can significantly influence the stress distribution in the composite and hence greatly influence strength. This chapter addresses the issue of the microstructure of the fiber, its influence on transverse elastic constants, and the resulting variations in thermal stress distributions.

High axial stiffness in graphite fibers is obtained by processing the fiber precursor such that the stiff basal planes of the graphite crystals Figure 90 are oriented nearly parallel to the longitudinal axis of the fiber. [32 33 34 35 36] In the transverse direction, however, the orientation of the basal planes can result in many different microstructures. Examples of four types of microstructures observed in graphite fibers are shown in Figure 91. In Figure 91a the basal planes are arranged circumferentially around the fiber. This structure is commonly called an "onionskin" structure, and it would be expected that $E_z > E_r$. In Figure 91b the basal planes are arranged radially, for which $E_r > E_\theta$. Figures 91c and d show combinations of radial and circumferential microstructures. Figure 91c shows a radially oriented core with an onionskin sheath. Figure 91d shows a random core with a radially oriented sheath. The structures shown in Figure 91a and Figure 91c are normally associated with polyacronitrile-based (PAN) fibers and the structures shown in Figure 91b and Figure 91d are commonly associated with pitch-base fibers. [37 38 39 40 41]

The elasticity formulation used in this paper follows the previous works of St. Venant [42], Voigt [43], Mitinskii [44], Lekhnitskii [45 46], and Cohen et al. [47 48 49] Lekhnitskii provides the form of the solution for a variety of loading conditions on solid and hollow cylinders possessing "cylindrical anisotropy". [45] Cohen and co-workers provided explicit forms of the equations for laminated composite tubes subjected to thermal loading

In this chapter, the anisotropic elasticity solution is used to explore the interrelationship between fiber orthotropy, as exhibited by the transverse microstructures, and the stress distributions in a fiber-matrix composite under uniform thermal load As will be shown, the type of orthotropy radically affects the thermal stress distribution in the fiber In particular, radial orthotropy ($C_{rr} > C_{\theta\theta}$) in the center of the fiber (Figure 91b-c) results in singular stresses at the center of the fiber for all three normal components of stress This has obvious negative consequences for the development of damage in the form of fiber splitting and fiber breakage

The results of this analysis provide helpful insight into the structural integrity of the fiber as a function of microstructure. Such insight may prove helpful in choosing a fiber for a par-

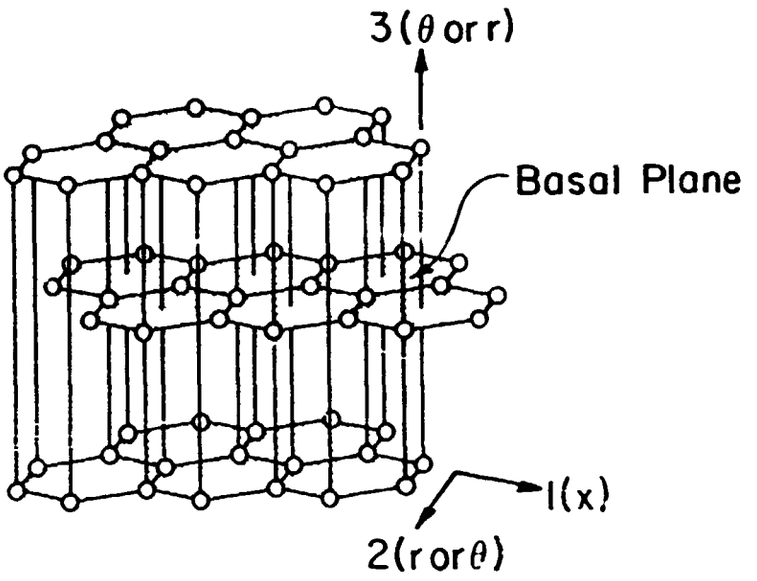

Figure 90. The Graphite Crystal Structure

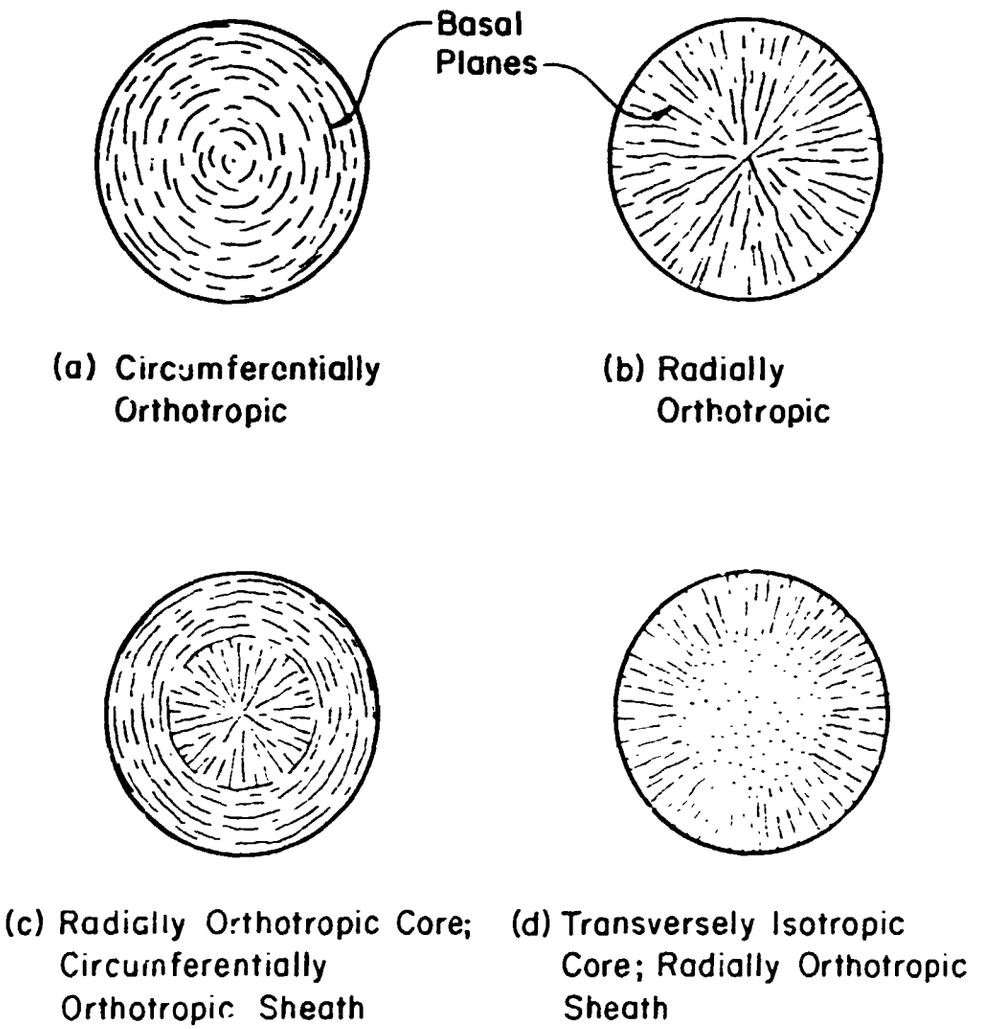

Figure 91. Transverse Microstructures of Graphite Fibers

ticular application, such as in carbon-carbon composites, which are subjected to large thermal loads. In addition, the results may aid in guiding fiber development for improved properties.

4.2 Mathematical Formulation

Consider a long fiber of radius a in an isotropic matrix of thickness $b - a$ under uniform thermal load (Figure 92).

Due to axial symmetry the hoop displacements are zero, stresses and strains are independent of θ, and there is no shear-extension coupling.

Therefore, the thermoelastic stress-strain relations are

$$\begin{Bmatrix} \sigma_x \\ \sigma_\theta \\ \sigma_r \end{Bmatrix} = \begin{bmatrix} C_{xx} & C_{x\theta} & C_{xr} \\ C_{\theta x} & C_{\theta\theta} & C_{\theta r} \\ C_{rx} & C_{r\theta} & C_{rr} \end{bmatrix} \begin{Bmatrix} \varepsilon_x - \alpha_x \Delta T \\ \varepsilon_\theta - \alpha_\theta \Delta T \\ \varepsilon_r - \alpha_r \Delta T \end{Bmatrix} \qquad [4.1]$$

$$\tau_{r\theta} = G_{r\theta}\gamma_{r\theta}; \quad \tau_{xr} = G_{xr}\gamma_{xr}; \quad \tau_{\theta x} = G_{\theta x}\gamma_{\theta x}$$

where C_{ij} are stiffness coefficients and $[C]$ represents the appropriate matrix for the three normal components of stress, α_i are coefficients of thermal expansion, and ΔT is the uniform temperature change. The nonvanishing equilibrium equations for this axisymmetric problem are

$$\frac{\partial \sigma_r}{\partial r} + \frac{1}{r}(\sigma_r - \sigma_\theta) = 0 \qquad [4.2a]$$

$$\frac{\partial \tau_{xr}}{\partial r} + \frac{1}{r}\tau_{xr} = 0 \qquad [4.2b]$$

The strain-displacement relations can be written

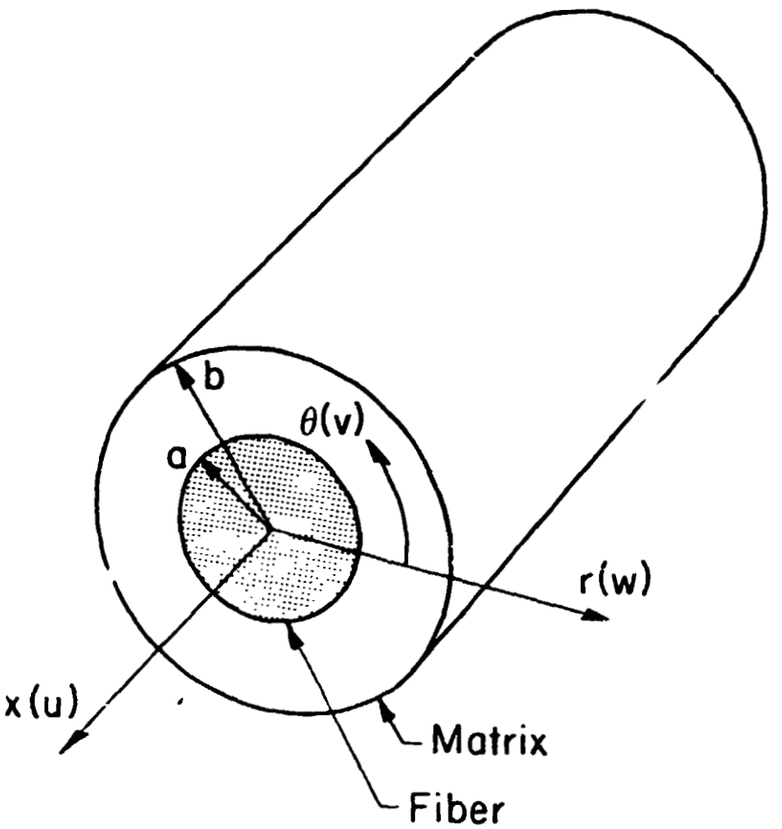

Figure 92. Composite geometry and coordinate system.

$$\varepsilon_r = \frac{\partial w}{\partial r} \qquad [4.3a]$$

$$\varepsilon_\theta = \frac{v}{r} \qquad [4.3b]$$

$$\varepsilon_x = \frac{\partial u}{\partial x} \qquad [4.3c]$$

$$\gamma_{r\theta} = 0 \qquad [4.3d]$$

$$\gamma_{xr} = \frac{\partial u}{\partial r} \qquad [4.3e]$$

$$\gamma_{\theta x} = 0 \qquad [4.3f]$$

where u, v, and w are axial, hoop, and radial displacements, respectively.

Substituting Eqns. 4.3a-f into Eqn. 4.1 and substituting the resulting equations into the equilibrium equation 4.2a yields the governing differential equation

$$C_{rr}\left[\frac{\partial^2 w}{\partial r^2} + \frac{1}{r}\frac{\partial w}{\partial r}\right] - C_{\theta\theta}\frac{w}{r^2} = \frac{1}{r}(C_{\theta x} - C_{rx})\varepsilon_x + \frac{1}{r}(C_{rj} - C_{\theta j})\alpha_j \Delta T \qquad [4.4]$$

for generalized plane strain with uniform axial strain ε_x. Here and throughout the paper repeated subscripts i,j are summed over x, r, and θ. Equation 4 may be solved for the case of applied thermal load or the case of applied axial strain.

The general solutions to Eqn. 4 following Cohen and Hyer's[48] treatment of an orthotropic tube under uniform thermal load are:

a. transversely orthotropic fiber ($C_{\theta\theta} \neq C_{rr}$),

$$w(r) = A_1 r^{\lambda_1} + A_2 r^{\lambda_2} + H_1 \varepsilon_x r + H_2 \Delta T r \qquad [4.5a]$$

where

$$H_1 = \frac{C_{\theta x} - C_{rx}}{C_{rr} - C_{\theta\theta}} \qquad [4.5b]$$

$$H_2 = \frac{(C_{ri} - C_{\theta i})\alpha_i}{(C_{rr} - C_{\theta\theta})} \qquad [4.5c]$$

b. transversely isotropic fiber ($C_{\theta\theta} = C_{rr}$),

$$w(r) = A_1 r^{\lambda_1} + A_2 r^{\lambda_2} + G_1 \varepsilon_x r \ln r + G_2 \Delta T r \ln r \qquad [4.6a]$$

where

$$G_1 = \frac{C_{\theta x} - C_{rx}}{2C_{\theta\theta}} \qquad [4.6b]$$

$$G_2 = \frac{(C_{ri} - C_{\theta i})\alpha_i}{2C_{\theta\theta}} \qquad [4.6c]$$

In both of the above displacement fields (4.5a and 4.6a), $\lambda_{1,2}$ are defined

$$\lambda_{1,2} = \pm \left[\frac{C_{\theta\theta}}{C_{rr}}\right]^{0.5} \qquad [4.7]$$

The solution of the second equilibrium equation (4.2b) is

$$\tau_{xr} = \frac{K}{r} \qquad [4.8]$$

where K is a constant of integration determined from the boundary condition on τ_{xr} at $r = b$

For a composite with an orthotropic fiber and an isotropic matrix the equations for the radial displacements are

$$w^f(r) = A_1^f r^{\lambda_1^f} + A_2^f r^{\lambda_2^f} + H_1^f \varepsilon_x r + H_2^f \Delta T r \qquad [4.9a]$$

$$w^m(r) = A_1^m r + A_2^m \frac{1}{r} \qquad [4.9b]$$

where the superscripts f and m refer to the fiber and matrix, respectively, $\lambda_{1,2}^m = \pm 1$, and $G_1^m = G_2^m = 0$ for a material which is transversely isotropic in both elastic and thermal constants.

The equations for the normal components of stress, for the fiber and matrix, can be obtained by substituting Eqns. 4.5-4.6 into Eqns. 4.3a-b and then substituting the results into the constitutive relations (Eqn. 4.1). The resulting equations are:

a. transversely isotropic fiber ($C_{rr}^f = C_{\theta\theta}^f$, $\lambda_{1,2} = \pm 1$),

$$\sigma_i^f = A_1^f\left(C_{i\theta}^f + C_{ir}^f\right) + A_2^f\left(C_{i\theta}^f - C_{ir}^f\right)\frac{1}{r^2} + C_{ix}^f\varepsilon_x - C_{ij}^f\alpha_j^f\Delta T \qquad [4.10a]$$

b. transversely orthotropic fiber ($C_{rr}^f \neq C_{\theta\theta}^f$),

$$\sigma_i^f = A_1^f\left(C_{i\theta}^f + C_{ir}^f\lambda_1^f\right)r^{\lambda_1 - 1} + A_2^f\left(C_{i\theta}^f + C_{ir}^f\lambda_2^f\right)r^{\lambda_2 - 1} + L_i^f\varepsilon_x + N_i^f\Delta T \quad [4.10b]$$

where

$$L_i^f = C_{ix}^f + H_1^f\left(C_{i\theta}^f + C_{ir}^f\right)$$

$$N_i^f = H_2^f\left(C_{i\theta}^f + C_{ir}^f\right) - C_{ij}^f\alpha_j^f$$

c. isotropic matrix,

$$\sigma_i^m = A_1^m\left(C_{i\theta}^m + C_{ir}^m\right) + A_2^m\left(C_{i\theta}^m - C_{ir}^m\right)\frac{1}{r^2} + C_{ix}^m\varepsilon_x - C_{ij}^m\alpha_j^m\Delta T \qquad [4.10c]$$

The five constants A_1^f, A_2^f, A_1^m, A_2^m, and ε_x, are determined from the following five conditions.

1. The radial displacement w must be zero at $r = 0$. This condition, plus the fact that $\lambda_2^f < 0$ (Eqn. 4.7), requires A_2^f be zero to avoid a singularity in w at $r = 0$ for both transversely orthotropic and transversely isotropic fibers (Eqn. 5.5 and 5.6).

2. Continuity of w at the fiber-matrix interface $w^f(a) = w^m(a)$ requires that:

   a. for a transversely orthotropic fiber ($C_{rr}^f \neq C_{\theta\theta}^f$),

$$A_1^f a^{\lambda_1^f} + a\left(H_1^f \varepsilon_x + H_2^f \Delta T\right) = A_1^m a + A_2^m \frac{1}{a} \qquad [4.11a]$$

   b. for a transversely isotropic fiber ($C_{rr}^f = C_{\theta\theta}^f$)

$$A_1^f a = A_1^m a + A_2^m \frac{1}{a} \qquad [4.11b]$$

3. Continuity of the radial stress σ_r at the fiber matrix interface, $\sigma_r^f(a) = \sigma_r^m(a)$ requires that:

   a. for a transversely orthotropic fiber

$$A_1^f\left(C_{r\theta}^f + C_{rr}^f \lambda_1^f\right) a^{\lambda_1^f - 1} + L_j^f \varepsilon_x + N_j^f \Delta t$$

$$= A_1^m\left(C_{r\theta}^m + C_{rr}^m\right) + A_2^m\left(C_{r\theta}^m - C_{rr}^m\right)\frac{1}{a^2} - C_{rj}^m \alpha_j^m \Delta T + C_{rx}^m \varepsilon_x \qquad [4.12a]$$

   or

   b. for a transversely isotropic fiber

$$A_1^f\left(C_{r\theta}^f + C_{rr}^f\right) + C_{rx}^f \varepsilon_x - C_{rj}^f \alpha_j^f \Delta T +$$

$$= A_1^m\left(C_{r\theta}^m + C_{rr}^m\right) + A_2^m\left(C_{r\theta}^m - C_{rr}^m\right)\frac{1}{a^2} + C_{rx}^m \varepsilon_x - C_{rj}^m \alpha_j^m \Delta T \qquad [4.12b]$$

4. Since there are no tractions applied at the outer boundary of the matrix $\sigma_r(b)$ and $\tau_{xr}(b)$ equal zero. the condition on σ_r requires that

$$A_1^m(C_{r\theta}^m + C_{rr}^m) + A_2^m \frac{1}{b^2}(C_{r\theta}^m - C_{rr}^m) + C_{rx}^m \varepsilon_x - C_{rj}^m \alpha_j^m \Delta T = 0 \qquad [4.13]$$

The traction free condition on τ_{xr} requires that K in Eqn. 4.8 equal zero. Thus, there are no shear stresses in the fiber or matrix.

5. The final condition for the case of pure thermal loading is that the net axial force P on the fiber-matrix composite be zero. This is expressed mathematically as

$$P = 2\pi \int_0^b \sigma_x r dr = 0 \qquad [4.14]$$

and for a transversely orthotropic fiber results in the condition

$$A_1^f\left(C_{x\theta}^f + C_{xr}^f \lambda_1^f\right)\frac{a^{\lambda_1^f + 1}}{\lambda_1^f + 1} + A_1^m(C_{xr}^m)(b^2 - a^2) + \frac{1}{2}[C_{xx}^m(b^2 - a^2) + L_x^f a^2]\varepsilon_x + \frac{1}{2}[N_x^f a^2 - C_{xj}^m \alpha_j^m (b^2 - a^2)]\Delta T = 0 \qquad [4.15a]$$

For a transversely isotropic fiber ($C_{rr}^f = C_{\theta\theta}^f$), the form of Eqn. 4.14 is:

$$A_1^f \frac{1}{2}\left(C_{x\theta}^f + C_{xr}^f\right)a^2 + A_1^m C_{xr}^m (b^2 - a^2) + \frac{1}{2}\left[C_{xx}^m(b^2 - a^2) + C_{xx}^f a^2\right]\varepsilon_x - \frac{1}{2}\left[C_{xj}^f \alpha_j^f a^2 + C_{xj}^m \alpha_j^m (b^2 - a^2)\right]\Delta T = 0 \qquad [4.15b]$$

The constants A_1^f, A_1^m, A_2^m, and ε_x are obtained by solving Eqns. 4.11-4.13 and 4.15 simultaneously. It is noted that the axial loading case can be considered for a given axial strain ε_x or a given axial force P. In addition, the radial loading case may also be considered by appropriate modification of Eqn. 4.13.

4.3 Results and Discussion

Thermal stress distributions were determined for three types of fiber properties: (1) transversely isotropic ($C_{rr} = C_{\theta\theta}$); (2) circumferentially orthotropic ($C_{rr} < C_{\theta\theta}$); (3) radially orthotropic ($C_{rr} > C_{\theta\theta}$). The matrix was considered to be isotropic. The fiber and matrix properties used for the calculations are given in Table 10. A uniform temperature increase of 1°C was used for loading. Results for a fiber volume fraction $V_f = 0.623$ are presented in Figs. 93-95 and results for variable V_f are presented in Figs. 96-98.

Transversely Isotropic Fiber ($C_{rr} = C_{\theta\theta}$)

The stress distributions for the case of a transversely isotropic fiber (Fig. 93) exhibit a uniform positive axial stress and uniform compressive hoop and radial stresses in the fiber. These distributions can be explained by examining the equation of the stress distribution in a transversely isotropic fiber (Eqn. 4.10a). Recalling that $A_2^f = 0$ in order to eliminate singular w displacements at $r = 0$ allows Eqn. 4.10a to be restated as

$$\sigma_i^f = A_1^f\left(C_{i\theta}^f + C_{ir}^f\right) + C_{ix}^f\varepsilon_x - C_{i,}^f\alpha_j^f\Delta T \qquad [4.16]$$

It is evident from Eqn. 4.16 that the fiber stresses are independent of radial coordinate. The stress distributions in the matrix are described by Eqn 4.10c. A relatively large, positive hoop stress is present in the matrix. The hoop stress attains a maximum at the fiber-matrix interface (Fig. 93). The decay in the magnitude of the radial and hoop matrix stresses with radial coordinate can be explained by examining the A_2^m term in Eqn. 4.10c. The stresses decay as a function of $1/r^2$. The axial stress is constant in the matrix because $C_{i\theta}^m = C_{ir}^m$ when $i = x$. Thus the A_2^m term in Eqn. 4.10c is zero and there is no axial stress dependence on the radial coordinate. For these stress distributions, fiber failure (if present) is expected to be an axial tensile fracture

Table 10. Fiber and matrix properties

	Radially Orthotropic Fiber	Circumferentially Orthotropic Fiber	Transversely Isotropic Fiber	Matrix
E_x MSI(GPa)	32(220)	32(220)	32(220)	5(34.5)
E_θ MSI(GPa)	4(27.5)	32(220)	4(27.5)	5(34.5)
E_r MSI(GPa)	32(220)	4(27.5)	4(27.5)	5(34.5)
$\nu_{x\theta}$	.20	.20	.20	.12
ν_{xr}	.25	.25	.20	.12
$\nu_{\theta r}$	.025	.25	.25	.12
$\alpha_x(10^{-6}°C)$	0.28	0.28	0.28	1.11
$\alpha_\theta(10^{-6}°C)$	5.56	0.28	5.56	1.11
$\alpha_r(10^{-6}°C)$	0.28	5.56	5.56	1.11

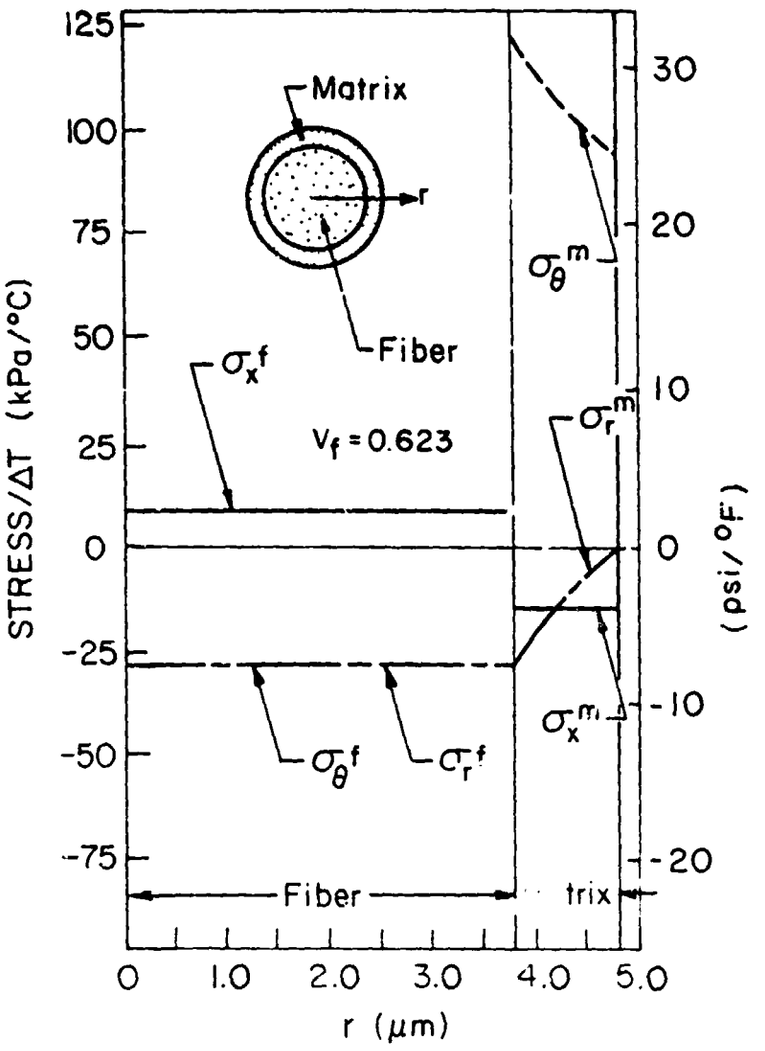

Figure 93. Thermal stress distribution in a composite with a transversely orthotropic fiber.

Radially Orthotropic Fiber ($C_{rr} > C_{\theta\theta}$)

Figure 94 shows the thermal stress distributions for the case of a fiber with radial orthotropy. All three components of stress are positive and singular at the center of the fiber. These distributions can be explained by examining Eqn. 4.10b. For radial orthotropy $C_{rr} > C_{\theta\theta}$ and λ_1^f is less than unity. Defining $\delta = (1 - \lambda_1^f)$, and recalling once again that $A_2^f = 0$, Eqn. 4.10b can be written

$$\sigma_i^f = A_1^f\left(C_{i\theta}^f + C_{ir}^f\lambda_1^f\right)\frac{1}{r^\delta} + L_i^f\varepsilon_x + N_i^f\Delta T \qquad [4.17]$$

For the example problem considered here $\lambda_1^f = 0.343$ and $\delta = 0.657$. Therefore, a stress singularity of order δ exists at $r = 0$ for $\lambda_1^f < 1.0$. It should be noted that δ is a function only of the fiber properties C_{rr}^f and $C_{\theta\theta}^f$. The term $A_1^f(C_{i\theta}^f + C_{ir}^f\lambda_1^f)$, which defines the strength of the singularity, is a function of fiber and matrix properties, fiber volume fraction, and boundary conditions.

A similar singularity was shown by Lekhnitskii to exist in an anisotropic disk under radial compression.[45] Lekhnitskii also notes that for the limiting case $r = 0$ there is no difference in material properties between the r and θ directions; therefore, the fiber must be transversely isotropic at $r = 0$. Such a condition precludes the existence of a mathematical singularity at the center of the fiber. (This point is also mentioned in a later paper by Olson and Bert.)[50] However, the singular nature of the stress distributions as r approaches zero remains valid for the actual case.

The potential failure mode of the fiber can be addressed by examining the relationship between the orientation of the graphite crystals in the fiber and the mechanical properties of a graphite crystal. For a radially orthotropic fiber, the basal planes of the graphite crystals Figure 90, which exhibit maximum strength are oriented parallel to the radial and axial directions [36] Thus, the direction of minimum strength is in the hoop direction. Therefore, fiber splitting due to σ_θ is a potential failure mode for a radially orthotropic fiber which exhibits singular hoop stresses.

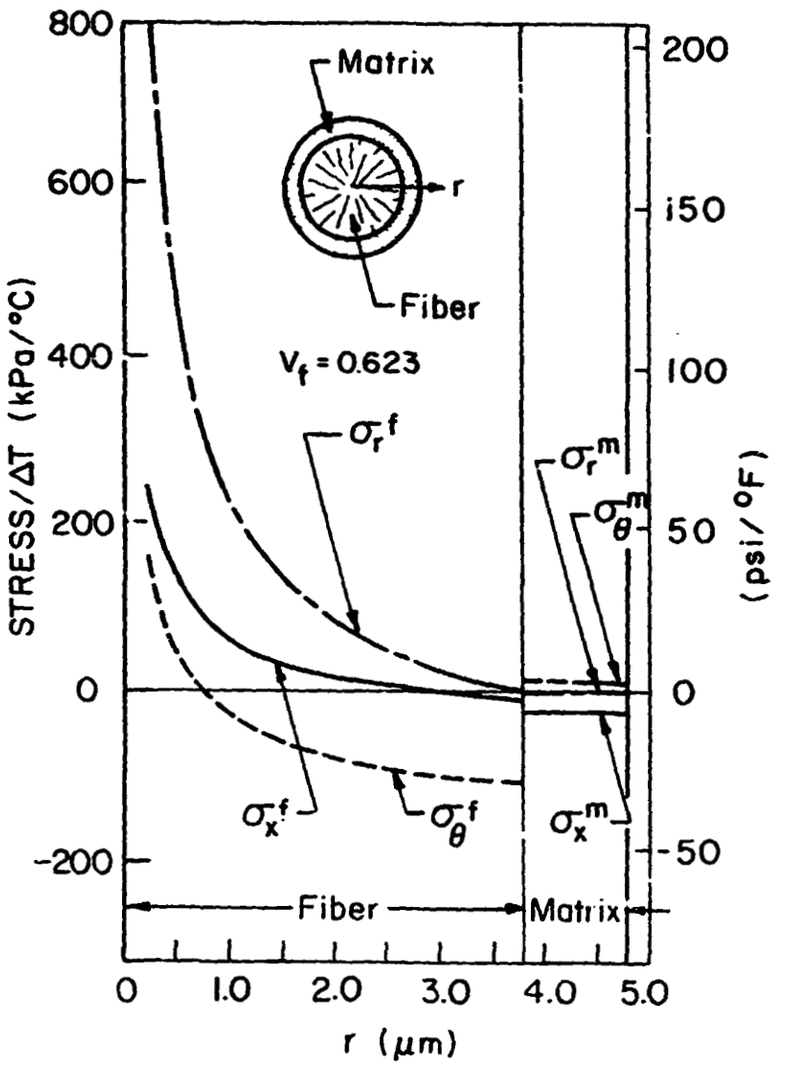

Figure 94. Thermal stress distribution in a composite with a radially orthotropic fiber.

Circumferentially Orthotropic Fiber ($C_{\theta\theta} > C_{rr}$)

Stress distributions for circumferentially orthotropic fibers are shown in Figure 95. The stresses in the fiber are governed by the reduced form of Eqn. 4.10b, which is now written in the form

$$\sigma_i^f = A_1^f\left(C_{i\theta}^f + C_{ir}^f\lambda_1^f\right)r^{\lambda_1^f - 1} + L_i^f\varepsilon_x + N_i^f\Delta T \qquad [4.18]$$

and it is noted that $\lambda_1^f - 1 > 0$. Comparison of the stress distributions in Figure 94and Figure 95 (or comparison of equations 4.17 and 4.18) shows that the distributions in fibers with circumferential orthotropy (Figure 95) are completely different from those in radially orthotropic fibers (Figure 94). The distribution of axial and hoop stresses in circumferentially orthotropic fibers varies uniformly from compression along the centerline ($r = 0$) to tension at the fiber-matrix interface. The radial stress is compressive throughout the fiber. For this case $\lambda_1^f = 2.876$; therefore, Eqn. 4.18 reveals that the stresses have a power function distribution. The matrix exhibits compressive radial and axial stresses, but positive hoop stresses. All matrix stresses are relatively small in magnitude.

In the circumferentially orthotropic fiber, the basal planes are oriented parallel to the axial and circumferential directions. Thus, the directions of maximum fiber strength are expected to be in the axial and hoop directions with minimum fiber strength in the radial direction. Therefore, the maximum tensile stresses are in the directions of maximum strength. The direction of minimum strength is under compression throughout the fiber. For this type of fiber orthotropy, failure, should it occur, would be expected to be via fiber splitting at the fiber-matrix interface. It is interesting to note that under a uniform temperature decrease the signs of the stresses will change, resulting in a positive radial stress. In this case the maximum tensile stress will be in the direction of minimum strength. Therefore, the fiber may be more likely to fail during a cooling cycle than a heating cycle.

It is noted that the solution presented here for a fiber in an isotropic matrix is quite different than that of Chen & Diefendorf for a single fiber.[51]

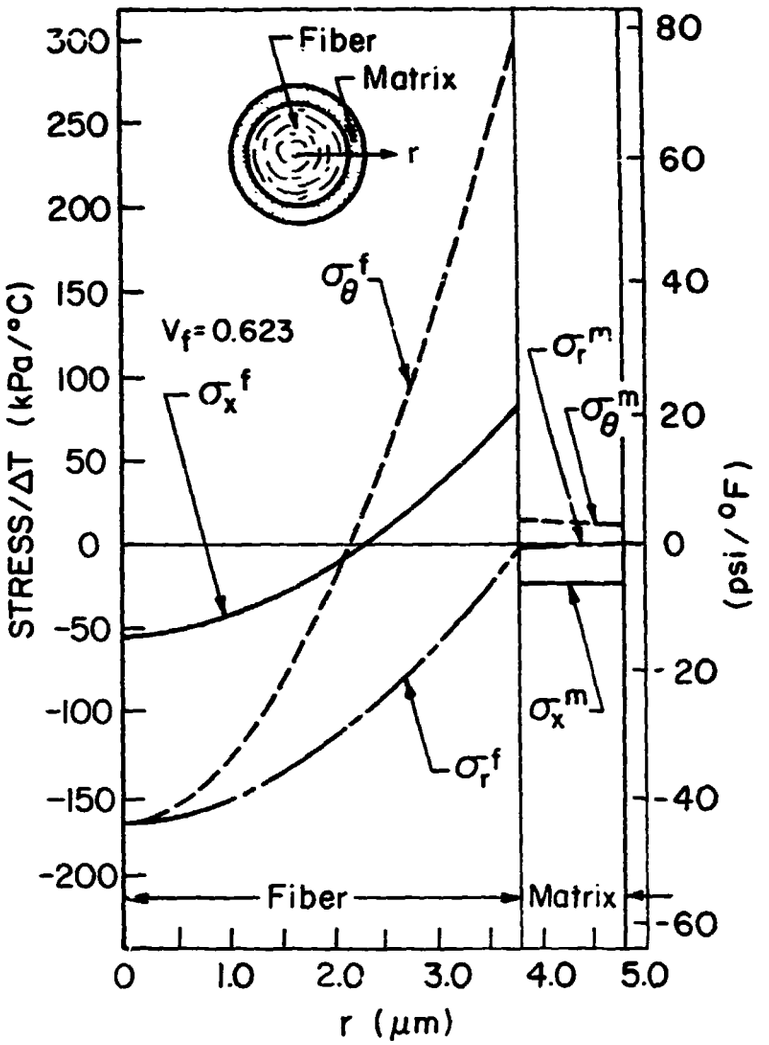

Figure 95. Thermal stress distribution in a composite with a circumferentially orthotropic fiber.

Influence of Fiber Volume Fraction

The influence of fiber volume fraction on the distribution of thermal stresses is demonstrated in Figure 96 through Figure 98. Figure 96 shows the results for a transversely isotropic fiber, Figure 97 for a fiber with radial orthotropy, and Figure 98 a fiber with circumferential orthotropy. The fiber volume fraction was varied by changing the thickness of the matrix layer surrounding the fiber and holding the fiber radius constant. results are presented for fiber volume fractions in the range 0.391-1.0.

These figures show that the axial component of stress is a function of fiber volume fraction for all three types of fiber microstructure. This is a direct consequence of the equilibrium requirement of zero axial force for pure thermal loading. Equilibrium must always be satisfied regardless of material properties. A somewhat surprising result is the fact that the distributions of radial and hoop stresses are essentially independent of fiber volume fraction for both types of transversely orthotropic fibers considered (Figure 97b-c and Figure 98b-c), but the distributions of these two stress components varies considerably with fiber volume fraction for the case of a transversely isotropic fiber. These results can be explained by considering the equations for the stress distributions in each type of fiber (Eqns. 4.16-4.18).

In the transversely orthotropic fibers, A_1^f is relatively independent of volume fraction, differing by less than 4 percent in the volume fraction range 0.391-1.0. In contrast, ε_x differs by more than 30 percent in the same volume fraction range. Detailed examination of the equations shows that the hoop and radial stresses are a strong function of the term containing A_1^f and a weak function of the term containing ε_x since $(C_{i\theta}^f + \lambda_1^f C_{ir}^f)$ is large and L_i is small for $i = r$ or θ. Thus, it can be concluded that in transversely orthotropic fibers the hoop and radial stresses are relatively independent of fiber volume fraction. The axial stresses in the transversely orthotropic fibers, however, show a greater dependence on fiber volume fraction. In this case $(C_{x\theta}^f + \lambda_1^f C_{xr}^f)$ is smaller and L_x is more than two orders of magnitude greater than the corresponding terms mentioned above. Consequently, the axial stresses are a stronger function of fiber volume fraction through the term associated with axial strain. In transversely isotropic fibers, however, both A_1^f and ε_x are strong functions of fiber volume fraction. A_1^f and

ε_x vary by approximately 23 and 40 percent, respectively, in the fiber volume fraction range 0.391 - 1.0. Thus, all stresses will be greatly influenced by fiber volume fraction.

An equally surprising result is that the stresses in transversely orthotropic fibers are non-zero for a fiber volume fraction of 1.0, which corresponds to a fiber with no matrix surrounding it. The physical explanation is that as the fiber expands radially it also expands in the hoop direction; however, if there is a mismatch in the thermal expansion coefficients in the radial and hoop directions the expansion in the hoop direction can't compensate for the radial expansion. Thus, an internal constraint exists which gives rise to internal stresses. It should be noted that the presence of non-zero stresses in a single fiber is a function of the mismatch in radial and hoop thermal expansion coefficients only and not a function of material stiffness coefficients.

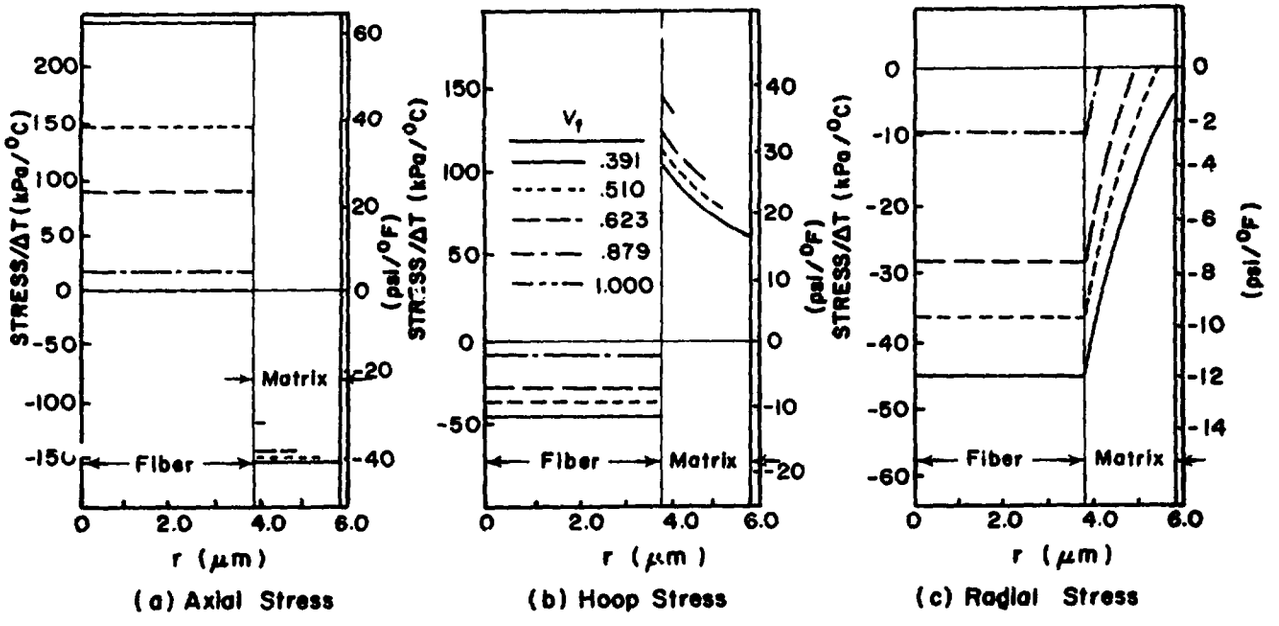

Figure 96. Effect of volume fraction on thermal stress distributions in a composite with a transversely isotropic fiber.

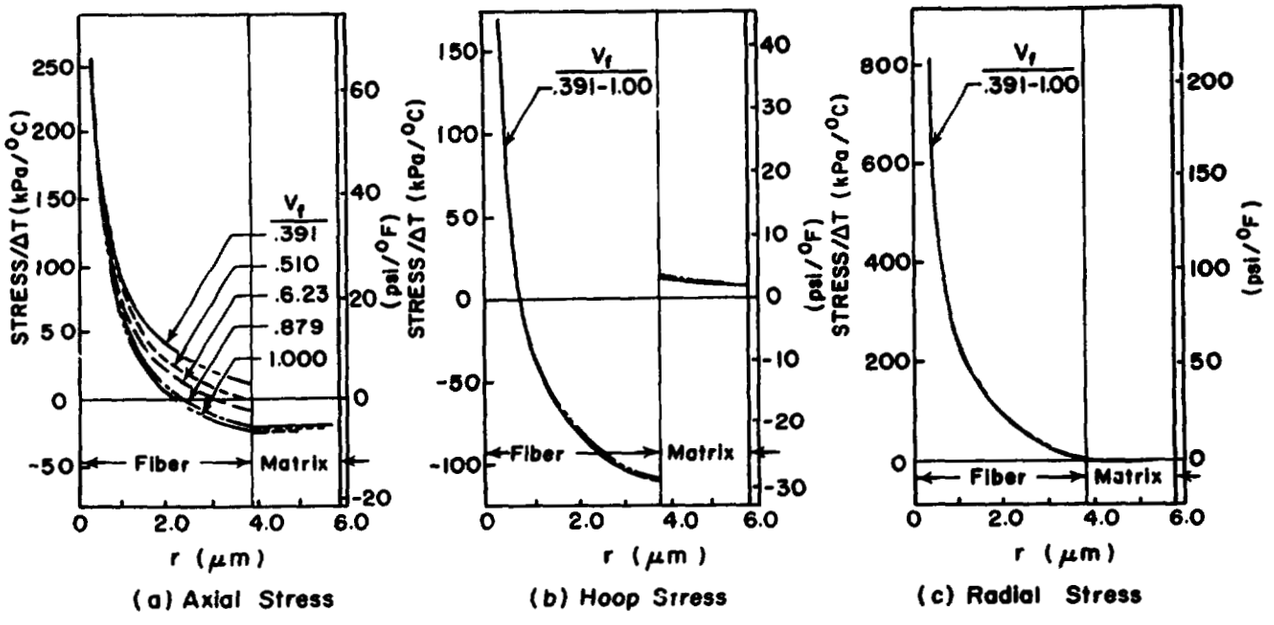

Figure 97. Effect of volume fraction on thermal stress distributions in a composite with a radially orthotropic fiber.

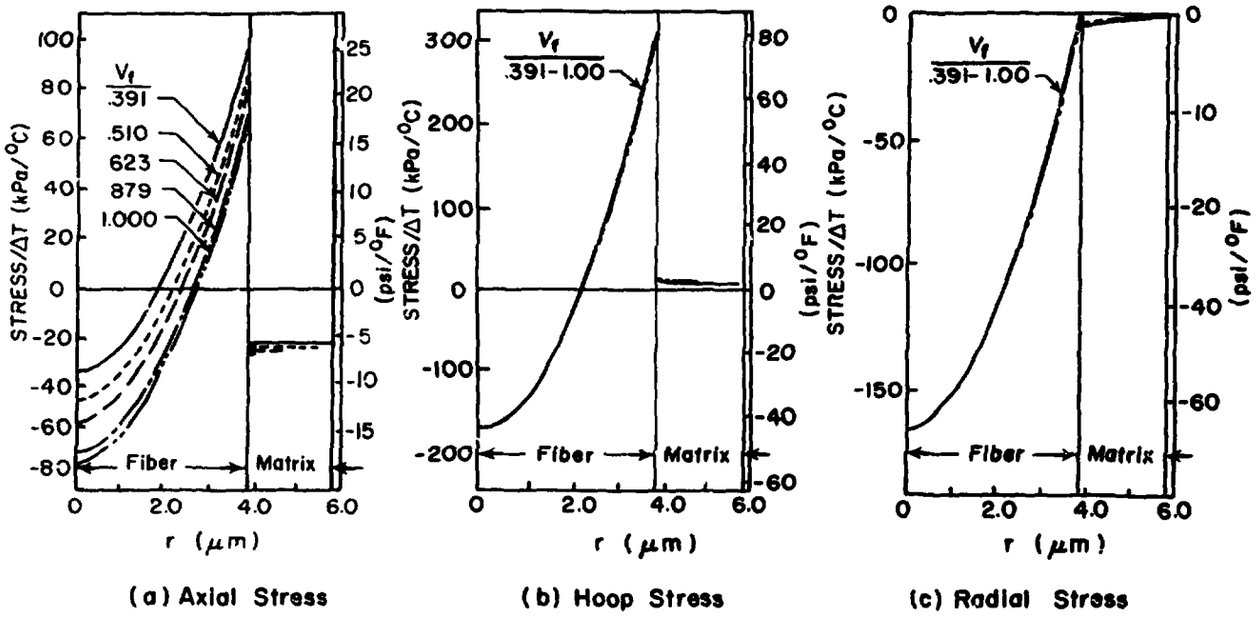

Figure 98. Effect of volume fraction on thermal stress distributions in a composite with a circumferentially orthotropic fiber.

5.0 Conclusions

A carbon-carbon composite manufactured from an 8-harness satin woven graphite cloth and a phenolic resin precursor was investigated both experimentally and numerically. The experimental portion of the study consisted of performing an out-of-plane tensile test in a scanning electron microscope and videotaping crack propagation. Additional scanning electron microscope studies were performed in order to determine the failure modes. The numerical portion of this study consisted of developing a finite element model and performing analyses on a two-layer woven fabric laminate for in-plane, out-of-plane, and thermal loading in order to characterize stress states in the laminate as a function of geometric parameters. Additionally, an elasticity solution was presented which investigates the influence of fiber anisotropy on thermal stress distributions in composites. A summary of the results of these studies are presented below.

5.1.1.1 Experimental

1. Failure due to out-of-plane loading was interlaminar, occurring at the interface between adjacent plies.

2. Cracks propagated between the fiber-matrix interface. The cleanliness of fiber surfaces subsequent to failure indicated low fiber-matrix bond strength.

5.1.1.2 Finite Element Analyses

Out-of-Plane Loading

1. The interlaminar normal stress σ_z is the dominant stress, and is relatively independent of stacking sequence, axial coordinate, undulation offset ratio, and undulation aspect ratio.

2. The interfacial σ_x and τ_{xz} components of stress are strong functions of stacking sequence and undulation aspect ratio. Additionally, σ_x and τ_{xz} are strong functions of the undulation offset ratio **R** for $R < 1$, but relatively independent of **R** for $R \geq 1$. The interfacial σ_y is relatively independent of geometric parameters.

3. The best approach to increasing the out-of-plane tensile strength of a 2-D carbon-carbon laminate is to increase the fiber-matrix bond strength This is based on the following factors: (1) experimental observation of failure revealed that failure occurred between adjacent plies and that cracks propagated along the fiber-matrix interface; (2) finite element analyses indicates that the stress state between adjacent plies is relatively independent of material geometry.

In-Plane Loading

1. Large interlaminar stresses are predicted in the region of undulation. This may explain the delamination observed in woven fabric graphite/polyimide composite by Wagnecz [31].

2. A high in-plane normal stress σ_x, up to 170% of the far-field value, is predicted for the region of undulation, and is due to the bending of the tows.

3. The presence of undulations reduces the in-plane modulus E_x 6-18 percent from that of a comparable $(0/90)_s$ laminate.

4. The in-plane modulus E_x is essentially independent of **R** for $\mathbf{R} \geq 0.5$.

5. The predicted values of E_x and E_y in the $(F/W_2/F)$ laminate differ by approximately 10 percent.

6. All components of stress are affected by stacking sequence and undulation aspect ratio Ω. The predicted values tend towards CLPT as the undulation aspect ratio increases.

7. All components of stress are relatively independent of undulation offset ratio **R** for $\mathbf{R} \geq 1$.

Thermal Loading

1. Large in-plane normal stresses are predicted throughout the laminate for thermal loading. The maximum predicted values of σ_x and σ_y are 25 psi/°F and 10 psi/°F, respectively.

2. Interlaminar stresses (σ_z and τ_{xz}) on the order of 3-6 psi/°F are predicted for the region of undulation

Finite Element With Variable Material Properties

1. A finite element has been developed which allows the material properties to vary with element curvature. This allows curved domains to be modeled without mismatches in material properties at element boundaries and hence reduces the number of elements required to obtain an accurate solution.

5.1.1.3 *Effect of Fiber Anisotropy on Thermal Stresses*

1. The distribution of thermal stresses in a fiber reinforced composite material is affected significantly by the microstructure of the fiber.

   a. If the fiber exhibits radial orthotropy, the distributions of all three components of normal stress exhibit a singularity of type $r^{-\delta}$, where the order of the singularity is a function of the radial and circumferential stiffness coefficients of the fiber.

   b. For circumferentially and transversely orthotropic fibers there is no singularity in the stresses.

2. Fiber volume fraction has essentially no influence on the radial and hoop stresses in orthotropic fibers. The axial stresses in orthotropic fibers and all three components of normal stress in transversely isotropic fibers are a function of fiber volume fraction.

3. Single fibers exhibit non-zero stresses when there is a mismatch in the radial and circumferential thermal expansion coefficients.

6.0 References

1 Donald R. Rummler. "Advances in Carbon-Carbon Materials, Current and Future Applications." NASA/AIAA Fibrous Ceramic Materials Technology Seminar. NASA/Johnson Space Center, Houston, Texas March 23, 1983.

2 Schmidt, Donald L. "Carbon/Carbon Composites." *SAMPE Journal*, Vol. 3, May/June 1972, pp. 9-19.

3 Adams, Donald F. "Transverse Tensile and Longitudinal Shear Behavior of Unidirectional Carbon-Carbon Composites." *Materials Science and Engineering* 17(1975) 139-152.

4 Perry, John L. and Adams, Donald F. "An Experimental Study of Carbon-Carbon Composite Materials," *Journal of Materials Science*, 9 (1974) 1764-1774.

5 Rolincik, P.G., "Properties and Application of Mod-3 Pierced Fabric Reinforced Carbon/Carbon Composite," AVCO Corporation, Systems Division, Lowell, Massachusetts.

6 Dexter, Benson. NASA-Langley Research Center. Personal communication.

7 Ishikawa, T., "Anti-Symmetric Elastic Properties of Composite Plates of Satin Weave Cloth." *Fib. Sci. Tech.*, Vol. 15 (1981), p.127.

8 Ishikawa, T and Chou, T.W., "Elastic Behavior of Woven Fabric Composites," *J. Composite Materials*, Vol. 16 (1982), p. 2.

9 Ishikawa, T. and Chou, T.W., "One-Dimensional Analysis of Woven Fabric Composites," *AIAA Journal*, Vol. 21. No. 12 (1983), p. 1714.

10 Ishikawa, T. and Chou, T.W., "Stiffness and Strength of Woven Fabric Composites," *J. Materials Science*, Vol. 17(1982), p. 3211.

11 Ishikawa, T. and Chou, T.W., "Stiffness and Strength Properties of Woven Fabric Composites," Proceedings of ICCM 4 (Tokyo), (1982), p. 489.

12 Ishikawa, T. and Chou, T.W., "In-Plane Thermal Expansion and Thermal Bending Coefficients of Fabric Composites," *J. Composite Materials*, Vol. 17, March 1983, pp.92-104.

13 Ishikawa, T. and Chou, T.W., "Nonlinear Behavior of Woven Fabric Composites," *J. Composite Materials*, Vol. 17, Sept. 1983, pp. 399-412.

[14] Kriz, Ronald D. "Stiffness and Internal Stresses of Woven-Fabric Composites at Low Temperatures," *Advances in Cryogenic Engineering*,vol. 30 (1983). Edited by A.F. Clark andf R.P. Reed.

[15] Kriz, Ronald D. "Influence of Damage on Mechanical Properties of Woven Composites at Low Temperatures," *Journal of Composites Technology and Research*. Vol. 7, No. 2, Summer 1985, pp. 55-58.

[16] Kriz, Ronald D. "Edge Stresses in Woven Laminates at Low Temperatures" The 9th Symposium on Composite Materials: Fatigue and Fracture. 26th April 1987, Cincinnati, Ohio. (Accepted for Presentation)

[17] Kimpara, I., Hamamoto, A. and Takehana, M., "Analysis of First Knee Behavior of Woven Roving Composites," *Trans. JSCM*, Vol. 3, No. 1/2, Dec. 1977.

[18] Jortner, Julius. "A Mechanistic Model For Delamination of 2-D Carbon-Carbons," 7th JANNAF Rocket Nozzle Technology Meeting, Monterey, November 1985.

[19] Wu, E. M., "Application of Fracture Mechanics to Orthotropic Plates", *T&AM Report 275*, University of Illinois, Urbana, June 1963.

[20] Stanton, Edward L. and Kipp, Thomas E. "Nonlinear Mechanics of Two-Dimensional Carbon-Carbon Composite Structures and Materials," *AIAA Journal*, Vol. 23, No.8, August 1985, pp.1278-1284.

[21] Walrath, David E. and Donald F. Adams. *Finite Element Micromechanics and Minimechanics Modeling of a Three- Dimenisonal Carbon-Carbon Composite Material*.University of Wyoming, UWME-DR-501-106-1, December, 1985

[22] Howard Maahs. personal communication

[23] Wanda G. Bradshaw and Aldo E. Valdoz. "Fiber-Matrix Interactions in Unidirectional Carbon-Carbon Composites." *Ceramic Bulletin* vol. 57, No. 2 (1978) pp. 195-198

[24] W.G. Bradshaw, P.C. Pinoli, and A.E. Vidoz. Development of Manufacturing Process for Large-Diameter Composite Monofilaments by Pyrolysis of Resin-Impregnated Carbon-Fiber Bundles. NASA CR-120973, October, 1972. p. 15

[25] Zhao, J.X.;Bradt,R.C.; and Walker, P.L., Jr.: "The Fracture Toughness of Glassy Carbons at Elevated Temperatures." *Carbon* Vol. 23, No 1, pp. 15-18, 1985.

[26] Eitman, D.A.; L.B Greszczuk; J. Jortner and C.R. Rowe "Fiber-Matrix Interactions in Carbon-Carbon Composites." *New Industries and Applications for Advanced Materials Technology*. 19th Natl SAMPE Symposium and Exhibition vol. 19 Buena Park, CA April 23-25 1974. pp. 346-358

[27] "Typical Properties "Thornel" High Modulus Carbon Yarns and Their Composites." Bulletin No. 465-252. Union Carbide Corporation.

[28] Goetzel, C.G. "High-Temperature Properties of Some Carbon-Carbon Composites." *High Temperature - High Pressure*, vol. 12, 1980, pp. 11-22.

[29] Hashin, Z. "Analysis of Properties of Fiber Composites With Anisotropic Constituents." *Journal of Applied Mechanics*, Sept. 1979, vol. 46, pp. 543-550.

[30] Pagano, N.J. and J.C. Halpin. "Influence of End Constraint in the Testing of Anisotropic Bodies." *J. Composite Materials*, Vol. 2, No. 1 (Jan. 1968), p. 18.

[31] Wagner, Linda. *Mechanical Behavior and Damage Mechanisms of Woven Graphite-Polyimide Composite Materials.* Master's Thesis, Virginia Polytechnic Institute and State University. June, 1987.

[32] Johnson, D. L., "Structure and Physical Properties of Carbon Fibers," *Chemistry and Industry*, 18 Sept. 1982 pp. 692-698.

[33] Reynolds, W. N., and Sharp, J. V., "Crystal Shear Limit to Carbon Fibre Strength," *Carbon*, 12, 1974 pp. 103-110.

[34] Diefendorf, R. J., and Tokarsky, E., "High Performance Carbon Fibers," *Polymer Engineering and Science*, 15, 1975 pp. 150-159.

[35] Brydges, W. T., Badam, D. V., Joiner, J. C., and Jones, G. A., "The Structure and Elastic Properties of Carbon Fibers," *Applied Polymer Symposia*, 9, 1969 pp. 225-261.

[36] Kirk-Othmer, *Encyclopedia of Chemical Technology*, 3rd Ed. Vol. 4, New York: John Wiley and Sons, 1978 p. 622.

[37] Lemaistre, C. W., and Diefendorf, R. J., "The Origin of Structure in Carbonized PAN Fibers," SAMPE Quarterly, 4, 1973 pp. 1-6.

[38] Bennett, S. C., and Johnson, D. J., "Structural Heterogeneity in Carbon Fibers," Proceedings of the Fifth London International Carbon and Graphite Conference. (Society of Chemical Industry, London) 1978 p. 377.

[39] Bennett, S. C., and Johnson, D. J., "Electron-Microscope Studies of Structural Heterogeneity in PAN-based Carbon Fibers," Carbon, 17, 1979 p 25.

[40] Guigon, M., and Oberlin, A., "Structure and Microstructure of Some Pitch-Base Fibers," *Extended Abstracts and Program of the 16th Biennial Conference on Carbon*, 1983 p. 513.

[41] Ng, C. B., Henderson, G. W., Buechler, M., and White, J. L., "Fracture Behavior of Mesophase Carbon Fibers " *Extended Abstracts and Program of the 16th Biennial Conference on Carbon*, 1983 p. 515.

[42] St. Venant, B., "Memoire sur les divers genres d'homogeneite des corps solides," *Journal de Math. pures et appl.* (Louiville), 1865 t. 10.

[43] Voigt, W., "Ueber die Elastizitatsverhaltnisse zylinrisch aufgebauter Korper." Nachrichten v. d. Konigl. Gesellschaft der Wissenschaften und der Georg-Augustin zu Gottingen, No. 16, 1886.

[44] Mitinskii, A. N., "The Calculation of Stresses in a Drilled Wood Tube," Vestnik Inzhenerov i Tekhnikov, No. 5, 1936.

[45] Lekhnitskii, S. G., *Theory of Elasticity of an Anisotropic Body*, 1950, pp. 68-70. Moscow, (Mir Publishers, 1981).

[46] Lekhnitskii, S. G., "Anisotropic Plates," 1957 Moscow, (translation by Foreign Technology Division, Air Force Systems Command FTD-HT-23-608-67).

[47] Cohen, D., and Hyer, M. W., "Residual Thermal Stresses in Cross-Ply Graphite-Epoxy Tubes," *Advances in Aerospace Sciences and Engineering*, eds. U. Yuceoglu and R. Hesser, ASME Publication AD-08, pp. 87-93, 1984.

[48] Cohen, D., and Hyer, M. W., "Residual Stresses in Cross-Ply Composite Tubes," CCMS-84-04, Virginia Polytechnic Institute and State University, Blacksburg, Va, 1984

[49] Cohen, D., Hyer, M. W., and Tompkins, S. S., "The Effects of Thermal Cycling on Matrix Cracking and Stiffness Changes in Composite Tubes," CCMS-84-12, Virginia Polytechnic Institute and State University, Blacksburg, Va, 1934.

[50] Olson, W. A., and Bert, C. W., "Analysis of Residual Stresses in Bars and Tubes of Cylindrically Orthotropic Materials," *Experimental Mechanics*, Vol. 6, No. 9, 451-457, 1966.

[51] Chen, K. J., and Diefendorf, R. J., "A Theoretical Calculation of Residual Stresses in Carbon Fibers," Proceedings of the 17th Biennial Conference on Carbons, 1985.

[52] Ekvall, J.C. and Griffin, C.F., "Design Allowables for T300/5208 Graphite/Epoxy Composite Materials," *J. Aircraft*, Vol. 19, No. 8 August 1982, p. 661. Errata in *J. Aircraft*, Vol. 20, No. 6 1983, p. 576.

[53] Reddy, J.N., *An Introduction to the Finite Element Method*, McGraw-Hill Book Company, 1984.

[54] Bathe, K.J., and E.L. Wilson, *Numerical Methods in Finite Element Analysis*, Prentice-Hall Inc., New Jersey, 1982.

[55] Branca, T.R., "Creep of a Uniaxial Metal Matrix Composite Subjected to Axial and Normal Lateral Loads," TAM Report 341, Univ. Illinois, June, 1971.

[56] Crane, D.A. and Adams, D.F., "Finite Element Micromechanical Analysis of a Unidirectional Composite Including Longitudinal Shear Loading," Report UWME DR-001-101-1, Univ. Wyoming, February, 1981.

[57] Adams, D.S., "Characteristics of Thermally-Induced Transverse Cracks in Graphite-Epoxy Composite Laminates," VPI-E-83-23, Virginia Polytechnic Institute and State University, Blacksburg, VA, June, 1983.

[58] Stanton, E.L., L.M. Crane, and T.F. Neu, "A Parametric Cubic Modelling System For General Solids of Composite Materials," *Int. J. Num. Meth. Engng*, 11 , 653-670 (1977).

[59] Stanton, E.L., *A Three-Dimensional Parametric Cubic Discrete Element Program for the Analysis of Composite Structures*, McDonnell Douglas Astronautics Company, Report No. MDC G5716 (1975)

[60] Coons, S.A., "Surfaces for Computer-Aided Design of Space Forms," Massachusetts Institute of Technology, Report No. MAC-TR-41 (1967).

Appendix A. Contour and Interfacial Stress Distributions

The following figures show the stress contours for the $(F/W_z/F)_f$, R = 1 and 4 laminates for in-plane loading ε_x = 0.1% and out-of-plane loading ε_z = 0.1%. Additionally, interfacial stress distributions are presented for those $(F/W_z/F)_f$, $(F/W_z/F)_w$, and $(F/W)_z$ laminates that were not discussed in detail Chapter 3.

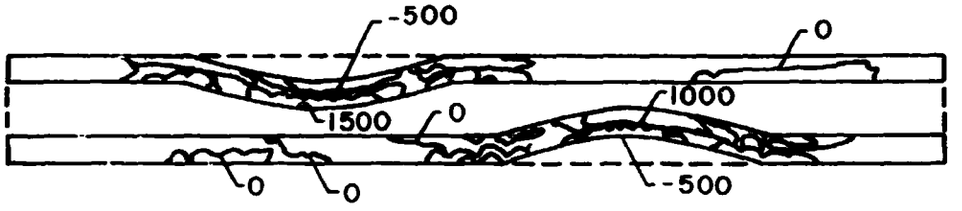

a) Fill Tows

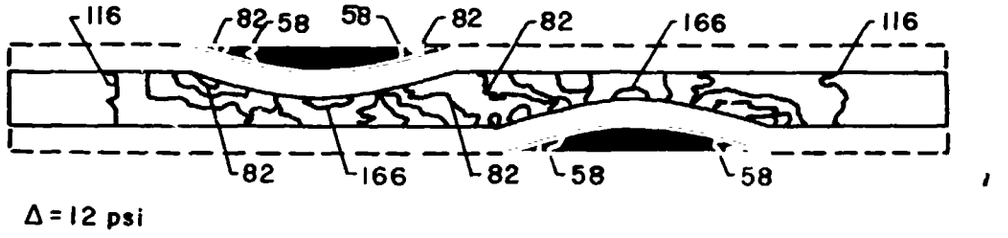

b) Warp Tows

Figure 99. Contour plot of σ_x in $(F/W_2/F)_1$ laminate. $R=1$, $\varepsilon_z = 0.1\%$.

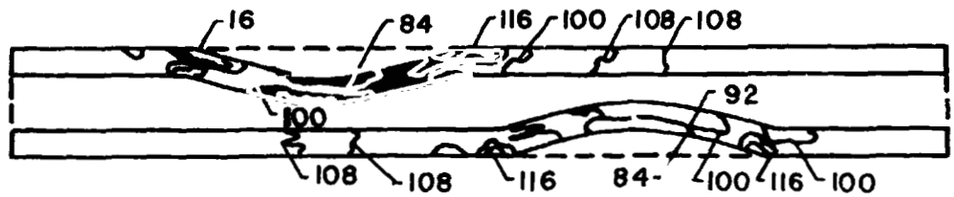

Δ = 8 psi

a) Fill Tows

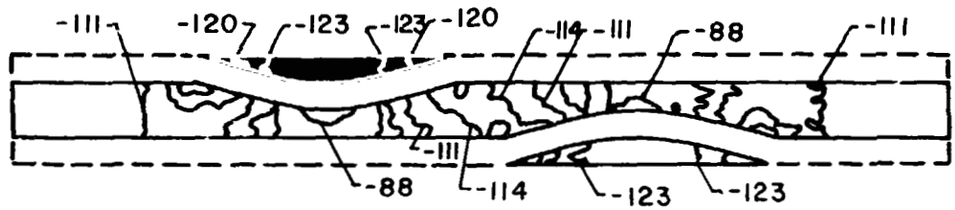

Δ = 3 psi

b) Warp Tows

Figure 100. Contour plot of σ_y in $(F/W_2/F)_t$ laminate. R=1, ε_z =0.1%.

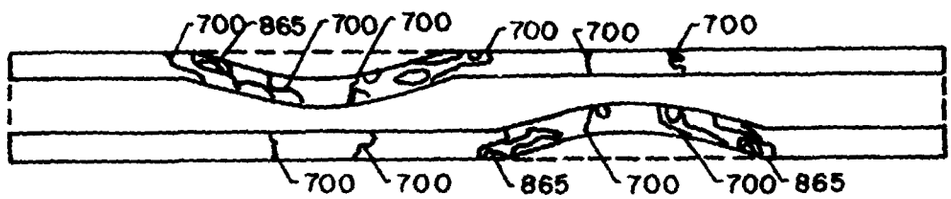

a) Fill Tows

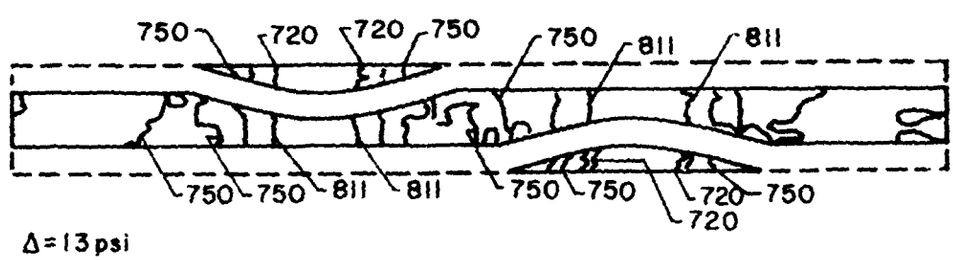

b) Warp Tows

Figure 101. Contour plot of σ_z in $(F/W_2/F)_f$ laminate. $R = 1$, $\varepsilon_z = 0.1\%$.

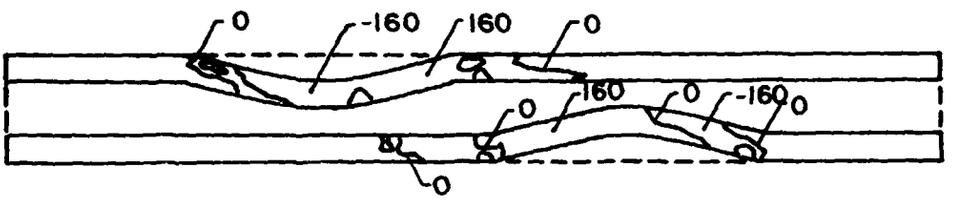

a) Fill Tows

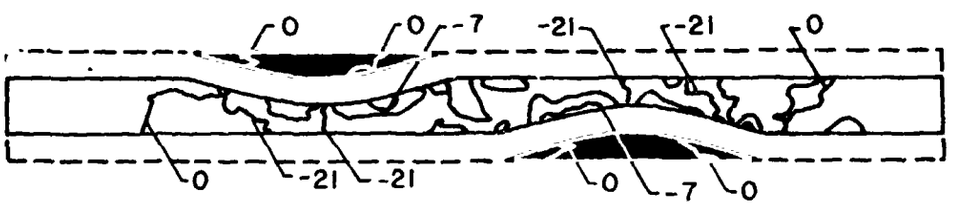

b) Warp Tows

Figure 102. Contour plot of τ_{xz} in $(F/W_2/F)_f$ laminate. $R=1$, $\varepsilon_z = 0.1\%$.

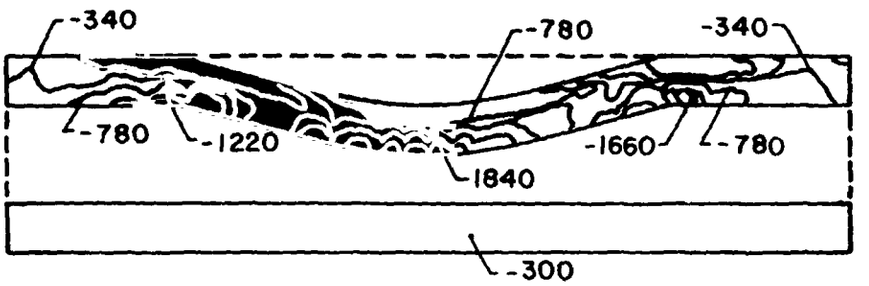

Δ = 440 psi

a) Fill Tows

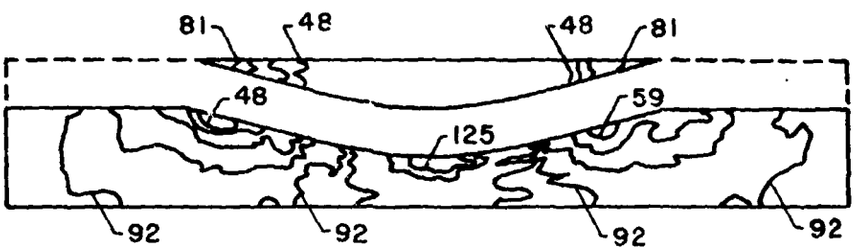

Δ = 11 psi

b) Warp Tows

Figure 103. Contour plot of σ_x in $(F/W_2/F)_1$ laminate. $R=4$, $\varepsilon_z = 0.1\%$.

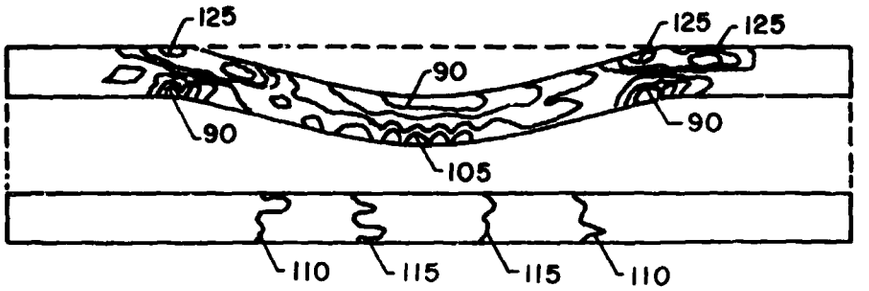

Δ = 5 psi

a) Fill Tows

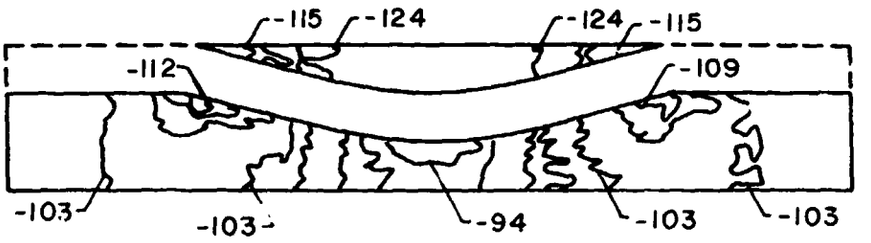

Δ = 3 psi

b) Warp Tows

Figure 104. Contour plot of σ_y in $(F/W_2/F)_t$ laminate. R=4, ε_z =0.1%.

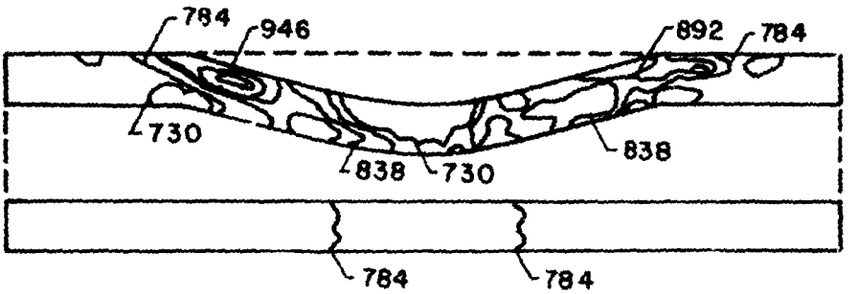

Δ = 54 psi

a) Fill Tows

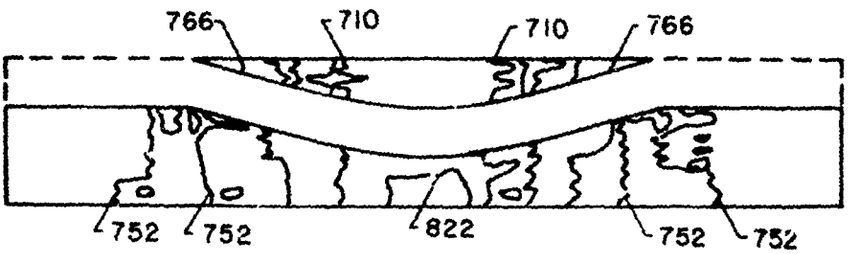

Δ = 14 psi

b) Warp Tows

Figure 105. Contour plot of σ_z in $(F/W_2/F)_t$ laminate. $R=4$, $\varepsilon_z=0.1\%$.

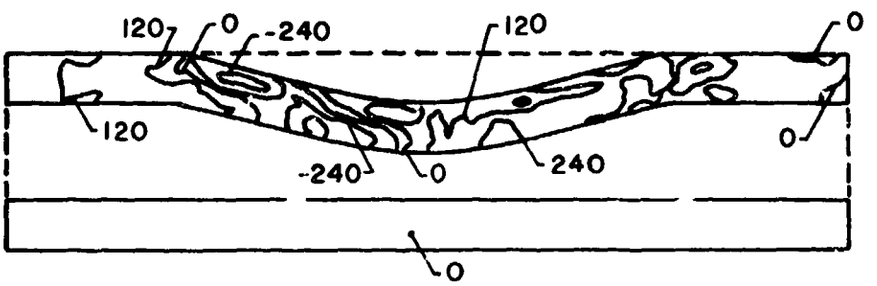

a) Fill Tows

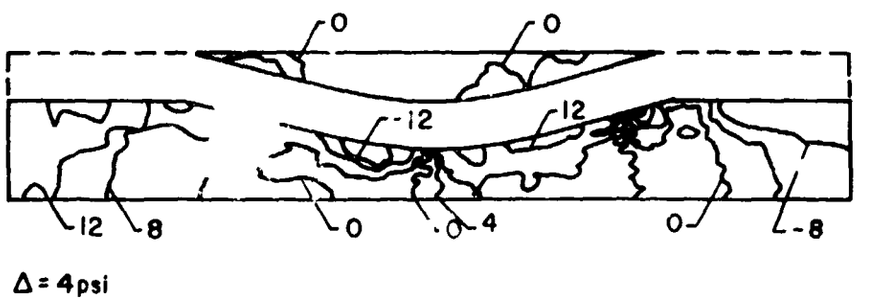

b) Warp Tows

Figure 106. Contour plot of τ_{xz} in $(F/W_2/F)_t$ laminate. $R=4$, $\varepsilon_z = 0.1\%$.

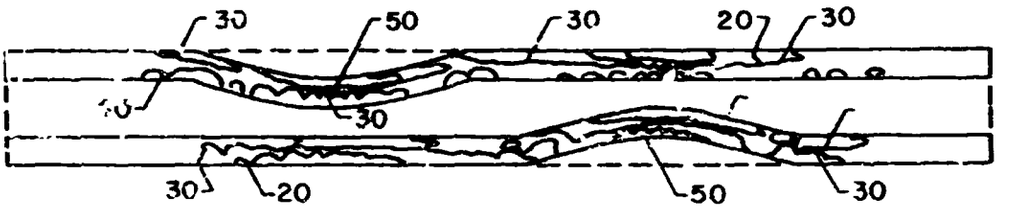

a) Fill Tows

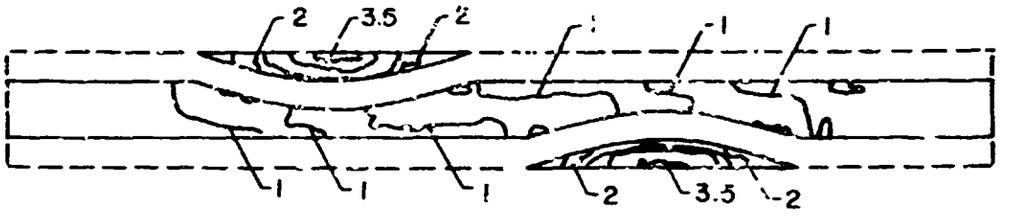

b) Warp Tows

Figure 107. Contour plot of σ_x in $(F/W_2/F)_t$ laminate. R = 1, ε_x = 0.1%.

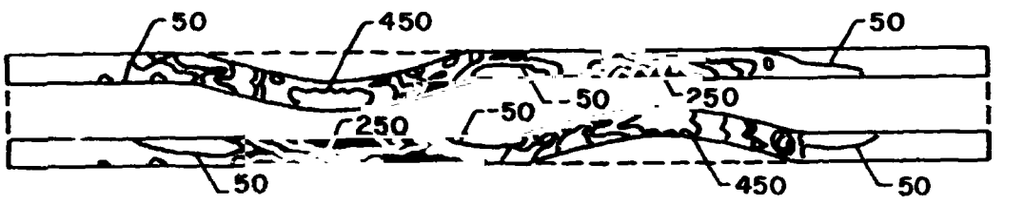

Δ = 50psi

a) Fill Tows

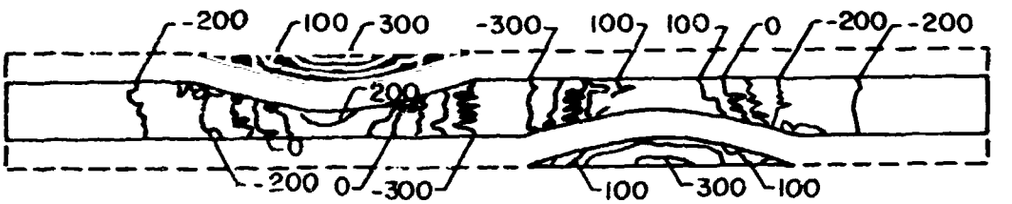

Δ = 100psi

b) Warp Tows

Figure 108. Contour plot of σ_y in $(F/W_2/F)_t$ laminate. R = 1, ε_x = 0.1%.

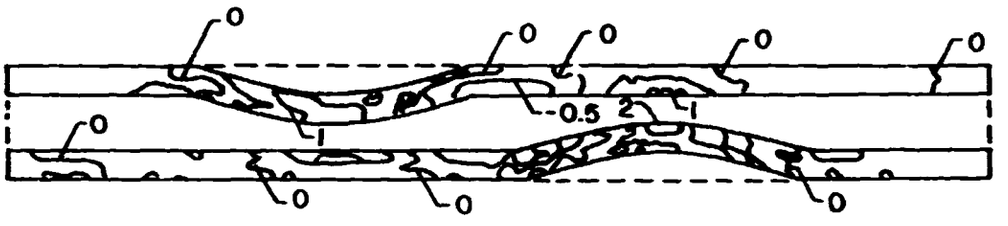

Δ = 0.5 ksi

a) Fill Tows

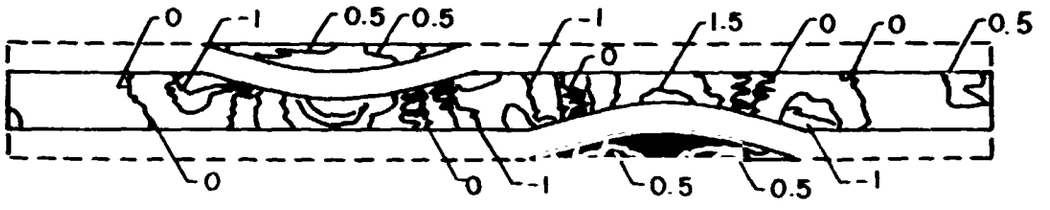

Δ = 0.5 ksi

b) Warp Tows

Figure 109. Contour plot of σ_z in $(F/W_2/F)_t$ laminate. R = 1, ε_x = 0.1%.

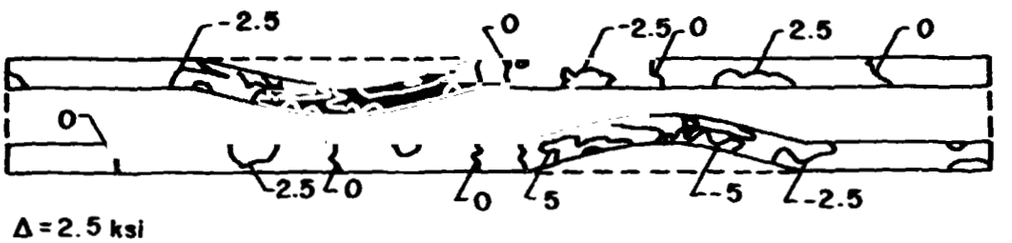

a) Fill Tows

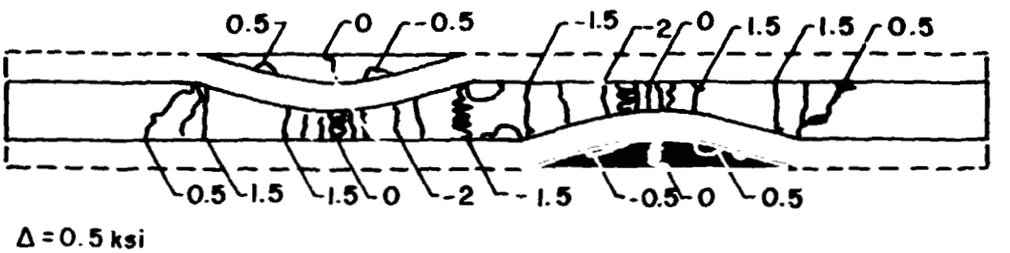

b) Warp Tows

Figure 110. Contour plot of τ_{zz} in $(F/W_2/F)_f$ laminate. $R = 1$, $\varepsilon_x = 0.1\%$.

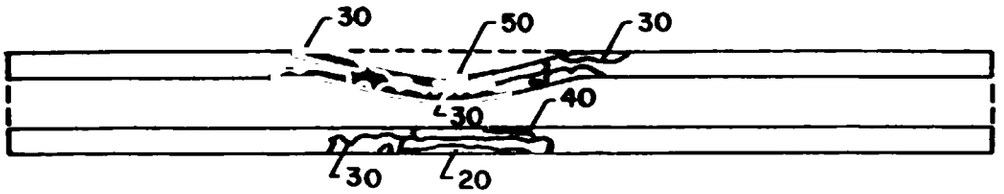

Δ = 10 ksi

a) Fill Tows

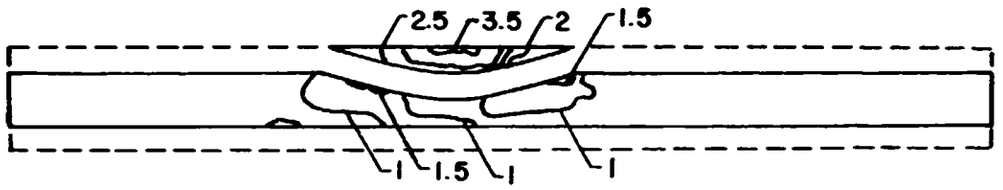

Δ = 0.5 ksi

b) Warp Tows

Figure 111. Contour plot of σ_x in $(F/W_2/F)_t$ laminate. $R=4$, $\varepsilon_x = 0.1\%$.

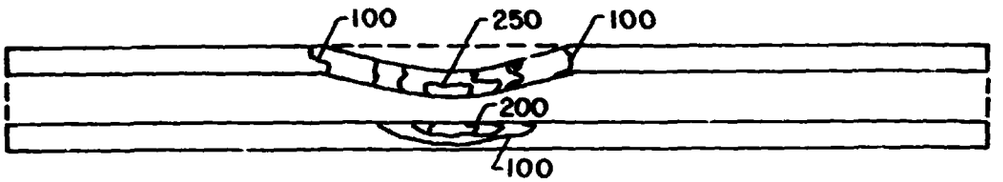

Δ = 50 psi

a) Fill Tows

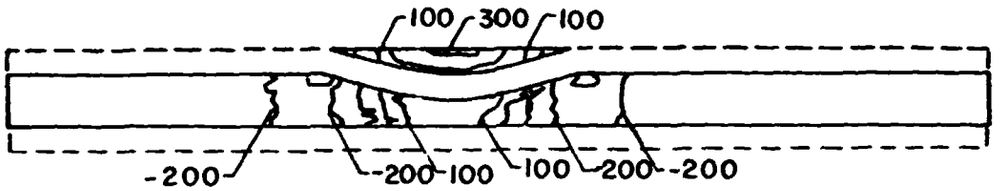

Δ = 100 psi

b) Warp Tows

Figure 112. Contour plot of σ_y in $(F/W_2/F)_1$ laminate. R=4, ε_x = 0.1%.

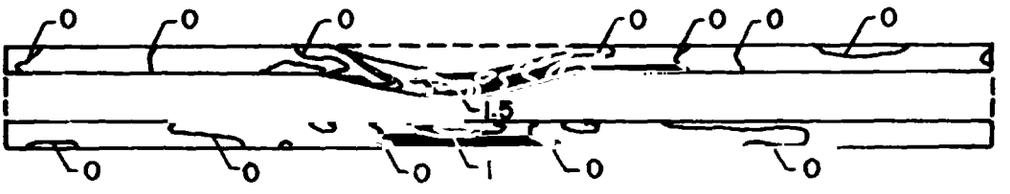

Δ = 0.5 ksi

a) Fill Tows

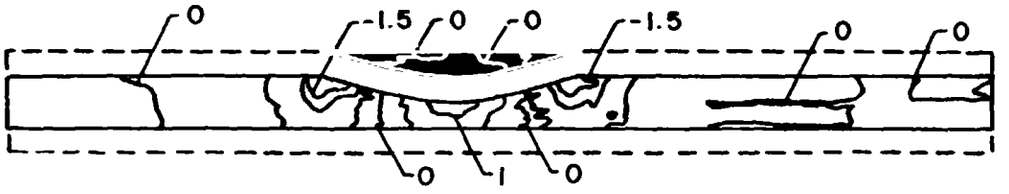

Δ = 0.5 ksi

b) Warp Tows

Figure 113. Contour plot of σ_z in $(F/W_2/F)_t$ laminate. R=4, ε_x = 0.1%.

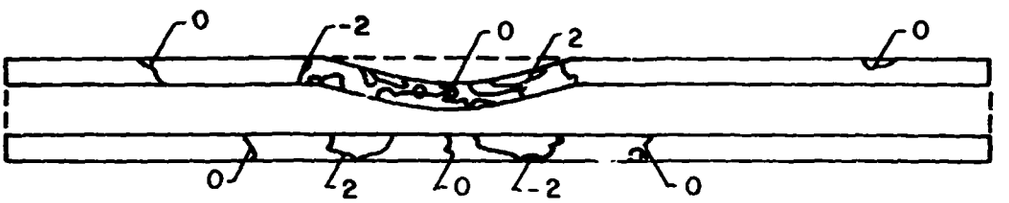

Δ = 2 ksi

a) Fill Tows

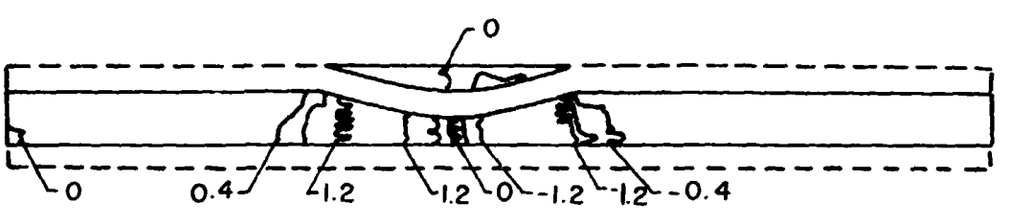

Δ = 0.4 ksi

b) Warp Tows

Figure 114. Contour plot of τ_{xz} in $(F/W_2/F)_f$ laminate. $R=4$, $\varepsilon_x = 0.1\%$.

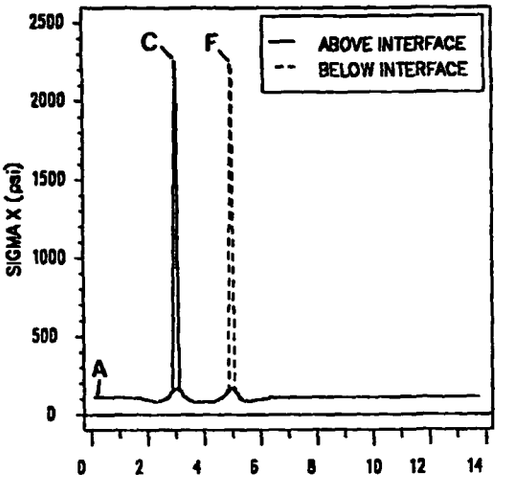

a) Interfacial σ_x.

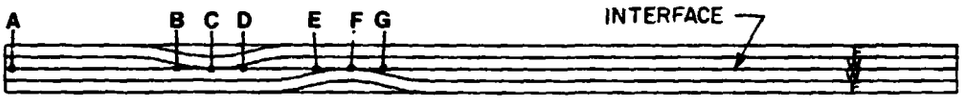

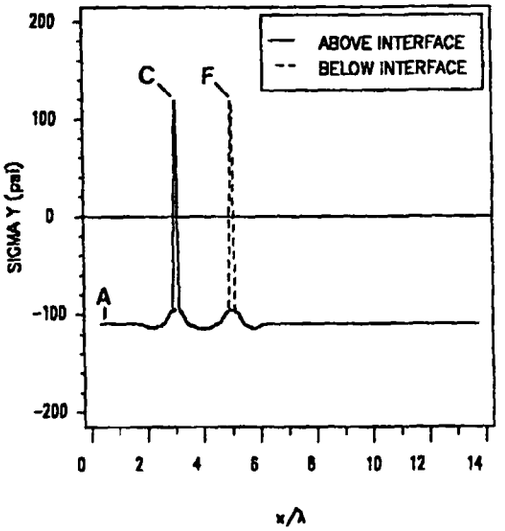

b) Interfacial σ_y.

Figure 115. Interfacial σ_x and σ_y in $(F/W_2/F)_f$ laminate. $R=1$, $\varepsilon_z = 0.1\%$.

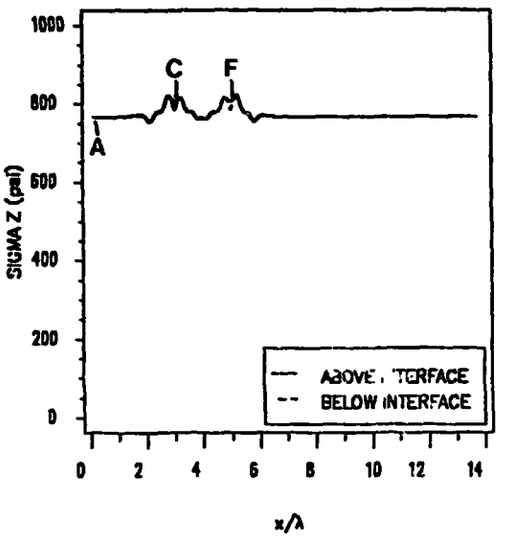

a) Interfacial σ_z.

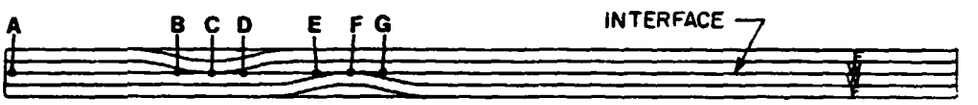

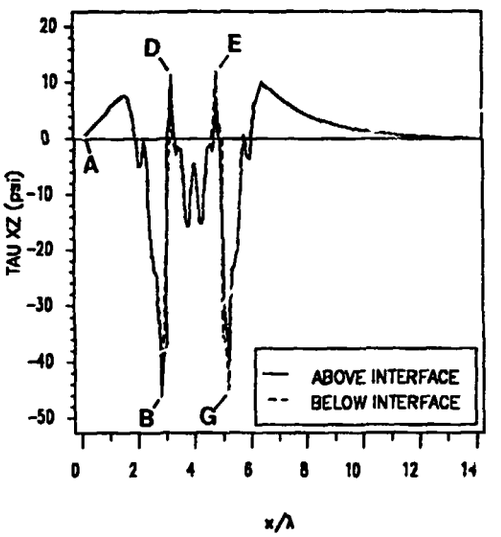

b) Interfacial τ_{xz}.

Figure 116. Interfacial σ_z and τ_{xz} in $(F/W_2'/F)_f$ laminate. R=1, ε_z = 0.1%.

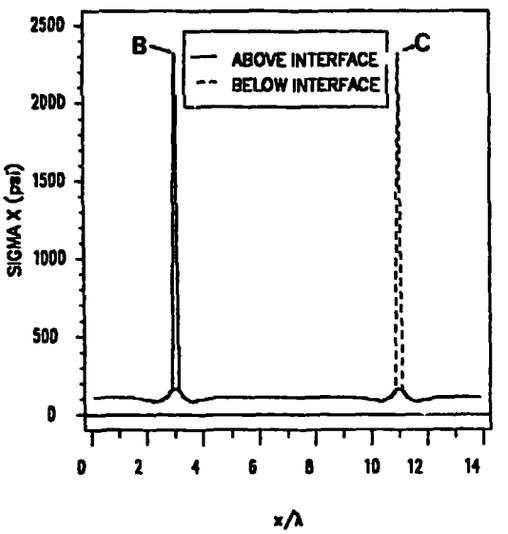

a) Interfacial σ_x.

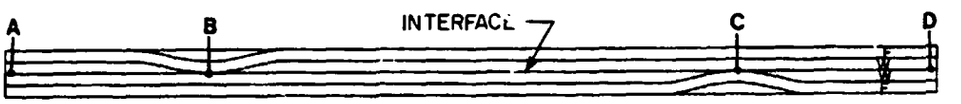

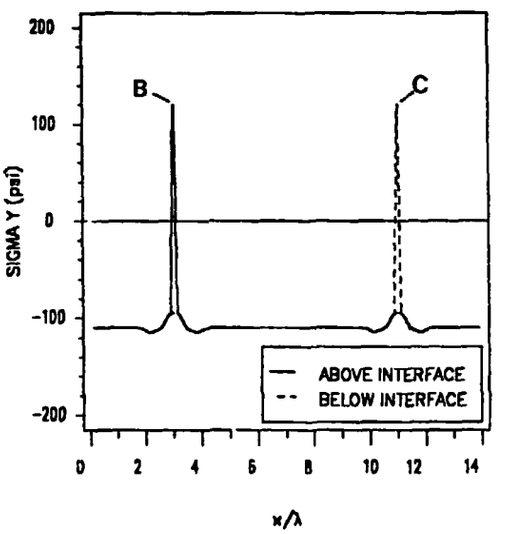

b) Interfacial σ_y.

Figure 117. Interfacial σ_x and σ_y in $(F/W_2/F)_t$ laminate. R=4, ε_z = 0.1%.

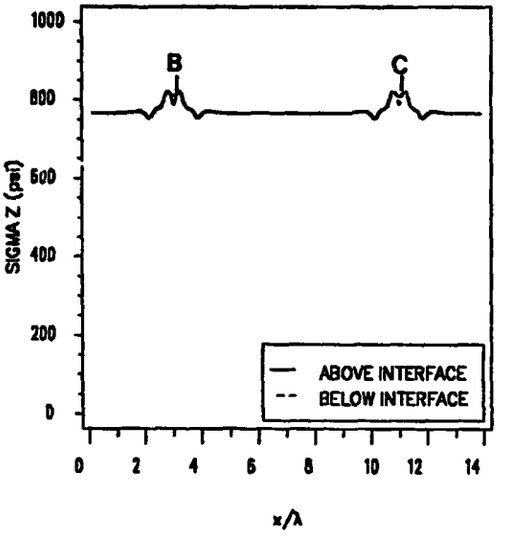

a) Interfacial σ_z.

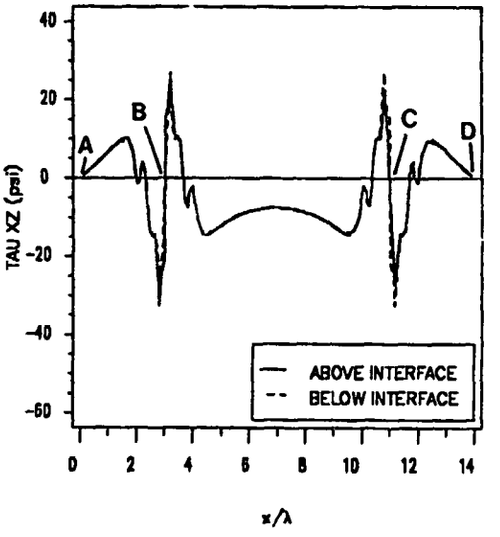

b) Interfacial τ_{xz}.

Figure 118. Interfacial σ_z and τ_{xz} in $(F/W_2/F)_t$ laminate. R=4, ε_z = 0.1%.

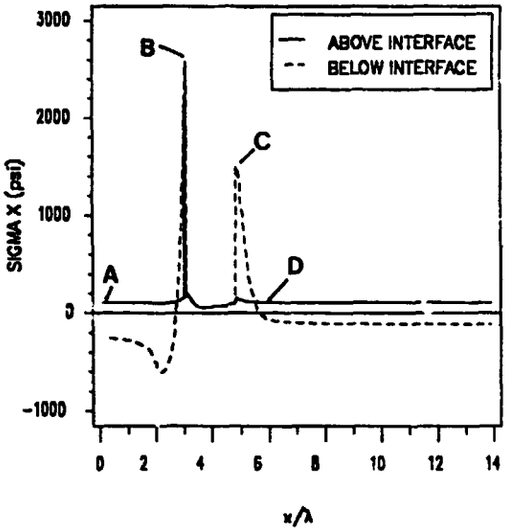

a) Interfacial σ_x.

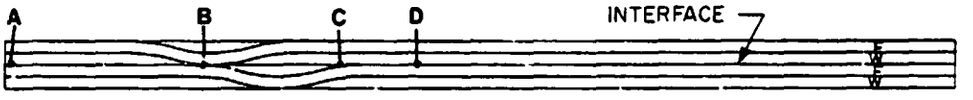

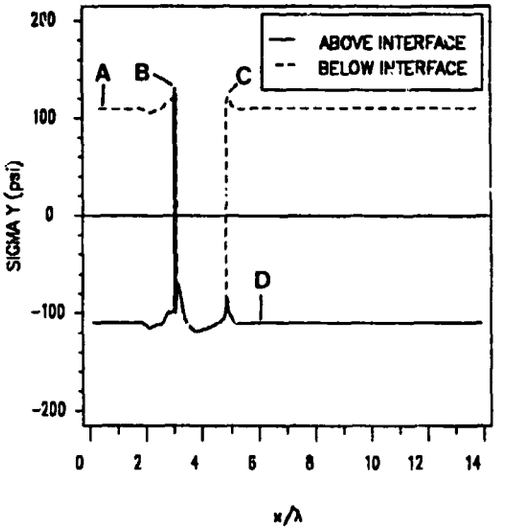

b) Interfacial σ_y.

Figure 119. Interfacial σ_x and σ_y in $(F/W)_2$ laminate. R=0.5, ε_z = 0.1%.

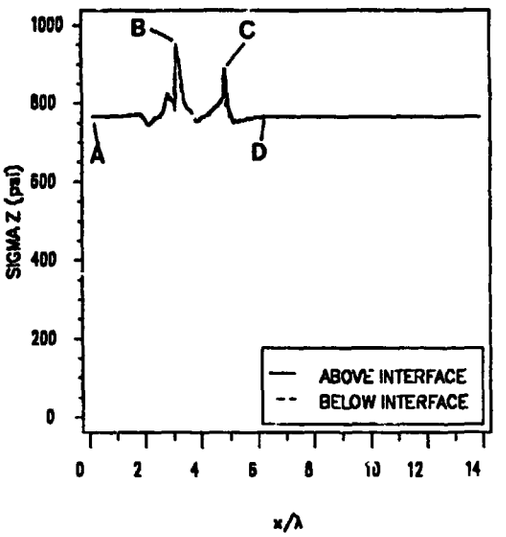

a) Interfacial σ_z.

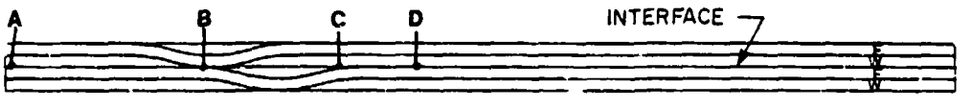

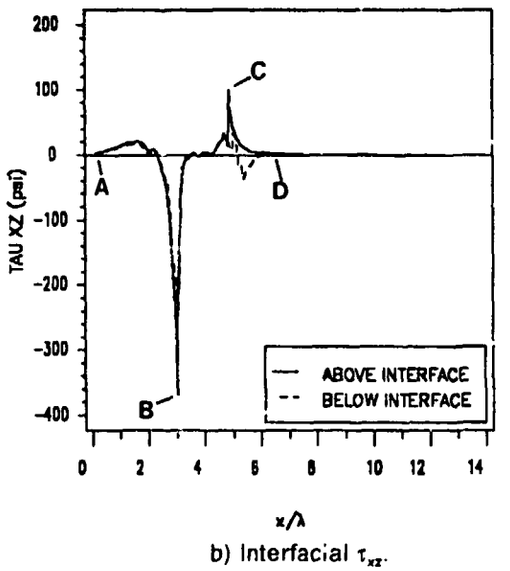

b) Interfacial τ_{xz}.

Figure 120. Interfacial σ_z and τ_{xz} in $(F/W)_2$ laminate. R=0.5, ε_z = 0.1%.

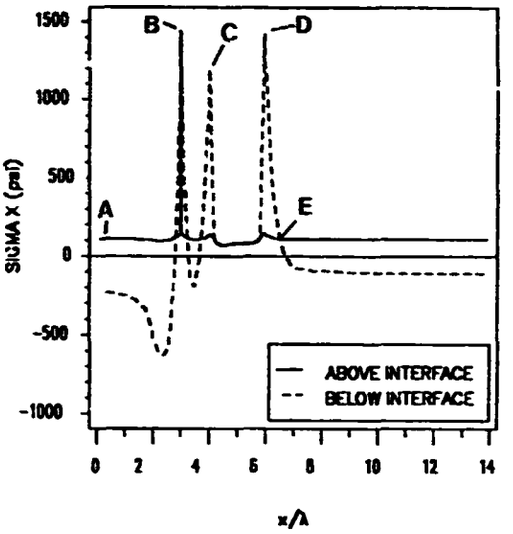

a) Interfacial σ_x.

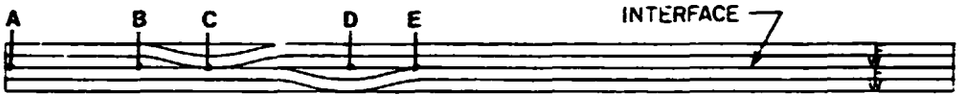

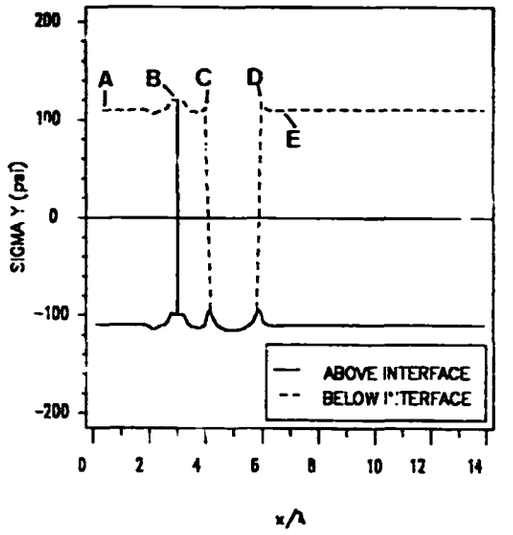

b) Interfacial σ_y.

Figure 121. Interfacial σ_x and σ_y in $(F/W)_2$ laminate. R = 1, ε_z = 0.1%.

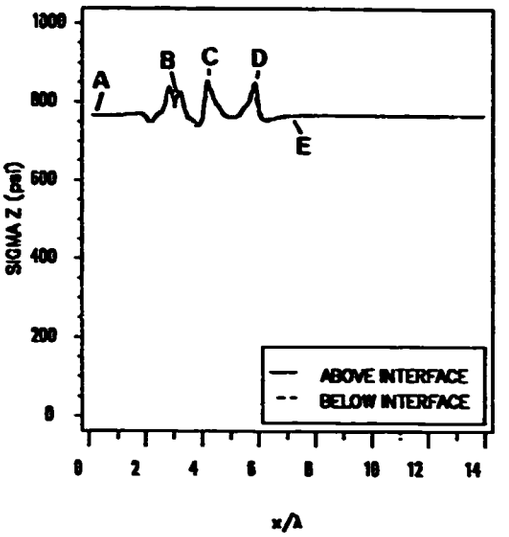

a) Interfacial σ_z.

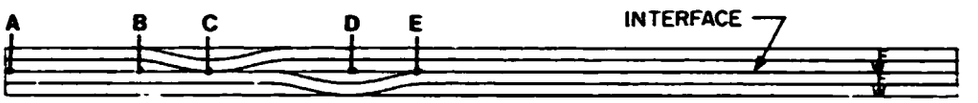

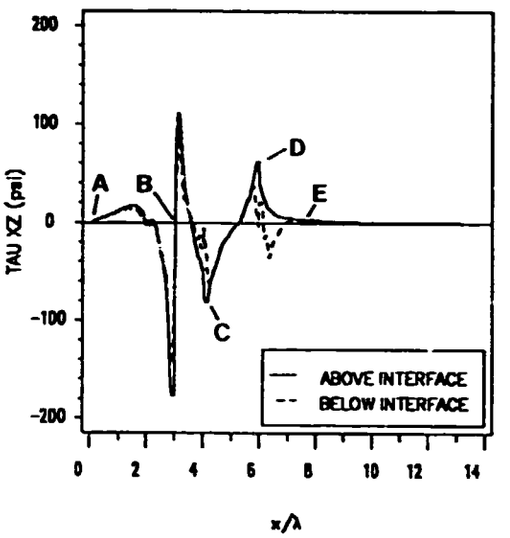

b) Interfacial τ_{xz}.

Figure 122. Interfacial σ_z and τ_{xz} in $(F/W)_2$ laminate. $R=1$, $\varepsilon_z = 0.1\%$.

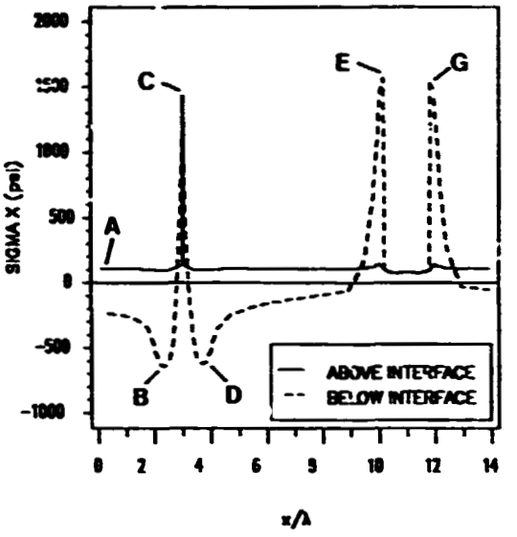

a) Interfacial σ_x.

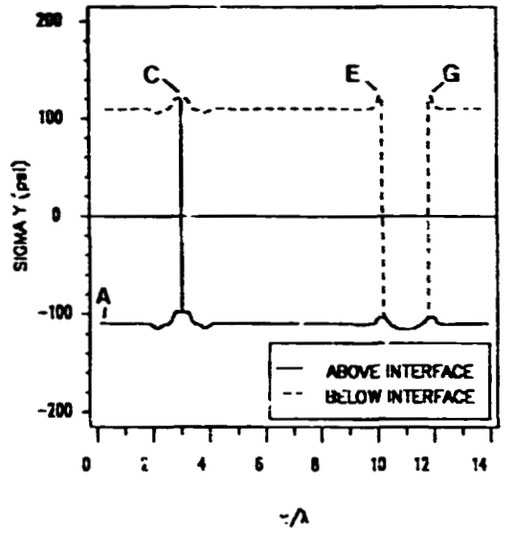

b) Interfacial σ_y.

Figure 123. Interfacial σ_x and σ_y in $(F/W)_2$ laminate. $R=4$, $\varepsilon_z = 0.1\%$.

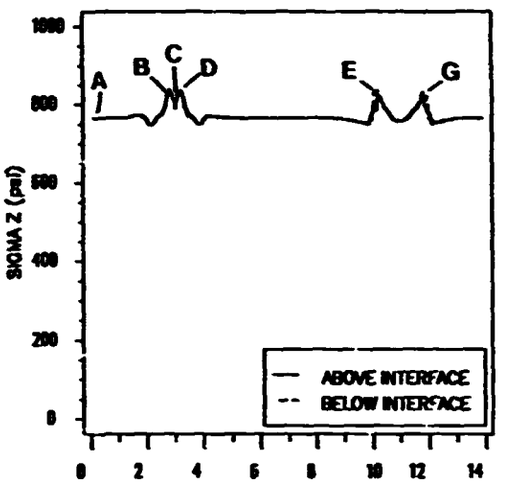

a) Interfacial σ_z.

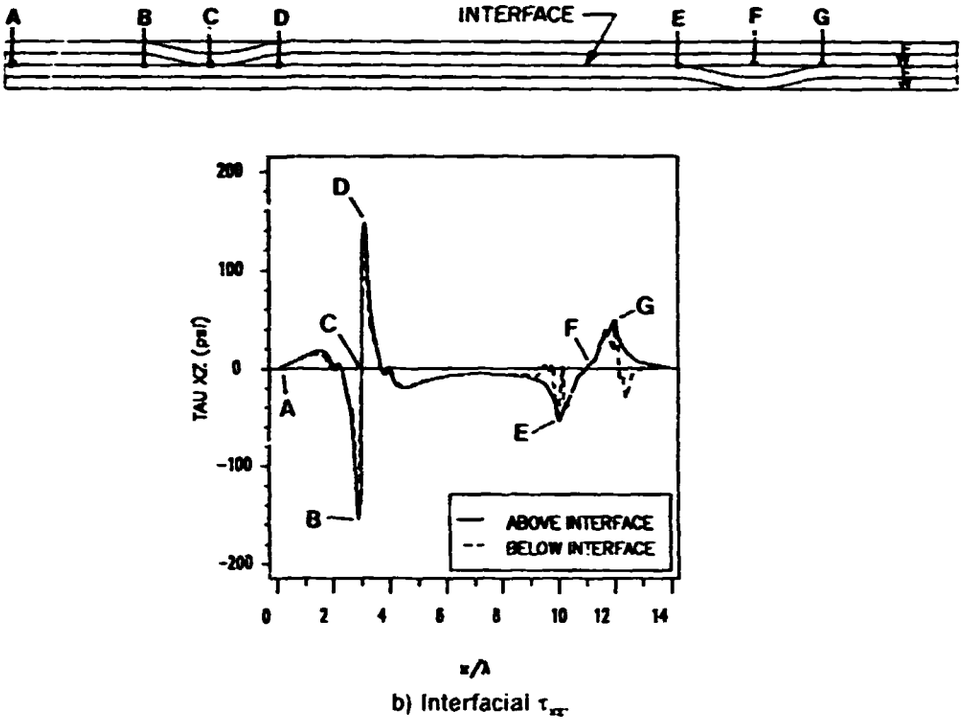

b) Interfacial τ_{xz}.

Figure 124. Interfacial σ_z and τ_{xz} in $(F/W)_2$ laminate. R=4, ε_z = 0.1%.

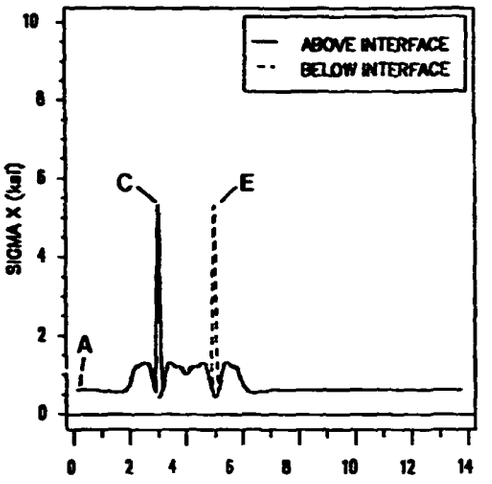

a) Interfacial σ_x.

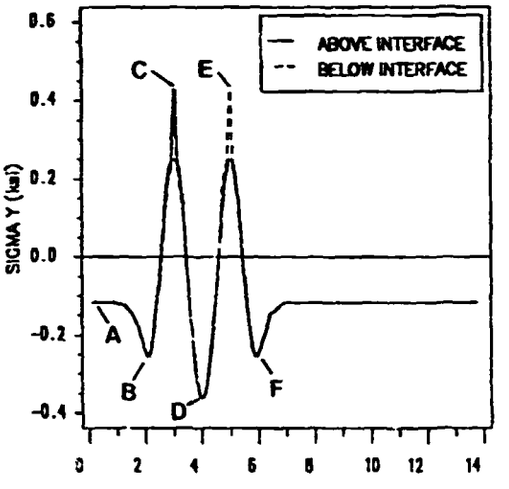

b) Interfacial σ_y.

Figure 125. Interfacial σ_x and σ_y in $(F/W_2/F)_t$ laminate. R = 1, ε_x = 0.1%.

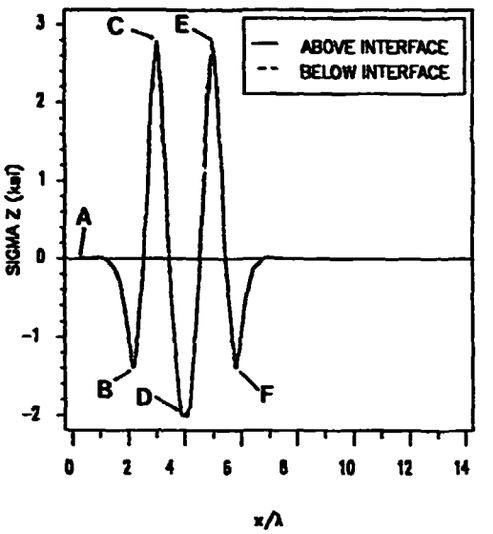

a) Interfacial σ_z.

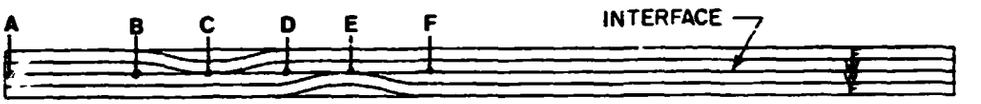

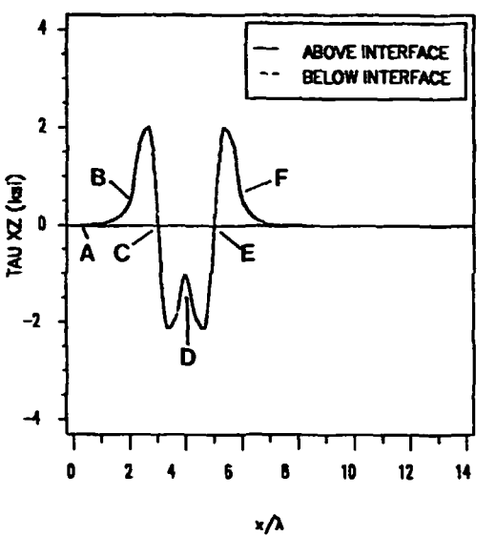

b) Interfacial τ_{xz}.

Figure 126. Interfacial σ_z and τ_{xz} in $(F/W_2/F)_1$ laminate. $R=1$, $\varepsilon_x = 0.1\%$.

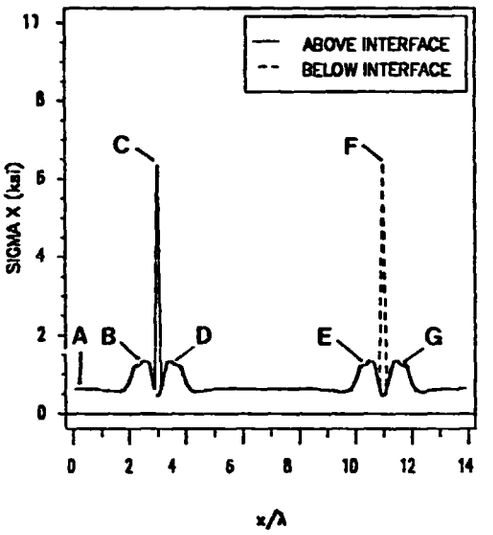

a) Interfacial σ_x.

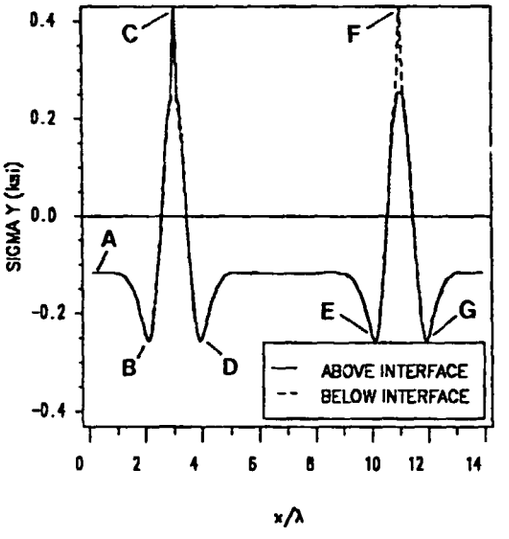

b) Interfacial σ_y.

Figure 127. Interfacial σ_x and σ_y in $(F/W_2/F)_t$ laminate. R=4, ε_x = 0.1%.

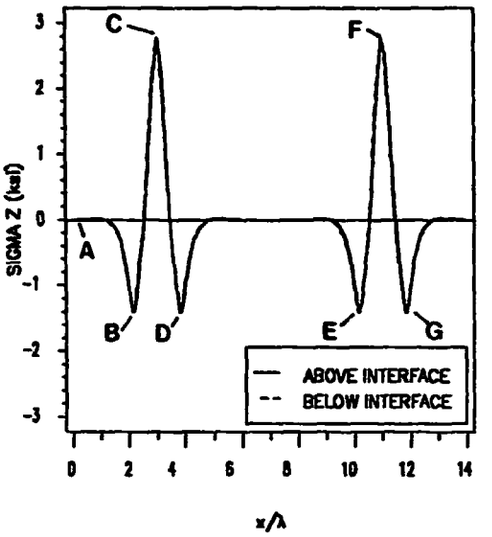

a) Interfacial σ_z.

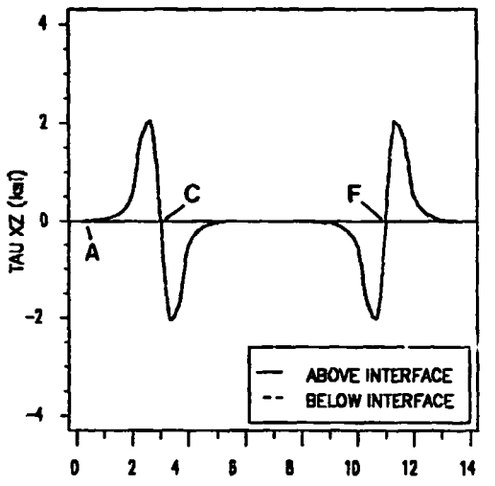

b) Interfacial τ_{xz}.

Figure 128. Interfacial σ_z and τ_{xz} in $(F/W_2/F)_f$ laminate. R=4, ε_x = 0.1%.

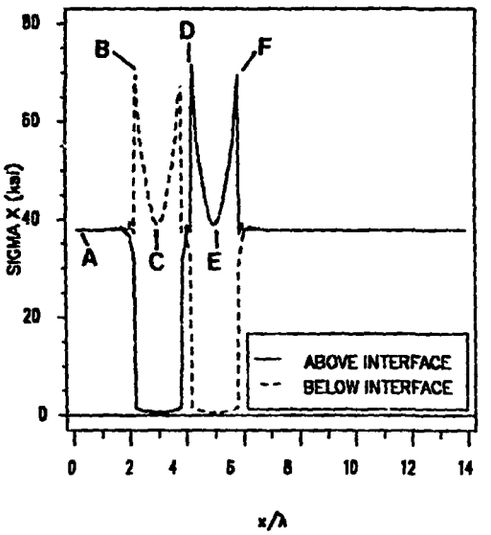

a) Interfacial σ_x.

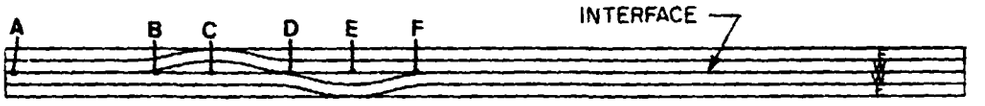

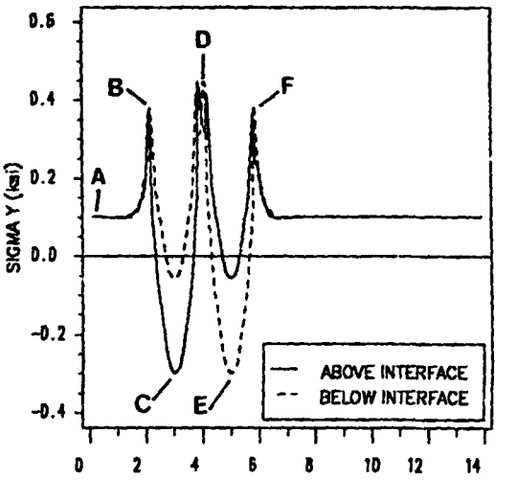

b) Interfacial σ_y.

Figure 129. Interfacial σ_x and σ_y in $(F/W_2/F)_w$ laminate. $R=1$, $\varepsilon_x = 0.1\%$.

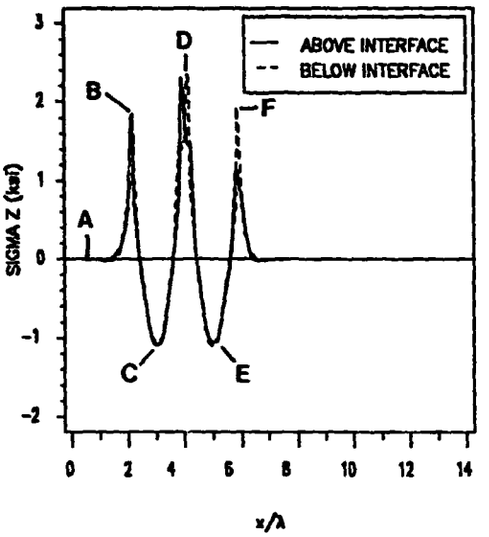

a) Interfacial σ_z.

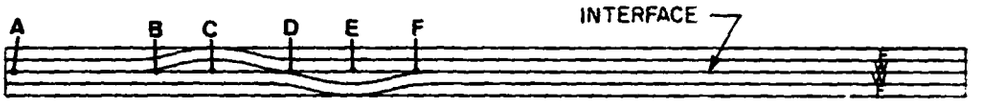

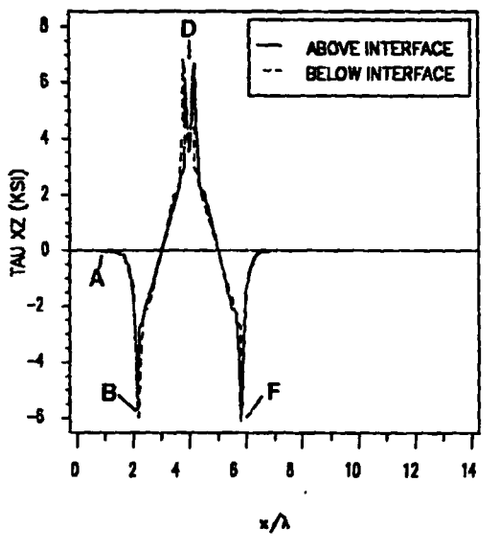

b) Interfacial τ_{xz}.

Figure 130. Interfacial σ_z and τ_{xz} in $(F/W_2/F)_w$ laminate. $R=1$, $\varepsilon_x=0.1\%$.

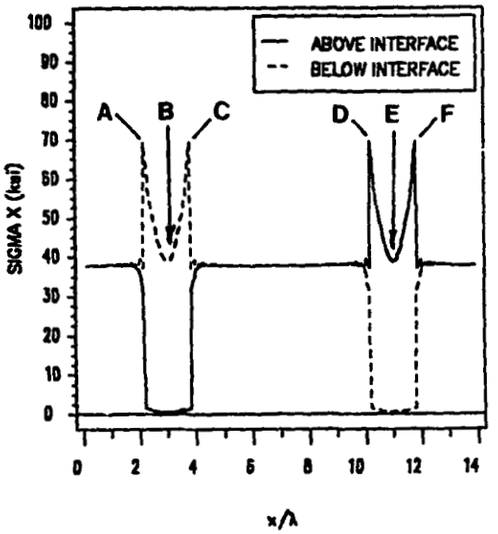

a) Interfacial σ_x.

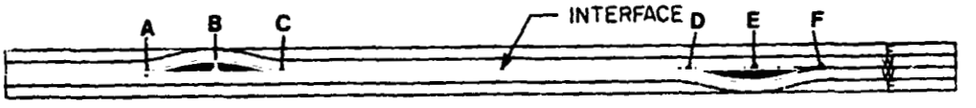

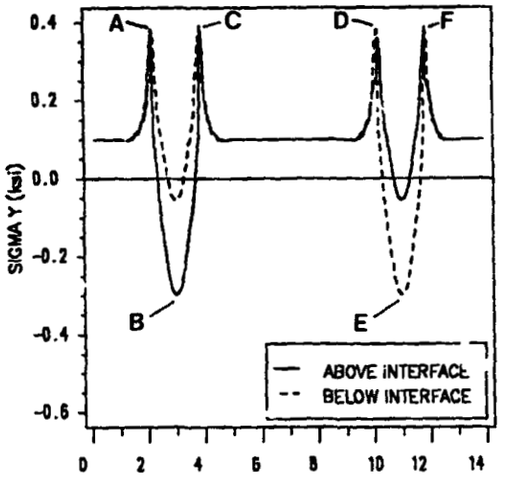

b) Interfacial σ_y.

Figure 131. Interfacial σ_x and σ_y in $(F/W_2/F)_w$ laminate. $R=4$, $\varepsilon_x = 0.1\%$.

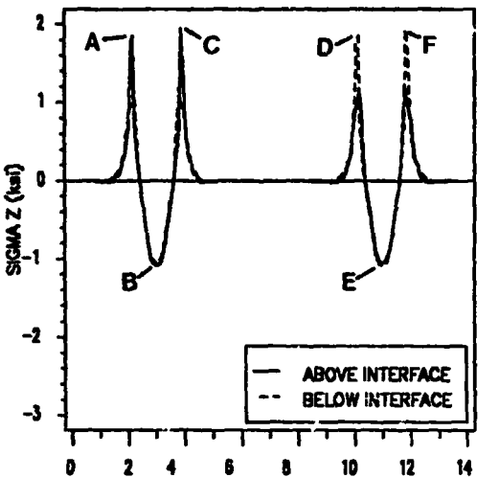

a) Interfacial σ_z.

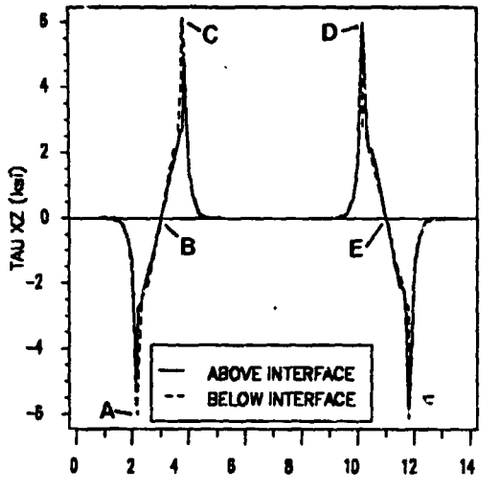

b) Interfacial τ_{xz}.

Figure 132. Interfacial σ_z and τ_{xz} in $(F/W_2/F)_w$ laminate. R=4, ε_x = 0.1%.

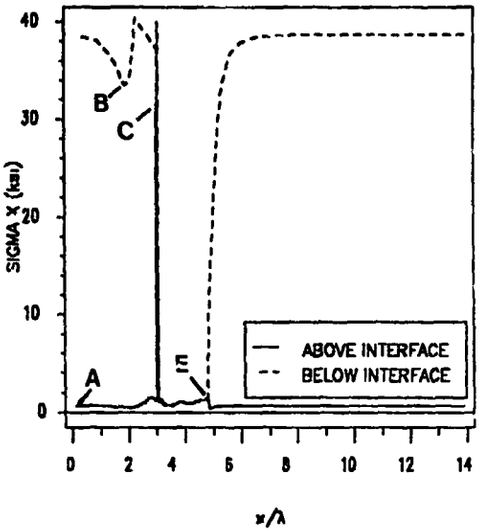

a) Interfacial σ_x.

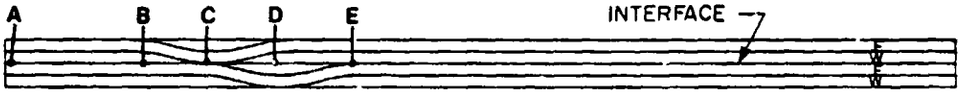

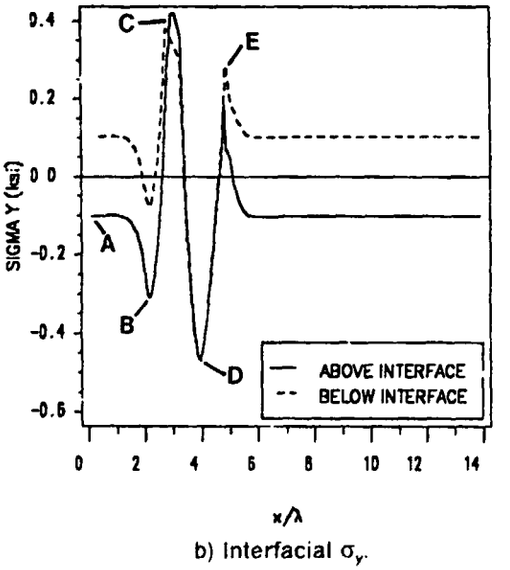

b) Interfacial σ_y.

Figure 133. Interfacial σ_x and σ_y in $(F/W)_2$ laminate. $R = 0.5$, $\varepsilon_x = 0.1\%$.

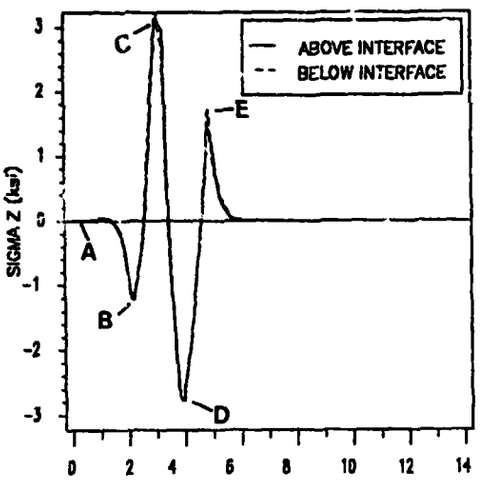

a) Interfacial σ_z.

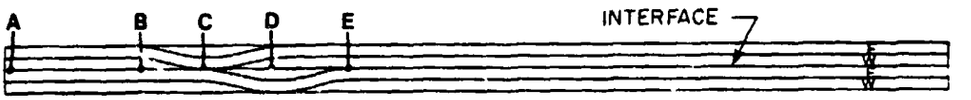

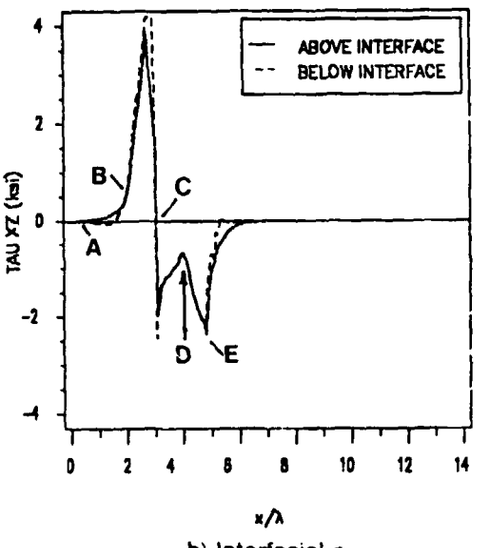

b) Interfacial τ_{xz}.

Figure 134. Interfacial σ_z and τ_{xz} in $(F/W)_2$ laminate $R=0.5$, $\varepsilon_y=0.1\%$.

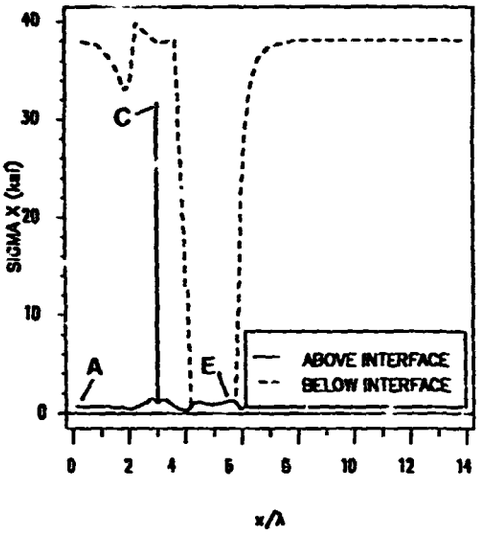

a) Interfacial σ_x.

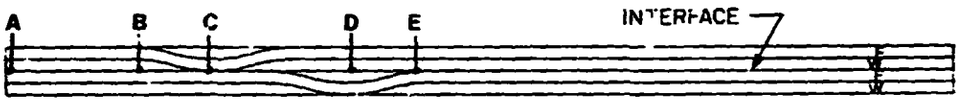

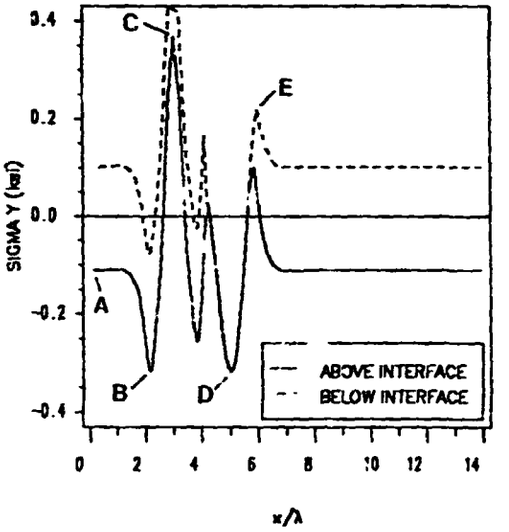

b) Interfacial σ_y.

Figure 135. Interfacial σ_x and σ_y in $(F/W)_2$ laminate. $R = 1$, $\varepsilon_x = 0.1\%$.

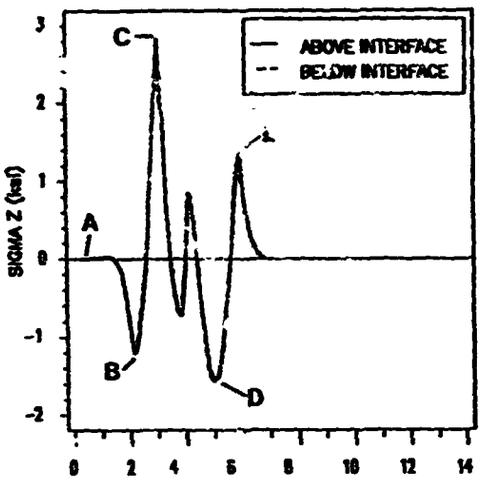

a) Interfacial σ_z.

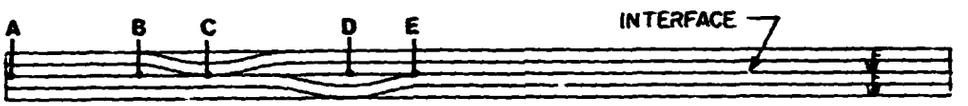

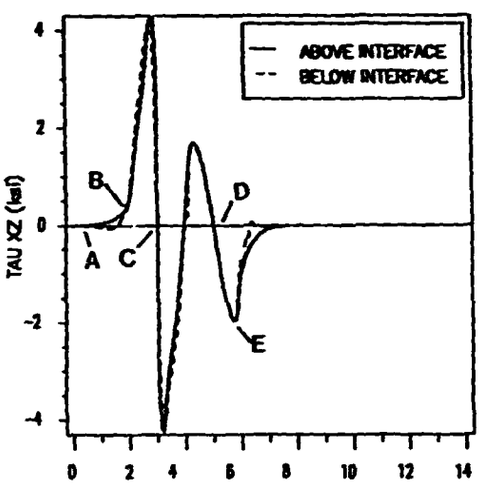

b) Interfacial τ_{xz}.

Figure 136. Interfacial σ_z and τ_{xz} in $(F/W)_2$ laminate. $R=1$, $\varepsilon_x=0.1\%$.

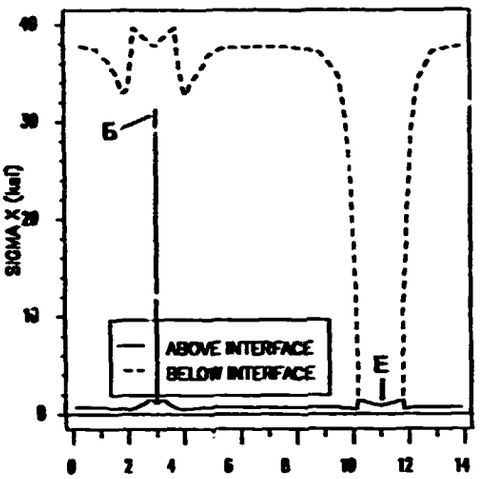

a) Interfacial σ_x.

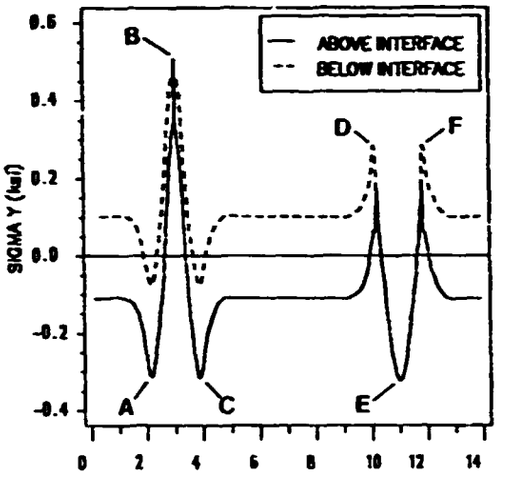

b) Interfacial σ_y.

Figure 137 Interfacial σ_x and σ_y in $(F/W)_2$ laminate. $R=4$, $\varepsilon_a=0.1\%$.

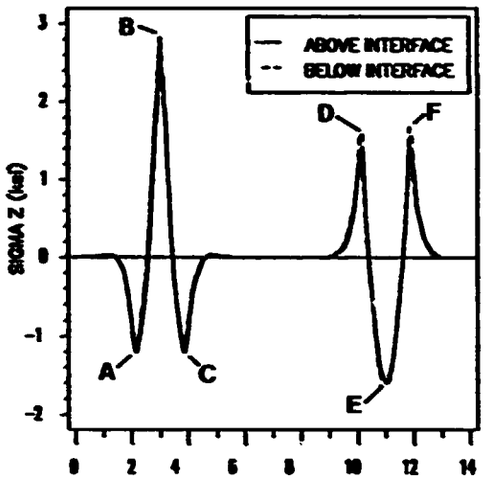

a) Interfacial σ_z.

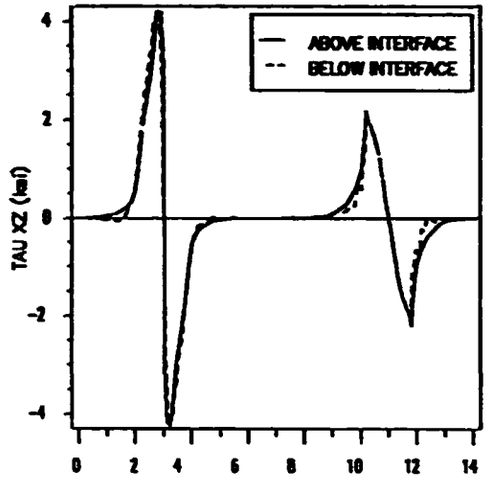

b) Interfacial τ_{xz}.

Figure 138. Interfacial σ_z and τ_{xz} in $(F/W)_2$ laminate. R=4, ε_x=0.1%.

Appendix B. Influence of Boundary Conditions on Finite Element Analysis

One characteristic of a two-layer woven fabric composite is that the geometry is periodic in x (Figure 17). Thus it can be divided into repeating unit cells (Figure 20a). Ideally the response of an entire laminate can be modeled using a single unit cell. This simplifies the problem and reduces effort and computational expense. A disadvantage of modeling a single unit cell is that the response of the laminate at the boundaries of the unit cell (**A-A** and **B-B** in Figure 20a) is unknown, yet any analytical or numerical analysis requires the imposition of some form of boundary condition at those locations.

In this study, a unit cell of a woven fabric composite was modeled using the boundary conditions illustrated in Figure 20. For both out-of-plane and thermal loading the ends of the unit cell ($x=0$, $x=L$) were constrained to remain straight and vertical. For in-plane loading the left end of the unit cell ($x=0$) was constrained to remain straight and vertical and the right end ($x=L$) was given a displacement corresponding to an axial strain $\varepsilon_x = 0.1\%$. In this appendix a comparison of the interfacial stress distributions for one and two unit cell models are made in order to test the validity of the boundary conditions stated above. The comparison is made for both in-plane and out-of-plane loading. No comparison is made for thermal

loading because the boundary conditions on the ends of the unit cell are the same for both the thermal loading and out-of-plane loading cases.

The analysis was done by building one unit cell and two unit cell finite element models of the $(F/W_2/F)_R$, R=4 laminate. The one unit cell model contained 452 elements and the two unit cell model contained 912 elements. This particular laminate was chosen because the undulations, which exhibit a complex stress distribution, are close to the ends of the models. Thus, this laminate provides a worst case test of the effect of the boundary conditions of the stress distribution in the laminate. The boundary and loading conditions for out-of-plane and in-plane loading corresponded to those illustrated in Figure 20b and c, respectively.

B.1 Out-Of-Plane Loading

The interfacial stress distributions of the one and two unit cell models subjected to out-of-plane loading are compared in Figure 139 through Figure 142. The in-plane stresses σ_x and σ_y show no variation in stress between the two models, nor does the interlaminar stress σ_z. The τ_{xz} distribution (Figure 142), however, does indicate a difference between the one and two unit cell models at region **B**. At $\frac{X}{\lambda} = 14$, τ_{xz} is zero in the one unit cell model but is approximately 7 psi in the two unit cell model. This difference is a direct result of the constraint on the one unit cell model that the laminate remain straight and vertical at x=L ($\frac{X}{\lambda} = 14$). This constraint prevents shear deformation of the laminate at the boundary of the laminate (x=L) and thus requires $\tau_{xz} = 0$. The two unit cell model is not constrained at $\frac{X}{\lambda} = 14$ and is thus allowed to shear.

The effects of the boundary conditions are also evident at regions **A** and **D**. At $\frac{X}{\lambda} = 0$ and $\frac{X}{\lambda} = 30$, τ_{xz} is zero. From the τ_{xz} distribution exhibited in region **B**, it can be concluded that should more than two unit cells of the laminate be modeled the distribution in region **D**

would be the same as that of the two unit cell distribution at **B** and that the true τ_{xz} distribution at region **A** should be the same as that at region **C**.

Away from the unit cell boundaries there is no difference in the τ_{xz} distributions between the one and two unit cell models, nor is there a difference in the maximum or minimum value of τ_{xz} in the laminate.

B.2 In-Plane Loading

The interfacial stress distributions of the one and two unit cell models are compared in Figure 143 through Figure 146. All components of stress show no variation with the number of unit cells mode u. This i attributed to two factors. First of all, under in-plane loading the right side of the model (x = L) is under load. Therefore, no artificial constraint exists at that location Secondly, under in-plane loading the interfacial stress distributions rapidly converge toward CLPT away from the undulation, and thus the boundary condition at x = 0 has no effect.

B.3 Conclusions

The results discussed above indicate that the boundary conditions on the one unit cell model have no influence on the stress distribution for the in-plane loading case. For the out-of-plane loading case only the interlaminar shear stress τ_{xz} is affected, and the effect is relatively small and limited to a small region near the boundary. Thus, it can be concluded that the woven fabric laminates analyzed in this study can be accurately modeled with a single unit cell.

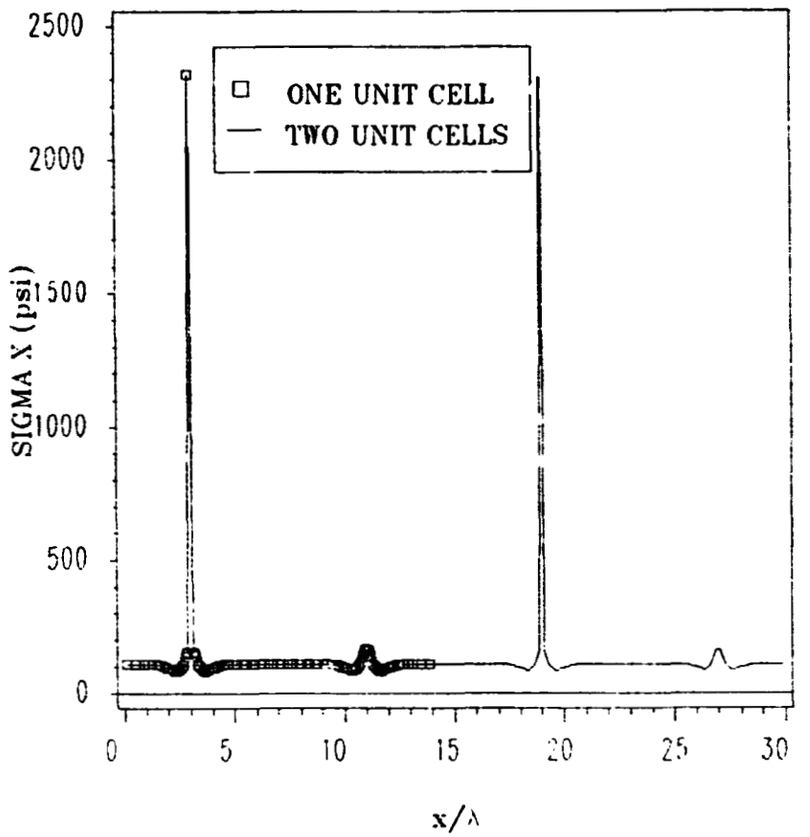

Figure 139. Comparison of interfacial σ_z distributions for one and two unit cell FEM models under out-of-plane loading: $(F/W_2/F)_t$ laminate, $R=4$, $\varepsilon_z=0.1\%$.

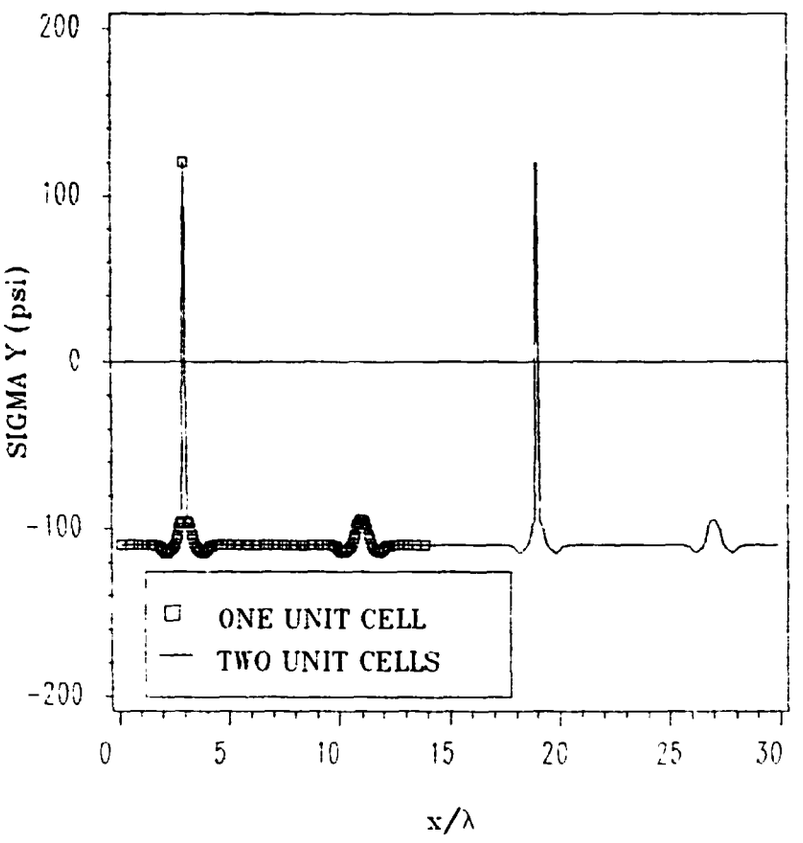

Figure 140. Comparison of interfacial σ_y distributions for one and two unit cell FEM models under out-of-plane loading: $(F/W_2^y/F)_f$ laminate, R = 4, $\varepsilon_z = 0.1\%$.

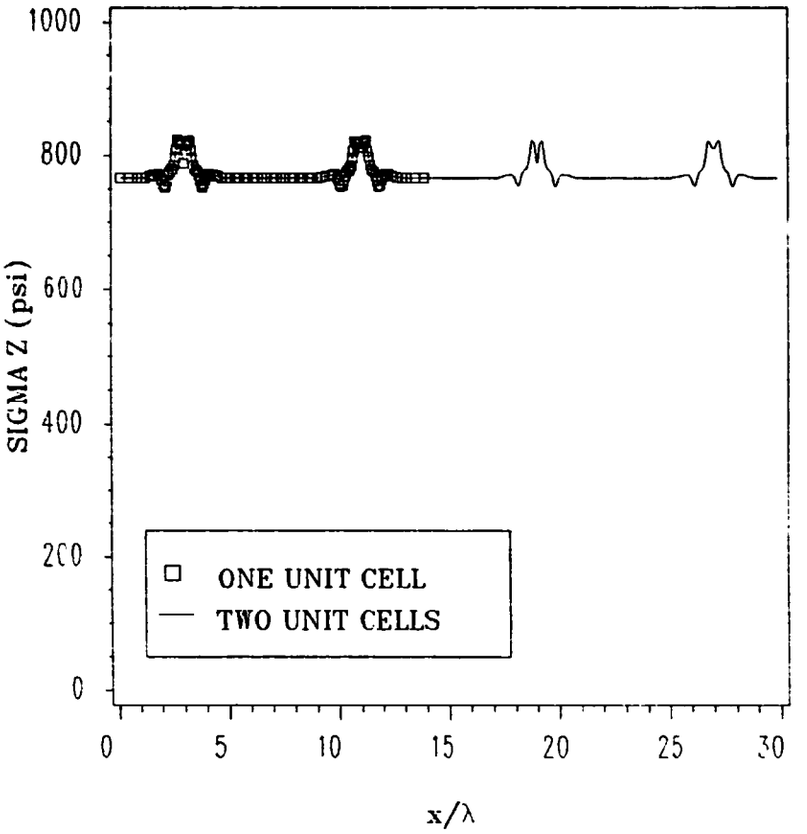

Figure 141. Comparison of interfacial σ_z distributions for one and two unit cell FEM models under out-of-plane loading: $(F/W_2/F)_1$ laminate, $R = 4$, $\varepsilon_z = 0.1\%$.

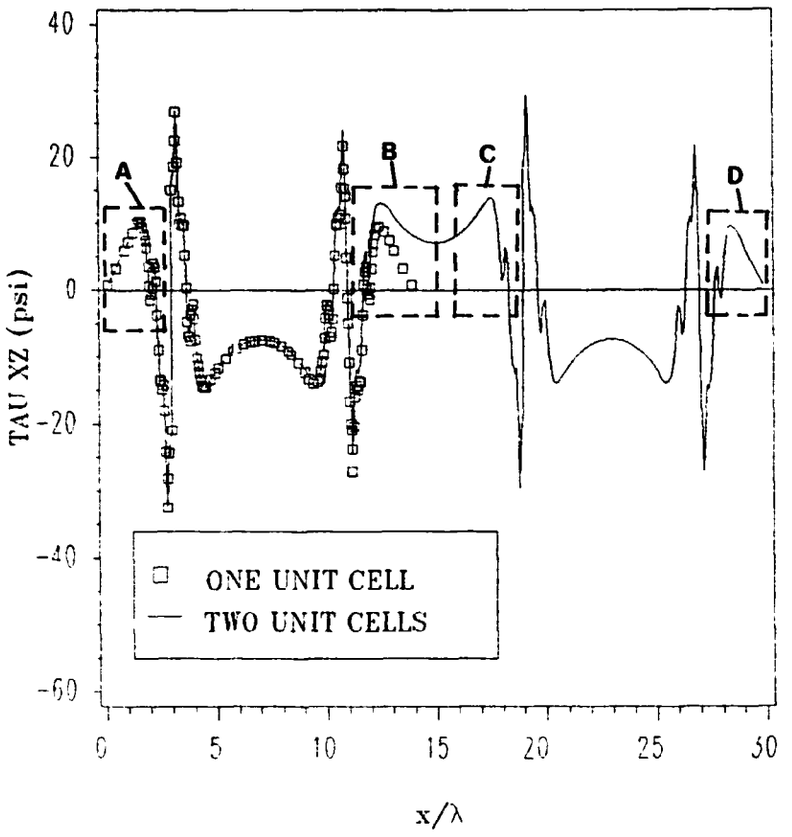

Figure 142. Comparison of interfacial τ_{xz} distributions for one and two unit cell FEM models under out-of-plane loading: $(F/W_2^{xz}/F)_t$ laminate, R = 4, $\varepsilon_z = 0.1\%$.

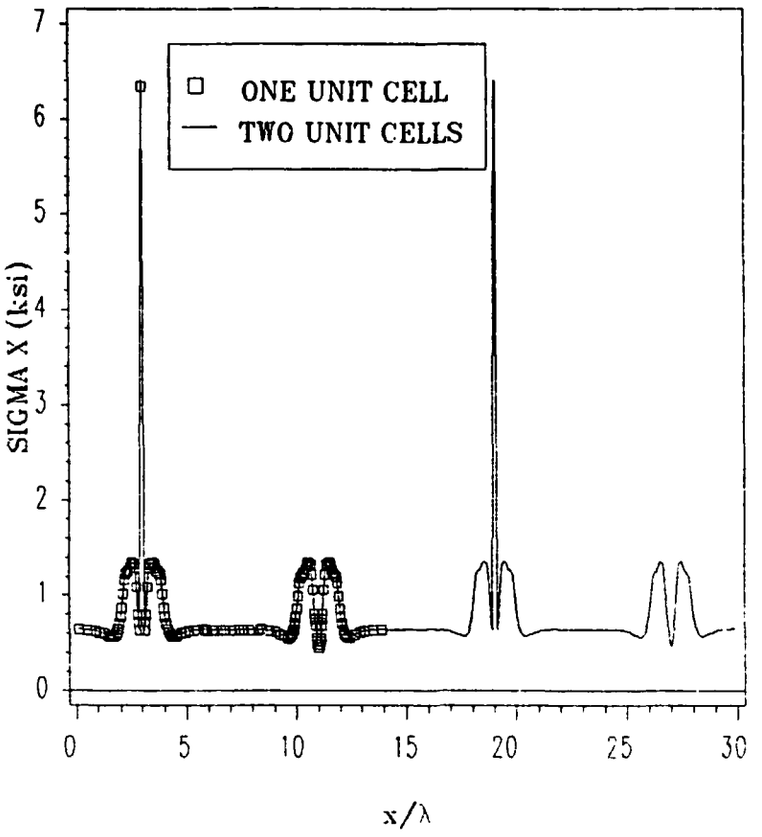

Figure 143. Comparison of interfacial σ_x distributions for one and two unit cell FEM models under axial loading: $:(F/W_2/F)_t$ laminate, $R = 4$, $\varepsilon_x = 0.1\%$.

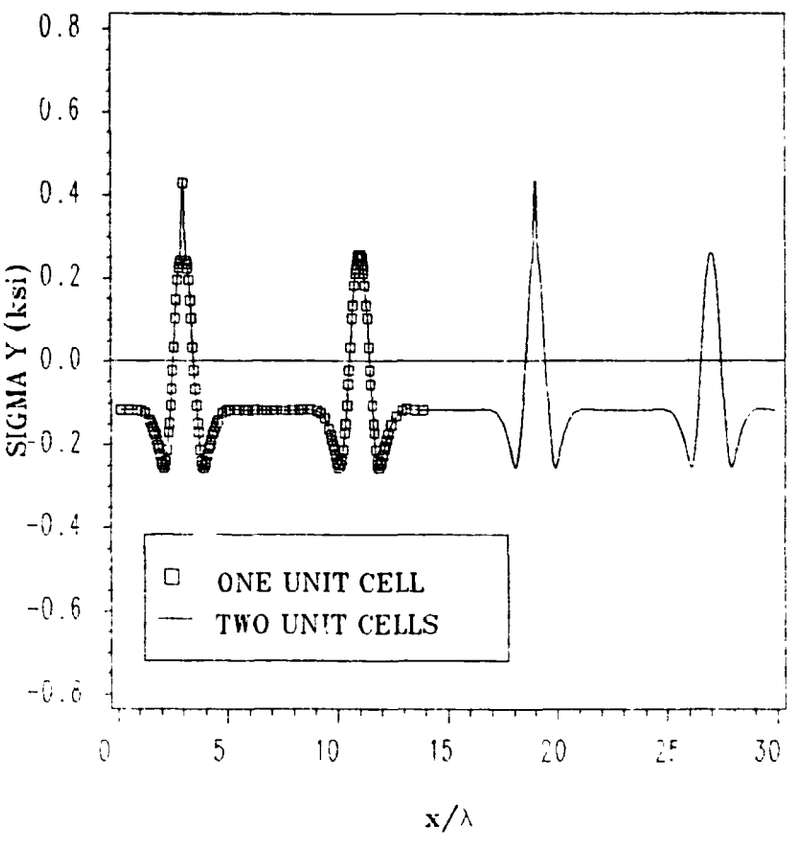

Figure 144. Comparison of interfacial σ_y distributions for one and two unit cell FEM models under axial loading: $(F/W_2/F)_t$ laminate, $R=4$, $\varepsilon_x=0.1\%$.

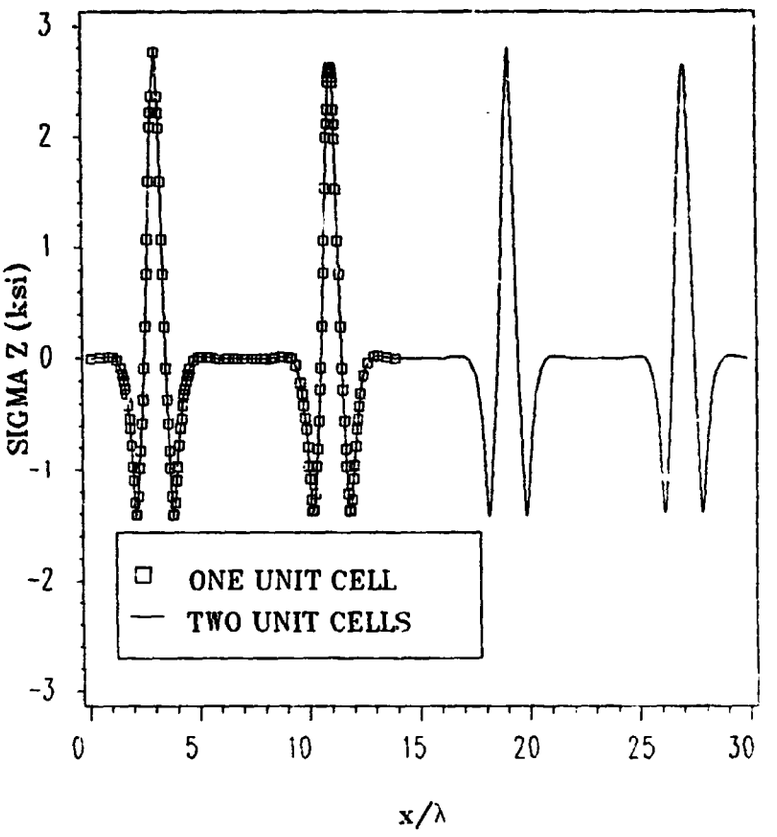

Figure 145. Comparison of interfacial σ_z distributions for one and two unit cell FEM models under axial loading: $(F/W_2/F)_t$ laminate, R = 4, ε_x = 0.1%.

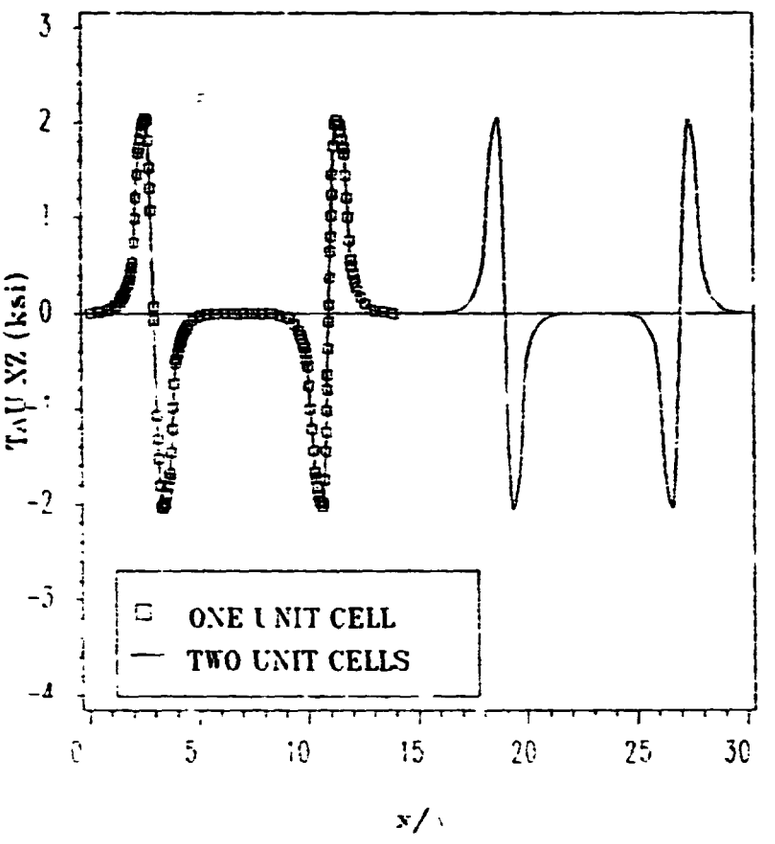

Figure 146. Comparison of interfacial σ_{zz} distributions for one and two unit cell FEM models under axial loading: $(F\ W_2/F)_1$ laminate, $R = 4$, $\varepsilon_a = 0.1\%$.

Appendix C. NVT3D User's Guide

C.1 Introduction

NVT3D is a linear elastic finite element code developed under the assumption of generalized plane strain. The assumption of generalized plane strain allows the user to study the response of an infinitely long body of arbitrary cross-section to various thermal-mechanical or hygro-mechanical loadings with the restriction that all quantities except axial displacement are independent of the axial coordinate z. This appendix is the user's guide to NVT3D. It contains the theoretical development of the finite element model for generalized plane strain and presents an overview of the program's capabilities, the input requirements, and output capabilities.

The formulation and assembly of the element stiffness matrices is based upon the method of Reddy [53]. The method of storing and solving the resulting system of equations is based upon the finite element program STAP (STatic Analysis Program) developed by Bathe and Wilson [54].

C.2 Generalized Plane Strain Finite Element Formulation

The most general displacement field for generalized plane strain problems can be written

$$u = U(x,y) \qquad [C.1a]$$

$$v = V(x,y) \qquad [C.1b]$$

$$w_0 = W(x,y) + \varepsilon_z z \qquad [C.1c]$$

The coordinate system used by NVT3D is shown in Figure 147. The x,y and z axes represent the global coordinate system while the material principal directions are represented by the 1,2 and 3 axes. The region to be modeled by finite elements is then a typical cross-section, which occupies the x-y plane.

For generalized plane strain the reduced from of the equilibrium equations are

$$\frac{\partial \sigma_x}{\partial x} + \frac{\partial \tau_{xy}}{\partial y} = 0 \qquad [C.2a]$$

$$\frac{\partial \tau_{xy}}{\partial x} + \frac{\partial \sigma_y}{\partial y} = 0 \qquad [C.2b]$$

$$\frac{\partial \tau_{xz}}{\partial x} + \frac{\partial \tau_{yz}}{\partial y} = 0 \qquad [C.2c]$$

and the reduced form of the strain-displacement relations are

$$\varepsilon_x = \frac{\partial u}{\partial x} \qquad [C.3a]$$

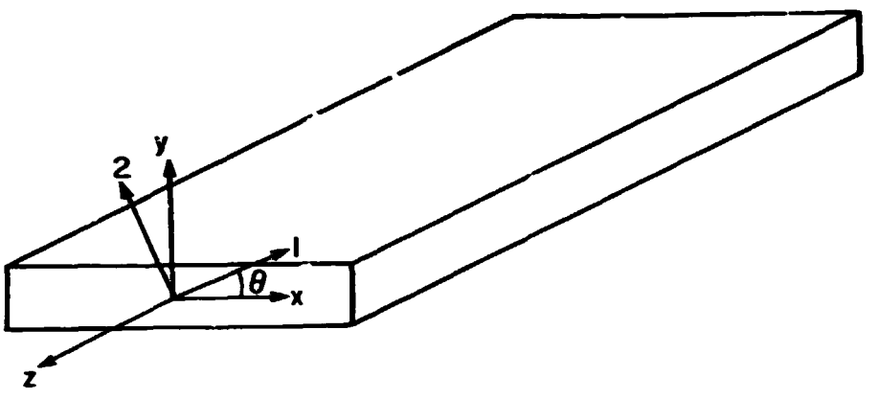

Figure 147. Definition of Material (1-2-3) and Global (x-y-z) Coordinate Systems Used in Finite Element Formulation

$$\varepsilon_y = \frac{\partial v}{\partial y} \qquad [C.3b]$$

$$\varepsilon_z = \frac{\partial w}{\partial z} \qquad [C.3c]$$

$$\gamma_{yz} = \frac{\partial w}{\partial y} \qquad [C.3d]$$

$$\gamma_{xy} = \frac{\partial u}{\partial y} + \frac{\partial v}{\partial x} \qquad [C.3e]$$

The linear stress-strain relationships are given by:

$$\begin{Bmatrix} \sigma_x \\ \sigma_y \\ \sigma_z \\ \tau_{yz} \\ \tau_{xz} \\ \tau_{xy} \end{Bmatrix} = [\bar{C}] \begin{Bmatrix} \varepsilon_x - \alpha_x \Delta T \\ \varepsilon_y - \alpha_y \Delta T \\ \varepsilon_z - \alpha_z \Delta T \\ \alpha_{yz} \\ \alpha_{xz} \\ \alpha_{xy} - \alpha_{xy} \Delta T \end{Bmatrix} \qquad [C.4]$$

$[\bar{C}]$ is the material stiffness matrix in terms of the global (x-y-z) coordinate system given by:

$$[\bar{C}] = [T_1]^{-1}[C][T_2] \qquad [C.5]$$

$[C]$ is the material stiffness matrix in the material (1-2-3) coordinate system and is given by:

$$[C] = \begin{bmatrix} C_{11} & C_{12} & C_{13} & 0 & 0 & 0 \\ . & C_{22} & C_{23} & 0 & 0 & 0 \\ . & & C_{33} & 0 & 0 & 0 \\ . & . & & C_{44} & 0 & 0 \\ . & sym. & & & C_{55} & 0 \\ . & & & & . & C_{66} \end{bmatrix} \qquad [C.6]$$

where:

$$C_{11} = \frac{1 - \nu_{23}\nu_{32}}{\Delta} E_{11} \qquad C_{12} = \frac{\nu_{12} + \nu_{13}\nu_{32}}{\Delta} E_{22} \qquad C_{13} = \frac{\nu_{13} + \nu_{12}\nu_{23}}{\Delta} E_{33}$$

$$C_{22} = \frac{1 - \nu_{13}\nu_{31}}{\Delta} E_{22} \qquad C_{23} = \frac{\nu_{23} + \nu_{21}\nu_{13}}{\Delta} E_{33} \qquad C_{33} = \frac{1 - \nu_{12}\nu_{21}}{\Delta} E_{33}$$

$$C_{44} = G_{23} \qquad C_{55} = G_{13} \qquad C_{66} = G_{12}$$

$$\Delta = 1 - \nu_{12}\nu_{21} - \nu_{13}\nu_{31} - \nu_{23}\nu_{32} - \nu_{12}\nu_{23}\nu_{31} - \nu_{21}\nu_{13}\nu_{32}$$

and the transformation matrices $[T_1]$ and $[T_2]$ for a rotation θ about the z axis are given by:

$$[T_1] = \begin{bmatrix} m^2 & n^2 & 0 & 0 & 0 & 2mn \\ n^2 & m^2 & 0 & 0 & 0 & -2mn \\ 0 & 0 & 1 & 0 & 0 & 0 \\ 0 & 0 & 0 & m & -n & 0 \\ 0 & 0 & 0 & n & m & 0 \\ -mn & mn & 0 & 0 & 0 & m^2 - n^2 \end{bmatrix} \qquad [C.7a]$$

$$[T_2] = \begin{bmatrix} m^2 & n^2 & 0 & 0 & 0 & mn \\ n^2 & m^2 & 0 & 0 & 0 & -mn \\ 0 & 0 & 1 & 0 & 0 & 0 \\ 0 & 0 & 0 & m & -n & 0 \\ 0 & 0 & 0 & n & m & 0 \\ -2mn & 2mn & 0 & 0 & 0 & m^2 - n^2 \end{bmatrix} \qquad [C.7b]$$

where $m = \cos\theta \quad n = \sin\theta$

Substituting [C.3a-e] and [C.4] into [C.2a-c] yields the governing equations for the deformation of a plane elastic body under generalized plane strain:

$$\frac{\partial}{\partial x}\left[\bar{C}_{11}\left(\frac{\partial u}{\partial x} - \alpha_x \Delta T\right) + \bar{C}_{12}\left(\frac{\partial v}{\partial y} - \alpha_y \Delta T\right) + \bar{C}_{13}(\varepsilon_z - \alpha_z \Delta T)\right.$$

$$\left. + \bar{C}_{16}\left(\frac{\partial u}{\partial y} + \frac{\partial v}{\partial x} - \alpha_{xy} \Delta T\right)\right] + \frac{\partial}{\partial x}\left[\bar{C}_{16}\left(\frac{\partial u}{\partial x} - \alpha_x \Delta T\right) + \bar{C}_{26}\left(\frac{\partial v}{\partial y} - \alpha_y \Delta T\right)\right. \qquad [C.8a]$$

$$\left. + \bar{C}_{36}(\varepsilon_z - \alpha_z \Delta T) + \bar{C}_{66}\left(\frac{\partial u}{\partial y} + \frac{\partial v}{\partial x} - \alpha_{xy} \Delta T\right)\right] = 0$$

$$\frac{\partial}{\partial x}\left[\bar{C}_{16}\left(\frac{\partial u}{\partial x} - \alpha_x \Delta T\right) + \bar{C}_{26}\left(\frac{\partial v}{\partial y} - \alpha_y \Delta T\right) + \bar{C}_{36}(\varepsilon_z - \alpha_z \Delta T)\right.$$

$$\left. + \bar{C}_{66}\left(\frac{\partial u}{\partial y} + \frac{\partial v}{\partial x} - \alpha_{xy} \Delta T\right)\right] + \frac{\partial}{\partial x}\left[\bar{C}_{12}\left(\frac{\partial u}{\partial x} - \alpha_x \Delta T\right) + \bar{C}_{22}\left(\frac{\partial v}{\partial y} - \alpha_y \Delta T\right)\right. \qquad [C.8b]$$

$$\left. + \bar{C}_{23}(\varepsilon_z - \alpha_z \Delta T) + \bar{C}_{26}\left(\frac{\partial u}{\partial y} + \frac{\partial v}{\partial x} - \alpha_{xy} \Delta T\right)\right] = 0$$

$$\frac{\partial}{\partial x}\left[\bar{C}_{55}\frac{\partial w}{\partial x}\right] + \frac{\partial}{\partial y}\left[\bar{C}_{44}\frac{\partial w}{\partial y}\right] = 0 \qquad [C.8c]$$

However, an additional equation is needed to govern the axial strain (ε_z) response, which is a variable in the generalized plane strain formulation. Thus, the net axial force F_z must be specified. This is expressed mathematically as

$$\int \sigma_z dxdy = F_z \qquad [C.9a]$$

In terms of the displacements it is of the form:

$$\int\left\{\bar{C}_{13}\left(\frac{\partial u}{\partial x} - \alpha_x \Delta T\right) + \bar{C}_{23}\left(\frac{\partial v}{\partial y} - \alpha_y \Delta T\right)\right. \qquad [C.9b]$$

$$\left. + \bar{C}_{33}(\varepsilon_z - \alpha_z \Delta T) + \bar{C}_{36}\left(\frac{\partial u}{\partial y} + \frac{\partial v}{\partial x} - \alpha_{xy}\Delta T\right)\right\} dxdy = F_z$$

Taking the variational form of [C.8a-c] and [C.9b], and separating them into terms associated with the primary variables u, v, w, and ε_z, yields the following finite element stiffness matrix:

$$[K^{11}] = \int\left(\bar{C}_{11}\frac{\partial \psi_i}{\partial x}\frac{\partial \psi_j}{\partial x} + \bar{C}_{16}\frac{\partial \psi_i}{\partial x}\frac{\partial \psi_j}{\partial y} + \bar{C}_{16}\frac{\partial \psi_i}{\partial y}\frac{\partial \psi_j}{\partial x} + \bar{C}_{66}\frac{\partial \psi_i}{\partial y}\frac{\partial \psi_j}{\partial y}\right)dxdy \qquad [C.10a]$$

$$[K^{12}] = \int\left(\bar{C}_{12}\frac{\partial \psi_i}{\partial x}\frac{\partial \psi_j}{\partial y} + \bar{C}_{16}\frac{\partial \psi_i}{\partial x}\frac{\partial \psi_j}{\partial x} + \bar{C}_{26}\frac{\partial \psi_i}{\partial y}\frac{\partial \psi_j}{\partial y} + \bar{C}_{66}\frac{\partial \psi_i}{\partial y}\frac{\partial \psi_j}{\partial x}\right)dxdy \qquad [C.10b]$$

$$[K^{22}] = \int\left(\bar{C}_{26}\frac{\partial \psi_i}{\partial x}\frac{\partial \psi_j}{\partial y} + \bar{C}_{66}\frac{\partial \psi_i}{\partial x}\frac{\partial \psi_j}{\partial x} + \bar{C}_{22}\frac{\partial \psi_i}{\partial y}\frac{\partial \psi_j}{\partial y} + \bar{C}_{26}\frac{\partial \psi_i}{\partial y}\frac{\partial \psi_j}{\partial x}\right)dxdy \qquad [C.10c]$$

$$[K^{33}] = \int\left(\bar{C}_{55}\frac{\partial \psi_i}{\partial x}\frac{\partial \psi_j}{\partial x} + \bar{C}_{44}\frac{\partial \psi_i}{\partial y}\frac{\partial \psi_j}{\partial y}\right)dxdy \qquad [C.10d]$$

$$[K^{14}] = \int\left(\frac{\partial \psi_i}{\partial x}\bar{C}_{13} + \frac{\partial \psi_j}{\partial y}\bar{C}_{36}\right)dxdy \qquad [C.10e]$$

$$[K^{24}] = \int\left(\frac{\partial\psi_i}{\partial x}\bar{C}_{36} + \frac{\partial\psi_i}{\partial y}\bar{C}_{23}\right)dxdy \qquad [C.10f]$$

$$[K^{34}] = 0 \qquad [C.10g]$$

$$[K^{44}] = \bar{C}_{33} \qquad [C.10h]$$

$$[K_{ij}^{21}] = [K_{ji}^{12}] \qquad [K^{13}] = [K^{23}] = [K^{32}] = [K^{31}] = 0 \qquad [C.10i]$$

The equations on the secondary variables are

$$\{F^1\} = \int\left\{\frac{\partial\psi_i}{\partial x}\left(\bar{C}_{11}\alpha_x\Delta T + \bar{C}_{12}\alpha_y\Delta T + \bar{C}_{13}\alpha_z\Delta T + \bar{C}_{16}\alpha_{xy}\Delta T\right)\right. \qquad [C.11a]$$
$$\left. + \frac{\partial\psi_i}{\partial y}\left(\bar{C}_{16}\alpha_x\Delta T + \bar{C}_{26}\alpha_y\Delta T + \bar{C}_{36}\alpha_z\Delta T + \bar{C}_{66}\alpha_{xy}\Delta T\right)\right\}\Delta T dA + \int_\Gamma \psi_i t_y d\Gamma$$

$$\{F^2\} = \int\left\{\frac{\partial\psi_i}{\partial x}\left(\bar{C}_{16}\alpha_x\Delta T + \bar{C}_{26}\alpha_y\Delta T + \bar{C}_{36}\alpha_z\Delta T + \bar{C}_{66}\alpha_{xy}\Delta T\right)\right. \qquad [C.11b]$$
$$\left. + \frac{\partial\psi_i}{\partial y}\left(\bar{C}_{12}\alpha_x\Delta T + \bar{C}_{22}\alpha_y\Delta T + \bar{C}_{23}\alpha_z\Delta T + \bar{C}_{26}\alpha_{xy}\Delta T\right)\right\}\Delta T dA + \int_\Gamma \psi_i t_x d\Gamma$$

$$\{F^3\} = \int_\Gamma \psi_i t_z d\Gamma \qquad [C.11c]$$

$$\{F^4\} = F_z \qquad [C.11d]$$

and represent the nodal forces and equivalent thermal loads.

The resulting system of linear equations is of the form:

$$[K^{11}]\{u\} + [K^{12}]\{v\} + [K^{13}]\{w\} + [K^{14}]\{\varepsilon_z\} = \{F^1\}$$

$$[K^{21}]\{u\} + [K^{22}]\{v\} + [K^{23}]\{w\} + [K^{24}]\{\varepsilon_z\} = \{F^2\} \qquad [C.12]$$

$$[K^{31}]\{u\} + [K^{32}]\{v\} + [K^{33}]\{w\} + [K^{34}]\{\varepsilon_z\} = \{F^3\}$$

$$[K^{41}]\{u\} + [K^{42}]\{v\} + [K^{43}]\{w\} + [K^{44}]\{\varepsilon_z\} = \{F^4\}$$

It should be noted that ε_z is not a nodal degree of freedom, but is constant over the entire model. Therefore, ε_z as a variable results in the addition of only one equation to the global stiffness matrix.

C.3 Element Geometries

Three elements are available in NVT3D. They are the 6-node triangular isoparametric element, the 8-node quadrilateral isoparametric element, and the SP-8 (SPecial 8-node) element. The geometries of the elements along with the node numbering and Gauss point numbering schemes are illustrated in Figure 148.

The 6-node triangular and 8-node quadrilateral elements are standard orthotropic elements. The SP-8 element has the same geometry and node numbering as the standard 8-node quadrilateral element, but in the SP-8 element the material stiffness matrix $[\bar{C}]$ is evaluated at each Gauss point in the element. This feature allows the material properties to vary within an element. It is useful where there is significant curvature in a model (e.g. axisymmetric geometries). This element allows curved geometries to be modelled more accurately with fewer elements.

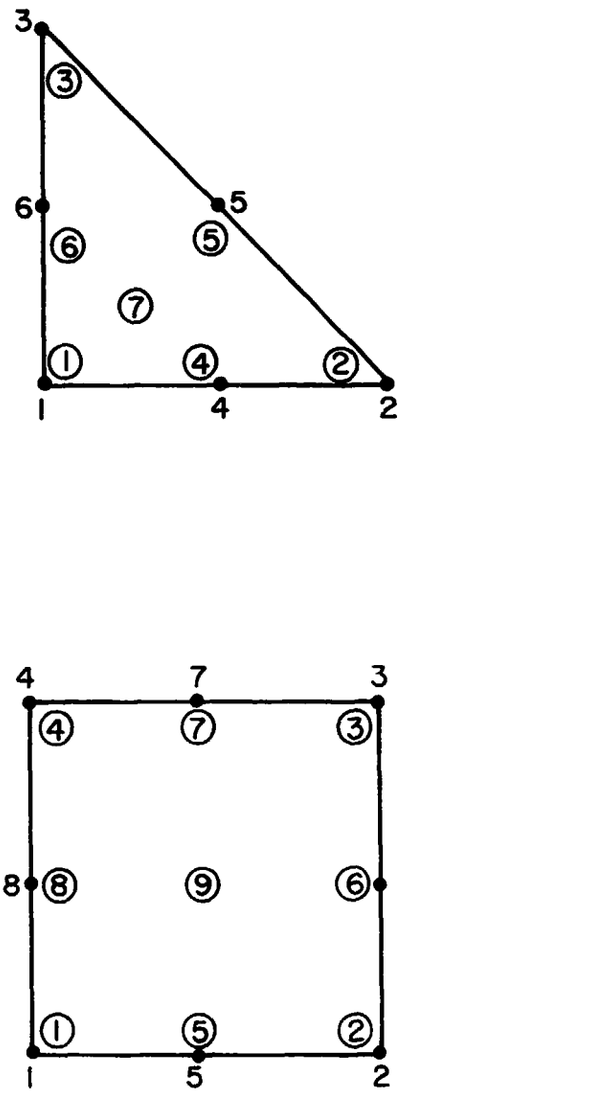

Figure 148. Available Element Geometries

C.3.1 Formulation and Use of the SP-8 Element

In practice, if a finite element is of a general two-dimensional shape, the integration of the [C.11] must be done numerically. The numerical integration is done by mapping the element into a "master" element which is a square for an 8-node element (Figure 149a). This method is convienent because the master element has constant limits of integration. The mapping functions are:

$$x = \Sigma x_i \psi_i \qquad [C.13a]$$

$$y = \Sigma y_i \psi_i \qquad [C.13b]$$

where x_i and y_i are the nodal coordinates in the global (x-y) system and $\psi_i = \psi_i(\xi, \eta)$ are the finite element interpolation functions.

Taking the derivative of [C.13] with respect to ξ yields the following equations:

$$\frac{\partial x}{\partial \xi} = \Sigma x_i \frac{\partial \psi_i}{\partial \xi} \qquad [C.14a]$$

$$\frac{\partial y}{\partial \xi} = \Sigma y_i \frac{\partial \psi_i}{\partial \xi} \qquad [C.14b]$$

Dividing [C.14b] by [C.14a] yields the form of the equation to determine the slope of any point in the global coordinate system with respect to the ξ axis:

$$\frac{\partial y}{\partial x} = \frac{\Sigma y_I \frac{\partial \psi_I}{\partial \xi}}{\Sigma x_I \frac{\partial \psi_I}{\partial \xi}} \qquad [C.15]$$

If the element material properties are described in the ξ-η coordinate system then the transformation angle θ between the material coordinate system and any point in the general element can be determined:

$$\theta = \tan^{-1}\left(\frac{\partial y}{\partial x}\right) \qquad [C.16]$$

Hence, the material stiffness matrix $[\bar{C}]$ can be calculated at any point in the element using [C.6-7].

This method is much simpler, though less general, than the parametric cubic modeling approach used by other researchers, which requires modification of the interpolation functions [58 59 60].

C.3.2 Implementation of SP-8 Element

To use the SP-8 element correctly, the correct element type must be specified (see INPUT REQUIREMENTS) and the material properties must be input such that the 1 and 2 directions in the material coordinate system correspond to the ξ and η directions, respectively, in the element. The best way to do that is to recall that the node numbering scheme is such that the line (or curve) formed by nodes 1, 5, and 2, lies along the ξ direction. As such, the following relationships hold.

$$E_1 = E_\xi \qquad E_2 = E_\eta \qquad E_3 = E_z$$

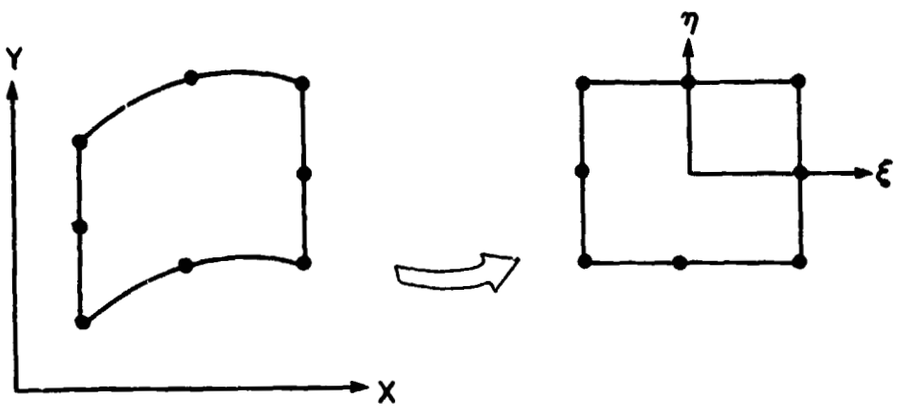

a) 8-Node Element of General Shape Mapped Into Master Element

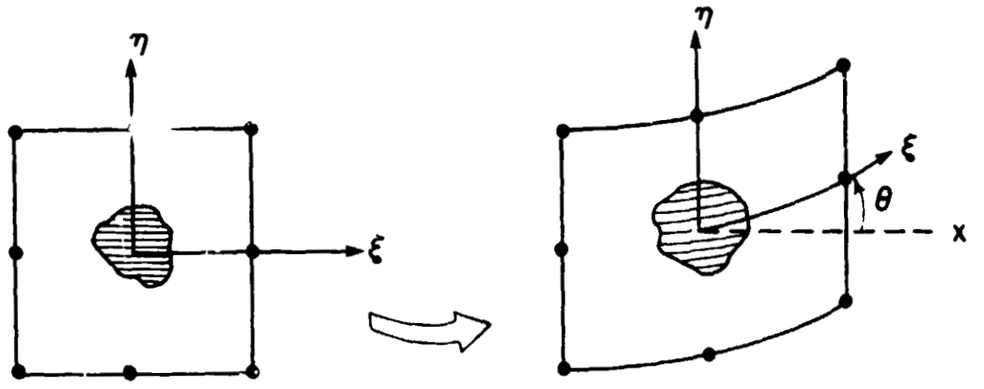

b) Transformation of Material Properties With Change In Element Shape

Figure 149. Mapping and Coordinate Transformation of SP-8 Element.

$$\nu_{23} = \nu_{\eta z} \qquad \nu_{13} = \nu_{\xi z} \qquad \nu_{12} = \nu_{\xi\eta}$$

$$G_{23} = G_{\eta z} \qquad G_{13} = G_{\xi z} \qquad G_{12} = G_{\xi\eta}$$

$$\alpha_1 = \alpha_\xi \qquad \alpha_2 = \alpha_\eta \qquad \alpha_3 = \alpha_z$$

Therefore, the user inputs the elastic constants in the ξ-η coordinate system and NVT3D calculates the transformation angle θ and subsequently $[\bar{C}]$ at each Gauss point in the element.

C.3.3 Verification of SP-8 Element

The accuracy of the SP-8 element was verified by comparing the finite element solution for a cylindrically orthotropic fiber under uniform thermal load with the elasticity solution presented in Chapter 4. The results were also compared with a finite element model using standard 8-node elements.

Two nine-element, quarter-symmetry finite models of a circumferentially orthotropic fiber under a uniform thermal load $\Delta T = 1°C$ were analyzed (Figure 150). Model **A** contained three 6-node triangular elements and six standard 8-node elements. The average transformation angle θ of each element was determined and entered into the input file. Model **B** contained three 6-node elements and six SP-8 elements. The average transformation angle θ was entered for the 6-node triangular element only. For the SP-8 elements the material properties were input such that the elastic constants in the 1-2 system corresponded to those of the ξ-η coordinate system.

The hoop, radial, and axial stresses (σ_θ, σ_r, and σ_z) of the three solutions are compared for each Gauss point in the model in Figure 151, Figure 152, and Figure 153, respectively. Since the problem is symmetric the stress distribution at all the Gauss points in the mesh should be equal. The results indicate excellent agreement between the elasticity solution and

the finite element solution using the SP-8 element. The difference between the solutions is less than 5% for all three components of stress. The finite element solution using the standard 8-node elements differs from the elasticity solution by up to 13% for σ_z and by up to 35% for the σ_θ and σ_r components of stress.

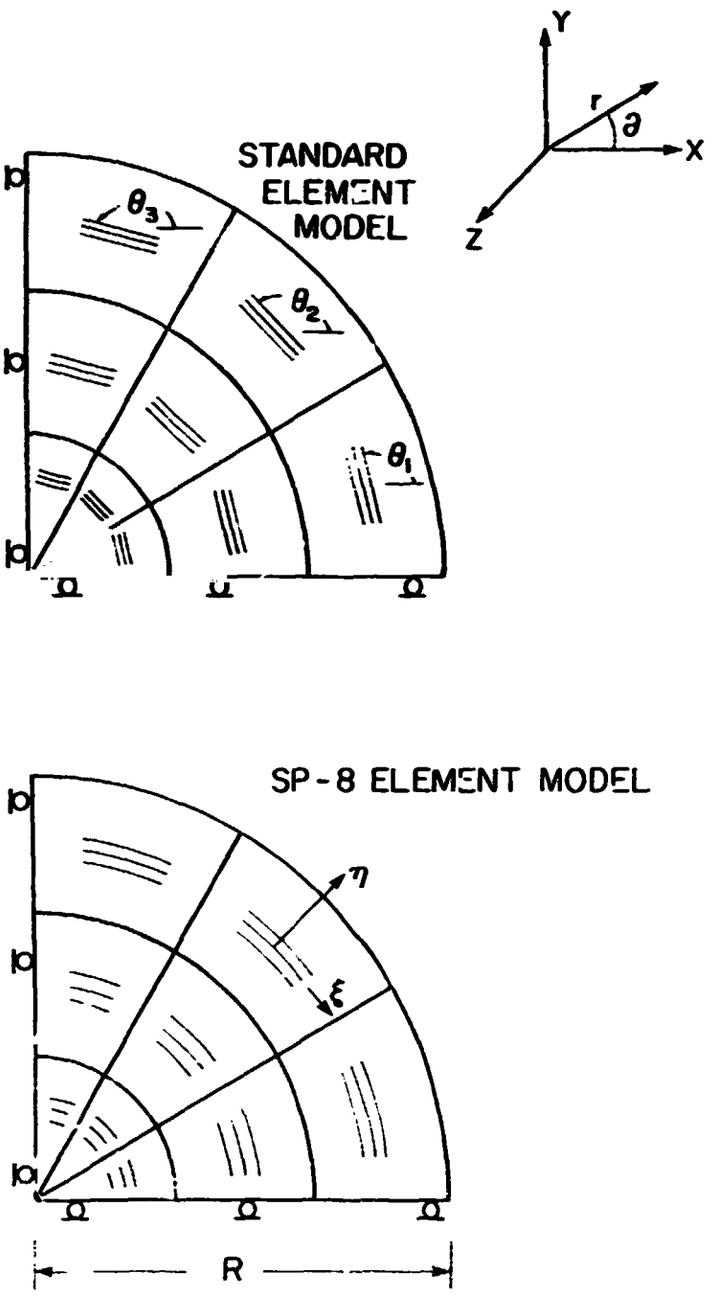

Figure 150. Finite element models of circumferentially orthotropic fiber under uniform thermal load. $\Delta T = 1°C$.

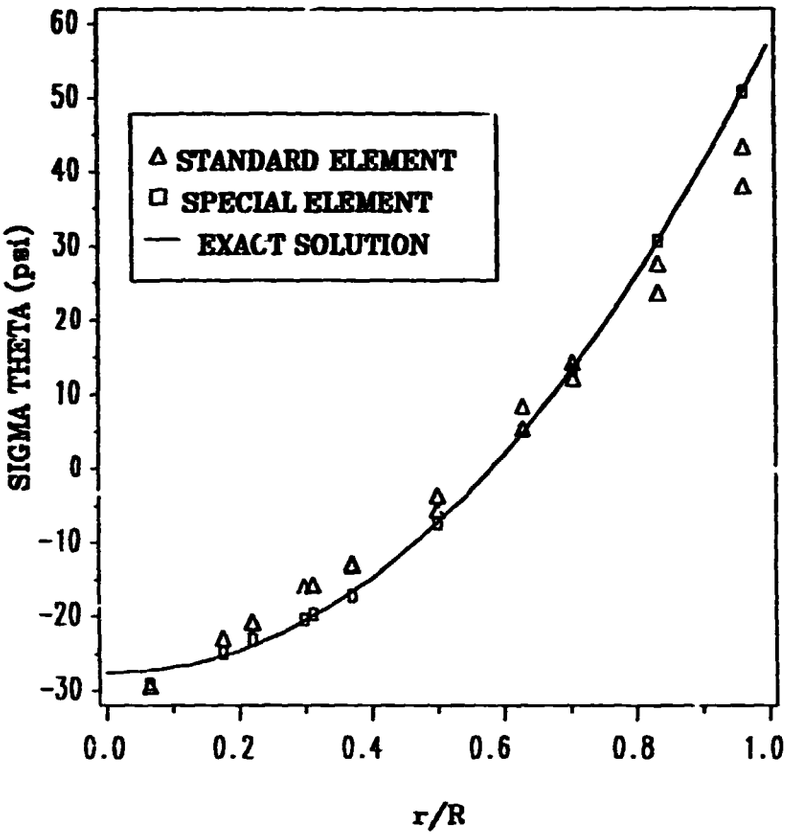

Figure 151. Comparison of FEM and exact solutions to σθ distribution for a fiber under thermal load.

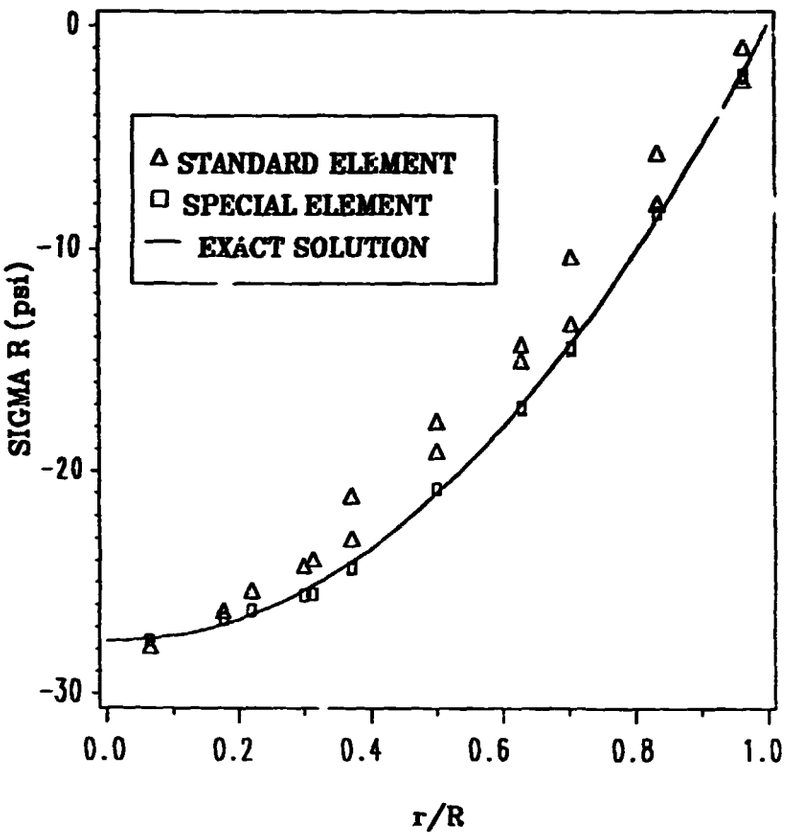

Figure 152. Comparison of FEM and exact solutions to σ_r distribution for a fiber under thermal load.

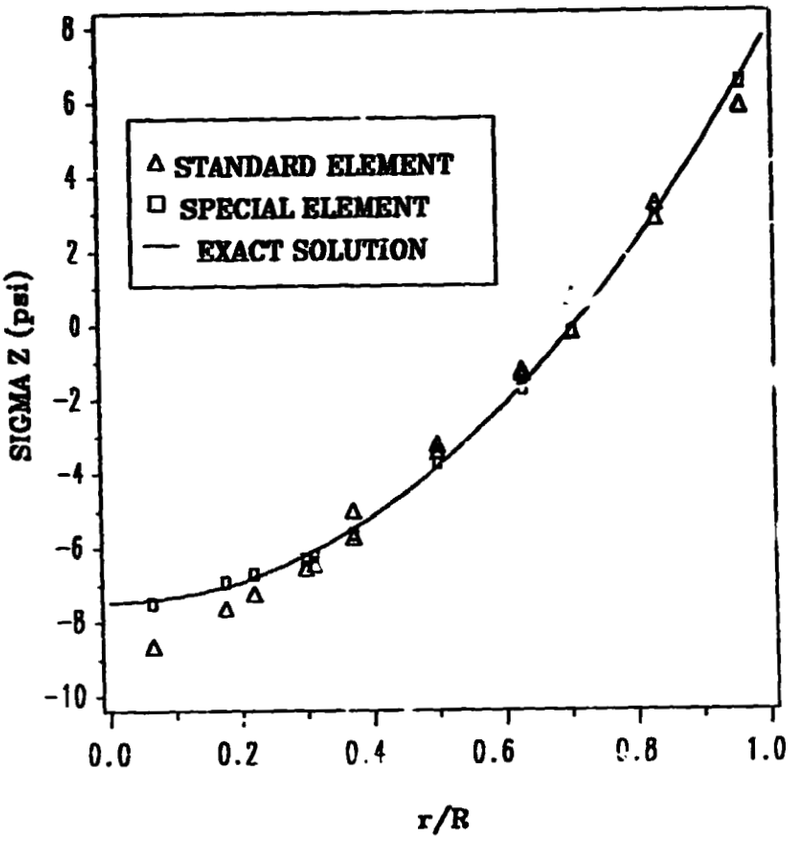

Figure 153. Comparison of FEM and exact solutions to σ_z distribution for a fiber under thermal load.

C.4 NVT3D Input Requirements

NVT3D was developed assuming that the input file would be submitted from a CRT and not typed on cards. Thus, the input structure has been designed such that there is room on each card for description(s) of the variable(s) that are read from that card. In this section a description of each type of card image in the input file is given. The required format of each card image is given in Section C.4.

- Title (Cards 1 and 2)
  - The title consists of two 80 character lines which will be printed on the output files and on the plots.
- Number of Element Groups (Card 3)
  - On this card the user specifies the number of element groups in the mesh. An element group consists of a set of elements, each having the same element type, the same material properties, and the same orientation θ (see Fig. 1).
- Number of Noues in the Mesh (Card 4)
- Nodal Coordinate X and Y Scale Factors (Card 5 & 6)
  - To ease input the user can specify scale factors which independently scale the magnitude of the x and y nodal coordinate values.
- Data Check Flag (Card 7)
  - This option allows the user to check the input without proceeding to the solution.

- **Print Nodal Coordinates (Card 8)**

  - **This option allows the user to inhibit the output of the nodal coordinates. This option is helpful in reducing the amount of output if multiple jobs are run using the same mesh. It should be noted that the nodal coordinates are always printed if the job is in the data check mode.**

- **Plotter Flags (Cards 9 & 10)**

  - **On this card the user sets the flags for plotting the undeformed and deformed meshes.**

- **Element Range to Plot (Card 11)**

  - **Sometimes it is desirable to plot just a portion of the finite element mesh. This option allows the user to specify the range of elements to be plotted.**

- **X and Y Offsets for Mesh Plot (Cards 12 & 13)**

  - **This option allows the user to shift the X and Y coordinates of the plots. It may be useful when using the 'Element Range to Plot' command (Card 11).**

- **Mesh Plot X and Y Scale Factors (Cards 14 & 15)**

  - **This option allows the user to scale the size of the plot. This option is especially useful when used with the Range to Plot card (Card 11) to plot very small elements. The y-coordinate scale factor (YMSCAL) must be set such that the maximum y-coordinate in the mesh will be scaled to a value less than or equal to nine inches.**

- **Maximum U and V Displacements (Cards 16 & 17)**

- This option allows the user to specify in inches the maximum u and v displacements. All of the smaller displacements are scaled proportionally to this value.

- Plane Strain/Plane Stress Flag (Card 18)
  - NVT2D: Specifies whether analysis is plane stress or plane strain.
  - NVT3D: Not used.
- Plate Thickness (Card 19)
  - Specifies the thickness of the plate being analyzed.
- Thermal Analysis Flag (Card 20)
  - This flag determines whether thermal (or hygro) analysis is implemented.
- Temperature Change (Card 21)
  - This card contains the temperature for thermal-mechanical loading or the moisture content for hygro-mechanical loading.
- Number of Specified Nodal Degrees of Freedom (Card 22)
  - The user inputs the number of specified displacements in the problem.
- Number of Specified Boundary Forces (Card 23)
  - The user inputs the number of specified forces in the problem.
- Number of Constrained Nodes (Card 24)

- The user has the option of specifying that certain nodes have the same, though unknown, displacements (e.g. an edge of a model must deform such that it remains straight). Examples of the use of this feature and the finite element formulation used to implement this feature can be found in Branca [55], Crane [56],and Adams [57]. This card specifies the number of nodes that are constrained to have the same displacement.

- Axial Load Flag (Card 25)

  - Specifies whether axial strain ε_z or average axial force F_z is applied.

- Magnitude of Axial Load (Card 26)

  - The user inputs the magnitude of the applied axial strain ε_z or the applied axial force F_z.

- Gauss Point Stress, Strain, and Strain Energy Dumps (Cards 27-29)

  - These options allow the user to dump all of the stresses, strains, and strain energies at all of the Gauss points to separate output files (see Output Capabilities for more information).

- Nodal Point Displacement Dump (Card 30)

  - This option allows the user to dump the displacements of all of nodes to a separate output file.

- Nodal Point Stress, Strain, and Strain Energy Dumps (Cards 31-33)

  - These options allow the user to dump all of the stresses, strains, and strain energies at all of the nodes to separate output files (see Output Capabilities for more information).

- **Element Group Data (Cards 34-40)**

  - ***Element Group Control Cards (Cards 34-39)***

    - ▲ **Card 34 is blank.**

    - ▲ **Card 35 contains the element type, the number of elements in the element group, the orientation angle of the elements with respect to the x-axis, and the parameter delta (delta is unused at this time).**

    - ▲ **Card 36 contains the elastic moduli E_1, E_2, and E_3.**

    - ▲ **Card 37 contains the Poisson's ratios ν_{23}, ν_{13}, and ν_{12}.**

    - ▲ **Card 38 contains the shear moduli G_{23}, G_{13} and G_{12}.**

    - ▲ **Card 39 contains the thermal expansion coefficients α_1, α_2 , and α_3 or the moisture expansion coefficients β_1, β_2 , and β_3.**

  - Element Connectivity and Print Card (Card 40)

    - ▲ This card contains the element connectivity matrix and output flags. This card is repeated for each element in the element group. See Fig. 2 for element numbering schemes.

  - Cards 34-40 are repeated NEG times, where NEG is the number of element groups in the mesh.

- Nodal Data Information (Card 41)

- The node number and node coordinates are specified on this card. Card 41 is repeated NNOD times, where NNOD is the number of nodes in the mesh.

- Specified Nodal Displacement Information (Card 42)

  - On this card the user identifies the node number, direction, and magnitude of the displacement of each specified degree of freedom. Card 42 is repeated NSDF times, where NSDF is the number of specified degrees of freedom.

- Specified Nodal Force Information (Card 43)

  - On this card the user specifies the node number, direction, and magnitude of each of the specified nodal forces. Card 43 is repeated NSBF times, where NSBF is the number of specified boundary forces. This card is omitted if NSBF equals zero.

- Specified Nodal Constraint Information (Card 44)

  - On this card the user specifies the node number and direction for each of the constrained degrees of freedom. This card is repeated NCON times, where NCON is the number of constrained displacements.

C.5 NVT3D Output Capabilities

NVT3D solves for the nodal displacements, stresses, strains, and strain energy densities for each element in the mesh. These values are calculated in the global (x, y, z) and principal material (1, 2, 3) coordinate systems.

The user has the ability to tailor the output file. By setting the output flags on Card 41, he can specify the output for each Gauss point and nodal point in the element. The output points for the eight-node and six-node elements are shown in Fig. 3.

To specify the Gauss point output for the eight-node element (six-node element) the Gauss point numbers for which output is desired are placed in columns 47-55 (47-53). For example, suppose output is desired for Gauss points 1, 3, 5, and 9. Columns 47-55 would therefore contain 135900000 . The order of the input does not matter. The input could be any of the following:

195300000

001090350

000013590

etc.

If output is desired for all of the Gauss points in the element columns 47-55 would read 123456789. If no output is desired for the element columns 47-55 would contain all zeros.

To specify the nodal output for the eight-node (six-node) element the local node numbers for which output is desired are placed in columns 57-64 (57-62). The input format is the same as that of the Gauss points.

It should be noted that the Gauss point output flags and the nodal point output flags are each read as one integer variable. This reduces execution time and the amount of memory required As a result, when the output flags are echoed to the output file a single zero will be printed in column 55 (53) if no Gauss point output is requested for the element. Similarly, if no nodal output is requested a single zero will be printed in column 64 (62).

Frequently it is desired to have all of the displacements, stresses, strains, or strain energy densities output in a format that is more conducive to post-processing. The output 'dump' flags (Card 7-33) allow the user to do this. Activating the appropriate flags will cause separate output files to be generated that contain the displacements, stresses, strains, or strain energy densities. Each line of the output file will contain the element number, the output point number (node number or Gauss point number), the coordinates of the output point, and

the values of the displacements, stresses, strains, or strain energy densities (depending on which flag is activated).

C.6 NVT3D Input Card Sequence

Card	Format	Variable	Contents
1	(20A4)	ITIT1	Title
2	(20A4)	ITIT2	Title
3	(T57,I2)	NEG	Number of Element Groups
4	(T57,I4)	NNOD	Number of Nodes in Mesh
5	(T57,E10.3)	XSCAL	X-Coordinate Scale Factor
6	(T57,E10.3)	YSCAL	Y-Coordinate Scale Factor
7	(T57,I1)	NCHK	Data Check Option
		0 = Data Check Mode	
		1 = Solution Mode	
8	(T57,I1)	NCPRT	Nodal Coordinate Print Option
		0 = Un-activated (unless NCHK = 0)	
		1 = Prints Nodal Coordinates	
9	(T57,I1)	MESHU	Undeformed Mesh Plot Option
		0 = No Plot	
		1 = Undeformed Mesh Plotted	
		2 = Undeformed Mesh Plotted (Node & Element No.)	
10	(T57,I1)	MESHD	Deformed Mesh Plot Option
		0 = No Plot	
		1 = Deformed Mesh Plotted If NCHK = 0	
11	(T57,I3,1X,I3)	LOWPLT	First Element Number Plotted
		IHIPLT	Last Element Number Plotted
		= 999 Then All Elements > = LOWPLT Plotted	

12	(T57,F8.4)	XOFF	X-Axis Offset of Plot
13	(T57,F8.4)	YOFF	Y-Axis Offset of Plot
14	(T57,E10.3)	XMSCAL	X-Coord. Scale Factor of Plot
15	(T57,E10.3)	YMSCAL	Y-Coord. Scale Factor of Plot
16	(T57,E10.3)	UMAX	Max. U Displ. of Deformed Mesh
17	(T57,E10.3)	VMAX	Max. V Displ. of Deformed Mesh
18	(T57,I1)	NPS	Plane Stress/Plane Strain Option
		0 = Plane Strain (NVT2D)	
		1 = Plane Stress (NVT2D)	
		Not Used By NVT3D	
19	(T57,E10.3)	THICK	Plate Thickness
20	(T57,I1)	NHEAT	Thermal/Hygro Analysis Option
		0 = No Thermal/Hygro Analysis	
		1 = Thermal/Hygro Analysis	
21	(T57,E10.3)	TEMP	Temperature/Moisture Content
22	(T57,I2)	NSDF	Number of Specified Displacements
23	(T57,I2)	NSBF	Number of Specified Forces
24	(T57,I2)	NCON	Number of Constrained Displacements
25	(T57,I2)	NEZ	Axial Load Flag
		0 = Axial Strain is Specified	
		1 = Axial Force is Specified	
26	(T57,E12.5)	VEZ	Magnitude of Axial Load
		= ε_z if NEZ = 0	
		= F_z if NEZ = 1	
27	(T57,I1)	NGP(1)	Gauss Point Stress Dump Option
		0 = Unactivated	
		1 = Global Coordinate System Only	
		2 = Local Coordinate System Only	
		3 = Global and Local Coordinate Systems	
28	(T57,I1)	NGP(2)	Gauss Point Strain Dump Option

0 = Unactivated
1 = Global Coordinate System Only
2 = Local Coordinate System Only
3 = Global and Local Coordinate Systems

29	(T57,I1)	NGP(3)	Gauss Pt. Strain Energy Dump Opt.

0 = Unactivated
1 = Activated

30	(T57,I1)	NPD(1)	Nodal Displacement Dump Option

0 = Unactivated
1 = Activated

31	(T57,I1)	NPD(2)	Nodal Stress Dump Option

0 = Unactivated
1 = Global Coordinate System Only
2 = Local Coordinate System Only
3 = Global and Local Coordinate Systems

32	(T57,I1)	NPD(3)	Nodal Strain Dump Option

0 = Unactivated
1 = Global Coordinate System Only
2 = Local Coordinate System Only
3 = Global and Local Coordinate Systems

33	(T57,I1)	NPD(4)	Nodal Strain Energy Dump Option

0 = Unactivated
1 = Activated

34		Blank Card
35	(T16,I1,T36,I4,T48,F6.2,T62,F6.2)	
	ITYPE	Element Type

1 = 6-Node Triangular Element
2 = Not Used
3 = 8-Node Quad. Element
4 = SP-8 Element

NUMEL	Number of Elements in Group

		ANGLE	Angle of Elements With Respect To Global Coordinate System
		DELTA	Not Used At This Time
36	(3(8X,E10.3))	PROP(1-3)	Elastic Moduli E_1, E_2, and E_3
37	(3(8X,E10.3))	PROP(4-6)	Poisson's Ratios ν_{23}, ν_{13}, ν_{12}
38	(3(8X,E10.3))	PROP(7-9)	Shear Moduli G_{23}, G_{13}, and G_{12}
39	(3(8X,E10.3))	PROP(10-12)	α_1, α_2, α_3 or β_1, β_2, β_3
40	(T2,6(1X,I4),T47,I7,T57,I6)		Six-Node Triangular Element
		NOD(1-6)	Element Connectivity Matrix
		KEYPT(1)	Gauss Point Print Flags
		KEYPT(2)	Nodal Print Flags
			or
	(T2,8(1X,I4),T47,I9,T57,I3)		Eight-Node Quadrilateral Element
		NOD(1-8)	Element Connectivity Matrix
		KEYPT(1)	Gauss Point Print Flags
		KEYPT(2)	Nodal Print Flags

Repeat Card 40 for each element in the element group.
Repeat Cards 34-40 for each element group in the mesh.

41	(Free-Format)		Input Nodal Coordinates
		IXY	Node Number
		X(IXY)	X-Coordinate of Node IXY
		Y(IXY)	Y-Coordinate of Node IXY
		Repeat Card 41 NNOD Times	
42	(Free-Format)		Input Specified Displacements
		ND	Node Number
		NUDIR(ND)	Direction of Specified Disp. (1 = u, 2 = v, 3 = w)
		VSD(ND)	Magnitude of Specified Disp.
		Repeat Card 42 NSDF Times	
43	(Free-Format)		Input Specified Forces
		NF	Node Number

		NFDIR(NF)	Direction of Specified Force (1 = u, 2 = v)
		VSF(NF)	Magnitude of Specified Force
		Repeat Card 43 NSBF Times Omit Card 43 IF NSBF = 0	
44	(Free-Format)		Input Constrained Displacements
		NCD	Node Number
		NCDIR(NCD)	Direction of Constrained Displacement (1 = u, 2 = v, 3 = w)
		Repeat Card 44 NCON Times Omit Card 44 IF NCON = 0	

C.7 Implementation of NVT3D

NVT3D was developed to run on and IBM 3090 operating under MVS or under VMBATCH.

C.7.1 Implementation under MVS

NVT3D may be executed under MVS by submitting the following files:

NVT3D JCL1

NVT3D FORTRAN

NVT3D JCL2

filename DATA

NVT3D JCL3

C.7.1.1 NVT3D JCL1

```
//Annnxxx JCB acct#,USERID,REGION=1500K,TIME=1
/*PRIORITY    IDLE
/*JOBPARM     LINES=50,CARDS=0
//STEP1 EXEC   FORTVCGV,PARM.FORT='NOSOURCE,NOSRCFLG'
//FORT.SYSIN DD *
```

where nnn is the user's output box number and xxx is the user's initials. The **REGION** and **TIME** statements may have to be changed depending on the size of the problem and the time needed for execution.

C.7.1.2 NVT3D JCL2

```
/*
//GO.FT06F001  DD SYSOUT=(A,,1)
//GO.PLOTLOG   DD SYSOUT=A
//GO.VECTR1    DD DSN=&&VECTR1,UNIT=3380,SPACE=(TRK,(10,1)),
//             DISP=(,PASS)
//GO.VECTR2    DD DSN=&&VECTR2,UNIT=3330,SPACE=(CYL,(5,1)),
//             DISP=(,PASS),DCB=(BLKSIZE=32002)
//GO.PLOTPARM  DD DUMMY
//GO.FT08F001  DD SYSOUT=(A,,2)
//GO.FT09F001  DD SYSOUT=(A,,3)
//GO.FT11F001  DD SYSOUT=(A,,4)
//GO.FT12F001  DD SYSOUT=(A,,5)
//GO.FT15F001  DD DUMMY
//GO.SYSIN  DD *
```

C.7.1.3 NVT3D JCL3

```
/*
//
```

C.7.2 Implementation Under VMBATCH

NVT3D may be submitted under VMBATCH by submitting the file NVTBATCH.

C.7.2.1 NVTBATCH EXEC

```
&TRACE ALL
CP LINK userid 191 100 RR password
&IF &RETCODE NE 0 &GOTO -ERRORS
ACCESS 100 B
&IF &RETCODE NE 0 &GOTO -ERRORS
GLOBAL TXTLIB VLNKMLIB VSF2FORT VPIUTIL CMSLIB TCSLIB AGIILIB PREVIEW
GLOBAL LOADLIB VSF2LOAD
&IF &RETCODE NE 0 &GOTO -ERRORS
&IFN = datafile
&2 = DATA
&3 = A1
&4 = OUT
FILEDEF 05 DISK &IFN &2 B
FILEDEF 06 DISK &IFN &4 &3
FILEDEF 08 DISK &IFN DISP &3 (RECFM U BLKSIZE 132
FILEDEF 09 DISK &IFN STRAINX &3 (RECFM U BLKSIZE 132
FILEDEF 12 DISK &IFN STRESS1 &3 (RECFM U BLKSIZE 132
FILEDEF 11 DISK &IFN STRESSX &3 (RECFM U BLKSIZE 132
FILEDEF 13 DISK &IFN ENERGY &3 (RECFM U BLKSIZE 132
FILEDEF 14 DISK &IFN STRAIN1 &3 (RECFM U BLKSIZE 132
LOAD NVT3D (CLEAR START
EXEC SENDFILE &IFN &4 &3 TO userid
EXEC SENDFILE &IFN DISP &3 TO userid
EXEC SENDFILE &IFN STRAINX &3 TO userid
EXEC SENDFILE &IFN STRESS1 &3 TO userid
EXEC SENDFILE &IFN STRESSX &3 TO userid
EXEC SENDFILE &IFN ENERGY &3 TO userid
EXEC SENDFILE &IFN STRAIN1 &3 TO userid
&EXIT
-ERRORS
&TYPE EXEC TERMINATING BECAUSE OF ERRORS
&TYPE RETCODE = &RETCODE
&EXIT
```

where **userid** is the account from which the program is being executed, **password** is the read password of the A-disk of the account, and **datafile** is the finite element data file. VMBATCH uses the compiled version of the source code; therefore, NVT3D TEXT must be on the A-disk in order for the program to run. Also, NVT3D must be compiled using Version 2 of VS Fortran.

The data file must be in the 80-column, fixed-format mode. When run under VMBATCH, NVT3D will not produce plots of deformed and undeformed meshes, and the job will abort if the plot flags are activated.

VIRGINIA TECH CENTER FOR COMPOSITE MATERIALS AND STRUCTURES

The Center for Composite Materials and Structures is a coordinating organization for research and educational activity at Virginia Tech. The Center was formed in 1982 to encourage and promote continued advances in composite materials and composite structures. Those advances will be made from the base of individual accomplishments of the forty members who represent ten different departments in two colleges.

The Center functions through an Administrative Board which is elected yearly and a Director who is elected for a three-year term. The general purposes of the Center include:

- collection and dissemination of information about composites activities at Virginia Tech,
- contact point for other organizations and individuals,
- mechanism for collective educational and research pursuits,
- forum and agency for internal interactions at Virginia Tech.

The Center for Composite Materials and Structures is supported by a vigorous program of activity at Virginia Tech that has developed since 1963. Research expenditures for investigation of composite materials and structures total well over seven million dollars with yearly expenditures presently approximating two million dollars.

Research is conducted in a wide variety of areas including design and analysis of composite materials and composite structures, chemistry of materials and surfaces, characterization of material properties, development of new material systems, and relations between damage and response of composites. Extensive laboratories are available for mechanical testing, nondestructive testing and evaluation, stress analysis, polymer synthesis and characterization, material surface characterization, component fabrication, and other specialties.

Educational activities include eight formal courses offered at the undergraduate and graduate levels dealing with the physics, chemistry, mechanics, and design of composite materials and structures. As of 1984, some 43 Doctoral and 53 Master's students have completed graduate programs and several hundred Bachelor-level students have been trained in various aspects of composite materials and structures. A significant number of graduates are now active in industry and government.

Various Center faculty are internationally recognized for their leadership in composite materials and composite structures through books, lectures, workshops, professional society activities, and research papers.

MEMBERS OF THE CENTER

Aerospace and Ocean Engineering
- Raphael T. Haftka
- Eric R. Johnson
- Rakesh L. Kapania

Chemical Engineering
- Donald G. Baird

Chemistry
- James E. McGrath
- Thomas C. Ward
- James P. Wightman

Civil Engineering
- R. M. Barker

Electrical Engineering
- Ioannis M. Besieris
- Richard O. Claus

Engineering Science and Mechanics
- Hal F. Brinson
- Robert Czarr
- David Dillard
- Norman E. L[illegible]g
- John C. Duke, Jr.
- Daniel Frederick
- O. Hayden Griffin, Jr.
- Zafer Gurdal
- Robert A. Heller
- Edmund G. Henneke, II
- Carl T. Herakovich
- Robert M. Jones
- Liviu Librescu
- Alfred C. Loos
- Don H. Morris
- John Morton
- Ali H. Nayfeh
- Marek Pindera
- Daniel Post
- J. N. Reddy
- Kenneth L. Reifsnider
- C. W. Smith
- Wayne W. Stinchcomb
- Surot Thangjitham

Industrial Engineering and Operations Research
- Joel A. Nachlas

Materials Engineering
- D. P. H. Hasselman
- Robert E. Swanson

Mathematics
- Werner E. Kohler

Mechanical Engineering
- Charles E. Knight

Inquiries should be directed to:

Center for Composite Materials and Structures
College of Engineering
Virginia Tech
Blacksburg, VA 24061
Phone: (703) 961-4969